

Dissertation zur Erlangung des Doktorgrades
der Fakultät für Chemie und Pharmazie
der Ludwig-Maximilians-Universität München

Design of photoelectrode morphologies for solar-driven water splitting

Ilina Tihomirova Kondofersky

aus

Sofia, Bulgarien

2016

Erklärung

Diese Dissertation wurde im Sinne von § 7 der Promotionsordnung vom 28. November 2011 von Herrn Prof. Dr. Thomas Bein betreut.

Eidesstattliche Versicherung

Diese Dissertation wurde eigenständig und ohne unerlaubte Hilfe bearbeitet.

München, den 12.05.2016

Ilina Kondofersky

Dissertation eingereicht am 12.05.2016

1. Gutachter: Prof. Dr. Thomas Bein
2. Gutachter: PD Dr. Dina Fattakhova-Rohlfing

Mündliche Prüfung am 28.06.2016

Acknowledgements

First and foremost I want to thank my supervisor Prof. Dr. Thomas Bein for the great research topic and the constant support and encouragement throughout my PhD study. I have always been amazed by your positivity, enthusiasm, patience, kindness and generosity both in science and in private matters. I would like to thank you for the great atmosphere during my PhD and the knowledge I gained over the years in your group. Coming to work was always a pleasure!

I would like to thank PD Dr. habil. Dina Fattakhova-Rohlfing for her relentless support and for always having time for me, my questions and my manuscripts. Thank you for all the wonderful ideas, fruitful discussions and corrected manuscripts. Your door was always open! I also greatly appreciate your support in private life, including all the wonderful daughter discussions and all the pretty things which Lina kindly gave to Lea.

In addition, I would like to thank Prof. Dr. Christina Scheu for all the great collaborations and the wonderful work on so many different projects. You were always very supportive and it was always a pleasure to be around you.

I would like to express my gratitude to Prof. Laurie Peter for his great expertise and his enthusiasm. Your contributions are valued greatly.

Next, I would like to thank my collaboration partners: Alexander Müller for all the hours at the TEM and all the great discussions; Bruce Parkinson for introducing me to the world of novel mixed metal oxides, Halina Dunn for her great support in my first years of water splitting; Goran Štefanić for all the Rietveld refinements; Hamid Hajiyani and Prof. Dr. Rossitza Pencheva for the DFT calculations

The members of AK Bein have greatly contributed to my my personal and professional time in the group. I would like to thank my office mates Fabi, Mona, Sabrina, Stefan, Alex, Enrico,

Benni, Torben, Hans and Flo for the wonderful office hours. Further I would like to acknowledge my colleagues in the water splitting subgroup for all the support and great discussions. Last but not least, I would like to say thank you to all the group members for the great and unforgettable time.

A big thank you to the students Bernhard, Jonathan, Sabine, Marina, Kyle, Nedz and Zach, who worked with me on the different research topics and dealt with all my crazy ideas.

I would also like to thank the financial support provided by CeNS, NIM, SolTech and the DFG. My special thanks goes to the NIM Gender Support which provided special daycare support for my daughter. Silke Mayerl-Kink, thank you for all the wonderful work we did together for so many different students from so many different schools. It was a great experience bringing chemistry to young and motivated students, thank you for the support.

Most of all I would like to thank my amazing family who supported me throughout the years. For my parents who raised me with a love for science and supported me in all my pursuits. To my loving and encouraging husband Ivan, thank you for your patience and support. A big thanks to our daughter Lea for arranging all the sleepless nights, time to think about science, and all the laughs and love she has brought into our lives.

Abstract

Driven by climate change, rapid population growth and dwindling resources, research into alternative, sustainable energies is thriving. Solar-driven electrolysis has shown to be a promising technique used to generate clean energy from sunlight by splitting water into hydrogen and oxygen gas thus converting and storing the energy from sunlight as chemical energy.

This thesis focusses on the synthesis, characterization and application of nanostructured materials for energy conversion. By creating advanced host guest architectures or dual absorber layers the efficiency of well-known photoelectrolysis materials such as Fe_2O_3 or WO_3 was sufficiently increased. The use of nanostructured antimony doped SnO_2 (ATO) or WO_3 scaffolds as extended current collectors underneath the absorber layer (Fe_2O_3) showed to increase the electron diffusion length in the electrode thus decreasing recombination. Further the light harvesting efficiency was optimized by the increased scattering effects and absorbance of the film.

Another device optimization approach focused on the synthesis and nanostructuring of novel materials with complex composition. The synthesis of the ternary metal oxide, $\text{Fe}_{0.84}\text{Cr}_1\text{Al}_{0.16}\text{O}_3$, first discovered by combinatorial studies, was developed and applied for the production of meso- and macroporous layers for hydrogen production. Using transmission electron microscopy and energy-dispersive X-ray spectroscopy, phase separation into Fe- and Cr-rich phases was observed for both morphologies. Further, the inverse opal structure showed to have a very beneficial influence on the photoelectrochemical performance of the film generating the highest current densities reported so far for this system (0.69 mA cm^{-2} at 0.5 V vs. RHE), even at a very early onset potential of 1.1 V vs. RHE .

The concept of finding new materials for water splitting was continued with the implementation of Li doped CuO as an efficient photocathode generating a photocurrent density of up to 3.3 mA cm^{-2} at 0 V vs. RHE without the use of further catalysts. The material optimization achieved through doping with small concentrations of Li was confirmed by DFT calculations showing that Li shifts the position of the valence and conduction band making $\text{Li}_x\text{Cu}_{1-x}\text{O}$ a semiconductor with a very pronounced p-type semiconductor behavior. Further, Li doping leads to a decrease in hydrogen absorption energy reducing the total reaction overpotential according to Sabatier principle.

This thesis offers a broad spectrum of different materials, synthesis and nanostructuring techniques used for the successful preparation of photoabsorber materials. It is a representative example of how the combination of different approaches can increase the efficiency of photoelectrochemical devices utilizing incident sunlight as a renewable energy resource.

Table of contents

1	Introduction.....	1
1.1	Climate change and the role of a hydrogen economy	1
1.2	Introduction to photoelectrochemical water splitting.....	5
1.3	Semiconductor metal oxide photoabsorbers.....	9
1.4	‘New materials genome’	20
1.5	Fabrication of photoelectrodes via colloidal crystal templating	24
1.6	Scope of the thesis.....	31
1.7	References	31
2	Characterization techniques	46
2.1	X-ray Diffraction.....	46
2.2	Raman Spectroscopy	48
2.3	Scanning Electron Microscopy	49
2.4	Transmission Electron Microscopy.....	51
2.5	UV-Vis Spectroscopy.....	52
2.6	Photoelectrochemical Characterization.....	54
2.7	References	58
3	Electron collection in host-guest nanostructured hematite photoanodes for water splitting: the influence of scaffold doping density.....	60
3.1	Introduction	61
3.2	Results and Discussion.....	64
3.3	Conclusion.....	75
3.4	Experimental	75
3.5	Supporting Information	78
3.6	References	86
4	Dual Absorber WO ₃ /Fe ₂ O ₃ Host-Guest Architectures for Improved Charge Generation and Transfer in Photoelectrochemical Water Splitting.....	90
4.1	Introduction	91
4.2	Results and Discussion.....	93
4.3	Conclusion.....	103
4.4	Experimental	104
4.5	Supporting Information	105

4.6	References	108
5	Ultrasmall Co_3O_4 nanocrystals strongly enhance solar water splitting on mesoporous hematite.....	112
5.1	Introduction	114
5.2	Results and Discussion.....	115
5.3	Conclusion.....	126
5.4	Experimental	127
5.5	Supporting Information	129
5.6	References	138
6	Nanostructured ternary FeCrAl oxide photocathodes for water photoelectrolysis.....	144
6.1	Introduction	145
6.2	Results and Discussion.....	147
6.3	Conclusion.....	158
6.4	Experimental	159
6.5	Supporting Information	159
6.6	References	167
7	Li_xCuO photocathodes for improved hole collection efficiency in photoelectrochemical water splitting.....	172
7.1	Introduction	173
7.2	Results and Discussion.....	176
7.3	Conclusion.....	186
7.4	Experimental	186
7.5	Supporting Information	192
7.6	References	201
8	Conclusion and Outlook	204
9	Curriculum Vitae	207
10	Publications and Presentations.....	210
10.1	Publications	210
10.2	Oral presentations.....	211
10.3	Poster presentations.....	211

1 Introduction

1.1 Climate change and the role of a hydrogen economy

Climate change, once considered a problem of the future, has already shown its immense impact on nature causing sufficient temperature increase, floods, droughts as well as increase of sea and ocean levels worldwide. These effects, and many more, have been traced back to human activity of high coal, oil and gas burning in conjunction with deforestation around the globe. The industrial activities along with the habits of modern civilization have caused a sufficient increase of human-generated ‘greenhouse gases’ which have had a major contribution to the increase of global temperatures over the past 70 years. Greenhouse gases is a collective term for a mixture of carbon dioxide, methane, nitrous oxide, water vapor and chlorofluorocarbons trapping heat radiation from Earth towards space.

Over the past century carbon dioxide levels have increased from 280 to 400 parts per million recording the highest concentrations of CO₂ in the past 600 000 years¹. The observed increase is mainly attributed to fossil fuel combustion and has the greatest long-term impact on climate change. The levels of nitrous oxide have also increased because of commercial soil cultivation fertilizers, burning of fossil fuels or biomass. The release of methane is closely connected to agriculture (especially rice cultivation) or ruminant digestion accumulating in the atmosphere. Chlorofluorocarbon gases have a major contribution to the destruction of the ozone layer and are of synthetic origin only, making mankind again responsible for the uncontrolled release.

As a consequence of the changed greenhouse gas balance in the atmosphere, the Earth’s climate is changing. Global temperatures have increased by 1.4 °C since 1880 and nine of the ten warmest years have been recorded after the year 2000. The significant loss of arctic and

land ice has caused the global sea levels to rise by 178 mm in the last 100 years thus becoming an ongoing process with expected rise of sea level values of 3.39 mm per year¹.

To stabilize the current greenhouse gas concentrations and avoid further damaging interference with our climate many associations and organizations have been found such as The Intergovernmental Panel on Climate Change (IPCC) or the United Nations Framework Convention on Climate Change (UNFCCC). The main task of those associations is the assessment and evaluation of scientific, technical and economic reports. Based upon the observed, decisions concerning climate change are settled determining future industrial or environmental activities.

The latest conference of the United Nations Framework Convention on Climate Change (UNFCCC) in December 2015 was the first to decide on a historic agreement between 195 nations on limiting global warming to 2 °C relative to pre-industrial values². This treaty is a symbol for international cooperation of the member countries on how to reduce global warming and how to cope with the resulting consequences.

Preventing climate change is closely related to finding novel sustainable energy sources. To maintain the modern way of life without affecting the environment, different power generating technologies have to play in concert. Wind power, hydropower, geothermal energy, bio energy and solar energy are some of the most important representatives when renewable energy sources are discussed. The contribution of clean energy to the European electricity market was summarized for the first half of 2015 by the World Nuclear Association as follows: 107 TWh generated from wind power and 60 TWh generated from solar power translating into a capacity factor of 25 % and 18 %, respectively³.

Incident sunlight provides our Earth with 120 000 TW⁴ of solar power making solar energy the most prominent power source available. The incoming solar energy exceeds the energy demand of mankind by far. Therefore, if captured, stored and transported efficiently, solar radiation would be the best way to produce clean and renewable energy. Solar cells have a long history in capturing the sun's energy with efficiencies reaching 17 % for conventional polycrystalline silicon solar cells. Silicon solar cells have been utilized on the large scale providing private homes and even industry with clean energy. One of the major drawbacks, however, is the high production cost which emerges from the production of high purity, defect free silicon cells. This issue has been resolved by developing novel solar cells such as i.e. dye sensitized⁵ or perovskite⁶ cells. All novel technologies notwithstanding, there are still system characteristic drawbacks such as decreased efficiency or high toxicity which need to be addressed. Another main challenge of solar cells is the storage and transport efficiency of solar energy, given that the amount of energy lost during storage in a battery or transport over the electric lead is sufficient, leading to an overall efficiency of electrical energy storage of about 50-85 %. For this reason other technologies have been developed, such as photoelectrochemical water splitting which are capable of converting solar into chemical energy⁷.

'Hydrogen economy' refers to the concept of replacing fossil fuels with clean and storable hydrogen gas as an energy carrier to save the environment⁸. As hydrogen has the highest energy content per unit weight it has attracted great attention over the past decades⁹. When combusted no pollutants are emitted into the atmosphere and the only byproduct is water¹⁰. Pure hydrogen gas is not available on earth making the production from other sources such as alcohol, natural gas, biomass and water challenging and energy consuming. Currently, hydrogen is produced from natural gas which does not reduce the carbon footprint. To avoid further climate change low-carbon hydrogen generation through renewable energies should be

pursued and developed. Photoelectrochemical photovoltaic cells or solar-driven water splitting devices are important processes for the clean production of hydrogen.

For hydrogen to be a competitive alternative to other energy sources, an estimation of several aspects and costs such as production, compression, distribution, transfer and storage is essential. These factors need to be then compared to the energy content delivered by hydrogen. Production of hydrogen is often associated with high energy losses. These can be compensated if the energy needed to drive the reaction comes from a clean source as for example solar energy.

One of the main advantages of a hydrogen economy is the ease of storage of hydrogen gas, which can be stored before conversion to heat or power without the need of large-scale batteries allowing the access to chemical energy whenever needed.

Many experts see hydrogen as the fuel of the future^{7, 11-12}. Its flexibility and diverse application field makes hydrogen gas one of the most promising zero-emissions energy systems. Hydrogen-powered cars, buses and ships are just a few examples of hydrogen powering our transportation needs. Furthermore, hydrogen has also been employed as a backup or an off-grid power supply, delivering electricity or heat whenever needed. The chemical industry has rich experience with the handling and distribution of hydrogen on a large scale given the broad application field including fertilizer synthesis (ammonia), oil refining, and the use as a rocket fuel. The safe and efficient use of hydrogen can be transferred to other industrial and private applications thus creating an environmentally friendly and efficient power source.

1.2 Introduction to photoelectrochemical water splitting

Photoelectrochemical water splitting is an elegant process to efficiently utilize solar energy for production of hydrogen from water. The water splitting reaction is an uphill reaction for which the required energy of $\Delta G = 237.2 \text{ kJ mol}^{-1}$ is ideally generated by sunlight¹³.



$$\Delta G = +237.2 \text{ kJ mol}^{-1} \quad \Delta E^0 = 1.23 \text{ V} \quad (1-2)$$

The water splitting reaction consists of two half reactions, the hydrogen (HER) and oxygen (OER) evolution reaction, respectively¹³.



When immersed in electrolyte, the Fermi level of the semiconductor equilibrates with the redox potential of the electrolyte¹⁴. Upon illumination of the photoabsorber with photon energy equal or larger than the band gap electrons and holes ($\text{e}^- - \text{h}^+$) are generated. As a result the generated electrons are excited from the valence to the conduction band whereas the holes remain in the valence band. In an n-type semiconductor, a photoanode, the generated holes accumulate at the semiconductor surface where they participate in the water oxidation process thus generating oxygen. The generated electrons, on the other hand, are transported to the counter electrode via an external circuit where they are used for the water reduction reaction (Figure 1-1a)¹³. In order to generate oxygen gas with a photoanode the position of the valence band has to be more positive than the oxygen evolution potential. The hydrogen evolution

reaction takes place on a p-type semiconductor, a photocathode, where the generated electrons are transported to the semiconductor-electrolyte junction thus reducing water to hydrogen gas (Figure 1-1b). In the case of a photocathode the position of the conduction band has to be more negative than the hydrogen evolution potential¹⁴. Both hydrogen and oxygen generation reactions are driven by minority carriers of the photoelectrode. Ideally the water splitting reaction should occur on a photoanode and photocathode in tandem configuration (Figure 1-1c).

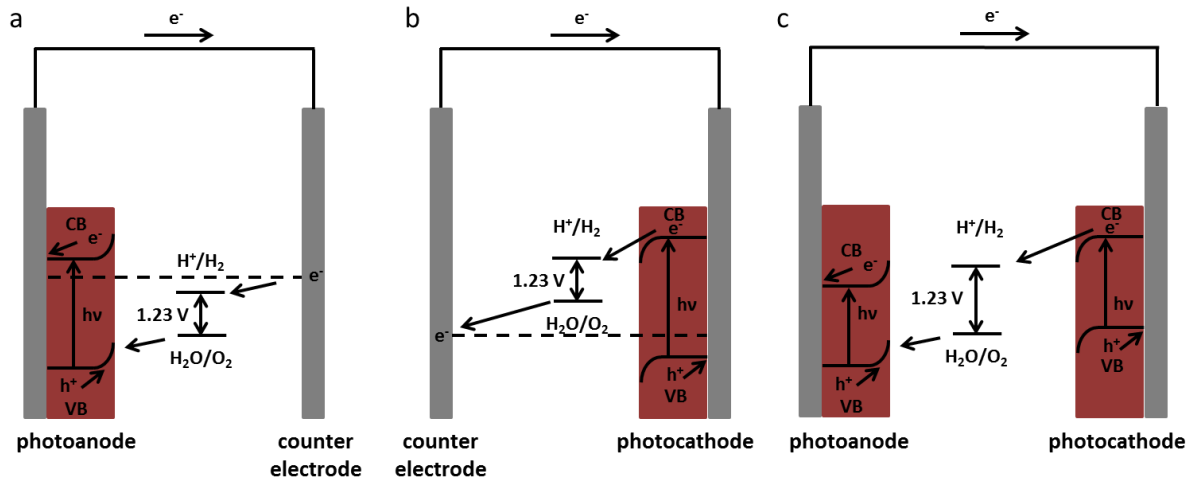


Figure 1-1: Energy diagrams of photoelectrochemical water splitting using a) a photoanode, b) a photocathode and c) a photoanode and cathode in a tandem cell configuration.

Several experimental techniques have been developed to estimate the efficiency of a photoabsorber. The solar-to-hydrogen conversion efficiency can be assessed under the assumption that the resulting current is completely generated by the water splitting reaction by applying the following equation¹⁴:

$$STH (\%) = \frac{\text{Output energy as } H_2}{\text{Energy of incident solar irradiation}} \times 100 \quad (1-5)$$

To improve the kinetics of/assist the water splitting reaction an external voltage can be applied to the system. In this case, the applied voltage has to be subtracted from the gained energy by applying equation 1-6 where j is the photocurrent density, V_{redox} the theoretical potential of the water splitting reaction (1.23 V) and V_{bias} the applied voltage resulting in the applied bias photon-to-current efficiency (ABPE)¹⁴⁻¹⁵.

$$ABPE = \frac{j \times (V_{redox} - V_{bias})}{\text{Energy of incident solar irradiation}} \quad (1-6)$$

The incident photon-to-current efficiency (IPCE) is a measure for the generated photocurrent (j_{photo}) at the intensity (P_{in}) of a corresponding wavelength (λ) according to equation 1-7¹⁶:

$$IPCE (\%) = \frac{\text{number of generated electrons}}{\text{number of incident photons}} \times 100 = \frac{1240 \times j_{photo}}{\lambda \times P_{in}} \times 100 \quad (1-7)$$

As the amount of the absorbed photons can be lower than that of incident ones due to light scattering and transmission effects, the absorbed photon-to-current efficiency (APCE) can be calculated by taking the number of absorbed photons directly into account. For this purpose, the light harvesting efficiency has to be assessed by UV-Vis spectroscopy and can be calculated from the wavelength dependent absorption coefficient $\alpha(\lambda)$ and the film thickness (d) as shown in equation (1-8)¹⁷.

$$\eta_{LH} = 1 - e^{-\alpha(\lambda)d} \quad (1-8)$$

The APCE can be determined by applying equation x thus evaluating the efficiency of a PEC device with respect to collected current density per absorbed photon:

$$APCE (\%) = \frac{IPCE}{\eta_{LH}} \quad (1-9)$$

The IPCE is also referred to as a product of the light harvesting efficiency (η_{LH}), the transfer efficiency (η_{trans}) and separation efficiency (η_{sep}) (equation 1-10)¹⁷.

$$IPCE (\%) = \eta_{LH} \cdot \eta_{trans} \cdot \eta_{sep} \quad (1-10)$$

The transfer efficiency can be experimentally determined by transient current measurements. When a photoabsorber is illuminated, electrons generated in the space charge region are rapidly transferred to the semiconductor electrolyte junction. Over time a considerable amount of electrons builds up at the interface until the rate of arrival of electrons is balanced by the rates of charge transfer and recombination resulting in a steady state current. The instantaneous photocurrent measured upon illumination corresponds to a charging current caused by the initial movement of generated electrons to the interface. The steady state photocurrent corresponds to the flux of electrons successfully transferred to the electrolyte without recombining with holes at the surface¹⁸⁻²¹. The ratio of steady state to instantaneous photocurrent is therefore generally considered as a measure for the transfer efficiency of minority carriers from the electrode to the electrolyte²¹:

$$\eta_{trans} = \frac{J_{ss}}{J_{inst}} = \frac{k_{trans}}{k_{trans} + k_{rec}} \quad (1-11)$$

Equation 1-11 describes the flux of minority carriers to the electrolyte under the assumption that both hole and electron transfer and recombination are pseudo first order with k_{trans} and k_{rec} being the first order rate constants for transfer and recombination, respectively.

The separation efficiency is the only factor which cannot be determined experimentally. Therefore, η_{sep} has to be calculated from the experimentally available factors (IPCE, η_{LH} and η_{trans}).

1.3 Semiconductor metal oxide photoabsorbers

Semiconductor materials play an important role as photoabsorbers for PEC water splitting. This chapter aims to give an overview of different materials used either for the HER or OER which have been studied over the past years.

In general there are several requirements which a photoabsorber should fulfill¹⁰⁻¹¹:

1. High light harvesting efficiency
2. Chemical stability during the PEC reaction
3. Suitable band positions with respect to the water oxidation and reduction potential
4. Efficient charge transport throughout electrode
5. Material abundancy/scalability
6. No/low toxicity
7. Low production costs

To evaluate the light harvesting efficiency of a semiconductor the solar irradiation spectrum should be considered. Sunlight (AM 1.5G) can be divided in three components: the infrared (IR) range ($\lambda < 800$ nm), the visible range ($800 > \lambda > 400$ nm) and the ultraviolet (UV) range ($\lambda < 400$ nm) which account for 49 %, 46 % and 5 % of the sun's radiation, respectively¹⁴. The solar spectrum region absorbed by the semiconductor depends on the corresponding band gap. Given the required energy to split water is 1.23 eV and considering some thermodynamic losses and overpotentials required for a reaction with fast kinetics, the minimum band gap is positioned at 1.9 eV which corresponds to an absorption at around 650 nm. Given the weak intensity of UV light below 400 nm the maximum band gap is estimated to be around 3.1 eV making the visible range of the solar spectrum essential for an efficient solar-to-hydrogen conversion (Figure 1-2).

$$\lambda \text{ (nm)} \leq 1240/E_g \text{ (eV)} \quad (1-12)$$

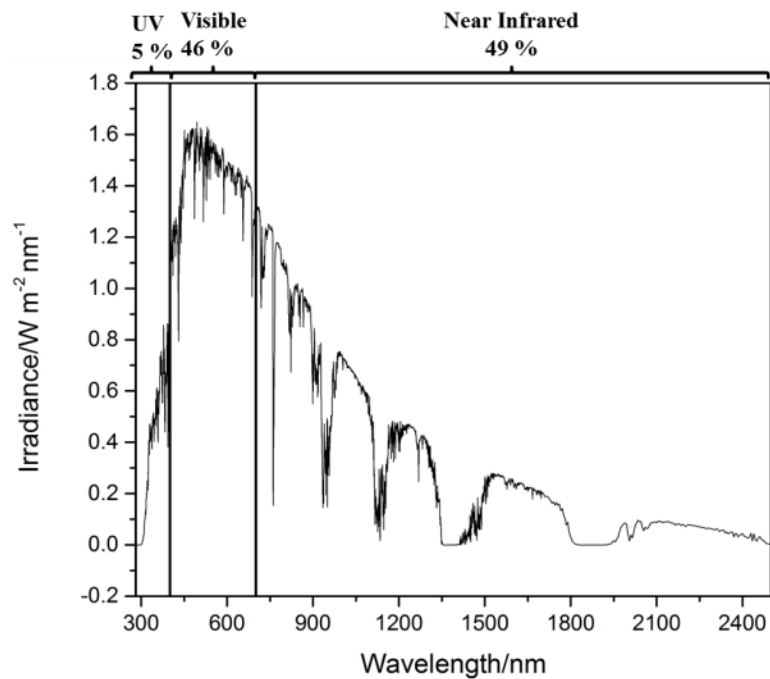


Figure 1-2: Air Mass 1.5 solar spectrum (AM1.5) with irradiance as a function of wavelength. The Air Mass defines the path incident light goes through the atmosphere normalized to the shortest path possible while considering the power loss of sunlight attributed to the absorption of light by air and dust.

The band gap is characteristic for each material²². Nevertheless, band gap engineering is a commonly applied technique used to enhance the band gap by introducing structural defects or impurities to the crystal structure resulting in change of optical properties influencing electron and charge transport properties in the materials, to some extent²³⁻²⁴. Doping is a representative example how the absorption of visible light can be enhanced by the formation of localized or delocalized electronic states²⁵⁻²⁶. Further, the electron-hole separation efficiency can be substantially optimized.

A further essential requirement for semiconductors is the position of the valence and conduction bands indicating which half reaction will occur on the working electrode²⁷. Figure 1-3 shows a summary of several materials which have been the center of interest for the past years. Metal oxides such as WO_3 , Fe_2O_3 or BiVO_4 provide energy only for the oxygen evolution reaction whereas Cu_2O or CuFeO_4 drive the hydrogen evolution reaction. TiO_2 , CdS or CdSe , on the other hand, have suitable band positions for the overall photoelectrolysis reaction into oxygen and hydrogen gas²⁸.

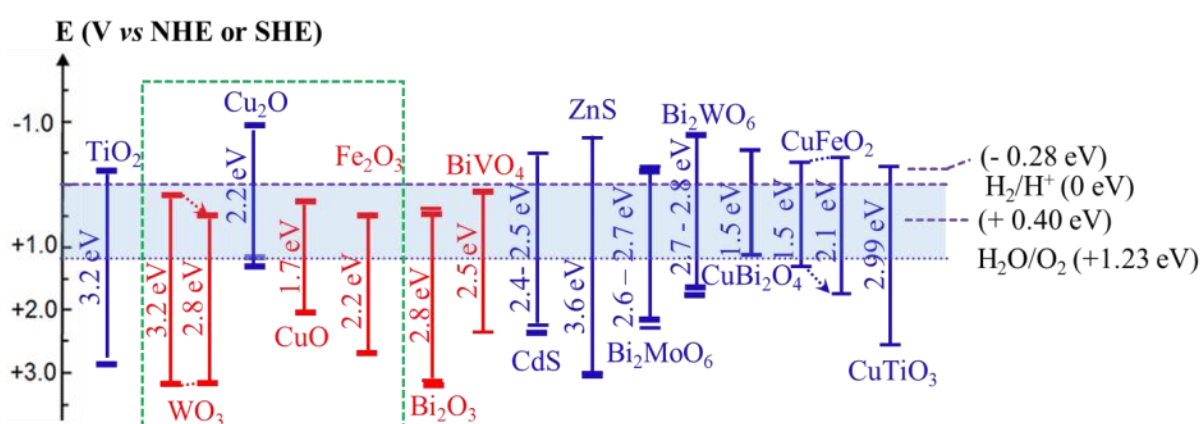


Figure 1-3: Band gaps and valence and conduction bands positions with respect to the redox potential of water at $\text{pH} = 0$ for selected semiconductors²⁸.

Chemical stability of semiconductors is a major factor for future applications in water photoelectrolysis. Photocorrosion or pH -instability limits the performance of some promising materials¹². Generally, materials with a wide band gap are stable against photocorrosion unlike materials with small band gaps¹¹. The stability of electrodes can be optimized by deposition of protection/passivation layers such as Al_2O_3 or TiO_2 typically using atomic layer deposition (ALD) thus eliminating the direct contact of the photoactive film with the electrolyte²⁹.

The elements and materials used for the synthesis of large-scale photoabsorbers have to be abundant or at least scalable. Many devices containing or decorated with for example Pt have shown good performance in the laboratory but contain rare elements making an upscale problematic when large numbers of water splitting panels have to be produced. Additionally to the material availability also the production methods have to be analyzed. Processes such as doctor blading, spin-coating or dip-coating have major advantages with respect to costs, production speed and application on large area substrates compared to other techniques such as chemical vapor deposition or atomic layer deposition. The subsequent post-annealing procedure of the films should be preferably carried out by lower temperatures still leading to the formation of highly crystalline materials.

The toxicity of photoabsorbers and photocatalysts is a very important parameter to be considered in the development of industrially compatible materials with respect to their impact on health and environment. Toxic devices are very unlikely to be produced on a large-scale given the toxicological concerns inspite of the good performance. The issue of element or compound toxicity has been recently shown for the example of Pb-containing perovskite solar cells. The perovskite solar cell efficiency has exceeded 20 % in the last 4 years but the challenge of substituting Pb still remains^{6, 30}. This is one of the main reasons why industrial applications of perovskite solar cells have not been accomplished yet.

In the following, some of the main metal oxide semiconductors will be introduced shortly with the emphasis on water-splitting related properties such as band gap and stability along with the corresponding applications.

1.3.1 Metal oxide photoanodes

Titanium dioxide (TiO₂)

Since the discovery of Fujishima and Honda in 1972, n-type TiO_2 has become the most intensively studied system for photoelectrochemical water splitting³¹. The electrochemically active phase of TiO_2 has shown to be rutile³² with a body-centered tetragonal unit cell. Therein Ti^{4+} is octahedrally coordinated by oxygen atoms creating edge sharing TiO_6 octahedra. The oxygen anions, on the other hand, show a coordination number of 3 with OTi_3 trigonal planar slices³³ (Figure 1-4).

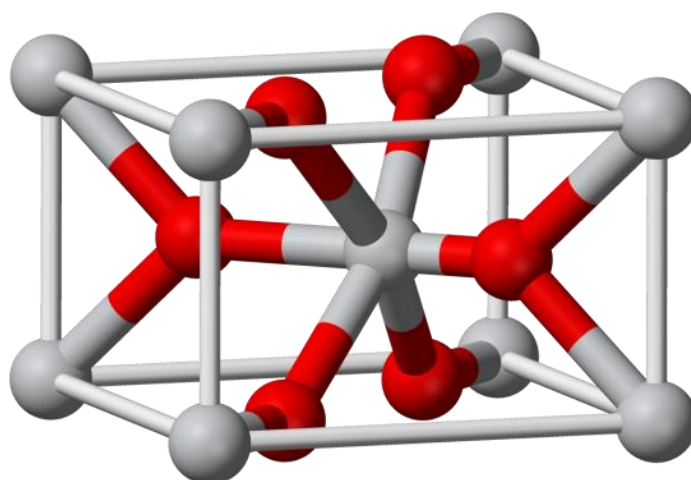


Figure 1-4: Crystal structure of the rutile TiO_2 unit cell³⁴.

The chemical stability, abundancy and low production costs make TiO_2 an attractive material able to split water upon illumination. TiO_2 delivers enough energy to drive the overall water splitting reaction due to the favorable position of the valence and conduction bands. The performance of TiO_2 is however limited due to its wide band gap (3.2 eV) and fast electron hole recombination rate³⁵⁻³⁶. Numerous publications have focused on the shifting optical absorption towards the visible range by i.e. doping TiO_2 with transition metals such as iron or chromium or sensitizing with other low band gap semiconductors thus shifting the absorption wavelength³⁷⁻³⁸. Transition metal doping of TiO_2 leads indeed to the shift of absorption wavelength but does not result in the expected increase in efficiency, as the defect states

formed due to doping act as recombination sites. For this reason, various nanostructuring techniques³⁹ have been applied to generate an increased active surface area and shorter hole diffusion lengths to the semiconductor-electrolyte interface. Different morphologies such as nanotubes⁴⁰, nanowires⁴¹, nanoflakes⁴², mesoporous⁴³ and inverse opal⁴⁴ films synthesized using different techniques such as sol-gel, chemical vapor deposition or electrodeposition. Combining nanostructured morphologies with selective doping the performance of TiO₂ can be sufficiently enhanced.

Tungsten trioxide (WO₃)

Tungsten trioxide is another photoanode material which has been thoroughly studied over the past years due to its low toxicity, abundancy, stability and low production costs⁴⁵. Orthorhombic WO₃ crystalizes in an almost ReO₃ structure of 3 dimensional array of corner linked WO₃ distorted octahedra. A band gap of 2.8 eV limits the absorption range of WO₃ making it a good UV photoabsorber and utilizing only a small part of the visible spectrum⁴⁶⁻⁴⁷. Similar to TiO₂, different nanostructuring techniques have been applied to WO₃ films with the aim to increase absorption, enhance charge separation and increase the active surface area. Different preparation techniques have been used to prepare a broad range of nanostructured WO₃ including hydrothermal⁴⁸, sol-gel⁴⁹⁻⁵⁰, electrodeposition⁵¹, CVD⁵², PVD⁵³ and anodization⁵⁴. As a result different nanostructured WO₃ electrodes have emerged as WO₃ nanotubes, nanowires, nanoplatelets or honeycombs indeed improving the electron transport pathways as well as the minority carrier collection at the semiconductor-electrolyte interface thus resulting in reduced electron-hole recombination⁵⁵⁻⁵⁷.

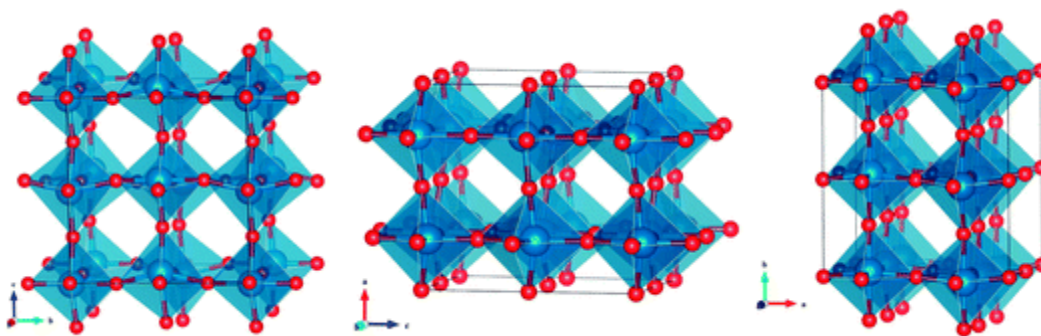


Figure 1-5: Crystal structure of an orthorhombic WO_3 unit cell⁵⁸.

WO_3 has been further applied as a high surface area scaffold material for other photoabsorbers covering the visible wavelength range such as i.e. $\alpha\text{-Fe}_2\text{O}_3$ ⁵². Beside the enhanced absorption in the UV range the WO_3 scaffolds contribute sufficiently to the charge separation of the broad wavelength absorbing material by extracting the majority carriers thus reducing electron-hole recombination in the system.

Hematite ($\alpha\text{-Fe}_2\text{O}_3$)

Hematite as an n-type semiconductor has been in the center of attention for the past decade given that iron is the fourth most abundant element in the earth's crust⁵⁹. $\alpha\text{-Fe}_2\text{O}_3$ has the corundum structure with Fe^{3+} being in a marginally distorted octahedral environment with FeO_6 octahedra sharing the edges with three other neighboring octahedra⁶⁰ (Figure 1-6). Apart from being abundant and inexpensive iron (III) oxide is non-toxic and stable in aqueous electrolyte as it is a natural mineral. The optical band has been reported to be 1.9-2.2 eV depending on the synthesis method meaning that it shows good light harvesting efficiency in the visible range¹⁰. Preparation methods of hematite include spray pyrolysis⁶¹, calcination of preformed hematite nanoparticles⁶², sol-gel reactions⁶³, anodization⁶⁴ or thermal oxidation of iron foils⁶⁵. The best performing hematite electrode, to this date, was synthesized using the

Atmospheric Pressure Chemical Vapor Deposition (APCVD) method resulting in a cauliflower-like morphology⁶⁶.

Hematite has shown to have good transport properties of majority charge carriers across the electrode. Its performance is however limited by the short hole diffusion length of 2-4 nm, poor electrical conductivity and high surface recombination⁶⁷⁻⁷⁰. Several approaches have been carried out to overcome the described drawbacks including nanostructuring⁶⁶, host-guest architectures⁷¹ and various catalysts such as IrO₂⁷², Co⁷³, or NiO⁷⁴ leading to performance improved photoelectrodes.

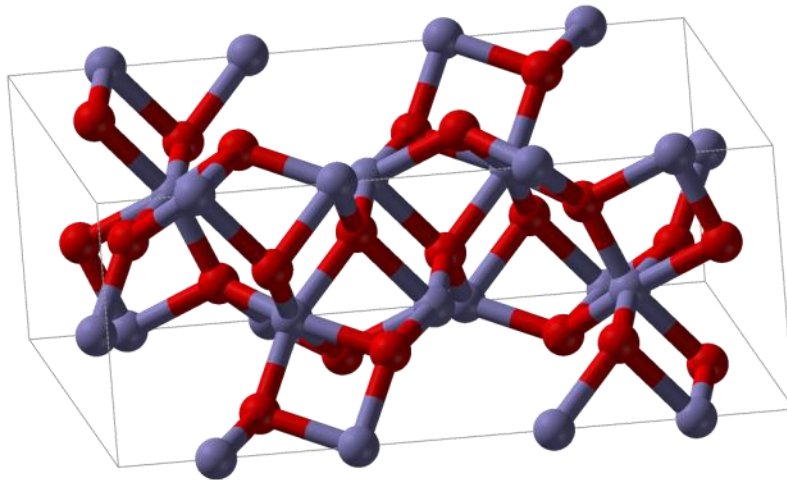


Figure 1-6: Crystal structure of a α -Fe₂O₃ unit cell⁷⁵.

Bismuth vanadate (BiVO₄)

Bismuth vanadate is an n-type semiconductor with a band gap of 2.4 eV absorbing a sufficient part of the visible range⁷⁶⁻⁷⁸. The only phase which exhibits photocatalytic behavior is the thermodynamically stable monoclinic phase⁷⁹. The Bi atom has a distorted oxygen octahedron coordination with various distances to the individual oxygen atoms between 2.35 and 2.53 Å. The V atom is located in the center of a distorted oxygen atom tetrahedron. There are two

types of oxygen atoms. One is connected to one Bi and one V atom while the other is coordinated by two Bi and one V atom⁸⁰ (Figure 1-7).

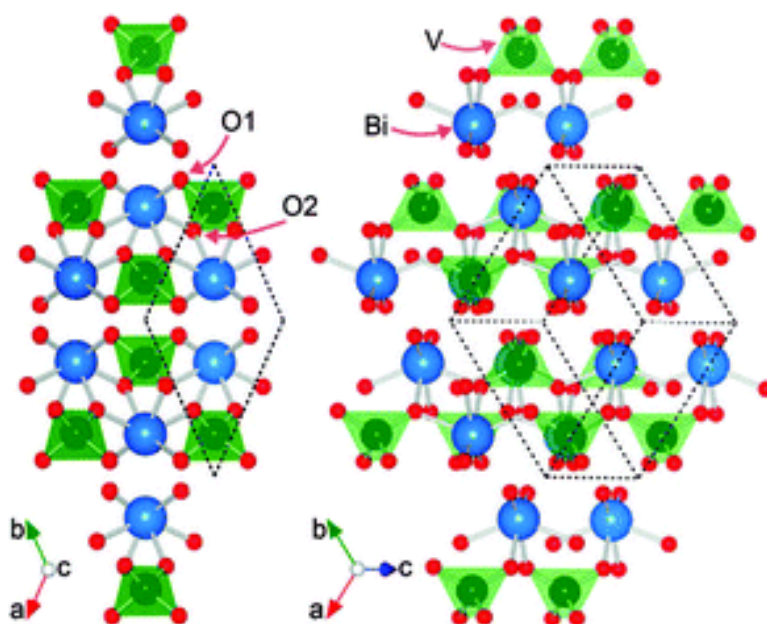


Figure 1-7: Crystal structure of BiVO_4 ⁸⁰.

BiVO_4 has a favorable position of the conduction band close to the hydrogen evolution potential. By combining BiVO_4 electrodes with oxygen evolution catalysts the kinetics of the material can be improved. Nevertheless the issue of inefficient charge separation caused by slow electron transfer still remains. Recent research has shown different approaches to improve the intrinsic mobility by developing a semiconductor with a built-in electric field. An elegant way to achieve band bending without introducing a large amount of defects which act as recombination sites is by gradual doping with for example tungsten (W)⁸¹. This is how a depletion layer can be formed between undoped and W-doped BiVO_4 with the electrons traveling from the doped to the undoped material. This approach is a set example of how charge separation can be enhanced by gradual doping of the photoabsorber.

1.3.2 Metal oxide photocathodes

Cuprous oxide (Cu_2O)

Cuprous oxide is an intensively studied p-type semiconductor used for water reduction⁸²⁻⁸⁵. The Cu_2O unit cell contains four Cu and two O atoms. The Cu atoms form a face-centered cubic structure with oxygen atoms occupying the tetrahedral sites (Figure 1-8).

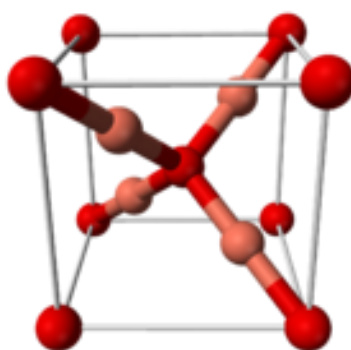


Figure 1-8: Crystal structure of Cu_2O ⁸⁶.

With a direct band gap of 2 eV the theoretically calculated photocurrent was determined to be -14.7 mA cm^{-2} corresponding to a solar-to-hydrogen conversion efficiency of 18 %^{83, 87-91}. Furthermore, Cu_2O has a very favorable band position of the conduction band at -0.7 V relative to the hydrogen evolution potential⁸⁷. The valence band is positioned slightly positive than the oxygen evolution potential. A major drawback for Cu_2O as a photocathode is the poor stability in aqueous electrolyte because of a well-known disproportionation of Cu (I) in water. Many approaches have been carried out to increase the stability of Cu_2O electrodes with conformal surface coatings such as ZnO, Al_2O_3 , TiO or CuO ^{84-85, 92}. Passivation of Cu_2O is more challenging when a highly porous structure has to be treated. It is important that the Cu_2O remains active for water splitting after passivation.

Cupric oxide (CuO)

Cupric oxide is a well-known p-type semiconductor that has been studied for PEC water electrolysis⁹³⁻⁹⁷. CuO has a tenorite structure with each copper atom surrounded by four coplanar oxygen atoms. A strongly distorted octahedron is observed when considering the six nearest oxygen atoms surrounding the copper atom. The oxygen atom, on the other hand, is coordinated by four copper atoms on the corners of a distorted tetrahedron⁹⁸ (Figure 1-9).

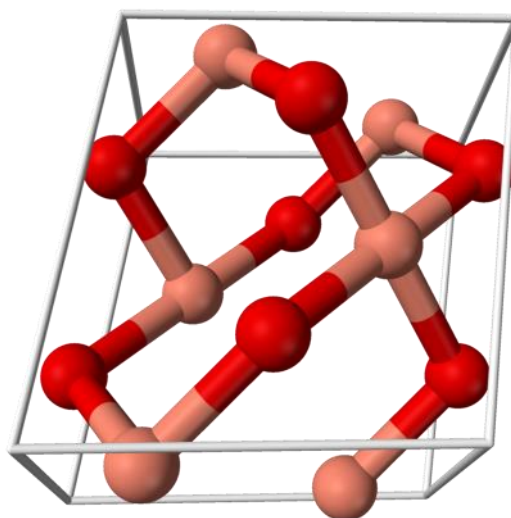


Figure 1-9: Crystal structure of CuO⁹⁹.

The indirect band gap of 1.2-1.8 eV allows light absorption in the UV and visible range⁹³. Further advantages of CuO as a photoabsorber are abundancy, nontoxicity, low production costs and stability. Although CuO has a smaller band gap than Cu₂O it has received less attention compared to cuprous oxide. In terms of photocurrent Cu₂O has been shown to outperform CuO. The stability of CuO, however, is still superior to that of Cu₂O making the material interesting for optimization. CuO has been even used as a protective layer for Cu₂O electrodes thus reducing the photocorrosion process⁸⁴. Literature reports different synthesis of CuO including electrodeposition, spray pyrolysis, thermal oxidation of Cu foils or sol-gel reactions^{95-97, 100-102}. After deposition all films are typically submitted to post-synthetic annealing at temperatures between 400-900 °C.

1.4 'New materials genome'

The materials studied and applied as photoabsorbers for water splitting to this date have not shown the expected performance. This is also one of the main reasons why photoelectrochemical cells have not yet outperformed and replaced electrolyzes coupled to solar cells. As described in the previous chapter, most materials have major drawbacks limiting the performance of the photoelectrodes. The discovery of new photoabsorber materials becomes therefore a very important but also extremely demanding task given that the number of possible element combinations is practically unlimited.

Promising and intensively investigated classes of metal oxide photoabsorbers are complex mixture of two, three or even more elements¹⁰³⁻¹⁰⁵. Given the number of elements which are interesting for photoelectrolysis is around 50, the number of possible element combinations in a ternary system would be over 19 000 when only considering the ratio of 1:1:1. A deviation from the 1:1:1 ratio would mean additional millions of combinations making this task shoreless. These calculations reach even higher numbers when referring to materials composed of 4 or more multicomponents thus making the development of such high-throughput set-ups essential.

In the following the main techniques to finding new promising material candidates will be discussed.

1.4.1 High-throughput combinatorial screening

High-throughput combinatorial screening is one of the powerful methods for the screening and discovery of new potential water splitting materials¹⁰⁶⁻¹⁰⁸. Common synthesis methods implemented for high-throughput screening include ink-jet printing or magnetron sputtering of

different mixed metal oxide compositions on FTO generating a complete library of a certain material^{103, 109}. Figure 1-10a shows an FTO substrate after ink-jet printing and calcination of Fe, Cr and Al nitrate salts.

After deposition of different mixed metal oxides with varying composition on FTO, the small photoelectrodes ($\sim 30 \mu\text{m}$) are immersed in electrolyte, illuminated with a laser and characterized with respect to the photoelectrochemical behavior by obtaining current-voltage (Figure 1-10b) and IPCE data¹⁰³. Some set-ups have shown to have built-in X-ray diffractometers and scanning electron microscopes to study the crystal structure, composition and morphology of the individual compositions prior to electrochemical measurements.

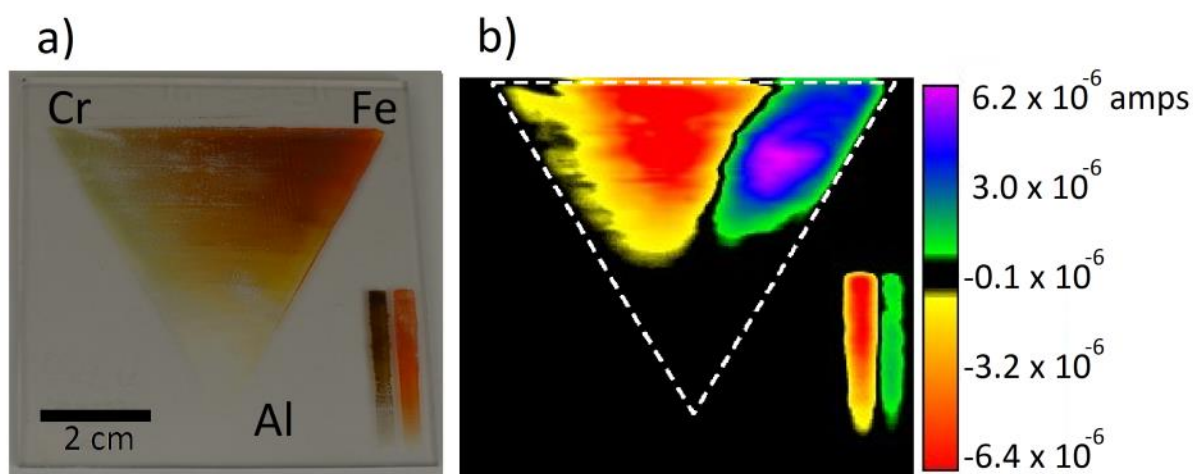


Figure 1-10: a) Example of an ink-jet printed ternary gradient FeCrAl oxide film on FTO. b) False color photocurrent map of the ink ink-jet printed ternary gradient FeCrAl oxide film¹⁰³.

The success of this technique is reflected in the numerous novel materials which have been discovered and further optimized for successful water splitting. $\text{Fe}_{0.84}\text{Cr}_{1.0}\text{Al}_{0.16}\text{O}_3$, $\text{Fe}_2\text{O}_6\text{W}$ $\text{Si}:\text{Cu}_{75}\text{Ti}_{25}\text{O}_x$, $\text{Ti}:\text{Cu}_{50}\text{Si}_{50}\text{O}_x$, or CuNbO_3 are just a few examples showing the large potential of high-throughput experiments^{103-105, 110}. The idea of distributed research has gained great attention over the past years with researchers providing experimental results accessible to

everyone worldwide¹⁰⁸. One of the biggest platforms for combinatorial screening libraries is the so called Solar Army¹¹¹, a joined project between different platforms such as SHArK, SEAL, HARPOON and Westside Science Club, accelerating the discovery progress of photoelectrodes and photocatalysts for solar-driven water splitting.

1.4.2 Computational screening methods

Computational screening methods are a further approach for a fast determination of new materials^{21, 112-115}. The computational methods have designated descriptors which narrow down the number of candidates with respect to the required material properties. The main descriptors are: chemical and structural stability, light absorption and band gap determination, band edge positions relative to the reduction and oxidation potential of water, electron-hole mobility and catalytic properties¹¹⁶. By taking these factors into account, different material classes can be calculated by using ab-initio density functional theory (DFT). To this date, thousands of compounds have been evaluated for one or two-photon water splitting including single metal bulk materials, single metal oxides, bi-metal oxides as well as single and bi-metal oxinitrides. Calculations have been mainly applied to over 19 000 cubic perovskite structures thus discovering 32 promising candidates showing good light absorption¹¹³⁻¹¹⁴. To assess the stability of the electrodes in water Pourbaix diagrams were evaluated¹¹⁷.

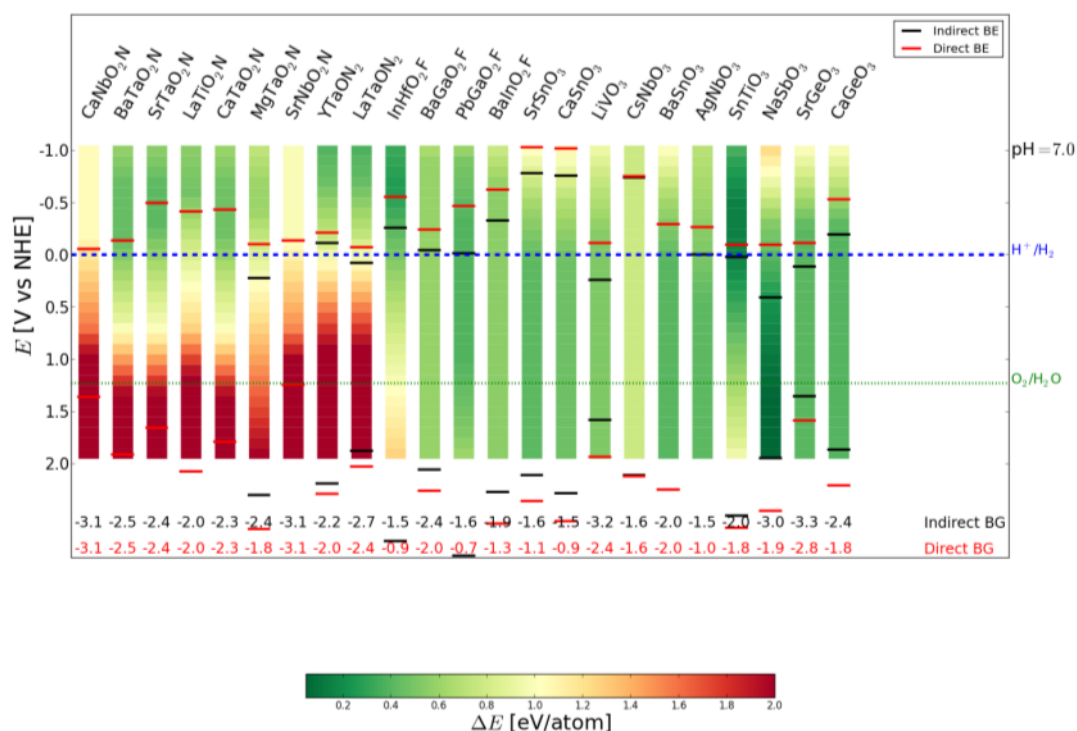


Figure 1-11: Computational calculations of the band gap, valence and conduction band positions relative to the water oxidation and reduction potential for different perovskite structures¹¹⁸.

There are several databases available for computationally calculated water splitting materials. The Computational Materials Repository offers a large collection of calculated compounds relevant to light harvesting materials¹¹⁹. The repository is among others an important source for finding new competitive material compositions.

1.5 Fabrication of photoelectrodes via colloidal crystal templating

Sol-gel, hydrothermal and solvothermal reactions represent important synthesis routes for metal oxide materials with given properties. The following chapter will describe the theory behind the applied synthesis methods and describe the experimental procedures.

1.5.1 Macroporous films by colloidal crystal templating

Colloidal crystal templating is an important route enabling the formation of periodically ordered materials used in a broad range of nanotechnologies¹²⁰⁻¹²¹. The idea behind the procedure consists in mimicking Nature's opals by creating a long range of three-dimensionally packed spherical nanoparticles by self-assembly. By subsequently depositing the metal oxide precursor solution, the voids between the spheres are infiltrated. Upon calcination, the template particles are removed leaving an inverse opal or a negative replica of the template behind (Figure 1-12).

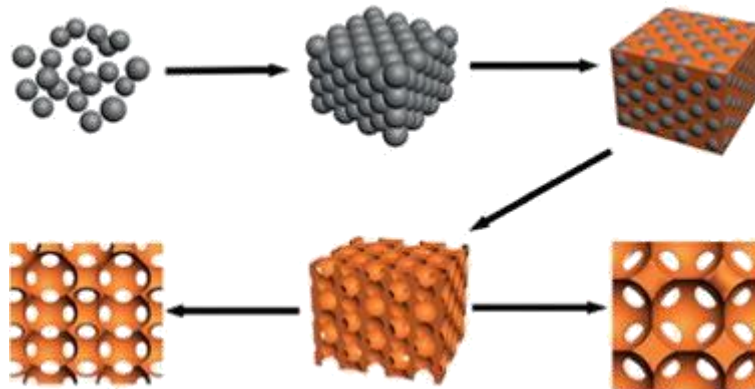


Figure 1-12: Synthesis route for preparation of inverse opal films¹²².

Colloidal crystal templating gives access to highly ordered porous structures with high surface to volume ratio and thus a high accessible surface area. The pore size and the interconnecting

pore voids can be specifically tuned by adjusting the size of the templating nanoparticles. To this date, a variety of different materials has been employed as templates including silica, polystyrene (PS), latex or polymethyl methacrylate (PMMA) nanoparticles¹²³⁻¹²⁶. These can all be synthesized and deposited with a desired diameter and thickness, respectively.

The deposition of template spheres can be accomplished with different techniques¹²⁷. The procedure used in this thesis is based on horizontal deposition by ultra-slow dip-coating under a nitrogen stream or vertical drying of a substrate in a template containing solution¹²⁸⁻¹²⁹. Both of these techniques result in the successful deposition of highly ordered cubic closed packed structures of the template spheres. All these techniques allow the deposition of films with variable thickness that depends on the sphere size and the template solution concentration. When depositing films with a thickness $> 3 \mu\text{m}$, however, peeling of the template film from the substrate can be observed.

The quality of the inverse opal films strongly depends on the packing of the template. The deposition of the spheres is very sensitive to experimental factors such as air flow, vibrations, humidity or temperature. Therefore, often defects in the stacking are observed¹²⁹⁻¹³². Further, the negative replica of the templated films usually shows cracks which are attributed to the combustion of the polymer spheres during the simultaneous crystallization of the precursor solution causing shrinkage of the template.

Inverse opal films have a very wide application range. They have been employed in photonic devices, catalysis, sorption, thermal insulation, sensors and batteries¹³³⁻¹³⁵. In this thesis the inverted opal structures were used for two different applications: as a scaffold in host guest structures or as a photoabsorber with high surface area available for the photoelectrolysis reaction¹³⁶⁻¹³⁷. In the case of the scaffold structure, the macroporous film provides high surface area for deposition of the absorber material. Further, it acts as majority carrier extraction layer thus increasing the corresponding diffusion length and reducing recombination in the absorber

material itself. In the second case, a photoabsorber can be synthesized with an inverse opal structure. The main advantages of this approach are the increased optical diffraction of the film resulting in higher light harvesting efficiency and the increased surface area available for the water splitting reaction.

1.5.2 Mesoporous materials

The definition ‘mesoporous’ refers to porous materials with a pore size range between 2-50 nm. Materials with a pore diameter smaller than 2 nm are called microporous and pores with pores larger than 50 nm are referred to as macroporous solids¹³⁸. High surface area and good accessibility of the pores make mesoporous materials very attractive for a variety of different applications involving catalysis, optics, adsorption and energy conversion, and storage¹³⁹⁻¹⁴⁵.

To obtain a mesoporous structure, different approaches can be carried out. In the absence of a templating agent, disordered mesoporous materials can be synthesized by i.e. sintering of preformed nanoparticles or solvent evaporation during calcination of the material. The fabrication of periodic mesoporous materials can be achieved by a structure-driven spontaneous self-assembly of ligands containing multiple binding sites as shown for covalent (COFs) and metal organic frameworks (MOFs). Similar to the macroporous materials described above, periodic materials can be obtained using templating approaches with so called “hard” or shape-persistent templates with a suitable pore size. Beside latex beads or colloidal nanoparticles resulting in a cubic closed packing, nanocellulose has also proven to be a promising hard template for different metal oxides¹⁴⁶.

Another common technique used to introduce periodically organized mesopores to a solid material is called the evaporation-induced self-assembly (EISA) process, which is particularly

suitable for fabricating mesoporous films on solid substrates¹⁴⁷⁻¹⁴⁸. Micelles of ionic surfactants or amphiphilic block-copolymer molecules serve as structure directing agents when combined with a precursor solution (**Figure 1-13**). After deposition of the solution containing an inorganic precursor and a surfactant on a substrate the surfactant begins to self assemble/aggregate to the point of critical micellar concentration caused by solvent evaporation^{147, 149}. With progressive drying, condensation and a following calcination, the soft template is removed and the metal precursor crystallizes under the emergence of a mesoporous material¹⁵⁰. The EISA process can be easily influenced by ambient factors such as temperature, humidity, concentration or surfactant-to-precursor ratio resulting in different structures¹⁵¹.

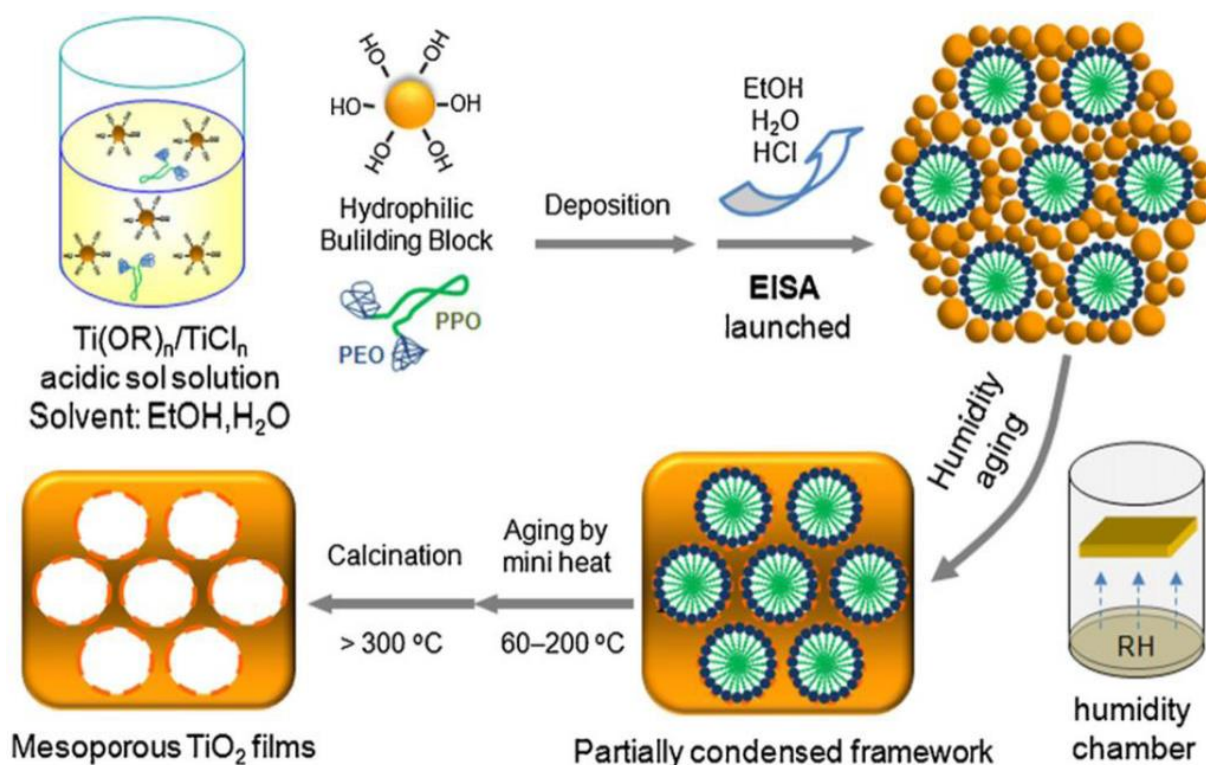


Figure 1-13: Synthesis scheme of mesoporous TiO₂ by the evaporation-induced self-assembly (EISA) process¹⁵².

1.5.3 Sol-gel reactions

Sol-gel reactions are one of the easiest and cheapest methods for the production of large area metal oxide films qualifying this approach for future industrial synthesis of metal oxide photoabsorber materials. The first described sol-gel reaction from 1846 deals with hydrolysis and condensation of metal halide or alkoxide-based precursors such as titanium tetrachloride (TiCl_4) or tetraethyl orthosilicate ($\text{Si}(\text{OEt})_4$)¹⁵³⁻¹⁵⁴. Eversince, sol-gel reactions have been extended and carried out with a variety of precursors. In general, the individual steps of the sol-gel reaction can be described as follows¹⁵⁵:

1. Sol formation: the molecular metal precursor solution (containing metal halogenides, alkoxides or metal salts) is completely or partially hydrolyzed.
2. Gel formation: gelification of the sol by polycondensation or polyesterification reactions causing the formation of oxide or alcohol-bridged networks with increased viscosity.
3. Gel aging (syneresis): further polycondensation reactions lead to the formation of a solidified gel mass upon gel contraction and solvent exclusion from the porous gel.
4. Gel drying: the solvents are removed from the gel by either thermal treatment or extraction under supercritical conditions resulting in a xerogel or an aerogel, respectively.
5. Dehydration and stabilization: the surface-bound hydroxyl groups are removed thus stabilizing the gel against rehydration at temperatures up to 800 °C. Temperatures above 800 °C lead to densification and decomposition of the gel applied for the production of i.e. ceramics.

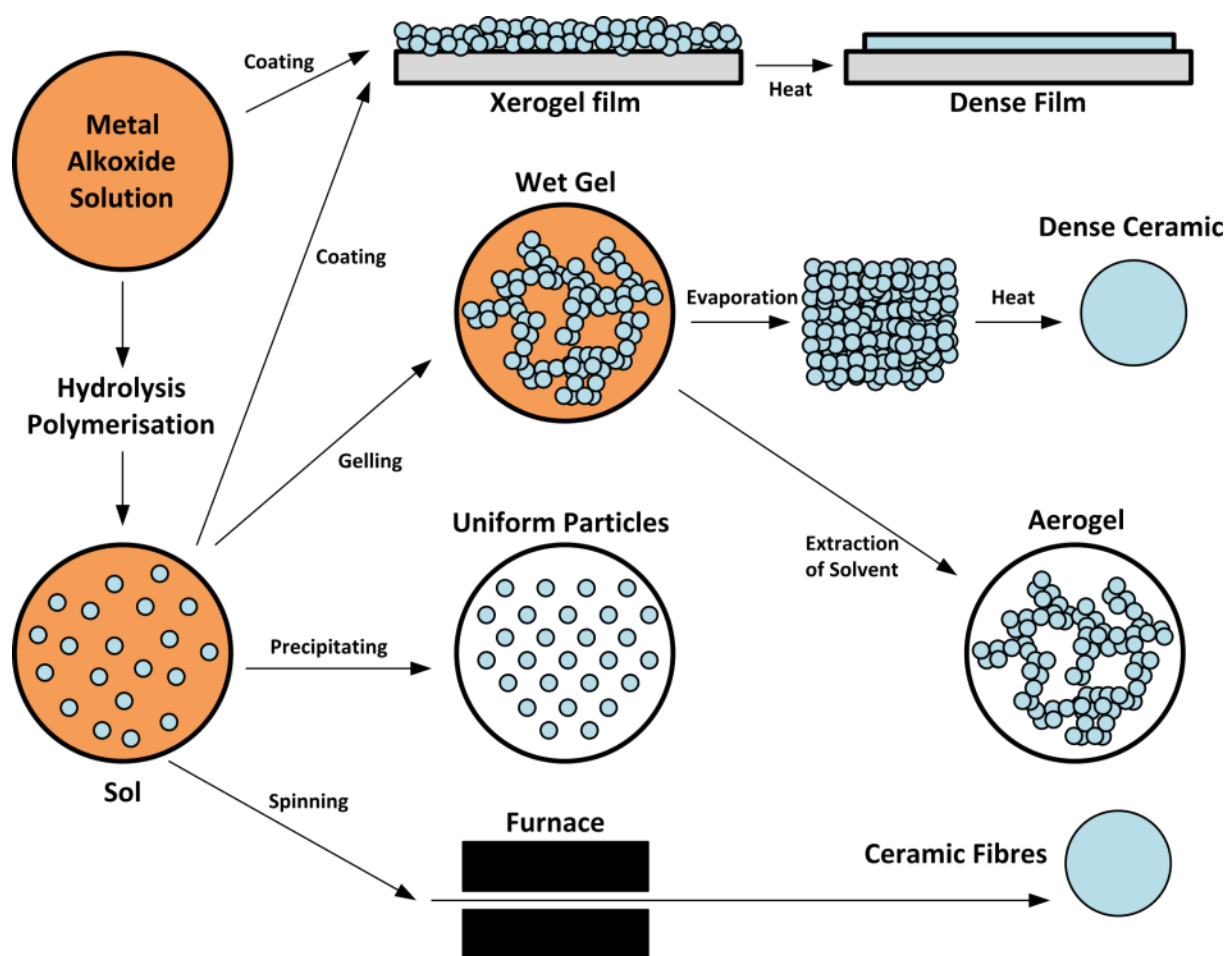


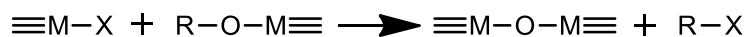
Figure 1-14: Summary of sol-gel reactions and the resulting products according to the synthesis route¹⁵⁶.

The procedures used for the fabrication of metal oxide films used in this work is based on sol-gel reactions. The individual metal oxide salts are dissolved in an organic solvent (non-hydrolytic) or water (hydrolytic solvent).

When performing a sol-gel reaction in an organic solvent (alcohol, ether, ketone or aldehyde) water is excluded from the solvent forming crystalline metal oxide nanoparticles with controllable domain size¹⁵⁷⁻¹⁵⁸. The organic solvent can also act as a surfactant introducing a porous structure to the metal oxide film. Further it can supply oxygen for the metal oxide

formation or form in situ organic condensation products. The condensation steps in organic solvents are summarized in Figure X^{155, 158-159}.

Alkyl halide elimination



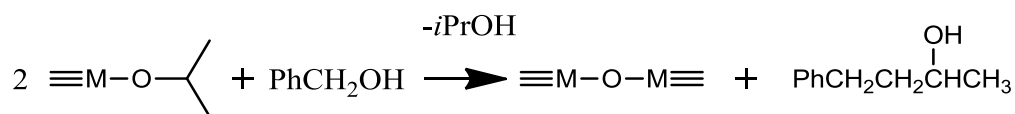
Ether elimination



Condensation of carboxylate groups (ester and amide eliminations)



C-C coupling of benzylic alcohols and alkoxide molecules



Aldol condensation

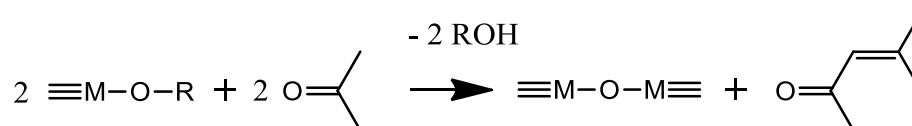


Figure 1-15: Summary of sol-gel condensation steps in an organic solvent¹⁶⁰.

When a sol-gel reaction is carried out in water, the reaction mechanism becomes more complicated. Water acts as a ligand and as a solvent at the same time with the metal oxides showing high reactivity towards water. The reaction is usually highly sensitive towards changes in pH, temperature or reaction rates making a reproducible synthesis challenging.

Independent from the used solvent, all synthesized films required post-synthetic annealing to obtain highly crystalline materials suitable for photoelectrochemical water splitting.

1.6 Scope of the thesis

The main aim of presented thesis was the optimization of known and novel photoabsorber materials through selective nanostructuring or deposition on charge collection selective layers. The macroporous-host/absorber-guest technique was studied on two different systems, ATO/Fe₂O₃ and WO₃/Fe₂O₃, showing the advantages of majority carrier extracting scaffolds on the corresponding minority charge carrier diffusion length. The performance of Fe₂O₃ was further improved by employing the so-called dual absorber technique by depositing an additional layer of WO₃ on top of Fe₂O₃ thus resulting in higher efficiencies and improved kinetics.

With TiO₂, Fe₂O₃ and WO₃ not being the ‘holy grail’ material for water splitting, novel materials and material classes have emerged as potential photoabsorber candidates. In the second part of this thesis, binary and ternary mixed metal oxides such as FeCrAl or LiCu oxides were investigated. The performance of the obtained electrodes was sufficiently improved by nanostructuring or doping resulting in the highest currents obtained so far for the individual systems. Additionally, a new class of materials, covalent organic frameworks (COFs) was tested here for the first time as photoabsorbers showing photocurrents in aqueous electrolyte which are attributed to the water reduction reaction generating hydrogen gas.

1.7 References

1. Administration, N. A. a. S. "Global Climate Change: Evidence." NASA Global Climate Change and Global Warming: Vital Signs of the Planet. Jet Propulsion Laboratory. (accessed 14.02.2016).
2. Hulme, M., 1.5 [deg] C and climate research after the Paris Agreement. *Nature Climate Change* **2016**.

3. <http://www.world-nuclear.org/information-library/energy-and-the-environment/renewable-energy-and-electricity.aspx> (accessed 25.2.2016).
4. Smil, V., General energetics: energy in the biosphere and civilization. In *General energetics: energy in the biosphere and civilization*, John Wiley & Sons: 1991.
5. Grätzel, M., Dye-sensitized solar cells. *Journal of Photochemistry and Photobiology C: Photochemistry Reviews* **2003**, *4* (2), 145-153.
6. Liu, M.; Johnston, M. B.; Snaith, H. J., Efficient planar heterojunction perovskite solar cells by vapour deposition. *Nature* **2013**, *501* (7467), 395-398.
7. Gratzel, M., Photoelectrochemical cells. *Nature* **2001**, *414* (6861), 338-344.
8. Barroso, M.; Mesa, C. A.; Pendlebury, S. R.; Cowan, A. J.; Hisatomi, T.; Sivula, K.; Grätzel, M.; Klug, D. R.; Durrant, J. R., Dynamics of photogenerated holes in surface modified α -Fe₂O₃ photoanodes for solar water splitting. *Proceedings of the National Academy of Sciences* **2012**, *109* (39), 15640-15645.
9. Wiberg, E.; Wiberg, N., *Inorganic Chemistry*. Academic Press: 2001.
10. Sivula, K.; Le Formal, F.; Grätzel, M., Solar Water Splitting: Progress Using Hematite (α -Fe₂O₃) Photoelectrodes. *ChemSusChem* **2011**, *4* (4), 432-449.
11. van de Krol, R.; Liang, Y.; Schoonman, J., Solar hydrogen production with nanostructured metal oxides. *Journal of Materials Chemistry* **2008**, *18* (20), 2311-2320.
12. Kang, D.; Kim, T. W.; Kubota, S. R.; Cardiel, A. C.; Cha, H. G.; Choi, K.-S., Electrochemical Synthesis of Photoelectrodes and Catalysts for Use in Solar Water Splitting. *Chemical reviews* **2015**, *115* (23), 12839-12887.
13. Van de Krol, R.; Grätzel, M.; Grätzel, M.; Grätzel, M., *Photoelectrochemical hydrogen production*. Springer: 2012; Vol. 90.
14. Hisatomi, T.; Kubota, J.; Domen, K., Recent advances in semiconductors for photocatalytic and photoelectrochemical water splitting. *Chemical Society Reviews* **2014**, *43* (22), 7520-7535.
15. Chen, Z.; Jaramillo, T. F.; Deutsch, T. G.; Kleiman-Shwarsstein, A.; Forman, A. J.; Gaillard, N.; Garland, R.; Takanabe, K.; Heske, C.; Sunkara, M., Accelerating materials development for photoelectrochemical hydrogen production: Standards for methods, definitions, and reporting protocols. *J. Mater. Res* **2010**, *25* (1), 3.
16. Li, X.; Yu, J.; Low, J.; Fang, Y.; Xiao, J.; Chen, X., Engineering heterogeneous semiconductors for solar water splitting. *Journal of Materials Chemistry A* **2015**, *3* (6), 2485-2534.

17. Dunn, H. K.; Feckl, J. M.; Muller, A.; Fattakhova-Rohlfing, D.; Morehead, S. G.; Roos, J.; Peter, L. M.; Scheu, C.; Bein, T., Tin doping speeds up hole transfer during light-driven water oxidation at hematite photoanodes. *Physical Chemistry Chemical Physics* **2014**, *16* (44), 24610-24620.
18. Peter, L.; Ponomarev, E.; Fermin, D., Intensity-modulated photocurrent spectroscopy: reconciliation of phenomenological analysis with multistep electron transfer mechanisms. *Journal of Electroanalytical Chemistry* **1997**, *427* (1), 79-96.
19. Ponomarev, E.; Peter, L., A generalized theory of intensity modulated photocurrent spectroscopy (IMPS). *Journal of Electroanalytical Chemistry* **1995**, *396* (1), 219-226.
20. Peter, L. M.; Wijayantha, K. U.; Tahir, A. A., Kinetics of light-driven oxygen evolution at α -Fe₂O₃ electrodes. *Faraday discussions* **2012**, *155*, 309-322.
21. Lewerenz, H.-J.; Peter, L., *Photoelectrochemical water splitting: materials, processes and architectures*. Royal Society of Chemistry: 2013.
22. Sun, J.; Zhong, D. K.; Gamelin, D. R., Composite photoanodes for photoelectrochemical solar water splitting. *Energy & Environmental Science* **2010**, *3* (9), 1252-1261.
23. Bryan, J. D.; Gamelin, D. R., Doped semiconductor nanocrystals: synthesis, characterization, physical properties, and applications. *Prog. Inorg. Chem* **2005**, *54*, 47-126.
24. Queisser, H. J.; Haller, E. E., Defects in semiconductors: some fatal, some vital. *Science* **1998**, *281* (5379), 945-950.
25. Serpone, N.; Emeline, A., Semiconductor Photocatalysis • Past, Present, and Future Outlook. *The journal of physical chemistry letters* **2012**, *3* (5), 673-677.
26. Mocatta, D.; Cohen, G.; Schattner, J.; Millo, O.; Rabani, E.; Banin, U., Heavily doped semiconductor nanocrystal quantum dots. *Science* **2011**, *332* (6025), 77-81.
27. Kudo, A.; Miseki, Y., Heterogeneous photocatalyst materials for water splitting. *Chemical Society Reviews* **2009**, *38* (1), 253-278.
28. Basnet, P. *Metal Oxide Photocatalytic Nanostructures Fabricated by Dynamic Shadowing Growth*. University of Georgia, 2015.
29. Wang, T.; Luo, Z.; Li, C.; Gong, J., Controllable fabrication of nanostructured materials for photoelectrochemical water splitting via atomic layer deposition. *Chemical Society Reviews* **2014**, *43* (22), 7469-7484.
30. Grätzel, M., The light and shade of perovskite solar cells. *Nature materials* **2014**, *13* (9), 838-842.

31. Fujishima, A.; Honda, K., Electrochemical Photolysis of Water at a Semiconductor Electrode. *Nature* **1972**, *238* (5358), 37-38.
32. Maeda, K., Photocatalytic properties of rutile TiO₂ powder for overall water splitting. *Catalysis Science & Technology* **2014**, *4* (7), 1949-1953.
33. Liao, Y.; Que, W.; Jia, Q.; He, Y.; Zhang, J.; Zhong, P., Controllable synthesis of brookite/anatase/rutile TiO₂ nanocomposites and single-crystalline rutile nanorods array. *Journal of Materials Chemistry* **2012**, *22* (16), 7937-7944.
34. <https://en.wikipedia.org/wiki/Rutile#/media/File:Rutile-unit-cell-3D-balls.png> (accessed 24.2.2016).
35. Tian, J.; Zhao, Z.; Kumar, A.; Boughton, R. I.; Liu, H., Recent progress in design, synthesis, and applications of one-dimensional TiO₂ nanostructured surface heterostructures: a review. *Chemical Society Reviews* **2014**, *43* (20), 6920-6937.
36. Chen, X.; Mao, S. S., Titanium dioxide nanomaterials: synthesis, properties, modifications, and applications. *Chemical reviews* **2007**, *107* (7), 2891-2959.
37. Maruska, H. P.; Ghosh, A. K., Transition-metal dopants for extending the response of titanate photoelectrolysis anodes. *Solar Energy Materials* **1979**, *1* (3), 237-247.
38. Kato, H.; Kudo, A., Visible-light-response and photocatalytic activities of TiO₂ and SrTiO₃ photocatalysts codoped with antimony and chromium. *The Journal of Physical Chemistry B* **2002**, *106* (19), 5029-5034.
39. Fattakhova-Rohlfing, D.; Zaleska, A.; Bein, T., Three-Dimensional Titanium Dioxide Nanomaterials. *Chemical Reviews* **2014**, *114* (19), 9487-9558.
40. Zhang, Z.; Hossain, M. F.; Takahashi, T., Photoelectrochemical water splitting on highly smooth and ordered TiO₂ nanotube arrays for hydrogen generation. *International Journal of Hydrogen Energy* **2010**, *35* (16), 8528-8535.
41. Wang, G.; Wang, H.; Ling, Y.; Tang, Y.; Yang, X.; Fitzmorris, R. C.; Wang, C.; Zhang, J. Z.; Li, Y., Hydrogen-Treated TiO₂ Nanowire Arrays for Photoelectrochemical Water Splitting. *Nano Letters* **2011**, *11* (7), 3026-3033.
42. Tang, Y.; Wee, P.; Lai, Y.; Wang, X.; Gong, D.; Kanhere, P. D.; Lim, T.-T.; Dong, Z.; Chen, Z., Hierarchical TiO₂ Nanoflakes and Nanoparticles Hybrid Structure for Improved Photocatalytic Activity. *The Journal of Physical Chemistry C* **2012**, *116* (4), 2772-2780.
43. Hartmann, P.; Lee, D.-K.; Smarsly, B. M.; Janek, J., Mesoporous TiO₂: comparison of classical sol-gel and nanoparticle based photoelectrodes for the water splitting reaction. *ACS nano* **2010**, *4* (6), 3147-3154.

44. Cheng, C.; Karuturi, S. K.; Liu, L.; Liu, J.; Li, H.; Su, L. T.; Tok, A. I. Y.; Fan, H. J., Quantum-Dot-Sensitized TiO₂ Inverse Opals for Photoelectrochemical Hydrogen Generation. *Small* **2012**, *8* (1), 37-42.
45. Liu, X.; Wang, F.; Wang, Q., Nanostructure-based WO₃ photoanodes for photoelectrochemical water splitting. *Physical Chemistry Chemical Physics* **2012**, *14* (22), 7894-7911.
46. Butler, M., Photoelectrolysis and physical properties of the semiconducting electrode WO₂. *Journal of Applied Physics* **1977**, *48* (5), 1914-1920.
47. Koffyberg, F.-P.; Dwight, K.; Wold, A., Interband transitions of semiconducting oxides determined from photoelectrolysis spectra. *Solid State Communications* **1979**, *30* (7), 433-437.
48. Jiao, Z.; Sun, X. W.; Wang, J.; Ke, L.; Demir, H. V., Hydrothermally grown nanostructured WO₃ films and their electrochromic characteristics. *Journal of Physics D: Applied Physics* **2010**, *43* (28), 285501.
49. Hilaire, S.; Suess, M. J.; Kranzlin, N.; Bienkowski, K.; Solarska, R.; Augustynski, J.; Niederberger, M., Microwave-assisted nonaqueous synthesis of WO₃ nanoparticles for crystallographically oriented photoanodes for water splitting. *Journal of Materials Chemistry A* **2014**, *2* (48), 20530-20537.
50. Solarska, R.; Alexander, B. D.; Augustynski, J., Electrochromic and photoelectrochemical characteristics of nanostructured WO₃ films prepared by a sol-gel method. *Comptes Rendus Chimie* **2006**, *9* (2), 301-306.
51. Hill, J. C.; Choi, K.-S., Effect of Electrolytes on the Selectivity and Stability of n-type WO₃ Photoelectrodes for Use in Solar Water Oxidation. *The Journal of Physical Chemistry C* **2012**, *116* (14), 7612-7620.
52. Sivula, K.; Formal, F. L.; Grätzel, M., WO₃-Fe₂O₃ photoanodes for water splitting: A host scaffold, guest absorber approach. *Chemistry of Materials* **2009**, *21* (13), 2862-2867.
53. Singh, T.; Müller, R.; Singh, J.; Mathur, S., Tailoring surface states in WO₃ photoanodes for efficient photoelectrochemical water splitting. *Applied Surface Science* **2015**, *347*, 448-453.
54. Cristino, V.; Caramori, S.; Argazzi, R.; Meda, L.; Marra, G. L.; Bignozzi, C. A., Efficient photoelectrochemical water splitting by anodically grown WO₃ electrodes. *Langmuir* **2011**, *27* (11), 7276-7284.

55. Rao, P. M.; Cho, I. S.; Zheng, X., Flame synthesis of WO₃ nanotubes and nanowires for efficient photoelectrochemical water-splitting. *Proceedings of the Combustion Institute* **2013**, *34* (2), 2187-2195.
56. Zheng, J. Y.; Song, G.; Hong, J.; Van, T. K.; Pawar, A. U.; Kim, D. Y.; Kim, C. W.; Haider, Z.; Kang, Y. S., Facile Fabrication of WO₃ Nanoplates Thin Films with Dominant Crystal Facet of (002) for Water Splitting. *Crystal Growth & Design* **2014**, *14* (11), 6057-6066.
57. Chang, Y.; Yu, K.; Zhang, C.; Li, R.; Zhao, P.; Lou, L.-L.; Liu, S., Three-dimensionally ordered macroporous WO₃ supported Ag₃PO₄ with enhanced photocatalytic activity and durability. *Applied Catalysis B: Environmental* **2015**, *176–177*, 363-373.
58. Kaper, H.; Djerdj, I.; Gross, S.; Amenitsch, H.; Antonietti, M.; Smarsly, B. M., Ionic liquid- and surfactant-controlled crystallization of WO₃ films. *Physical Chemistry Chemical Physics* **2015**, *17* (27), 18138-18145.
59. Ahmed, S.; Leduc, J.; Haller, S., Photoelectrochemical and impedance characteristics of specular hematite. 1. Photoelectrochemical parallel conductance, and trap rate studies. *The Journal of Physical Chemistry* **1988**, *92* (23), 6655-6660.
60. Pauling, L.; Hendricks, S. B., The crystal structures of hematite and corundum. *Journal of The American Chemical Society* **1925**, *47* (3), 781-790.
61. Le Formal, F.; Grätzel, M.; Sivula, K., Controlling Photoactivity in Ultrathin Hematite Films for Solar Water-Splitting. *Advanced Functional Materials* **2010**, *20* (7), 1099-1107.
62. Sivula, K.; Zboril, R.; Le Formal, F.; Robert, R.; Weidenkaff, A.; Tucek, J.; Frydrych, J.; Grätzel, M., Photoelectrochemical Water Splitting with Mesoporous Hematite Prepared by a Solution-Based Colloidal Approach. *J. Am. Chem. Soc.* **2010**, *132* (21), 7436-7444.
63. Lian, X.; Yang, X.; Liu, S.; Xu, Y.; Jiang, C.; Chen, J.; Wang, R., Enhanced photoelectrochemical performance of Ti-doped hematite thin films prepared by the sol-gel method. *Applied Surface Science* **2012**, *258* (7), 2307-2311.
64. Jun, H.; Im, B.; Kim, J. Y.; Im, Y.-O.; Jang, J.-W.; Kim, E. S.; Kim, J. Y.; Kang, H. J.; Hong, S. J.; Lee, J. S., Photoelectrochemical water splitting over ordered honeycomb hematite electrodes stabilized by alumina shielding. *Energy & Environmental Science* **2012**, *5* (4), 6375-6382.
65. Grigorescu, S.; Lee, C.-Y.; Lee, K.; Albu, S.; Paramasivam, I.; Demetrescu, I.; Schmuki, P., Thermal air oxidation of Fe: rapid hematite nanowire growth and

- photoelectrochemical water splitting performance. *Electrochemistry Communications* **2012**, *23*, 59-62.
66. Cesar, I.; Sivula, K.; Kay, A.; Zboril, R.; Grätzel, M., Influence of Feature Size, Film Thickness, and Silicon Doping on the Performance of Nanostructured Hematite Photoanodes for Solar Water Splitting. *The Journal of Physical Chemistry C* **2008**, *113* (2), 772-782.
67. Katz, M. J.; Riha, S. C.; Jeong, N. C.; Martinson, A. B.; Farha, O. K.; Hupp, J. T., Toward solar fuels: Water splitting with sunlight and “rust”? *Coordination Chemistry Reviews* **2012**, *256* (21), 2521-2529.
68. Dotan, H.; Sivula, K.; Grätzel, M.; Rothschild, A.; Warren, S. C., Probing the photoelectrochemical properties of hematite ($\alpha\text{-Fe}_2\text{O}_3$) electrodes using hydrogen peroxide as a hole scavenger. *Energy & Environmental Science* **2011**, *4* (3), 958-964.
69. Hamann, T. W., Splitting water with rust: hematite photoelectrochemistry. *Dalton Transactions* **2012**, *41* (26), 7830-7834.
70. Dare-Edwards, M. P.; Goodenough, J. B.; Hamnett, A.; Trevellick, P. R., Electrochemistry and photoelectrochemistry of iron (III) oxide. *Journal of the Chemical Society, Faraday Transactions 1: Physical Chemistry in Condensed Phases* **1983**, *79* (9), 2027-2041.
71. Stefik, M.; Cornuz, M.; Mathews, N.; Hisatomi, T.; Mhaisalkar, S.; Grätzel, M., Transparent, Conducting Nb:SnO₂ for Host–Guest Photoelectrochemistry. *Nano Letters* **2012**, *12* (10), 5431-5435.
72. Tilley, S. D.; Cornuz, M.; Sivula, K.; Grätzel, M., Light-Induced Water Splitting with Hematite: Improved Nanostructure and Iridium Oxide Catalysis. *Angew. Chem. Int. Ed.* **2010**, *49* (36), 6405-6408.
73. Du, P.; Eisenberg, R., Catalysts made of earth-abundant elements (Co, Ni, Fe) for water splitting: recent progress and future challenges. *Energy & Environmental Science* **2012**, *5* (3), 6012-6021.
74. Fominykh, K.; Feckl, J. M.; Sicklinger, J.; Döblinger, M.; Böcklein, S.; Ziegler, J.; Peter, L.; Rathousky, J.; Scheidt, E. W.; Bein, T., Ultrasmall Dispersible Crystalline Nickel Oxide Nanoparticles as High-Performance Catalysts for Electrochemical Water Splitting. *Advanced Functional Materials* **2014**, *24* (21), 3123-3129.
75. [https://en.wikipedia.org/wiki/Iron\(III\)_oxide#/media/File:Haematite-unit-cell-3D-balls.png](https://en.wikipedia.org/wiki/Iron(III)_oxide#/media/File:Haematite-unit-cell-3D-balls.png) (accessed 24.2.2016).
76. Kudo, A.; Omori, K.; Kato, H., A novel aqueous process for preparation of crystal form-controlled and highly crystalline BiVO₄ powder from layered vanadates at room

temperature and its photocatalytic and photophysical properties. *Journal of the American Chemical Society* **1999**, *121* (49), 11459-11467.

77. Park, Y.; McDonald, K. J.; Choi, K.-S., Progress in bismuth vanadate photoanodes for use in solar water oxidation. *Chemical Society Reviews* **2013**, *42* (6), 2321-2337.

78. Li, Z.; Luo, W.; Zhang, M.; Feng, J.; Zou, Z., Photoelectrochemical cells for solar hydrogen production: current state of promising photoelectrodes, methods to improve their properties, and outlook. *Energy & Environmental Science* **2013**, *6* (2), 347-370.

79. Pihosh, Y.; Turkevych, I.; Mawatari, K.; Uemura, J.; Kazoe, Y.; Kosar, S.; Makita, K.; Sugaya, T.; Matsui, T.; Fujita, D.; Tosa, M.; Kondo, M.; Kitamori, T., Photocatalytic generation of hydrogen by core-shell WO₃/BiVO₄ nanorods with ultimate water splitting efficiency. *Scientific Reports* **2015**, *5*, 11141.

80. Huang, Z.-F.; Pan, L.; Zou, J.-J.; Zhang, X.; Wang, L., Nanostructured bismuth vanadate-based materials for solar-energy-driven water oxidation: a review on recent progress. *Nanoscale* **2014**, *6* (23), 14044-14063.

81. Abdi, F. F.; Han, L.; Smets, A. H. M.; Zeman, M.; Dam, B.; van de Krol, R., Efficient solar water splitting by enhanced charge separation in a bismuth vanadate-silicon tandem photoelectrode. *Nat Commun* **2013**, *4*.

82. Paracchino, A.; Mathews, N.; Hisatomi, T.; Stefiik, M.; Tilley, S. D.; Gratzel, M., Ultrathin films on copper(i) oxide water splitting photocathodes: a study on performance and stability. *Energy & Environmental Science* **2012**, *5* (9), 8673-8681.

83. Kondo, J., Cu₂O as a photocatalyst for overall water splitting under visible light irradiation. *Chemical Communications* **1998**, (3), 357-358.

84. Zhang, Z.; Wang, P., Highly stable copper oxide composite as an effective photocathode for water splitting via a facile electrochemical synthesis strategy. *Journal of Materials Chemistry* **2012**, *22* (6), 2456-2464.

85. Paracchino, A.; Laporte, V.; Sivula, K.; Grätzel, M.; Thimsen, E., Highly active oxide photocathode for photoelectrochemical water reduction. *Nat Mater* **2011**, *10* (6), 456-461.

86. [https://en.wikipedia.org/wiki/Copper\(I\)_oxide#/media/File:Copper\(I\)-oxide-unit-cell-A-3D-balls.png](https://en.wikipedia.org/wiki/Copper(I)_oxide#/media/File:Copper(I)-oxide-unit-cell-A-3D-balls.png) (accessed 24.2.2016).

87. De Jongh, P.; Vanmaekelbergh, D.; Kelly, J. J. d., Photoelectrochemistry of Electrodeposited Cu₂O. *Journal of The Electrochemical Society* **2000**, *147* (2), 486-489.

88. Siripala, W.; Ivanovskaya, A.; Jaramillo, T. F.; Baeck, S.-H.; McFarland, E. W., A Cu₂O/TiO₂ heterojunction thin film cathode for photoelectrocatalysis. *Solar Energy Materials and Solar Cells* **2003**, *77* (3), 229-237.
89. Hu, C.-C.; Nian, J.-N.; Teng, H., Electrodeposited p-type Cu₂O as photocatalyst for H₂ evolution from water reduction in the presence of WO₃. *Solar Energy Materials and Solar Cells* **2008**, *92* (9), 1071-1076.
90. Nian, J.-N.; Hu, C.-C.; Teng, H., Electrodeposited p-type Cu₂O for H₂ evolution from photoelectrolysis of water under visible light illumination. *International Journal of Hydrogen Energy* **2008**, *33* (12), 2897-2903.
91. Barreca, D.; Fornasiero, P.; Gasparotto, A.; Gombac, V.; Maccato, C.; Montini, T.; Tondello, E., The potential of supported Cu₂O and CuO nanosystems in photocatalytic H₂ production. *ChemSusChem* **2009**, *2* (3), 230-233.
92. Li, C.; Hisatomi, T.; Watanabe, O.; Nakabayashi, M.; Shibata, N.; Domen, K.; Delaunay, J.-J., Positive onset potential and stability of Cu₂O-based photocathodes in water splitting by atomic layer deposition of a Ga₂O₃ buffer layer. *Energy & Environmental Science* **2015**, *8* (5), 1493-1500.
93. Koffyberg, F.; Benko, F., A photoelectrochemical determination of the position of the conduction and valence band edges of p-type CuO. *Journal of Applied Physics* **1982**, *53* (2), 1173-1177.
94. Hsu, Y.-K.; Yu, C.-H.; Lin, H.-H.; Chen, Y.-C.; Lin, Y.-G., Template synthesis of copper oxide nanowires for photoelectrochemical hydrogen generation. *Journal of Electroanalytical Chemistry* **2013**, *704*, 19-23.
95. Chiang, C.-Y.; Shin, Y.; Aroh, K.; Ehrman, S., Copper oxide photocathodes prepared by a solution based process. *international journal of hydrogen energy* **2012**, *37* (10), 8232-8239.
96. Chiang, C.-Y.; Aroh, K.; Franson, N.; Satsangi, V. R.; Dass, S.; Ehrman, S., Copper oxide nanoparticle made by flame spray pyrolysis for photoelectrochemical water splitting—Part II. Photoelectrochemical study. *international journal of hydrogen energy* **2011**, *36* (24), 15519-15526.
97. Lim, Y.-F.; Chua, C. S.; Lee, C. J. J.; Chi, D., Sol-gel deposited Cu₂O and CuO thin films for photocatalytic water splitting. *Physical Chemistry Chemical Physics* **2014**, *16* (47), 25928-25934.

98. Cupric oxide (CuO) crystal structure, lattice parameters. In *Non-Tetrahedrally Bonded Elements and Binary Compounds I*, Madelung, O.; Rössler, U.; Schulz, M., Eds. Springer Berlin Heidelberg: Berlin, Heidelberg, 1998; pp 1-3.
99. [https://en.wikipedia.org/wiki/Copper\(II\)_oxide#/media/File:Copper\(II\)-oxide-unit-cell-3D-balls.png](https://en.wikipedia.org/wiki/Copper(II)_oxide#/media/File:Copper(II)-oxide-unit-cell-3D-balls.png) (accessed 24.2.2016).
100. Sagu, J. S.; Peiris, T. N.; Wijayantha, K. U., Rapid and simple potentiostatic deposition of copper (II) oxide thin films. *Electrochemistry Communications* **2014**, *42*, 68-71.
101. Guo, X.; Diao, P.; Xu, D.; Huang, S.; Yang, Y.; Jin, T.; Wu, Q.; Xiang, M.; Zhang, M., CuO/Pd composite photocathodes for photoelectrochemical hydrogen evolution reaction. *International Journal of Hydrogen Energy* **2014**, *39* (15), 7686-7696.
102. Zhao, X.; Wang, P.; Yan, Z.; Ren, N., Ag nanoparticles decorated CuO nanowire arrays for efficient plasmon enhanced photoelectrochemical water splitting. *Chemical Physics Letters* **2014**, *609*, 59-64.
103. Rowley, J. G.; Do, T. D.; Cleary, D. A.; Parkinson, B. A., Combinatorial Discovery Through a Distributed Outreach Program: Investigation of the Photoelectrolysis Activity of p-Type Fe, Cr, Al Oxides. *ACS Applied Materials & Interfaces* **2014**, *6* (12), 9046-9052.
104. Sliozberg, K.; Schäfer, D.; Meyer, R.; Ludwig, A.; Schuhmann, W., A Combinatorial Study of Photoelectrochemical Properties of Fe-W-O Thin Films. *ChemPlusChem* **2015**, *80* (1), 136-140.
105. Stein, H. S.; Gutkowski, R.; Siegel, A.; Schuhmann, W.; Ludwig, A., New materials for the light-induced hydrogen evolution reaction from the Cu–Si–Ti–O system. *Journal of Materials Chemistry A* **2016**.
106. Woodhouse, M.; Parkinson, B. A., Combinatorial approaches for the identification and optimization of oxide semiconductors for efficient solar photoelectrolysis. *Chemical Society Reviews* **2009**, *38* (1), 197-210.
107. Woodhouse, M.; Parkinson, B. A., Combinatorial Discovery and Optimization of a Complex Oxide with Water Photoelectrolysis Activity. *Chemistry of Materials* **2008**, *20* (7), 2495-2502.
108. Parkinson, B., Distributed research: a new paradigm for undergraduate research and global problem solving. *Energy & Environmental Science* **2010**, *3* (5), 509-511.
109. Sliozberg, K.; Stein, H. S.; Khare, C.; Parkinson, B. A.; Ludwig, A.; Schuhmann, W., Fe–Cr–Al Containing Oxide Semiconductors as Potential Solar Water-Splitting Materials. *ACS Applied Materials & Interfaces* **2015**, *7* (8), 4883-4889.

110. Skorupska, K.; Maggard, P. A.; Eichberger, R.; Schwarzburg, K.; Shahbazi, P.; Zoellner, B.; Parkinson, B. A., Combinatorial Investigations of High Temperature CuNb Oxide Phases for Photoelectrochemical Water Splitting. *ACS combinatorial science* **2015**.
111. McKone, J. R.; Ardo, S.; Blakemore, J. D.; Bracher, P. J.; Dempsey, J. L.; Darnton, T. V.; Hansen, M. C.; Harman, W. H.; Rose, M. J.; Walter, M. G.; Dasgupta, S.; Winkler, J. R.; Gray, H. B., The Solar Army: A Case Study in Outreach Based on Solar Photoelectrochemistry. *Reviews in Advanced Sciences and Engineering* **2014**, *3* (4), 288-303.
112. Singh, A. K.; Mathew, K.; Zhuang, H. L.; Hennig, R. G., Computational Screening of 2D Materials for Photocatalysis. *The Journal of Physical Chemistry Letters* **2015**, *6* (6), 1087-1098.
113. Castelli, I. E.; Olsen, T.; Datta, S.; Landis, D. D.; Dahl, S.; Thygesen, K. S.; Jacobsen, K. W., Computational screening of perovskite metal oxides for optimal solar light capture. *Energy & Environmental Science* **2012**, *5* (2), 5814-5819.
114. Castelli, I. E.; Landis, D. D.; Thygesen, K. S.; Dahl, S.; Chorkendorff, I.; Jaramillo, T. F.; Jacobsen, K. W., New cubic perovskites for one- and two-photon water splitting using the computational materials repository. *Energy & Environmental Science* **2012**, *5* (10), 9034-9043.
115. Greeley, J.; Jaramillo, T. F.; Bonde, J.; Chorkendorff, I.; Norskov, J. K., Computational high-throughput screening of electrocatalytic materials for hydrogen evolution. *Nat Mater* **2006**, *5* (11), 909-913.
116. Castelli, I. E., *Computational Screening of Materials for Water Splitting Applications: Ph.D. Thesis*. Center for Atomic-scale Materials Design, Technical University of Denmark: 2013.
117. Castelli, I. E.; Thygesen, K. S.; Jacobsen, K. W., Calculated Pourbaix Diagrams of Cubic Perovskites for Water Splitting: Stability Against Corrosion. *Topics in Catalysis* **2013**, *57* (1), 265-272.
118. https://cmr.fysik.dtu.dk/cubic_perovskites/cubic_perovskites.html (accessed 24.2.2016).
119. Landis, D. D.; Hummelshoj, J. S.; Nestorov, S.; Greeley, J.; Dulak, M.; Bligaard, T.; Norskov, J. K.; Jacobsen, K. W., The computational materials repository. *Computing in Science & Engineering* **2012**, *14* (6), 51-57.
120. Velev, O. D.; Kaler, E. W., Structured Porous Materials via Colloidal Crystal Templating: From Inorganic Oxides to Metals. *Advanced Materials* **2000**, *12* (7), 531-534.

121. Stein, A.; Wilson, B. E.; Rudisill, S. G., Design and functionality of colloidal-crystal-templated materials—chemical applications of inverse opals. *Chemical Society Reviews* **2013**, *42* (7), 2763-2803.
122. Chen, K.; Tüysüz, H., Morphology-Controlled Synthesis of Organometal Halide Perovskite Inverse Opals. *Angewandte Chemie International Edition* **2015**, *54* (46), 13806-13810.
123. Zakhidov, A. A.; Baughman, R. H.; Iqbal, Z.; Cui, C.; Khayrullin, I.; Dantas, S. O.; Marti, J.; Ralchenko, V. G., Carbon structures with three-dimensional periodicity at optical wavelengths. *Science* **1998**, *282* (5390), 897-901.
124. Velev, O. D.; Jede, T.; Lobo, R.; Lenhoff, A., Microstructured porous silica obtained via colloidal crystal templates. *Chemistry of materials* **1998**, *10* (11), 3597-3602.
125. Holland, B. T.; Blanford, C. F.; Stein, A., Synthesis of macroporous minerals with highly ordered three-dimensional arrays of spheroidal voids. *Science* **1998**, *281* (5376), 538-540.
126. Hatton, B.; Mishchenko, L.; Davis, S.; Sandhage, K. H.; Aizenberg, J., Assembly of large-area, highly ordered, crack-free inverse opal films. *Proceedings of the National Academy of Sciences* **2010**, *107* (23), 10354-10359.
127. **!!! INVALID CITATION !!!**
128. Born, P.; Blum, S.; Munoz, A.; Kraus, T., Role of the meniscus shape in large-area convective particle assembly. *Langmuir* **2011**, *27* (14), 8621-8633.
129. Stöber, W.; Fink, A.; Bohn, E., Controlled growth of monodisperse silica spheres in the micron size range. *Journal of colloid and interface science* **1968**, *26* (1), 62-69.
130. Marlow, F.; Muldarisnur; Sharifi, P.; Brinkmann, R.; Mendive, C., Opals: Status and Prospects. *Angewandte Chemie International Edition* **2009**, *48* (34), 6212-6233.
131. Hoogenboom, J. P.; Derks, D.; Vergeer, P.; van Blaaderen, A., Stacking faults in colloidal crystals grown by sedimentation. *The Journal of chemical physics* **2002**, *117* (24), 11320-11328.
132. Hilhorst, J.; van Schooneveld, M. M.; Wang, J.; de Smit, E.; Tyliczszak, T.; Raabe, J.; Hitchcock, A. P.; Obst, M.; de Groot, F. M.; Petukhov, A. V., Three-dimensional structure and defects in colloidal photonic crystals revealed by tomographic scanning transmission X-ray microscopy. *Langmuir* **2012**, *28* (7), 3614-3620.
133. Aguirre, C. I.; Reguera, E.; Stein, A., Tunable colors in opals and inverse opal photonic crystals. *Advanced Functional Materials* **2010**, *20* (16), 2565-2578.

134. Dusastre, V., Inverse opal catalysts. *Nature materials* **2013**, *12* (12), 1080-1080.
135. Esmanski, A.; Ozin, G. A., Silicon Inverse-Opal-Based Macroporous Materials as Negative Electrodes for Lithium Ion Batteries. *Advanced Functional Materials* **2009**, *19* (12), 1999-2010.
136. Kondofersky, I.; Müller, A.; Dunn, H. K.; Ivanova, A.; Štefanić, G.; Ehrensperger, M.; Scheu, C.; Parkinson, B. A.; Fattakhova-Rohlfing, D.; Bein, T., Nanostructured Ternary FeCrAl Oxide Photocathodes for Water Photoelectrolysis. *Journal of the American Chemical Society* **2016**, *138* (6), 1860-1867.
137. Kondofersky, I.; Dunn, H.; Müller, A.; Mandlmeier, B.; Feckl, J. M.; Fattakhova-Rohlfing, D.; Scheu, C.; Peter, L. M.; Bein, T., Electron collection in host-guest nanostructured hematite photoanodes for water splitting: the influence of scaffold doping density. *ACS Applied Materials & Interfaces* **2015**.
138. McCusker, L.; Liebau, F.; Engelhardt, G., Nomenclature of structural and compositional characteristics of ordered microporous and mesoporous materials with inorganic hosts (IUPAC Recommendations 2001). *Pure and Applied Chemistry* **2001**, *73* (2), 381-394.
139. Corma, A., From microporous to mesoporous molecular sieve materials and their use in catalysis. *Chemical reviews* **1997**, *97* (6), 2373-2420.
140. Ying, J. Y.; Mehnert, C. P.; Wong, M. S., Synthesis and applications of supramolecular-templated mesoporous materials. *Angewandte Chemie International Edition* **1999**, *38* (1-2), 56-77.
141. Davis, M. E., Ordered porous materials for emerging applications. *Nature* **2002**, *417* (6891), 813-821.
142. Schüth, F., Non-siliceous mesostructured and mesoporous materials. *Chemistry of Materials* **2001**, *13* (10), 3184-3195.
143. Bruce, P. G.; Scrosati, B.; Tarascon, J. M., Nanomaterials for rechargeable lithium batteries. *Angewandte Chemie International Edition* **2008**, *47* (16), 2930-2946.
144. Innocenzi, P.; Malfatti, L., Mesoporous thin films: properties and applications. *Chemical Society Reviews* **2013**, *42* (9), 4198-4216.
145. Ren, Y.; Ma, Z.; Bruce, P. G., Ordered mesoporous metal oxides: synthesis and applications. *Chemical Society Reviews* **2012**, *41* (14), 4909-4927.
146. Ivanova, A.; Fattakhova-Rohlfing, D.; Kayaalp, B. E.; Rathouský, J.; Bein, T., Tailoring the morphology of mesoporous titania thin films through biotemplating with

- nanocrystalline cellulose. *Journal of the American Chemical Society* **2014**, *136* (16), 5930-5937.
147. Brinker, C. J.; Lu, Y.; Sellinger, A.; Fan, H., Evaporation-induced self-assembly: nanostructures made easy. *Advanced materials* **1999**, *11* (7), 579-585.
148. Förster, S.; Antonietti, M., Amphiphilic block copolymers in structure-controlled nanomaterial hybrids. *Advanced Materials* **1998**, *10* (3), 195-217.
149. Sanchez, C.; Boissiere, C.; Grosso, D.; Laberty, C.; Nicole, L., Design, synthesis, and properties of inorganic and hybrid thin films having periodically organized nanoporosity†. *Chemistry of materials* **2008**, *20* (3), 682-737.
150. Grosso, D.; Cagnol, F.; Soler-Illia, G. d. A.; Crepaldi, E. L.; Amenitsch, H.; Brunet-Bruneau, A.; Bourgeois, A.; Sanchez, C., Fundamentals of mesostructuring through evaporation-induced self-assembly. *Advanced Functional Materials* **2004**, *14* (4), 309-322.
151. Mahoney, L.; Koodali, R. T., Versatility of evaporation-induced self-assembly (EISA) method for preparation of mesoporous TiO₂ for energy and environmental applications. *Materials* **2014**, *7* (4), 2697-2746.
152. Pan, J. H.; Zhao, X.; Lee, W. I., Block copolymer-templated synthesis of highly organized mesoporous TiO₂-based films and their photoelectrochemical applications. *Chemical Engineering Journal* **2011**, *170* (2), 363-380.
153. Rochow, E. G.; Gingold, K., The conversion of chlorosilanes to siloxanes by dimethylformamide. *Journal of the American Chemical Society* **1954**, *76* (19), 4852-4855.
154. Ebelmen, *Recherches sur les combinaisons des acides borique et silicique avec les éthers*. 1846.
155. Niederberger, M.; Pinna, N., *Metal oxide nanoparticles in organic solvents: synthesis, formation, assembly and application*. Springer Science & Business Media: 2009.
156. https://upload.wikimedia.org/wikipedia/commons/thumb/2/25/Sol-Gel_Scheme.svg/2000px-Sol-Gel_Scheme.svg.png (accessed 24.2.2016).
157. Debecker, D. P.; Mutin, P. H., Non-hydrolytic sol-gel routes to heterogeneous catalysts. *Chemical Society Reviews* **2012**, *41* (9), 3624-3650.
158. Niederberger, M., Nonaqueous sol-gel routes to metal oxide nanoparticles. *Accounts of chemical research* **2007**, *40* (9), 793-800.
159. Niederberger, M.; Garnweitner, G., Organic reaction pathways in the nonaqueous synthesis of metal oxide nanoparticles. *Chemistry—A European Journal* **2006**, *12* (28), 7282-7302.

160. Feckl, J. Synthesis route for ultra-small nanoparticles for energy applications. Imu, 2013.

2 Characterization techniques

Physical and electrochemical properties of the mixed metal oxide porous electrodes were characterized thoroughly by employing different materials science techniques. X-ray diffraction, Raman spectroscopy and XPS are commonly used to assess the composition and crystallinity of the material. Scanning and transmission electron microscopy are essential techniques for characterization of morphology and composition of defined porous structures. Optical measurements such as UV-Vis spectroscopy are crucial for the determination of the optical properties of the synthesized films, revealing characteristic parameters such as the band gap or the light harvesting efficiency. In the end, the measure for comparison among the different systems is the efficiency assessed by photoelectrochemical characterization.

2.1 X-ray Diffraction

After the discovery of X-rays by Röntgen in 1895 and the discovery of X-ray diffraction in crystals by Laue in 1913, X-ray diffraction (XRD) has become an essential non-destructive technique for the characterization of crystalline materials¹⁻². Composition, domain size, orientation and crystal structure are just a few factors which can be determined by XRD analysis. The X-rays are generated by an evacuated X-ray tube where current and high voltages are applied to a Cu-K α 1 ($\lambda = 1.54\text{\AA}$) or a Mo- K α 1 ($\lambda = 7.02\text{\AA}$) filament to trigger electron emission into vacuum. The generated electrons then strike an anode and X-rays are emitted. The XRD method is based on the elastic scattering of X-rays by the atoms in a periodic structure. Therefore, X-rays have to be focused on the sample surface to allow constructive interference of X-rays with the crystal structure, thus generating a unique pattern. The scattering angle of the X-ray beam and the distance of the lattice planes are described by Bragg's law:

$$n\lambda = 2d\sin\theta \quad (2-1)$$

n represents the order of interference and λ the wavelength of utilized X-rays depending on the used filament. The lattice spacing is shown as d and θ refers to the angle of incidence.

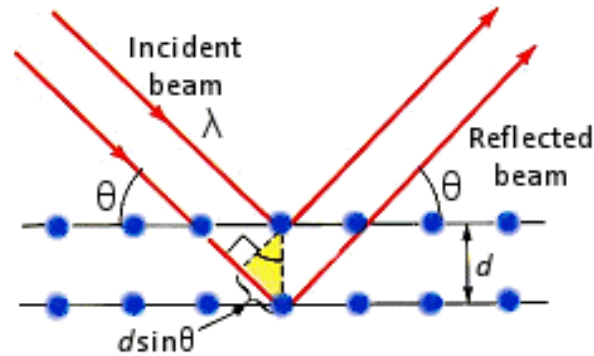


Figure 2-1: Scheme of X-ray scattering in crystals used for derivation of Bragg's law³.

Generally, X-ray diffraction techniques can be divided into Wide angle X-ray scattering (WAXS) and Small angle X-ray scattering (SAXS) which refers to the measurement angles used for the analysis. In the case of SAXS, the measured angles are between 0.1 and 10° 2θ and in the case of WAXS between 10 and 100° 2θ . By using SAXS periodic mesoporous structures can be characterized while WAXS delivers information concerning the phase and crystallinity of the material.

Further, the full width at half maximum (FWHM) of a reflection can be determined and used for the evaluation of domain sizes in the structure. The Scherrer equation describes the relation between the domain size and the corresponding diffraction peak broadening. In the Scherrer equation λ stands for the X-ray wavelength, k refers to the shape dependent form factor, β represents the peak broadening (FWHM) and θ the scattering angle.

$$D = \frac{k\lambda}{\beta \cos \theta} \quad (2-2)$$

X-ray diffraction analysis (XRD) was carried out on a STOE powder diffractometer (Cu K α 1, $\lambda = 1.5406 \text{ \AA}$) equipped with a position sensitive Mythen-1K detector in transmission geometry.

2.2 Raman Spectroscopy

Raman spectroscopy is an important non-destructive technique for characterization of phase composition and chemical composition of materials⁴. By observing vibrational, rotational and other low-frequency modes a fingerprint spectrum can be determined for an individual compound. During a Raman measurement the sample is irradiated by a monochromatic laser interacting with molecular vibrations causing excitement of the system from the ground state to a virtual energy state. The scattered light different from the excitation light is collected and dispersed onto a detector causing a shift of frequency corresponding to the specific energy levels of a material. Upon relaxation of the molecule to the ground state a photon is emitted. The resulting incident light can then undergo elastic or inelastic scattering (Figure 2-2). Elastic scattering or Rayleigh scattering is observed when the energies of the emitted and the absorbed photon are equal. In the case of inelastic scattering the emitted energy is different from the excitation energy. Stokes Raman scattering describes the phenomenon when a molecule is excited from the ground state and relaxes in a vibrational or rotational excited state thus emitting light of less energy. The anti-Stokes Raman scattering, on the other hand, describes the opposite effect where a molecule relaxes to an energetically lower state than the initial resulting in emission of light with higher energy.

A requirement for Raman active materials is the possible polarization of molecules upon irradiation. Stokes lines show higher intensity compared to anti-Stokes lines given the low occupation of excited states at room temperature.

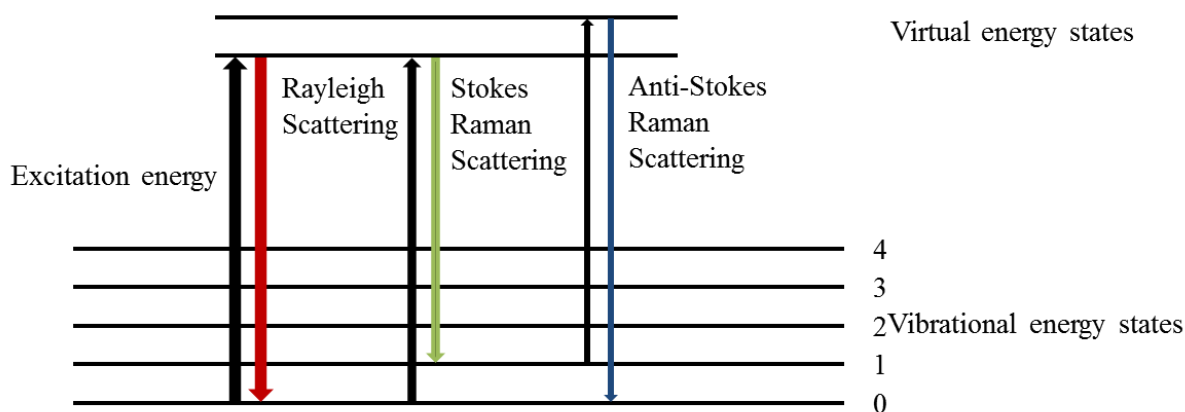


Figure 2-2: Scheme of Rayleigh-, Stokes- and anti-Stokes scattering processes occurring during Raman spectroscopy.

Raman spectra were acquired using a LabRAM HR UVVIS (HORIBA Jobin Yvon) Raman spectroscope (Olympus BX-41) with a Symphony CCD detector system and a He-Ne-Laser (wavelength: 633 nm).

2.3 Scanning Electron Microscopy

Scanning electron microscopy (SEM) is an essential non-destructive technique allowing a detailed characterization of a material with respect to morphology and composition.⁵⁻⁶ The working principle of SEM is based on scanning the sample surface with an electron beam, typically generated by a field emission gun and focused by electromagnetic and electrostatic lenses. The incident electrons interact with the sample resulting in deceleration and absorption of the electrons by the sample (Figure 2-3). The electron perturbation depth in the sample depends on the acceleration voltage. The detected electrons are collected and the information

2.3. Scanning Electron Microscopy

is used to produce an image of the surface. In general, there are two signals which can be used for creating an image, secondary and backscattered electrons. Secondary electrons offer spatial resolution and high surface sensitivity, given that they are generated close to the sample surface and have low energy. Backscattered electrons, on the other hand, have higher energy and originate from deeper perturbation of the sample. The resulting spatial resolution is lower but the sample can be characterized by visualizing different materials or phases, due to the strong dependence of back scattered electrons on the atomic number. The material of interest can be further investigated by determining the composition using energy- or wavelength-dispersive X-ray analysis. Here, generated primary electrons provide the needed energy to excite atomic transitions thus allowing a simultaneous analysis of the present elements. SEM measurements were performed on a JEOL JSM-6500F with a field emission gun run at 5 kV and equipped with an Oxford energy-dispersive X-ray (EDX) detector.

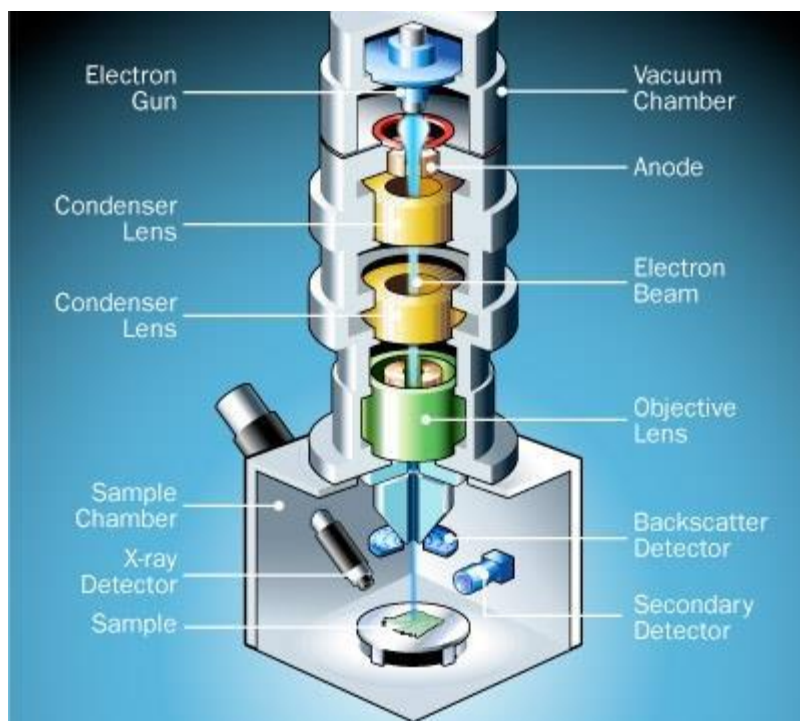


Figure 2-3: Illustration of a scanning electron microscope⁷.

2.4 Transmission Electron Microscopy

In the world of nanostructured materials transmission electron microscopy (TEM) is another important technique aiming at the optical and compositional characterization of a sample. In contrast to SEM, TEM uses transmitted electrons for imaging allowing higher magnification (Figure 2-4). Further, higher accelerating voltages are applied in the range between 80 to more than 400 kV allowing microscopy on the atomic scale. A probe-corrected FEI Titan Themis with an X-FEG operated at 300 kV was used for TEM investigations. Bright field (BF) and high-resolution TEM (HRTEM) images as well as diffraction patterns were acquired with a Ceta 16M camera, scanning TEM (STEM) images with a annular dark field (ADF) detector, and energy-dispersive X-ray (EDX) spectra and maps with four Super-X Bruker SDD detectors. Samples were prepared either by scraping material of the substrate with a razor blade and depositing it on a holey carbon grid or in a cross-sectional geometry as described by Strecker *et al.*⁸

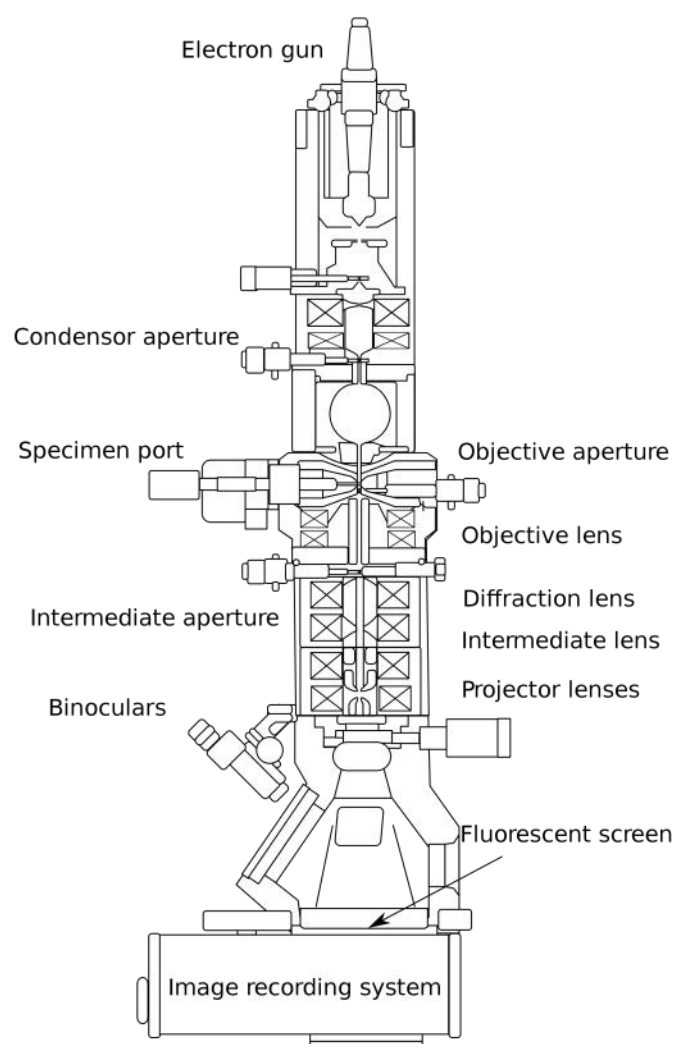


Figure 2-4: Illustration of a transmission electron microscope⁹.

2.5 UV-Vis Spectroscopy

UV-Vis spectroscopy is a commonly used technique for a quantitative characterization of light absorbing compounds such as solutions or solid materials. Within the measurement the sample is illuminated by monochromatic light with a wavelength covering the ultraviolet to the near infrared region. Upon illumination the sample absorbs photons causing electronic transitions exciting electrons in the valence band to higher excited states. By applying the Lambert-Beer law, the concentration of the absorbing species can be determined, where A is

the detected absorbance, I_0 the intensity of incident light, I the intensity of transmitted light, ϵ the material specific extinction coefficient and L the pathlength through the sample:

$$A = -\log \frac{I}{I_0} = \epsilon c L \quad (2-3)$$

The absorption by the sample is associated with electronic transitions from the ground state to higher excited states due to absorption of the photon energy of the incident light.

UV-Vis characterization is essential for the complete analysis of photoactive thin films. The amount of light absorbed by the sample is crucial for the photoelectrochemical performance, determining the wavelength region in which the film is active. For this measurement it is assumed that light absorbed, reflected or transmitted resulting in the following expression:

$$\%A + \%R + \%T = 1 \quad (2-4)$$

As films are often deposited on transparent conducting substrates (such as fluorine doped tin oxide, FTO or tin doped indium oxide, ITO), the substrate's reflectance has to be taken into account. For this purpose, the samples are measured in both transmission and reflectance mode. Furthermore, the transmission and reflectance of the uncoated substrate are measured as a reference. The absorbance of each sample was calculated from experimental reflectance and transmittance data¹⁰, using the expression:

$$Abs_F = \ln \left(\frac{T_{S+F}/T_S}{1 - \frac{R_{S+F} - R_S}{T_S^2}} \right) \quad (2-5)$$

Here T_S/T_{S+F} and R_S/R_{S+F} correspond to the wavelength dependent transmissions and the reflections of the FTO substrate and the film-coated substrate, respectively.

UV-Vis spectrometer consists of a light source, a monochromator a sample holder and a detector. Measurements were performed on a Perkin Elmer Lambda 1050 UV/Visible/NIR spectrophotometer with an integrating sphere.

2.6 Photoelectrochemical Characterization

Current-Voltage Characterization

Current-Voltage measurements are a standard technique used to evaluate the potential of a device with respect to the ability to generate current under applied bias¹¹. Photoelectrodes used for solar-driven water splitting were characterized by measuring current-voltage curves using a μ -Autolab III potentiostat equipped with a FRA2 impedance analyzer. The samples were masked with a Teflon-coated glass fiber adhesive tape, leaving an area of 0.144 cm² free for illumination. Samples were placed in a quartz cell filled with electrolyte and connected in 3 electrode mode, together with the Ag/AgCl reference electrode and the Pt mesh counter electrode, to the potentiostat. The films were then illuminated either through the substrate (SI) or the electrolyte (EI) side using an AM1.5 solar simulator (Solar Light Model 16S) at 100 mW cm⁻².

The individual systems required different measurement conditions including electrolyte type, scan rate or scan direction. Depending on the stability and photoactivity of an electrode, electrochemical reactions were carried out in an appropriate electrolyte solution. The characteristic settings used for the individual electrode systems are described in the corresponding chapter. The photocurrent is defined as the difference between the light and dark current.

Incident-Photon-to-Current Efficiency

Incident-Photon-to-Current Efficiency (IPCE) is a measure for the ratio of generated and collected charges to the number of all incident photons active on a defined device area as a function of the wavelength. The IPCE can be experimentally measured and is the product of light harvesting η_{lh} , transfer η_{tr} and separation efficiency η_{sep} ¹².

$$IPCE(\lambda) = \eta_{lh}(\lambda) \cdot \eta_{tr}(\lambda) \cdot \eta_{sep}(\lambda) \quad (2-6)$$

The light harvesting efficiency can be assessed by calculating the wavelength dependent absorption coefficient and the film thickness, under the assumption that light scattering and internal reflection are neglected.

$$\eta_{LH} = 1 - e^{-\alpha(\lambda)d} \quad (2-7)$$

The separation efficiency can be calculated and quantified from the measured IPCE, light harvesting and transfer efficiencies.

IPCE measurements can be performed under electrolyte (EI) or substrate (SI) illumination. For thin films, the IPCE values measured for EI and SI are similar suggesting that the amount of generated charges can be extracted efficiently regardless of the illumination direction, given the short distance majority carriers have to travel to the conducting substrate before undergoing recombination. Thicker films, on the other side, show higher recombination due to the longer pathways across the films. In the case of substrate illumination charges are generated close to the conducting substrate and can be still extracted successfully before recombination. Under electrolyte illumination, on the other side, charges are generated near the semiconductor-electrolyte interface, far from the conducting substrate and are more likely to undergo recombination resulting in lower IPCE values.

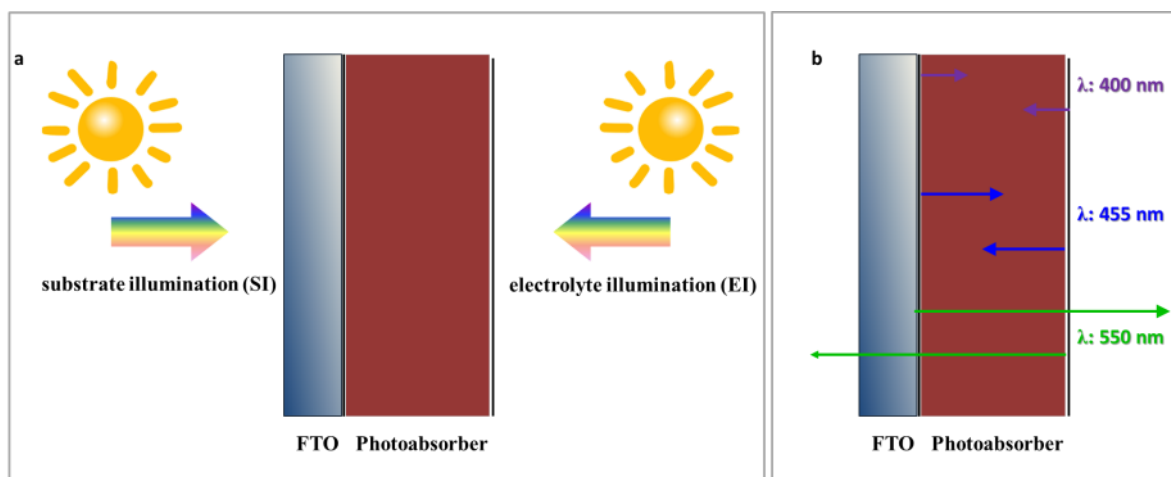


Figure 2-5: a) Illustration of substrate and electrolyte illumination of a photoabsorber. b) Wavelength dependent light penetration defining where charges are generated and how far they need to travel.

IPCE measurements were performed under low-frequency chopped monochromatic light (1 Hz). A 150 W Xenon lamp equipped with a monochromator and order-sorting filters was used as a light source. The sample bias was set to a fixed potential characteristic for the material under simulated solar irradiation to ensure realistic operating conditions. The light intensity was measured at the position of the electrode inside the cells using a 4 mm² photodiode, which had been calibrated against a certified Fraunhofer ISE silicon reference cell equipped with a KG5 filter.

Transient Photocurrent Characterization

The transfer efficiency of charges to the electrolyte η_{trans} can be assessed from transient current measurements¹³⁻¹⁴. By illuminating the electrode with chopped light at different chopping frequencies and potentials, photocurrent transients can be measured. From them, the instantaneous current I_{Inst} and the steady-state current I_{ss} can be determined. For a system

where kinetics at the surface is slower than electron generation, I_{Inst} is dominated by perfect electron transfer whereas I_{ss} shows an equilibrium of recombination and transfer. The ratio of I_{ss} and I_{Inst} is therefore a measure of the electron transfer efficiency η_{trans} calculated according to equation 2-8. This equation is valid under the assumption that the reaction is pseudo-first order.

$$\eta_{trans} = \frac{J_{ss}}{J_{inst}} = \frac{k_{trans}}{k_{trans} + k_{rec}} \quad (2-8)$$

Nanostructured photoelectrodes show a characteristic current response to chopped light. Figure 2-6 shows the response of an n-type semiconductor.

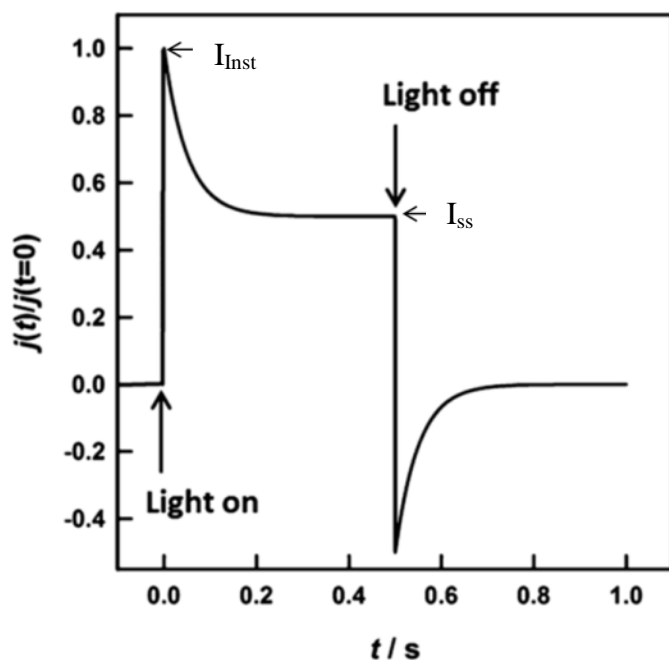


Figure 2-6: Response of an n-type semiconductor upon chopped illumination¹³.

To estimate the electron transfer efficiency, transient current measurements were performed by illuminating the electrode with a 455 nm light emitting diode. The light was switched on and off every 500 ms and the current was measured for different potentials.

2.7 References

1. Hildebrandt, G., The Discovery of the Diffraction of X-rays in Crystals — A Historical Review. *Crystal Research and Technology* **1993**, 28 (6), 747-766.
2. Fernández-García, M.; Martínez-Arias, A.; Hanson, J. C.; Rodriguez, J. A., Nanostructured Oxides in Chemistry: Characterization and Properties. *Chemical Reviews* **2004**, 104 (9), 4063-4104.
3. http://www.chemistryviews.org/details/ezone/2064331/100th_Anniversary_of_the_Discovery_of_X-ray_Diffraction.html (accessed 25.2.2016).
4. Gardiner, D. J., Introduction to Raman scattering. In *Practical Raman Spectroscopy*, Springer: 1989; pp 1-12.
5. McMullan, D., Scanning electron microscopy 1928–1965. *Scanning* **1995**, 17 (3), 175-185.
6. West, A. R., *Basic solid state chemistry*. John Wiley & Sons Inc: 1999.
7. <http://science.howstuffworks.com/scanning-electron-microscope2.htm> (accessed 27.2.2016).
8. Strecker, A., Salzberger, U. & Mayer, J. Specimen, Preparation for Transmission Electron Microscopy: Reliable Methods for Cross-Sections and Brittle Materials. *Praktische Metallographie* **1993**, 30, 482-495.
9. https://upload.wikimedia.org/wikipedia/commons/thumb/2/25/Scheme_TEM_en.svg/2000px-Scheme_TEM_en.svg.png (accessed 27.2.2016).
10. Klahr, B. M.; Martinson, A. B.; Hamann, T. W., Photoelectrochemical investigation of ultrathin film iron oxide solar cells prepared by atomic layer deposition. *Langmuir* **2010**, 27 (1), 461-468.
11. Walter, M. G.; Warren, E. L.; McKone, J. R.; Boettcher, S. W.; Mi, Q.; Santori, E. A.; Lewis, N. S., Solar Water Splitting Cells. *Chemical Reviews* **2010**, 110 (11), 6446-6473.
12. Dunn, H. K.; Feckl, J. M.; Muller, A.; Fattakhova-Rohlfing, D.; Morehead, S. G.; Roos, J.; Peter, L. M.; Scheu, C.; Bein, T., Tin doping speeds up hole transfer during light-driven water oxidation at hematite photoanodes. *Physical Chemistry Chemical Physics* **2014**, 16 (44), 24610-24620.
13. Lewerenz, H.-J.; Peter, L., *Photoelectrochemical water splitting: materials, processes and architectures*. Royal Society of Chemistry: 2013.

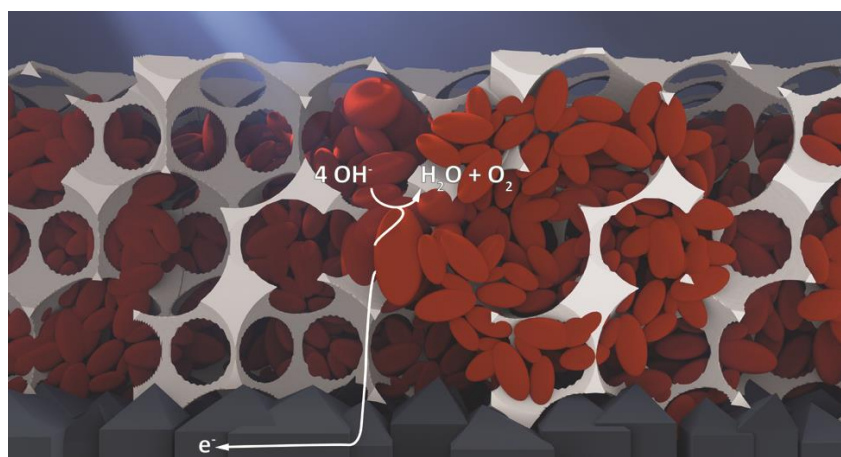
14. Peter, L. M., Energetics and kinetics of light-driven oxygen evolution at semiconductor electrodes: the example of hematite. *Journal of Solid State Electrochemistry* **2013**, *17* (2), 315-326.

3 Electron collection in host-guest nanostructured hematite photoanodes for water splitting: the influence of scaffold doping density

This chapter is based on the following publication:

Ilina Kondofersky*, Halina K. Dunn*, Alexander Müller, Benjamin Mandlmeier, Johann M. Feckl, Dina Fattakhova-Rohlfing, Christina Scheu, Laurence M. Peter and Thomas Bein, *ACS Appl. Mater. Interfaces*, **2015**, 7 (8), pp 4623–4630.

*These authors contributed equally.



Abstract

Nanostructuring has proven a successful strategy in overcoming the trade-off between light absorption and hole transport to the solid/electrolyte interface in hematite photoanodes for water splitting. The suggestion that poor electron (majority carrier) collection hinders the performance of nanostructured hematite electrodes has led to the emergence of host guest architectures in which the absorber layer is deposited onto a transparent high surface area electron collector. To date, however, state of the art nanostructured hematite electrodes still

outperform their host guest counterparts, and a quantitative evaluation of the benefits of the host guest architecture is still lacking. In this paper, we examine the impact of host guest architectures by comparing nanostructured tin-doped hematite electrodes with hematite nanoparticle layers coated onto two types of conducting macroporous SnO₂ scaffolds. Analysis of the external quantum efficiency spectra for substrate (SI) and electrolyte side (EI) illumination reveals that the electron diffusion length in the host-guest electrodes based on an undoped SnO₂ scaffold is increased substantially relative to the nanostructured hematite electrode without a supporting scaffold. Nevertheless, electron collection is still incomplete for EI illumination. By contrast, an electron collection efficiency of 100% is achieved by fabricating the scaffold using antimony-doped SnO₂, showing that the scaffold conductivity is crucial for the device performance.

3.1 Introduction

The demand for alternative energy resources has intensified research on photoelectrochemical systems for water splitting as a sustainable hydrogen source. Among the many semiconductors studied as possible candidates,¹⁻³ α -Fe₂O₃ hematite has received particular attention due to its chemical stability in basic solutions, its abundance and low production costs and a theoretical maximum solar to hydrogen efficiency of around 16 % in a tandem configuration in combination with a low band gap solar cell.^{1, 4-5}

One of the attractive features of hematite is that it absorbs light in the visible range up to a wavelength of around 600 nm. However, considering the small hole diffusion length in hematite of only 2-4 nm⁶, only holes photogenerated in the space charge region are likely to take part in the oxygen evolution reaction at the surface, while those generated in the bulk are mostly lost to recombination.⁷ These wasteful effects become increasingly significant for longer wavelengths, where most electron hole pairs are generated outside of the space charge

3. Introduction

region. One of the ways to improve the total charge collection efficiency of hematite photoanodes is nanostructuring, which addresses the trade-off between sufficient light harvesting and efficient hole collection by decoupling the hole collection depth from the light absorption depth. However, beside the increased photocurrents observed for different hematite nanomorphologies,⁸⁻¹³ nanostructuring also brings drawbacks such as longer and more tortuous paths for the transport of majority charge carriers (electrons) to the current collector, increasing the probability of their recombination with holes. Furthermore, the higher surface area can lead to additional electron recombination losses with species such as surface trapped holes and intermediates formed during the oxygen evolution reaction (OER). An alternative approach aiming to combine the advantages of both thin layer and nanostructured morphologies without the above mentioned limitations is the fabrication of hierarchical electrodes, in which the hole transport and the electron collection pathways are effectively decoupled from each other. In such electrodes (also called host guest architectures (HGA)), thin hematite layers are deposited on current collecting scaffolds with a high surface area.¹³⁻¹⁷ The current collector should be a wide band gap material with good electron transport properties and a suitable conduction band alignment to the hematite absorber so as to allow rapid electron extraction at the contact. Suitable scaffold materials include transparent conducting oxides (TCO) and semiconducting metal oxides.

Several studies have demonstrated the feasibility of the HGA concept for water splitting.¹⁵⁻²⁴ Sivula et al. were the first to demonstrate the suitability of WO_3 as an electron-extraction scaffold for hematite, although the enhancement in photocurrent was modest due to the low surface area of the WO_3 layers.¹⁵ Several authors have convincingly demonstrated that thin absorber layers deposited on high surface area current collectors generate photocurrents that are substantially higher than those measured for the same layers on a flat substrate.¹⁹⁻²⁰ However, the host guest concept has not yet delivered the promise of improved water splitting

performance. Despite intensive research activity in this area, state of the art host guest hematite-based photoanodes have, surprisingly, not yet outperformed their nanostructured hematite counterparts. Although significant currents have been reported for different host guest systems, such as 0.25 mAcm^{-2} ¹⁹ or 1 mAcm^{-2} ²⁰ at 1.23 V vs. RHE for thin layer hematite deposited on inverse opal indium tin oxide electrodes or porous niobium doped tin oxide, respectively, these HGA electrodes did not reach the efficiency of the best nanostructured electrodes (such as un-catalysed Si-doped hematite prepared by APCVD, which has reached 1.8 mAcm^{-2} under standard conditions at 1.23 V vs. RHE under AM 1.5 illumination).¹³

A central objective of this work was the investigation of host guest hematite architectures in water oxidation reactions aimed at understanding the factors that determine their efficiency. For this purpose we have studied the photoelectrochemical activity of nanostructured tin-doped hematite absorber layers deposited from precursor solutions. These films were fabricated on flat FTO substrates as well as on two types of macroporous SnO_2 scaffold with similar morphology but different electrical conductivity. Since improved electron collection is usually considered the main factor governing the performance of host guest electrodes, we have compared the electron diffusion length for nanostructured tin-doped hematite layers and the same layers coated on macroporous SnO_2 and Sb-doped SnO_2 host scaffolds with different conductivity. The electron diffusion length was determined from the spectral dependence of the ratio of the external quantum efficiency (EQE) for illumination through the electrolyte (EI) and through the substrate (SI). Based on the analysis of the EQE spectra for EI and SI illumination, we demonstrate that the deposition of the hematite layer on an undoped SnO_2 scaffold increases the electron collection efficiency significantly, although electron collection

is still incomplete for EI illumination. However, when Sb-doped SnO_2 is used, complete collection of electrons occurs, and EI and SI EQE spectra are identical.

3.2 Results and Discussion

The inverse opal host guest electrodes used in this work were fabricated via crystal templating (Figure 3-1).²⁵ The inverse opal morphology features uniform open pores that can be coated internally with the absorber material. The periodic network of interconnected walls is intended to act as a continuous pathway for electron transport to the anode contact. In a typical procedure, a template opal film was prepared by deposition of 300 nm polymethylmethacrylate (PMMA) spheres on an FTO substrate via ultra-slow dip coating resulting in an ordered close packing of spheres. Afterwards, the opal films were impregnated with a sol-gel oxide precursor via dip coating and calcined in air to remove the PMMA template. Two types of scaffolds with identical morphology but different electrical conductivity of the walls were prepared, namely tin oxide (SnO_2) and antimony-doped tin oxide ($\text{SnO}_2:\text{Sb}$). Additionally, insulating silica inverse opal layers were used to investigate the role of the scaffold conductivity on the performance of host guest electrodes.

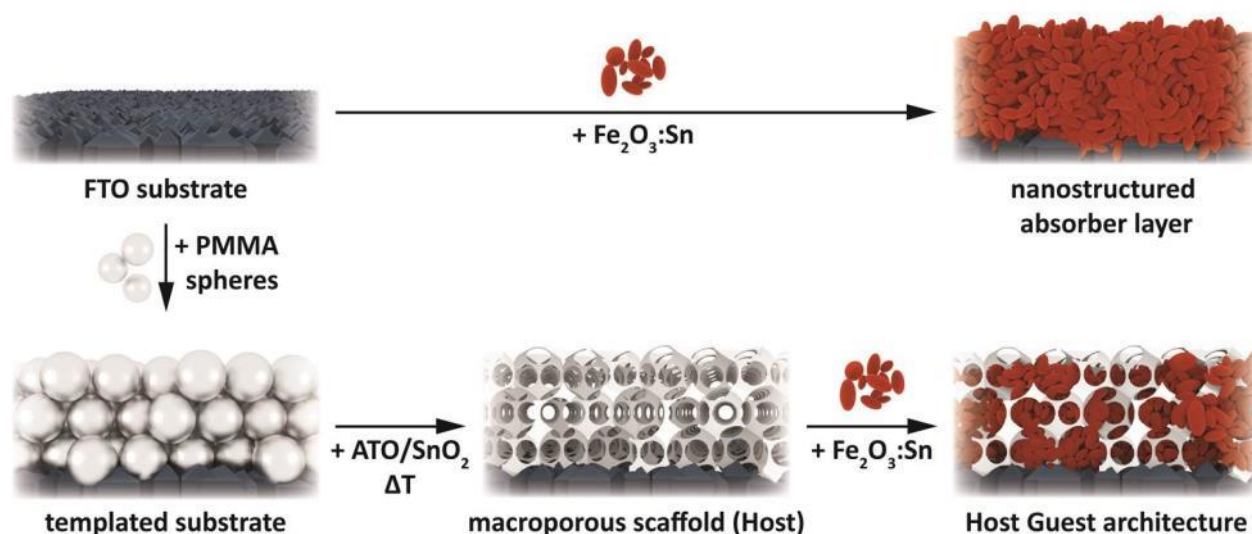


Figure 3-1: Synthesis scheme of macroporous host guest samples and nanostructured flat absorber films on FTO.

The macroporous SnO_2 and $\text{SnO}_2\text{:Sb}$ scaffolds obtained after calcination are composed of interconnected periodically ordered spherical pores with a diameter of 250 nm separated by ca. 30-40 nm thick crystalline pore walls and interconnected by openings around 80 nm in diameter. The size of the pores after calcination is about 17 % smaller than the diameter of the parent PMMA beads due to the crystallisation-induced shrinkage of the inorganic scaffold. The average thickness of the calcined films is about 2 μm . The donor doping density, estimated from the Mott Schottky analysis of compact layers of SnO_2 and $\text{SnO}_2\text{:Sb}$ (Figure 3-2), increases by around three orders of magnitude upon Sb doping, confirming that the latter acts as an electrical dopant (see Figure S 3-16 for further details).¹⁶

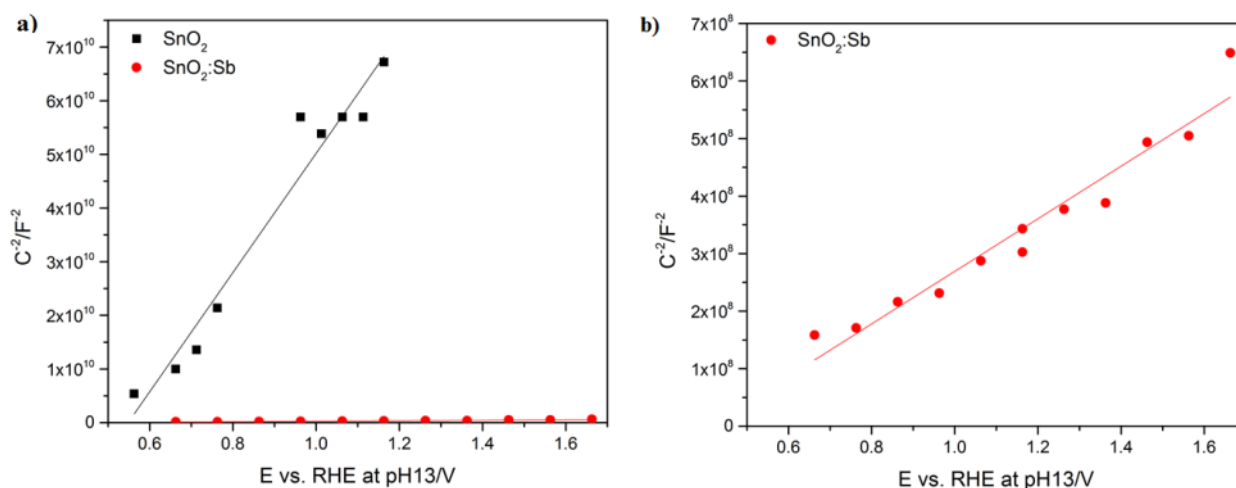


Figure 3-2: Capacitance data plotted in Mott-Schottky representation for $\text{SnO}_2\text{:Sb}$ and SnO_2 flat layers coated on FTO (a); (b) shows the plot for ATO at a different scale. Electrolyte 0.1 M NaOH, electrode area 0.2 cm^2 .

To fabricate working photoanodes, the macroporous structures were infiltrated with tin-doped hematite by spin coating the precursor solution, as summarized in Figure 1. The procedure for fabrication of nanostructured tin-doped hematite coatings on fluorine-doped tin oxide coated glass substrates via a solution-based method has been described by us elsewhere.²⁶ In a typical procedure, a precursor solution prepared from $\text{Fe}(\text{NO}_3)_3$, $\text{Sn}(\text{OAc})_4$, and Pluronic P123 in *tert*-butanol is spin-coated on different substrates and calcined at 600 °C to produce fully crystalline nanostructured tin-doped hematite films. The films obtained after one coating on a planar substrate are about 60 nm thick, corresponding roughly to a single layer of nanoparticles; the layer thickness can be increased by repeating the coating procedure. Figure 3-3b shows a SEM cross-section image of a typical $\text{Sn}:\text{Fe}_2\text{O}_3$ absorber layer obtained by sequential coating of three layers on a planar substrate, reaching a thickness of about 250 nm. The same protocol can be also applied to the impregnation of macroporous scaffolds aimed at the formation of host-guest electrodes as seen in Figure 3-3a,c. Simple visual inspection of the images does not suffice to assess the degree of infiltration of tin-doped hematite into the macroporous scaffold. To this end we have obtained EDX maps acquired in STEM mode on a cross section of the host-guest morphology (Figure 3-3c). Figure 3-3d shows a high resolution TEM image of a single pore. The EDX map shows excellent agreement between the Sn (blue) and Fe (red) rich corresponding respectively to the scaffold and absorber layer of the underlying TEM image. A large area EDX map across almost the entire thickness of the macroporous film shows successful infiltration of the tin-doped hematite reaching even the bottom pores close to the FTO substrate. We note that some pores, irrespective of their depth within the macroporous film, appear not to be filled, probably because there are inadequate openings to the adjacent pores in the scaffold structure. The hematite particle size in the scaffold is determined to be about 50 nm by TEM, (Figure S 3-11), which is the same

3 Electron collection in host-guest nanostructured hematite photoanodes for water splitting: the influence of scaffold doping density

as the particle size of the absorber layer obtained on the flat FTO substrate (Figure 3-3b), described by us elsewhere.²⁶

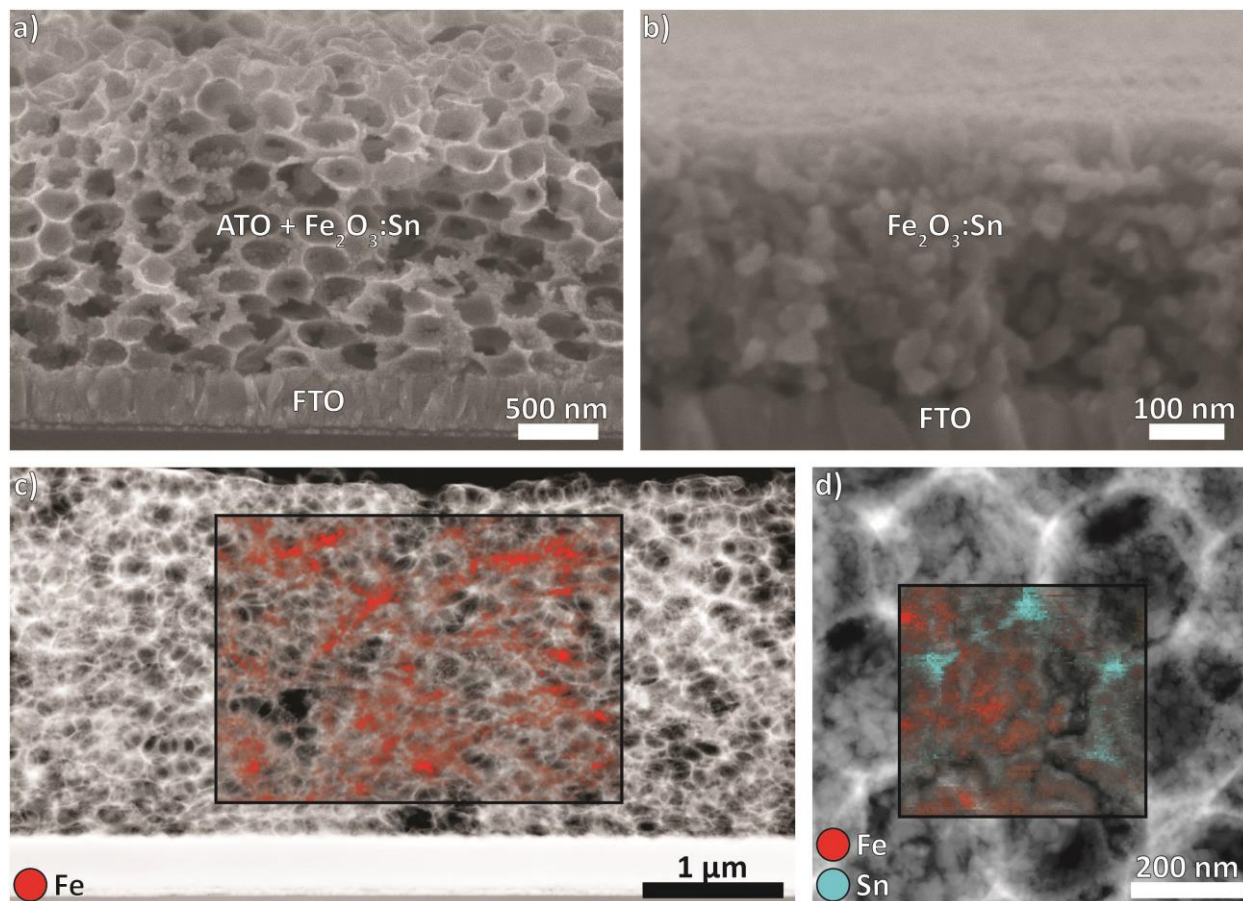


Figure 3-3: SEM cross section images of a) the SnO₂:Sb (ATO) + Sn:Fe₂O₃ host guest morphology and b) the mesoporous Sn:Fe₂O₃ absorber layer. In c) and d) EDX maps obtained in STEM mode on a cross section of the host-guest morphology are shown with red signifying tin-doped hematite and turquoise signifying SnO₂:Sb. c) shows good infiltration of the absorber in the scaffold down to the bottom, although some pores remain unfilled, and d) shows one pore in which several hematite nanoparticles can be seen. Both the TEM and SEM image show a three layer Sn:Fe₂O₃ film.

The absorbance spectra of the three different types of films studied are shown in Figure 3-4. It can be seen that the scaffold structures have higher absorbance than the ‘flat’ hematite electrode, indicating that the effective optical thickness of the absorber is greater for the same number of coating cycles.

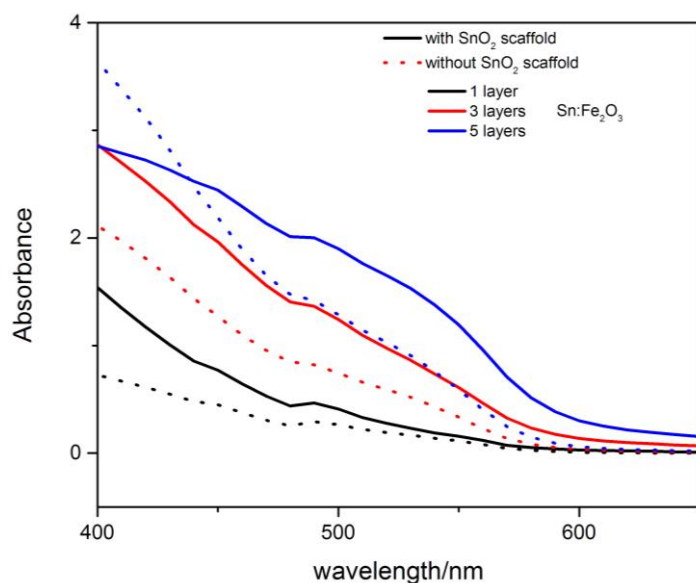


Figure 3-4: Absorbance spectra of macroporous tin oxide films covered with different numbers of coatings of tin-doped hematite (black: 1 layer; red: 3 layers, blue: 5 layers).

Dotted lines: without scaffold, full lines: with scaffold. The absorbance spectra are compared to the ones for the corresponding number of tin-doped hematite coatings on an FTO substrate.

The photocurrent voltage characteristics of tin-doped hematite coatings on the flat substrate (further referred to as a flat absorber layer) as well as the corresponding plots for the tin-doped hematite in the two types of macroporous scaffold (further referred to as host-guest electrodes) are shown in Figure 3-5, under AM 1.5 illumination through the substrate or electrolyte (SI or EI, respectively).

SnO₂:Sb host-guest electrodes give the highest dark current, which we attribute to oxygen evolution on the highly conducting scaffold (see Figure S 3-14). Under SI illumination, the current produced at 1.23 V vs. RHE by the SnO₂:Sb host-guest system is similar to the response of the flat hematite electrode. This indicates that SnO₂:Sb is an appropriate scaffold material for the absorber, but the lack of improvement in the SI photocurrent suggests that electron collection is not limiting the performance of the flat hematite electrode under SI conditions. By contrast, the undoped SnO₂ host-guest electrode produces less current than the flat electrode. This immediately suggests problems with the transfer of electrons from the hematite nanoparticles through the scaffold to the substrate

Under EI illumination, the situation is quite different, with the SnO₂:Sb host-guest system significantly outperforming the flat electrode. More importantly, the photocurrent density of the host-guest electrode with the SnO₂:Sb scaffold is the same *regardless of the illumination direction*, whereas the photocurrent for the flat electrode is much lower for EI than for SI illumination. We have recently shown²⁷ that the photocurrent in nanostructured tin-doped hematite is hindered by poor electron collection. The presence of a highly conductive macroporous SnO₂:Sb scaffold evidently lifts this limitation. The Sb doping is clearly the key here, since the SnO₂ host-guest system shows almost no photocurrent for EI illumination, indicating that electron collection is very inefficient.

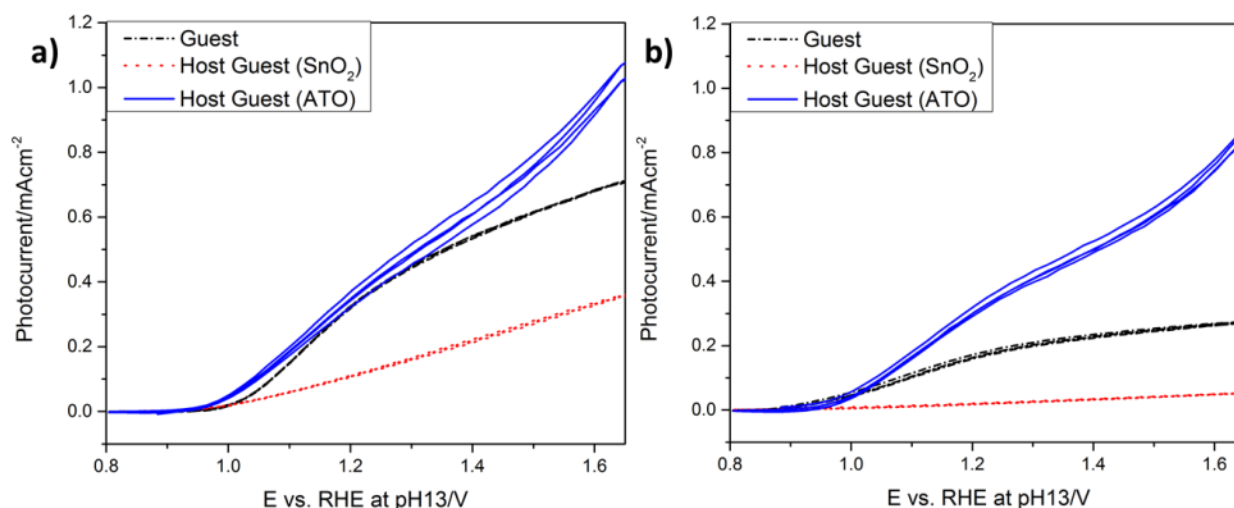


Figure 3-5: Cyclic voltammety curves for tin-doped hematite absorber films on flat FTO (dot-dash) or on macroporous SnO₂ (red dots)/SnO₂: Sb (blue line) host-guest scaffolds. In a) the films were illuminated through the substrate (SI) and in b) through the electrolyte side (EI) under AM 1.5 conditions. Two repeated scans are shown for each sample.

In order to clarify the role of electronic communication between the absorber layer and the FTO, insulating SiO₂ host-guest structures were prepared with the same macroporous morphology. Only a very small photocurrent is detected for these samples, regardless of illumination direction. This indicates that the interconnectivity between the hematite particles in the nanostructure is weak because electron collection involves tortuous pathways where recombination can occur. This contrasts with the situation in the scaffold structures, where the electrons can easily move through the conducting oxide scaffold to the contact.

Light absorption in a non-scattering material can be described in terms of a characteristic penetration depth $1/\alpha(\lambda)$, where $\alpha(\lambda)$ is the wavelength dependent absorption coefficient. The attenuation of the incident illumination as it passes into a semiconductor results in a wavelength dependence of the charge photogeneration profile. For short wavelengths, the majority of the incident radiation is absorbed close to the surface through which light enters.

It follows that for EI illumination, the majority of electron-hole pairs are generated far away from the substrate contact. In those cases where the short wavelength EQE is lower for EI than SI illumination, one can conclude that electrons generated on the electrolyte side of the film are lost during transit to the substrate. The problem is simplified if electron transport is by diffusion (i.e. the driving force is primarily due to a concentration gradient rather than an electric field). If under these conditions the loss of electrons can be described by a first order electron lifetime, τ_n , one can use the steady state solutions of the continuity equation given by Södergren et al.²⁸. The solutions for SI and EI illumination allow the determination of the electron collection length $L_n = (D_n \tau_n)^{1/2}$ from the ratio of external quantum efficiency spectra recorded for EI and SI illumination. Here D_n is the diffusion coefficient of electrons. This model has been applied to measure the electron diffusion lengths in mesoporous TiO₂²⁹ and WO₃³⁰ during light driven water oxidation, although it is not clear what the ‘recombination’ mechanism is nor why the rate should be first order in electron concentration.

The experimental EQE_{EI}/EQE_{SI} data were be fitted to the expression derived by Södergren et al.²⁸:

$$\frac{EQE_{EI}}{EQE_{SI}} = - \frac{(1 - R_{EI}) [(L\alpha + 1) e^{2d/L} - 2L\alpha e^{\alpha d + d/L} + L\alpha - 1]}{(1 - R_{SI}) [(L\alpha - 1) e^{\alpha d + 2d/L} + (L\alpha + 1) e^{\alpha d} - 2L\alpha e^{d/L}]} \quad (3-1)$$

Here, R_{EI} and R_{SI} are the reflectances measured through the electrolyte and substrate side, respectively, $\alpha(\lambda)$ is the optical absorption coefficient, d is the film thickness, and L_n is the only fitting parameter. Figure 3-6a) shows the ratio of the EQE measured under illumination through the electrolyte and substrate for a 250 nm thick flat Fe₂O₃ layer on FTO. Also shown are fits to equation (1) for various values of the L_n .

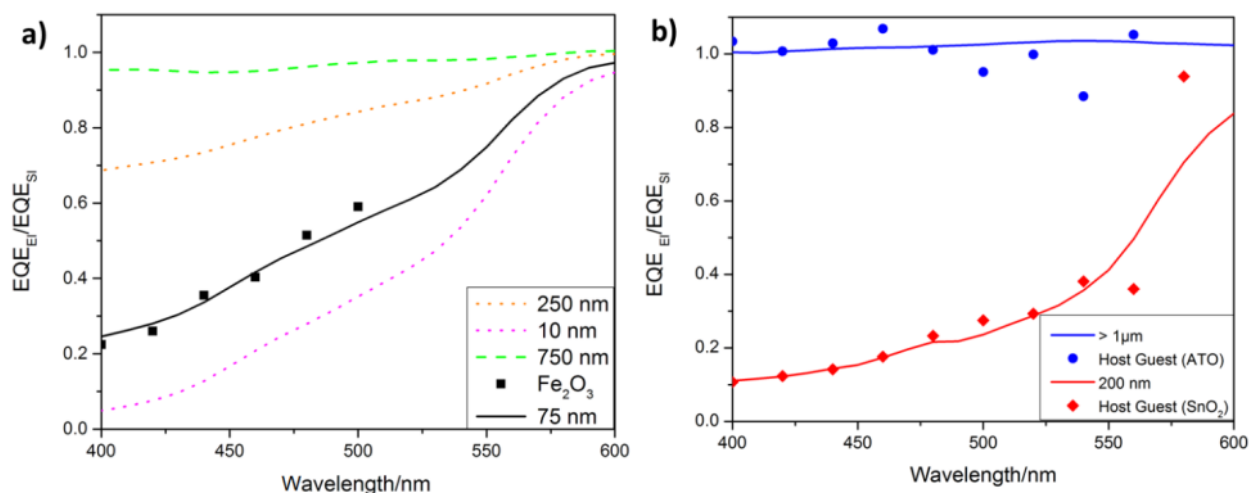


Figure 3-6: Ratio of EQE measured from the electrolyte and substrate side of a) flat absorber layer (black squares) and b) SnO_2 (red diamonds) and $SnO_2:Sb$ (blue points) based host-guest photoanodes. In a), theoretical traces of the EQE ratios for different electron diffusion lengths are given, as indicated in the figure. The data points are fitted according to the model of Södergren *et al.*,²⁸ suggesting an electron diffusion length of 75 nm for the flat Fe_2O_3 absorber layer, an increased electron diffusion length of 200 nm for the SnO_2 host-guest system, and a diffusion length larger than the film thickness itself for the $SnO_2:Sb$ host-guest system.

Figure 3-6b shows the same analysis made on the host-guest films. In the case of the SnO_2 scaffold, the EQE_{EI}/EQE_{SI} ratio can be fitted to an effective electron collection length of 200 nm. Given a film thickness of over a micron, this poor electron collection is consistent with the poor performance of these films, particularly for EI illumination, which is likely to be the most suitable geometry for practical application. $SnO_2:Sb$ based host-guest films, in contrast, exhibit a EQE_{EI}/EQE_{SI} ratio close to unity over the whole wavelength range, indicating that electron collection is very efficient. This result is consistent with the photocurrent-voltage curves shown in Figure 3-5a and b, which demonstrate that the

photocurrent is independent of the illumination direction for SnO₂:Sb based host-guest films. We conclude that macroporous SnO₂:Sb makes a very good scaffold for nanostructured tin-doped hematite absorber coatings, particularly for illumination from the electrolyte side. Under SI illumination, in contrast, the SnO₂:Sb host-guest films produce photocurrents very similar to those of flat absorber layer films. Evidently electron collection is not an important limitation when electron hole pairs are generated close to the substrate.

The preceding analysis has been applied elsewhere in the literature²⁸⁻³⁰ without a critical examination of why majority carriers (electrons) should be lost in transit to the substrate. In the case of a bulk n-type semiconductor/electrolyte junction, electron hole pairs are separated by the gradient of their respective quasi Fermi levels. Electrons move away from the interface into the bulk region where the electric field is very small (the so called quasi-neutral region). Here the hole density is vanishingly small, and there is no route by which electrons can be lost.

This work has shown that deposition of mesoporous hematite layers onto conducting scaffolds to form host-guest architectures significantly improves the electron collection resulting in higher photocurrents compared to planar hematite electrodes. The best results were obtained using antimony-doped SnO₂ as the scaffold. In this case, electron transport is evidently so rapid that electron collection is complete. In a nanostructured electrode, the situation differs from the dense bulk electrode case because the electrolyte permeates into the structure and the semiconductor electrolyte interface extends throughout the layer. This means that electrons in transit to the anode contact have to pass through regions where holes have accumulated at the semiconductor electrolyte interface as a result of the sluggish kinetics for oxygen evolution. In addition to mobile holes, there may be surface bound species such as surface-trapped holes

or intermediates in the water oxidation reaction. These act as sinks for the electrons moving toward the contact. The observation that the loss of electrons appears to be adequately characterized by a first order lifetime is surprising. It implies that the concentration of holes (or other species that can capture electrons) is in large excess so that the recombination becomes first order. This is clearly the case in the dye-sensitized solar cell, where the electron acceptor (tri-iodide) is indeed in large excess. The reason for the first order behavior in our case may be that the kinetics governing the consumption of holes in the water splitting reaction are so slow that a large density of holes builds up near the hematite/solution interface. This is consistent with the observation of a persistent photoinduced absorption in hematite that is attributed to holes.³¹

If we follow this line of argument, then we must conclude that electrons escape more easily if the scaffold is highly conducting. The relative widths of the space charge region in the two scaffolds at 1.23 V vs. RHE can be estimated from the Mott Schottky data. In the case of undoped SnO₂, the width of the space charge regions is expected to around 30 times thicker than in the case of the antimony-doped scaffold. This means that the quasineutral ‘core’ of the scaffold structure is squeezed into a very small volume, increasing the resistivity of the structure to such an extent that electron transport is slowed down significantly, enhancing the chance of electrons being lost in transit. This interpretation is supported by the almost linear photocurrent voltage plots observed for the undoped scaffold which suggests a significant iR drop. In the antimony-doped SnO₂, on the other hand, the space charge regions will be much thinner, probably only a few nm, leaving a wider highly conducting quasi-neutral core that allows much more rapid transport of electrons to the contact, thus escaping recombination. These are complex systems that are difficult to model, but the qualitative picture described

here is a first step towards understanding why highly doped tin oxide frameworks can collect electrons efficiently.

3.3 Conclusion

The utility of host-guest scaffold photoanodes for water splitting clearly depends on the ability of the scaffold to collect photogenerated electrons. In the case of the highly doped SnO₂, field driven collection of electrons involves rapid movement of electrons in very narrow quasi-neutral channels. However, the formation of depletion layers in the undoped SnO₂ scaffold appears to lead to problems under conditions in which the width of the space charge region becomes comparable with the thickness of the scaffold structure. Indeed, under some conditions, penetration of the electric field into the scaffold may no longer occur due to complete depletion of the structure. Electron collection would then involve diffusion, with no contribution from drift. This effect manifests itself most strongly when electron hole pairs are generated predominantly close to the electrolyte interface, as is the case for illumination from the electrolyte side. The slowing down of electron transport leaves electrons vulnerable to loss by recombination. These problems can be overcome if a highly conducting scaffold is used. In this case electron collection is so rapid that negligible losses occur when electrons move to the substrate contact. Under these conditions, electron collection is efficient even when the electrode is illuminated from the electrolyte side. The highly-doped scaffolds used here could therefore find application in devices for light-driven water splitting.

3.4 Experimental

Synthesis and deposition of polymethylmethacrylate (PMMA) spheres

3. Experimental

Polymethylmethacrylate (PMMA) spheres with a diameter of 300 nm were prepared according to a procedure described by Mandlmeier et al.²⁷ The particles were synthesized by adding methylmethacrylate (MMA) (35.6 g, 0.35 mol) and sodium dodecylsulfate (SDS) (5 mg, 0.02 mmol) to deoxygenated water (98 mL) under nitrogen purging at 40°C, heating the resulting emulsion to 70 °C for 1 hour under reflux, and vigorous stirring. The polymerization was then initiated by adding potassium peroxydisulfate (56 mg, 0.2 mmol) in water (2 mL) and carried out for 2.5 hours. The reaction was stopped by cooling the suspension to room temperature and stirring for another 30 minutes under atmospheric conditions. The resulting PMMA spheres were washed twice with water by centrifugation (19,000 rpm, 20 min) and re-dispersed in water.

Deposition of PMMA spheres on FTO substrates (TEC 15 Glass, Dyesol) was carried out by ultra-slow dip coating (0.45 mm/min) of a 5 wt. % PMMA suspension at 19% relative humidity, using a custom made coater connected to a humidity control box. The resulting films were dried in a nitrogen stream and heated to 80 °C for 2 h to increase adherence between the PMMA spheres (Figure S 3-7).

Preparation of macroporous SnO₂ films

The precursor solution for macroporous SnO₂ was prepared according to Fried et al.³² by adding 4 mL dry ethanol dropwise to SnCl₄ (1.2 g, 4.6 mmol, in air). 0.5 mL of deionized water (Millipore Q) was then added resulting in a 0.15 M SnCl₄ solution. This solution was dip-coated on previously prepared PMMA films under ambient conditions at a rate of 38 mm/min. The samples were subsequently calcined at 600 °C with a ramp of 3 °C/min and a dwell time of 30 min. Figure S 2 shows SEM images of such macroporous films.

Preparation of antimony-doped macroporous SnO₂ films

For the preparation of the Sb-doped SnO₂ samples, Sb(AcO)₃ (0.0672 g, 0.2 mmol) was added to 4 mL ethanol prior to adding SnCl₄ (1.14 g, 4.4 mmol). The subsequent steps were

followed as described above for SnO₂. The Sb:Sn ratio refers to the atomic ratio of these elements in the precursor solution. For further film synthesis, an identical procedure was used as already described for the undoped films. Figure S 3-9 shows the XRD analysis of macroporous SnO₂ and SnO₂:Sb films.

Synthesis and deposition of tin-doped hematite on FTO and macroporous SnO₂

A suspension of tin-doped hematite nanoparticles was synthesized as described by Dunn et al.²⁶ Briefly, 0.1106 g (0.3 mmol) Sn(CH₃COO)₄ was added to a solution of 0.25 g Pluronic® P123 and 10 mL *tert*-butanol. After vigorous stirring for 5 h, 0.505 g (1.25 mmol) Fe(NO₃)₃·9 H₂O was added and stirred at room temperature for another 15 min. After sonication for 15 min, 2.5 mL water was added and the solution was stirred for 17 h at room temperature. After filtration through a filter (pore diameter of 200 nm) the solution was ready for coating experiments. For preparation of flat Sn-containing hematite films, the solution (100 μL) was spun on FTO at 1000 rpm for 30 s. The resulting films were dried at 60 °C for 10 min and calcined at 600 °C with a ramp of 3 °C/min and a dwell time of 30 min. Typically, the filtered solution (100 μL) was cast on the macroporous scaffold (1 x 1 cm²), spun at 1000 rpm for 30 s, and finally dried at 60 °C for 10 min. To achieve an increased precursor loading, the previous step was repeated twice. After spin coating, the samples were calcined at 600 °C with a ramp of 3 °C/min and a dwell time of 30 min. Figure S 4 shows an SEM image of a tin-doped hematite film deposited on FTO with the corresponding XRD pattern after calcination. The feature size of the tin-doped hematite absorber material was determined to be around 50 nm from TEM particle size analysis (Figure S 3-11).

Synthesis and deposition of tin-doped hematite on macroporous silica (SiO₂) films

Macroporous silica (SiO₂) films were prepared according to the sol-gel route reported by Schuster et al.³³ Briefly, 6 mL tetraethyl orthosilicate (TEOS) was dissolved in ethanol and stirred for 5 min; upon adding 3 mL of water to the solution a phase separation was observed.

3. Supporting Information

1 mL of 37 % HCl was added and the solution became clear. The resulting solution was used as a precursor for dip coating PMMA films at 34 mm/min. Subsequently the samples were calcined at 500 °C (1 °C/min) for 5 h. These samples were then infiltrated with tin-doped hematite as already described for macroporous SnO₂:Sb. Figure S 3-12a shows an SEM image of the macroporous silica scaffold. Figure S 3-12b shows the photocurrent collected from the tin-doped hematite nanoparticles on the silica scaffold.

Preparation of flat SnO₂ and SnO₂:Sb films for electrochemical impedance spectroscopy measurements

Flat and compact SnO₂ and SnO₂:Sb films as shown in Figure S 3-13 were prepared using the corresponding precursor solution described for the synthesis of macroporous scaffolds. The solution was deposited on FTO by spin coating at 1000 rpm for 30 s. The samples were calcined at 600 °C with a ramp of 3 °C/min and a dwell time of 30 min.

3.5 Supporting Information

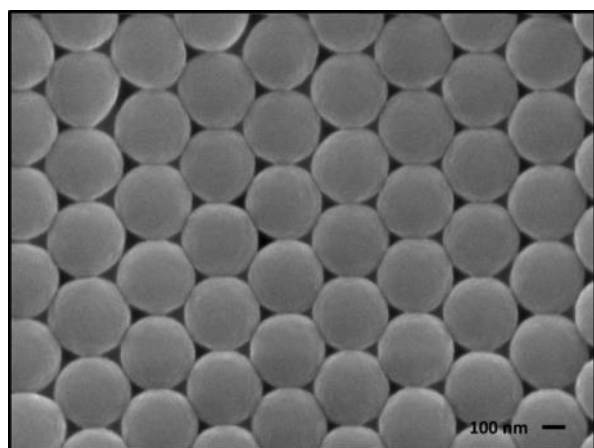


Figure S 3-7. SEM image of highly ordered PMMA spheres on FTO deposited via ultra-slow dip coating at 19% relative humidity.

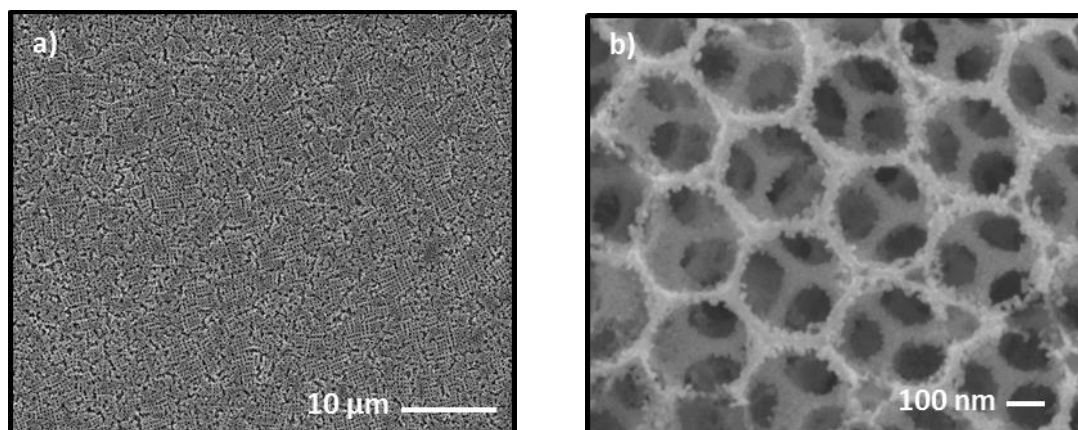


Figure S 3-8: SEM overview of a) macroporous crack free structure of SnO₂ film and b) close up of the macroporous SnO₂ scaffold with a pore size of 250 nm and a pore wall thickness of 30 nm.

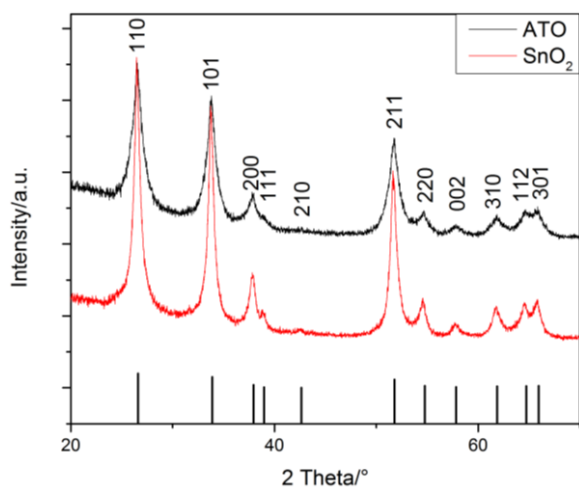


Figure S 3-9: XRD pattern of cassiterite (SnO₂) and ATO with the corresponding hkl values of the Bragg peaks. Below the ICDD card 00-041-1445 of cassiterite is shown.

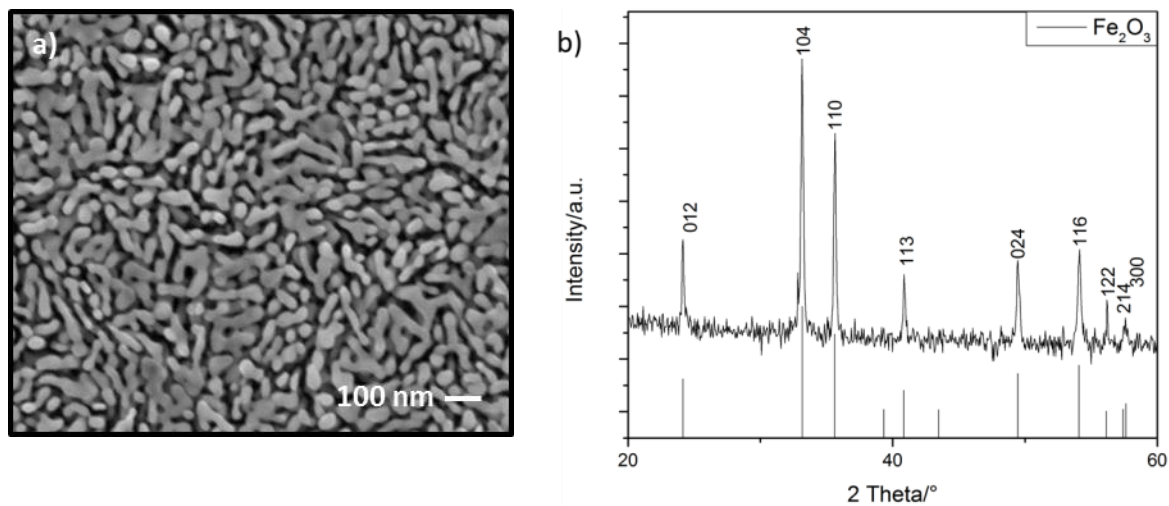


Figure S 3-10. (a) SEM image and (b) XRD of flat tin-enriched hematite film with the corresponding hkl values. Below the ICDD card 01-071-5088 of hematite is shown.

3 Electron collection in host-guest nanostructured hematite photoanodes for water splitting: the influence of scaffold doping density

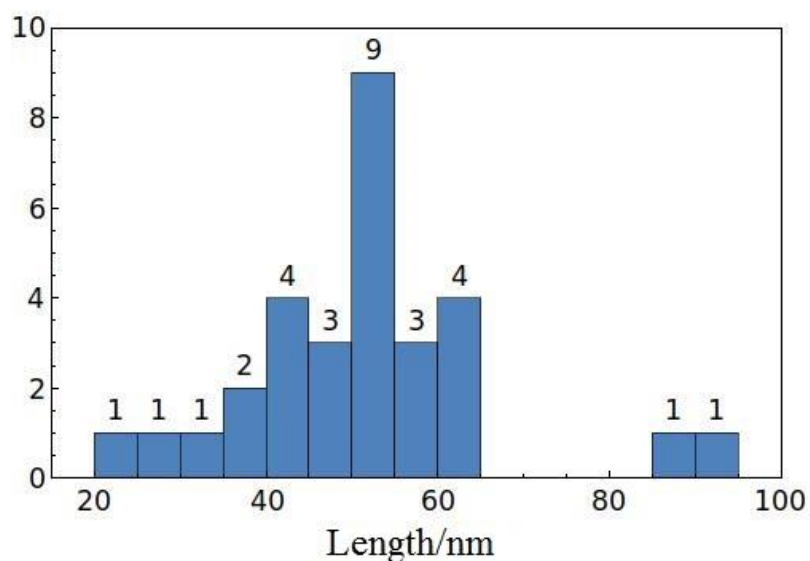


Figure S 3-11. Particle size distribution of tin-doped hematite particles in a macroporous ATO scaffold. The insert shows the aspect ratio of the analyzed particles.

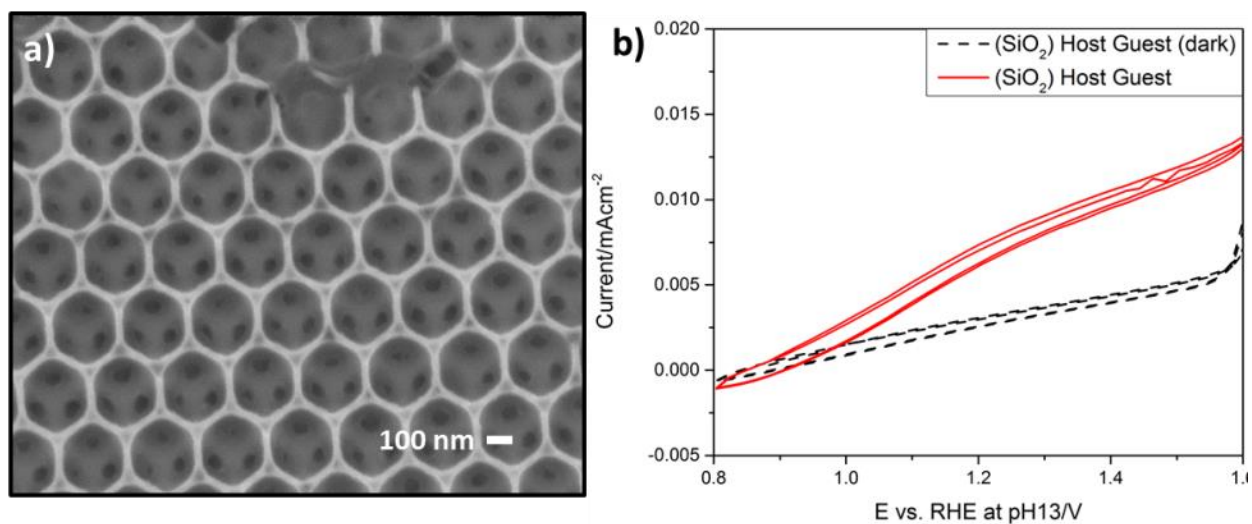


Figure S 3-12. (a) SEM image of the macroporous SiO_2 scaffold. (b) Photoelectrochemical performance of the (SiO_2) host guest scaffold with Fe_2O_3 absorber in the dark and under AM 1.5 illumination.

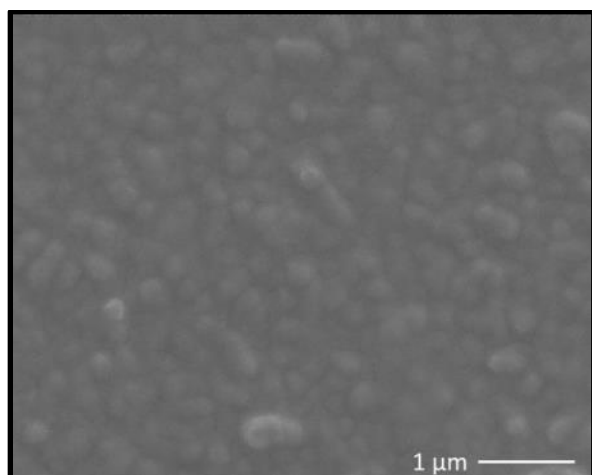


Figure S 3-13. SEM image of a compact ATO layer on FTO.

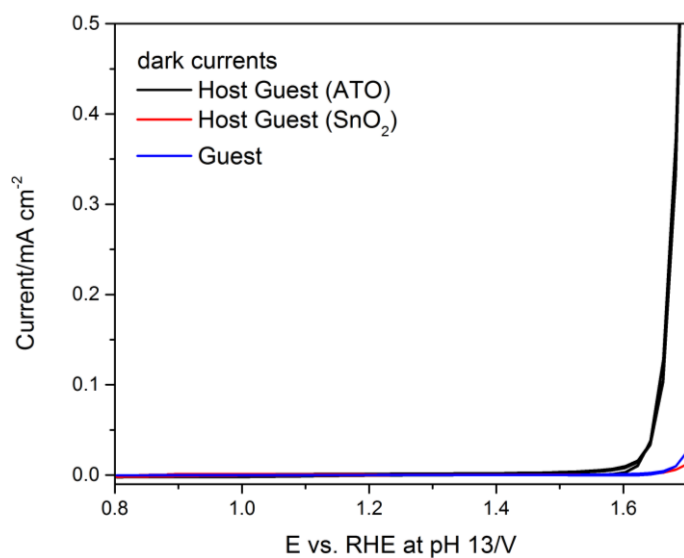


Figure S 3-14. Forward and reverse current-voltage curves in the dark for tin-doped hematite absorber films on flat FTO (blue line) or on macroporous SnO₂ (red line)/SnO₂:Sb (black line) 'host guest' scaffolds. Two repeated scans are shown for each sample.

3 Electron collection in host-guest nanostructured hematite photoanodes for water splitting: the influence of scaffold doping density

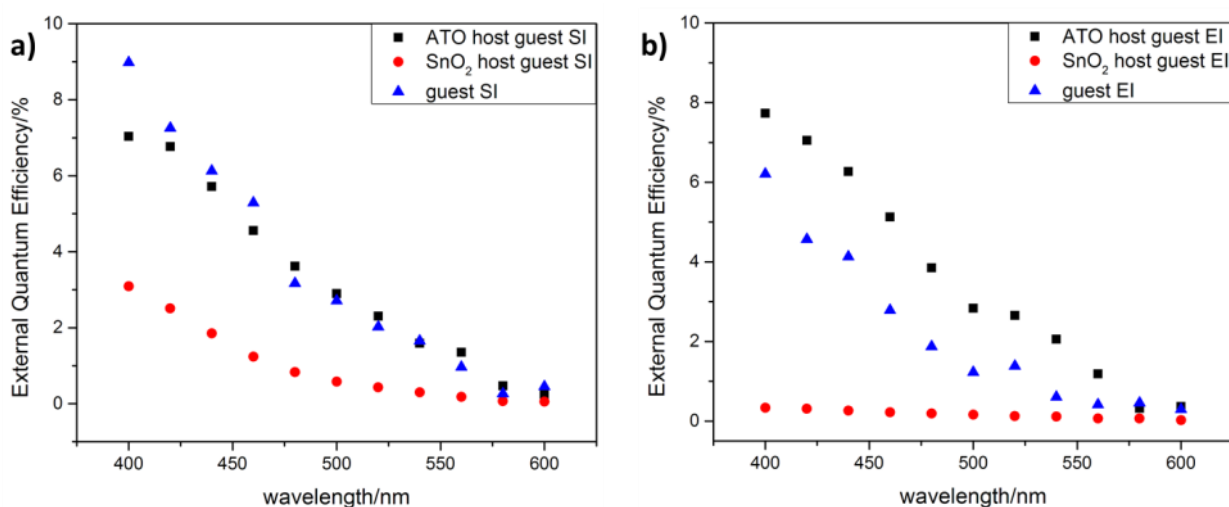


Figure S 3-15: EQE measured under AM 1.5 background illumination at thermodynamic potential for water oxidation (1.23 V vs RHE) for tin-doped hematite films on flat FTO or on various macroporous scaffolds. The films were illuminated through the **a)** substrate and **b)** electrolyte side.

Mott Schottky analysis of scaffold materials

In order to confirm successful Sb doping of the SnO₂ material, dark electrochemical impedance spectroscopy (EIS) measurements were conducted on 70 nm thick compact layers of SnO₂ and ATO (Figure S 3-16). EIS measurements were carried out in the dark under the same experimental conditions using a quartz cell filled with electrolyte (aqueous 0.1 M NaOH solution) and the sample connected in 3 electrode mode, together with the Ag/AgCl reference electrode and the Pt mesh counter electrode, to the potentiostat in the dark. During these measurements, the amplitude of the applied potential varied by 10 mV about a background value, and the frequency of this perturbation was swept from 10 kHz to 0.5 Hz. Such measurements were repeated at background potential values ranging from *ca.* 0.6 V vs. RHE

3. Supporting Information

to *ca.* 1.7 V vs. RHE. Bode plots, showing the magnitude and phase shift of the measured impedance are displayed in Figure S 3-16, along with fits to the Randles cell, which is shown as an inset, where C is the space charge layer capacitance, R_p is the resistance corresponding to charge transfer between the electrode and the electrolyte, and R_s is the series resistance associated with the FTO glass substrate. Despite the non-perfect capacitive behaviour of these systems, which is evident from the phase shift not reaching 90° at low frequencies, we chose to fit the data with a pure capacitive element in parallel with a large R_p (of the order of 10 – 1000 k Ω), in order to avoid the complications arising in interpreting data fits from constant phase elements.

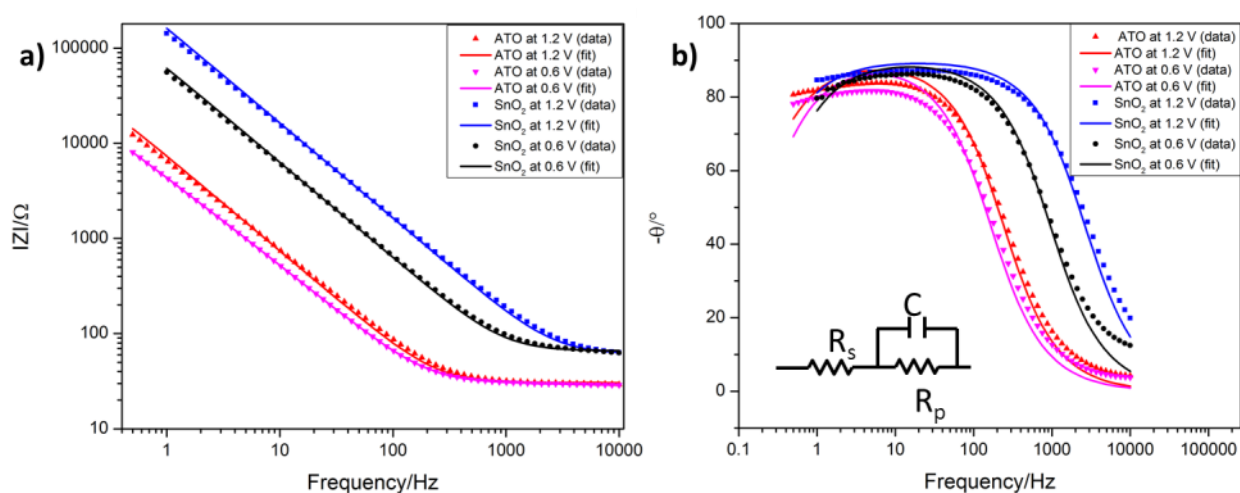


Figure S 3-16. Bode plots of a) amplitude and b) phase shift vs. frequency of ATO and SnO₂ flat layers on FTO measured at 0.6 and 1.2V vs. RHE. The data was fitted according to the equivalent circuit shown as an inset in b).

The capacitance data obtained in this manner are shown in **Error! Reference source not found.** in the Mott Schottky representation; as plots of $1/C^2$ vs E . The doping density, N_d , can be extracted from the slope of such plots, according to the Mott Schottky equation¹:

3 Electron collection in host-guest nanostructured hematite photoanodes for water splitting: the influence of scaffold doping density

$$\frac{1}{C_{sc}^2} = \frac{2}{\epsilon_r \epsilon_0 N_d \Re^2 A^2} \left[(V - V_{fb}) - \frac{k_B T}{q} \right]$$

Here V_{fb} is the flat band potential, ϵ_r is the relative permittivity, ϵ_0 is the permittivity of free space, A is the electrode area, \Re is the surface roughness factor, V is the applied potential, q is the elementary charge, k_B is Boltzmann's constant and T is the temperature. The slope of the SnO₂ Mott Schottky plot is approximately two orders of magnitude larger than that of the ATO sample, indicating successful doping of SnO₂ with Sb in the ATO sample. Assuming $\epsilon_r = 14$ for SnO₂, and a geometric surface area of 0.196 cm², we find the values of $N_d \Re^2$ to be of the order of 3x10²⁰ cm⁻³ for the SnO₂ sample, and 9x10²² cm⁻³ for the ATO sample. These values are in good agreement with those recently reported by Wang *et al.*² **Reliable estimation of \Re is difficult, so we have used only the relative values in the discussion.**

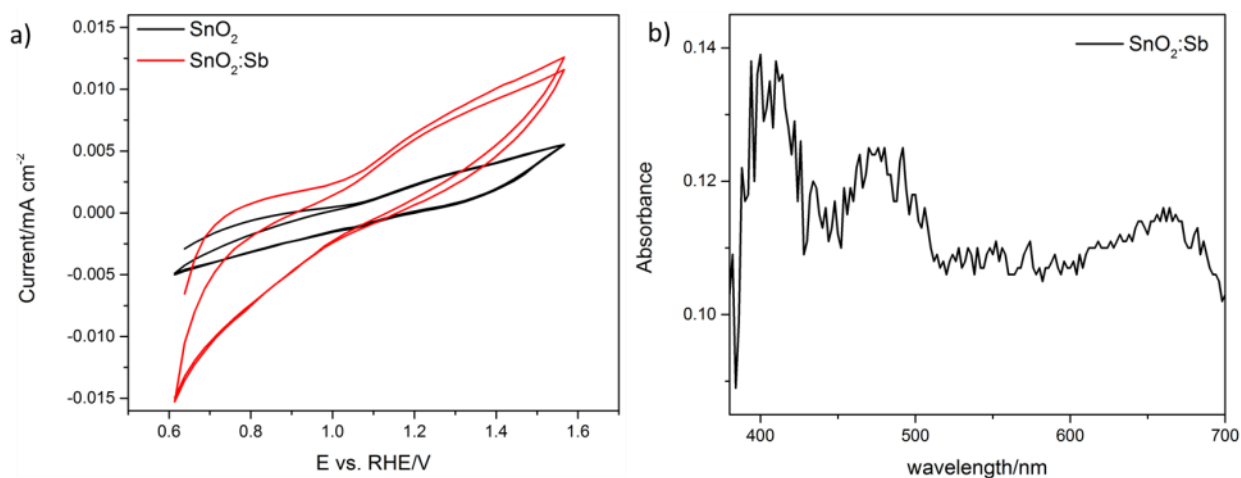


Figure S 3-17: a) Cyclic voltammety curves for macroporous SnO₂ and SnO₂:Sb on FTO and b) absorbance spectra of SnO₂:Sb on FTO.

3.6 References

1. Sivula, K.; Le Formal, F.; Grätzel, M., Solar Water Splitting: Progress Using Hematite (α -Fe₂O₃) Photoelectrodes. *ChemSusChem* **2011**, *4* (4), 432-449.
2. Grätzel, M., Photoelectrochemical cells. *Nature* **2001**, *414* (6861), 338-344.
3. Hara, M.; Kondo, T.; Komoda, M.; Ikeda, S.; N. Kondo, J.; Domen, K.; Hara, M.; Shinohara, K.; Tanaka, A., Cu₂O as a photocatalyst for overall water splitting under visible light irradiation. *Chem. Commun.* **1998**, (3), 357-358.
4. Sivula, K.; Zboril, R.; Le Formal, F.; Robert, R.; Weidenkaff, A.; Tucek, J.; Frydrych, J.; Grätzel, M., Photoelectrochemical Water Splitting with Mesoporous Hematite Prepared by a Solution-Based Colloidal Approach. *J. Am. Chem. Soc.* **2010**, *132* (21), 7436-7444.
5. Bolton, J. R.; Strickler, S. J.; Connolly, J. S., Limiting and realizable efficiencies of solar photolysis of water. *Nature* **1985**, *316* (6028), 495-500.
6. Dare-Edwards, M. P.; Goodenough, J. B.; Hamnett, A.; Trevellick, P. R., Electrochemistry and photoelectrochemistry of iron (III) oxide. *Journal of the Chemical Society, Faraday Transactions 1: Physical Chemistry in Condensed Phases* **1983**, *79* (9), 2027-2041.
7. Kennedy, J. H.; Frese, K. W., Photooxidation of Water at α -Fe₂O₃ Electrodes. *J. Electrochem. Soc.* **1978**, *125* (5), 709-714.
8. Fu, Y.; Chen, J.; Zhang, H., Synthesis of Fe₂O₃ nanowires by oxidation of iron. *Chem. Phys. Lett.* **2001**, *350* (5-6), 491-494.
9. Tilley, S. D.; Cornuz, M.; Sivula, K.; Grätzel, M., Light-Induced Water Splitting with Hematite: Improved Nanostructure and Iridium Oxide Catalysis. *Angew. Chem. Int. Ed.* **2010**, *49* (36), 6405-6408.
10. Mushove, T.; Blodgett, S.; Thompson, L. T. In *Design, Synthesis, and Characterization of Hematite Nanotubes for Photoelectrochemical Water Splitting*, Meeting Abstracts, The Electrochemical Society: 2013; pp 2541-2541.
11. Yuan, L.; Wang, Y.; Cai, R.; Jiang, Q.; Wang, J.; Li, B.; Sharma, A.; Zhou, G., The origin of hematite nanowire growth during the thermal oxidation of iron. *Materials Science and Engineering: B* **2012**, *177* (3), 327-336.

12. LaTempa, T. J.; Feng, X.; Paulose, M.; Grimes, C. A., Temperature-dependent growth of self-assembled hematite (α -Fe₂O₃) nanotube arrays: rapid electrochemical synthesis and photoelectrochemical properties. *The Journal of Physical Chemistry C* **2009**, *113* (36), 16293-16298.
13. Cesar, I.; Sivula, K.; Kay, A.; Zboril, R.; Grätzel, M., Influence of Feature Size, Film Thickness, and Silicon Doping on the Performance of Nanostructured Hematite Photoanodes for Solar Water Splitting. *The Journal of Physical Chemistry C* **2008**, *113* (2), 772-782.
14. Itoh, K. B., J.O'M., Thin film photoelectrochemistry: Iron oxide. *J. Electrochem. Soc.* **1984**, *131* (6), 1266-1271.
15. Sivula, K.; Formal, F. L.; Grätzel, M., WO₃-Fe₂O₃ photoanodes for water splitting: A host scaffold, guest absorber approach. *Chemistry of Materials* **2009**, *21* (13), 2862-2867.
16. Wang, L.; Palacios-Padrós, A.; Kirchgeorg, R.; Tighineanu, A.; Schmuki, P., Enhanced Photoelectrochemical Water Splitting Efficiency of a Hematite-Ordered Sb:SnO₂ Host-Guest System. *ChemSusChem* **2014**, n/a-n/a.
17. Sun, Y.; Chemelewski, W. D.; Berglund, S. P.; Li, C.; He, H.; Shi, G.; Mullins, C. B., Antimony-Doped Tin Oxide Nanorods as a Transparent Conducting Electrode for Enhancing Photoelectrochemical Oxidation of Water by Hematite. *ACS Applied Materials & Interfaces* **2014**.
18. Qiu, Y.; Leung, S.-F.; Zhang, Q.; Hua, B.; Lin, Q.; Wei, Z.; Tsui, K.-H.; Zhang, Y.; Yang, S.; Fan, Z., Efficient Photoelectrochemical Water Splitting with Ultrathin films of Hematite on Three-Dimensional Nanophotonic Structures. *Nano Letters* **2014**, *14* (4), 2123-2129.
19. Riha, S. C.; DeVries Vermeer, M. J.; Pellin, M. J.; Hupp, J. T.; Martinson, A. B. F., Hematite-based Photo-oxidation of Water Using Transparent Distributed Current Collectors. *ACS Applied Materials & Interfaces* **2013**, *5* (2), 360-367.
20. Stefik, M.; Cornuz, M.; Mathews, N.; Hisatomi, T.; Mhaisalkar, S.; Grätzel, M., Transparent, Conducting Nb:SnO₂ for Host-Guest Photoelectrochemistry. *Nano Letters* **2012**, *12* (10), 5431-5435.
21. Young Kim, J.; Jang, J.-W.; Hyun Youn, D.; Yul Kim, J.; Sun Kim, E.; Sung Lee, J., Graphene-carbon nanotube composite as an effective conducting scaffold to enhance the photoelectrochemical water oxidation activity of a hematite film. *RSC Advances* **2012**, *2* (25), 9415-9422.

3. References

22. Le Formal, F.; Grätzel, M.; Sivula, K., Controlling Photoactivity in Ultrathin Hematite Films for Solar Water-Splitting. *Advanced Functional Materials* **2010**, *20* (7), 1099-1107.
23. Hisatomi, T.; Dotan, H.; Stefik, M.; Sivula, K.; Rothschild, A.; Grätzel, M.; Mathews, N., Enhancement in the performance of ultrathin hematite photoanode for water splitting by an oxide underlayer. *Advanced Materials* **2012**, *24* (20), 2699-2702.
24. Wang, D.; Zhang, Y.; Wang, J.; Peng, C.; Huang, Q.; Su, S.; Wang, L.; Huang, W.; Fan, C., Template-free synthesis of hematite photoanodes with nanostructured ATO conductive underlayer for PEC water splitting. *ACS applied materials & interfaces* **2013**, *6* (1), 36-40.
25. Li, F.; Josephson, D. P.; Stein, A., Colloidal assembly: the road from particles to colloidal molecules and crystals. *Angewandte Chemie International Edition* **2011**, *50* (2), 360-388.
26. Dunn, H. K.; Feckl, J. M.; Muller, A.; Fattakhova-Rohlfing, D.; Morehead, S. G.; Roos, J.; Peter, L. M.; Scheu, C.; Bein, T., Tin doping speeds up hole transfer during light-driven water oxidation at hematite photoanodes. *Physical Chemistry Chemical Physics* **2014**, *16* (44), 24610-24620.
27. Mandlmeier, B.; Minar, N.; Feckl, J. M.; Fattakhova-Rohlfing, D.; Bein, T., Tuning the crystallinity parameters in macroporous titania films. *Journal of Materials Chemistry A* **2013**.
28. Sodergren, S.; Hagfeldt, A.; Olsson, J.; Lindquist, S. E., Theoretical models for the action spectrum and the current-voltage characteristics of microporous semiconductor films in photoelectrochemical cells. *J. Phys. Chem.* **1994**, *98*, 5552 - 5555.
29. Leng, W. H.; Barnes, P. R. F.; Juozapavicius, M.; O'Regan, B. C.; Durrant, J. R., Electron Diffusion Length in Mesoporous Nanocrystalline TiO₂ Photoelectrodes during Water Oxidation. *The Journal of Physical Chemistry Letters* **2010**, *1* (6), 967-972.
30. Wang, H.; Lindgren, T.; He, J.; Hagfeldt, A.; Lindquist, S.-E., Photoelectrochemistry of Nanostructured WO₃ Thin Film Electrodes for Water Oxidation: Mechanism of Electron Transport. *The Journal of Physical Chemistry B* **2000**, *104* (24), 5686-5696.
31. Le Formal, F.; Pendlebury, S. R.; Cornuz, M.; Tilley, S. D.; Grätzel, M.; Durrant, J. R., Back electron-hole recombination in hematite photoanodes for water splitting. *Journal of the American Chemical Society* **2014**, *136* (6), 2564-2574.

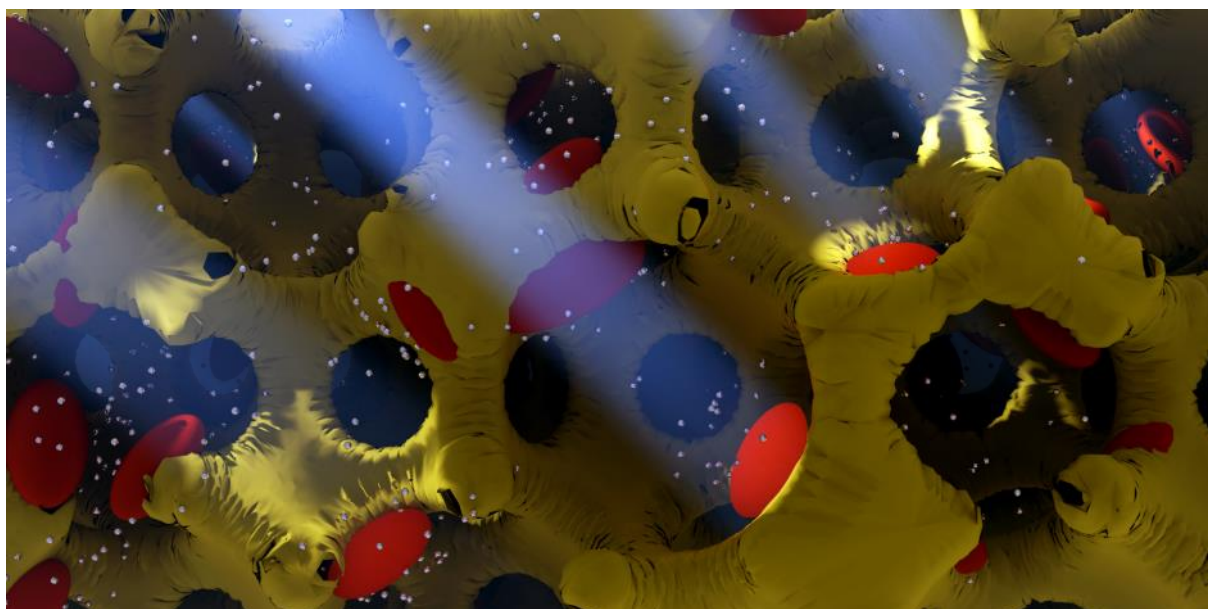
32. Fried, D. I.; Ivanova, A.; Müller, V.; Rathousky, J.; Smarsly, B. M.; Fattakhova-Rohlfing, D., A facile synthesis of mesoporous crystalline tin oxide films involving a base-triggered formation of sol–gel building blocks. *Nanoscale* **2011**, *3* (3), 1234-1239.
33. Schuster, J.; He, G.; Mandlmeier, B.; Yim, T.; Lee, K. T.; Bein, T.; Nazar, L. F., Spherical ordered mesoporous carbon nanoparticles with high porosity for lithium–sulfur batteries. *Angewandte Chemie International Edition* **2012**, *51* (15), 3591-3595.

4 Dual Absorber $\text{WO}_3/\text{Fe}_2\text{O}_3$ Host-Guest Architectures for Improved Charge Generation and Transfer in Photoelectrochemical Water Splitting

This chapter is based on the following publication:

Irina Kondofersky*, Alexander Müller*, Alena Folger, Dina Fattakhova-Rohlfing, Christina Scheu and Thomas Bein, submitted.

*These authors contributed equally.



Abstract

In this study we present $\text{Fe}_2\text{O}_3/\text{WO}_3$ dual absorbers in which WO_3 was systematically applied as a scaffold and/or as a surface treatment. Both the host-guest approach and the surface treatment strongly increased the performance compared to Fe_2O_3 alone. By applying both approaches, high current densities of about 0.7 mA/cm^2 at 1.23 V vs. RHE under AM 1.5 illumination with an IPCE of 17 % at 350 nm were achieved. We could identify several

beneficial interactions between Fe₂O₃ and WO₃. WO₃ strongly scatters visible light, resulting in increased absorption by Fe₂O₃ and higher current densities. We also determined a cathodic shift in the onset potential to 0.8 V and increased transfer rates of up to 88 %. This combination of beneficial effects proves the viability of the presented device architecture.

4.1 Introduction

Driven by climate change, rapid population growth and dwindling resources, research into alternative, sustainable energies is thriving. Solar cells and wind turbines, which harness the power of the sun, already play a major role in the energy mix of some countries, with their market share expected to increase. However, storage of the generated electricity is a challenge. One of many possible solutions is photoelectrochemical water splitting, which uses sun light as an energy source to generate oxygen and hydrogen from water. While suitable photoelectrode materials have been studied since 1972¹, research has intensified in the last few years and several photocathode and photoanode materials (such as TiO₂, Si or Cu₂O and Fe₂O₃, WO₃ or BiVO₄, respectively) have been investigated.²⁻⁴ Efficient photoanodes, in particular, are difficult to realize. Producing one oxygen molecule requires four holes, making recombination likely and requiring significant optimization of factors such as composition, electronic structure, and morphology. All efforts notwithstanding, it is becoming more and more obvious that limitations intrinsic to many single absorber materials investigated so far, such as large band gaps, slow surface kinetics or fast bulk electron-hole recombination, are difficult to overcome. One approach towards solving this problem is the combination of different photoabsorber materials. Such a combination can increase the efficiency in several ways, such as by optical absorption enhancement, enhanced charge separation, faster surface kinetics, or the modification of the electronic structure of the interface between both

materials.⁵ For photoanodes, a dual absorber approach has, for one reason or another, been successful for several systems such as WO_3/TiO_2 ⁶, $\text{WO}_3/\text{BiVO}_4$ ⁷, $\text{TiO}_2/\text{Fe}_2\text{O}_3$ ⁸ and $\text{WO}_3/\text{Fe}_2\text{O}_3$ ⁵.

The $\text{WO}_3/\text{Fe}_2\text{O}_3$ system is a good model and a promising photoanode for many reasons. The individual materials are abundant and therefore cheap, non-toxic and corrosion-resistant.⁹⁻¹⁰ Consequently, both materials have been intensively studied, and the influence of different morphologies, dopants, surface modifications etc. for both systems is well- investigated.^{9, 11} WO_3 has a band gap of 2.5-2.8 eV and absorbs mostly in the blue and UV spectral range.^{10, 12-13} Because of good charge transport properties and fast surface kinetics, it has been demonstrated to be a suitable candidate for water photoelectrolysis.¹³ However, the large band gap limits the overall theoretical solar-to-hydrogen efficiency to 8 %.¹⁴ Fe_2O_3 , on the other hand, has a band gap between 1.9 and 2.2 eV and also absorbs a large fraction of visible light, driving the potential solar-to-hydrogen efficiency up to 16.8 %.^{9, 14} Unfortunately, the expected efficiency is greatly reduced by several loss mechanisms such as high bulk and surface recombination rates and slow kinetics for the oxygen evolution reaction. Combining Fe_2O_3 and WO_3 can improve the performance of the individual materials in several ways. Compared to bare WO_3 , a larger spectral range is absorbed. The band alignment of Fe_2O_3 and WO_3 allows for the injection of electrons from Fe_2O_3 into WO_3 , with the latter being a better electron conductor.¹⁵ Sivula *et al.* found the deposition of Fe_2O_3 onto WO_3 scaffolds to drastically improve electron charge collection.¹⁶ Furthermore, the rate of the oxygen evolution reaction of Fe_2O_3 was shown to be significantly improved by surface treatment of Fe_2O_3 by WO_3 .^{5, 17}

In addition to the strategies discussed above, nanostructuring is commonly employed to improve photoelectrodes.¹⁸⁻¹⁹ Several morphologies have so far been synthesized in the

WO₃/Fe₂O₃ system, including flat and porous films²⁰⁻²⁴, host-guest architectures¹⁶ and nanowires^{5, 25}. Here we systematically employed WO₃ both as a scaffold and as a surface treatment, to identify correlations between morphology and performance. Mesoporous Sn-doped Fe₂O₃ photoabsorber layers were prepared by a sol-gel approach and deposited onto a continuous, macroporous WO₃ scaffold.²⁶ The performance was increased even further by depositing a WO₃ surface layer and increasing the Fe₂O₃/WO₃ interfacial area, thus reaching photocurrents of up to 0.7 mA/cm² at 1.23 V vs. the reversible hydrogen electrode (RHE). The viability of this host-guest approach was confirmed by comparing the macroporous photoanodes to mesoporous reference samples.^{16, 25, 27-31} As WO₃ only absorbs a small fraction of blue light, whereas hematite strongly absorbs in this region, measuring photocurrent transients under UV and under blue light illumination allowed for a more nuanced discussion of the impact of the morphology on the photoelectrochemical performance and gave further insights into a complex interplay of several effects.

4.2 Results and Discussion

Two series of samples were prepared via sol-gel synthesis procedures (Figure 4-1).

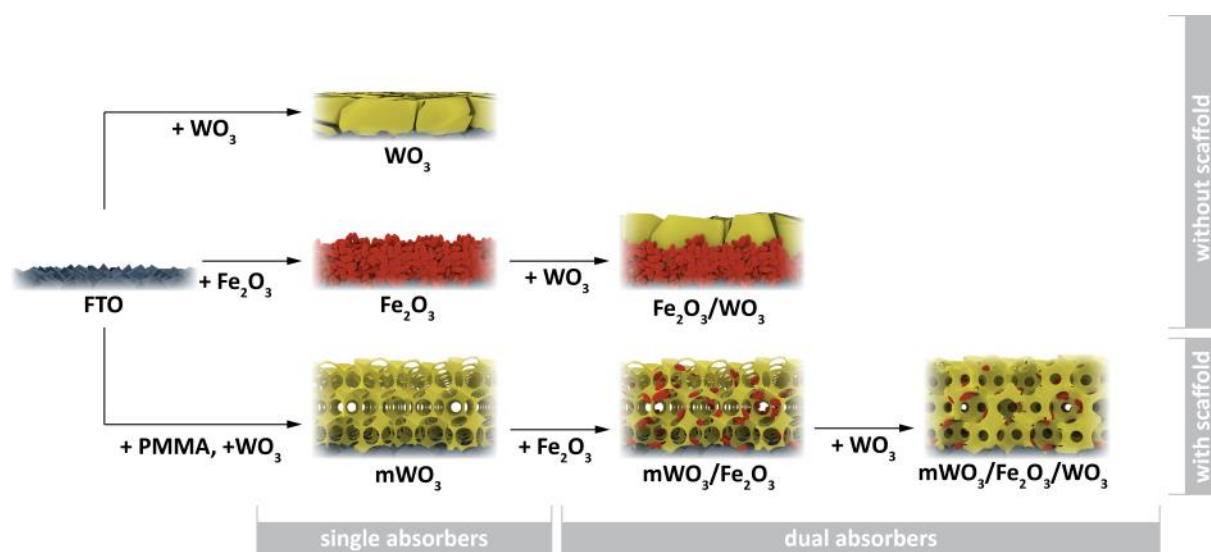


Figure 4-1: Schematic showing the synthesis procedures for all samples.

The first series of flat layers served as references with respect to the host-guest electrodes and allowed for analyzing performance-enhancing factors on simpler model systems. The model systems comprised three samples, including a compact WO_3 and a mesoporous $\text{Fe}_2\text{O}_3:\text{Sn}$ layer coated onto FTO, as well as a dual absorber photoelectrode prepared by depositing a WO_3 overlayer onto a $\text{Fe}_2\text{O}_3:\text{Sn}$ film. These samples are labeled “ WO_3 ”, “ Fe_2O_3 ” and “ $\text{Fe}_2\text{O}_3/\text{WO}_3$ ”, respectively. The second series demonstrated the performance-enhancing benefits of the host-guest architecture. A macroporous WO_3 scaffold was infiltrated by $\text{Fe}_2\text{O}_3:\text{Sn}$ and coated with an additional WO_3 overlayer. In the remainder of the text, these samples are labeled “ mWO_3 ”, “ $\text{mWO}_3/\text{Fe}_2\text{O}_3$ ”, and “ $\text{mWO}_3/\text{Fe}_2\text{O}_3/\text{WO}_3$ ”, respectively. It should be noted that WO_3 can potentially fulfill several functions. At wavelengths below the optical absorption limit, WO_3 acts as a photoabsorber. Furthermore, due to favorable band alignment, it can act as a majority charge carrier collector of electrons generated in Fe_2O_3 .¹⁶ Finally, WO_3 can serve as a surface layer deposited on Fe_2O_3 photoanodes, suppressing electron-hole recombination on the surface.⁵ Therefore, the samples in this study were prepared such that these possible performance-enhancing effects could be studied.

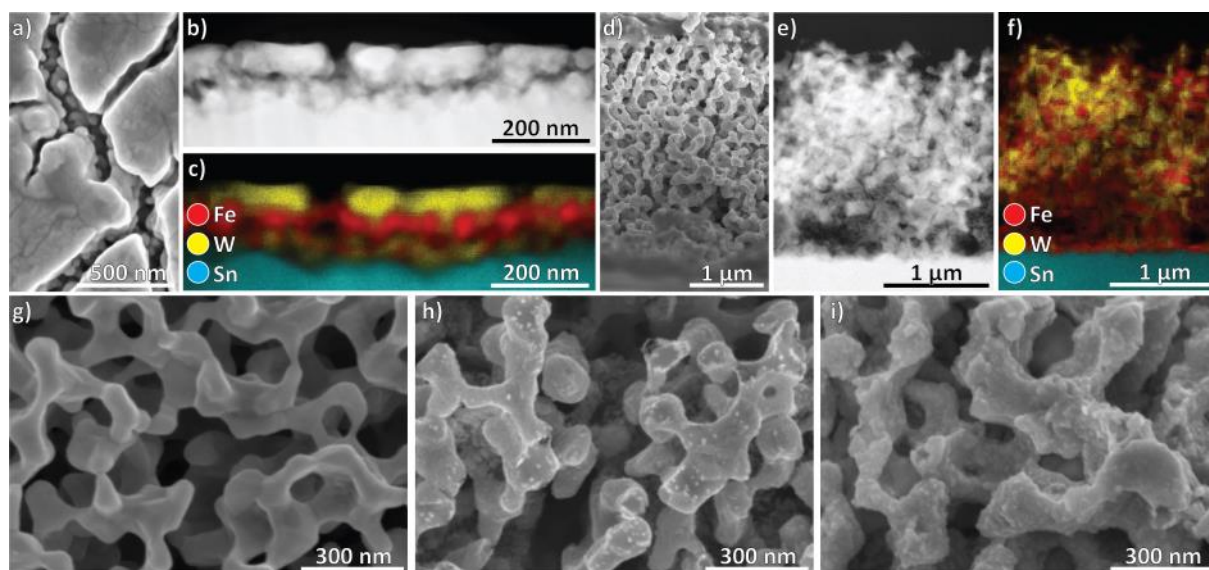


Figure 4-2: Morphological characterization. a) Top-view SEM image of the Fe₂O₃/WO₃ thin films. Fe₂O₃ is visible through cracks in the WO₃ layer. ADF-STEM images and EDX maps of Fe₂O₃/WO₃ are shown in b) and c). d) Cross-section SEM image of mWO₃/Fe₂O₃/WO₃. ADF-STEM images and EDX maps of mWO₃/Fe₂O₃/WO₃ are shown in e) and f) Compared to the pure WO₃ scaffold shown in g), deposited Fe₂O₃ nanoparticles are clearly seen in h). In i) a SEM image of mWO₃/Fe₂O₃/WO₃ is shown. By depositing a WO₃ overlayer, the whole structure is coated.

XRD patterns confirmed the successful synthesis of phase-pure Fe₂O₃:Sn in the hematite structure and monoclinic WO₃, respectively (Figure SI 4-1).³²⁻³³ Contaminant phases could not be detected by XRD, SEM or TEM. In accordance with previous work by Dunn *et al.*, cross-sectional analysis of mesoporous Fe₂O₃ layers showed ~ 50 nm thick mesoporous films composed of individual nanoparticles with an average size of ~ 40 nm x 80 nm (Figure 4-2b and c).²⁶ WO₃, in contrast, forms ~ 100 nm thick, cracked layers composed of large, compact platelets sized between a few hundred nanometers to a few micrometers (Figure SI 4-2). The Fe₂O₃/WO₃ dual absorber retains these morphologies, with WO₃ both infiltrating the Fe₂O₃

4. Results and Discussion

layer and forming a ~ 50 nm thick layer on top (Figure 4-2a, c and d). By forming a compact top layer, WO_3 decreases the exposed Fe_2O_3 surface area.

In contrast, the macroporous samples have an open, porous morphology (Figure 4-2d). The macroporous WO_3 scaffold forms a ~ 2.5 μm thick layer with ~ 150 nm wide pores (Figure 4-2g). Even though the scaffold is distorted compared to a perfect inverse opal structure it is continuous and reaches the back contact. This is expected to be beneficial for charge transport. Hematite nanoparticles fully infiltrate the scaffold and are homogeneously distributed throughout the whole film (Figure 4-2e and f). An additional thin layer of Fe_2O_3 nanoparticles forms on the FTO substrate (Figure 4-2f). In contrast to the flat layers, a WO_3 overlayer fully infiltrates the scaffold and thinly coats WO_3 scaffold and Fe_2O_3 nanoparticles alike, without top layer formation (Figure 4-2i).

The crystal structures of the materials were investigated by TEM. Monocrystallinity of the hematite nanoparticles has been shown by Dunn *et al.*²⁶ Both the WO_3 scaffold and the WO_3 overlayer are highly crystalline, with mWO_3 having domains of several hundred nanometers in size (Figure 4-3a and b). In both $\text{Fe}_2\text{O}_3/\text{WO}_3$ and $\text{mWO}_3/\text{Fe}_2\text{O}_3$, an abrupt interface between Fe_2O_3 and WO_3 without orientational relationship or amorphous phases could be found (Figure 4-3c).

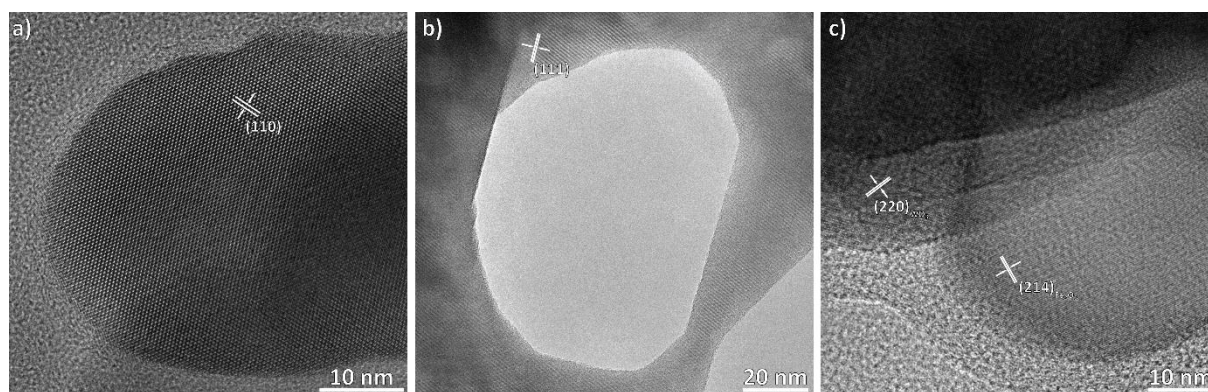


Figure 4-3: Investigation of the crystal structures of a) the WO₃ overlayer in Fe₂O₃/WO₃ and b) the WO₃ scaffold. c) Interface between Fe₂O₃ and WO₃.

Light absorption of all samples was assessed with UV-Vis measurements (Figure 4-4). To correlate them with photoelectrochemical measurements, they were measured under substrate illumination.

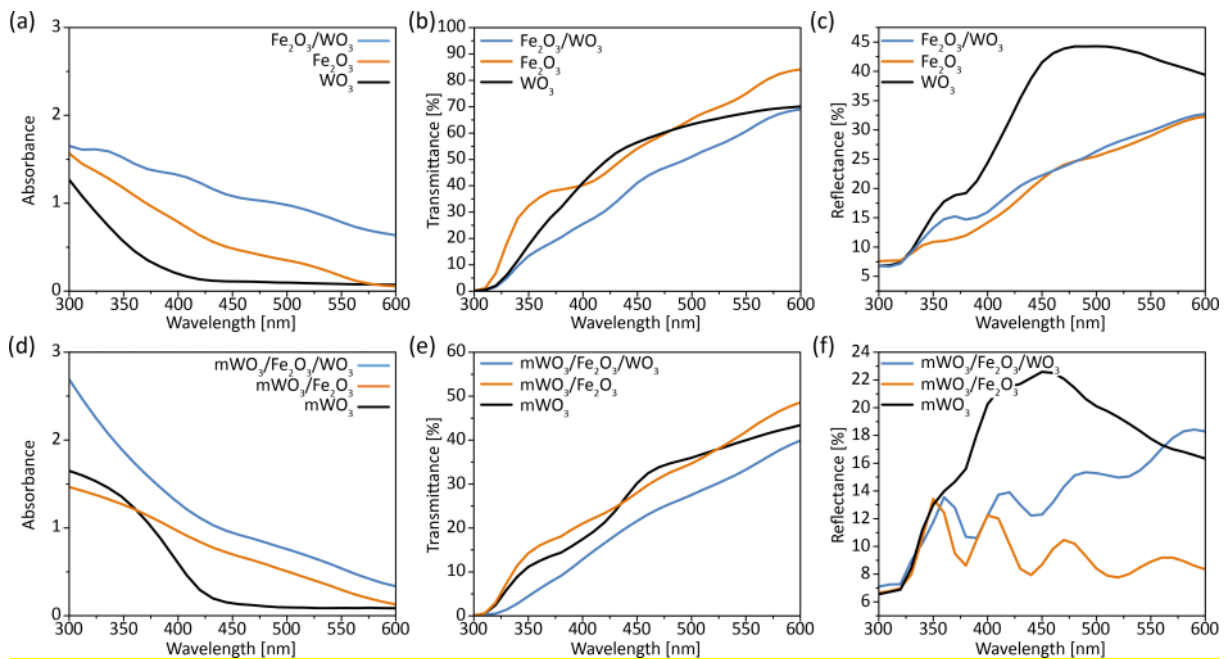


Figure 4-4: UV-Vis, reflectance and transmittance spectra of mesoporous (a, b and c) and macroporous (d, e and f) samples.

As expected based on the band gap, bare WO₃ only absorbs light to ~ 425 nm. In comparison, Fe₂O₃ absorbs light to ~ 560 nm, consistent with a band gap of 2.2 eV, and thereby a much larger percentage of the solar spectrum. Of the flat layers, Fe₂O₃ absorbs more light than WO₃ throughout the whole spectral range. In both flat and macroporous samples, more light is absorbed upon deposition of a mesoporous Fe₂O₃:Sn layer or a WO₃ overlayer. We note the strong scattering contribution of both compact and macroporous WO₃, which is reduced for

all dual absorbers (Figure 4-4c and f). As the UV-Vis spectra were acquired under substrate illumination, light must be backscattered by WO_3 and absorbed by the Fe_2O_3 layer. WO_3 thereby acts as a reflective layer and leads to significantly increased absorbance in the visible range.

All samples were photoelectrochemically characterized by CV measurements under AM 1.5 illumination and IPCE measurements (Figure 4-5). Among the flat layers, Fe_2O_3 has a higher current density than WO_3 , which can be explained by increased light harvesting in the visible region. In accordance with the drop in light absorbance seen in the UV/Vis spectra, the IPCE spectrum of bare WO_3 drops to 0 % at $\sim 425 \text{ nm}$, whereas the IPCE spectrum of Fe_2O_3 drops to 0 % at a much longer wavelength of $\sim 560 \text{ nm}$. Depositing a WO_3 layer onto Fe_2O_3 , thus creating a dual absorber, increases the current density threefold compared to Fe_2O_3 and 17-fold compared to WO_3 , with currents of 0.23 mA/cm^2 at 1.23 V vs. RHE and a maximum IPCE of up to 13 % at 340 nm . This dual absorber not only outperforms the single components, but also the sum of current densities obtained from the individual absorber layers, suggesting that the increased performance cannot be explained solely by increased light absorption. Another important feature of the dual absorber photoanodes is a cathodic shift of the onset potential by nearly 200 mV . Such a shift is usually attributed to the reduction of loss pathways due to either charge transfer catalysis or suppression of surface recombination.^{38–40}

4 Dual Absorber WO₃/Fe₂O₃ Host-Guest Architectures for Improved Charge Generation and Transfer in Photoelectrochemical Water Splitting

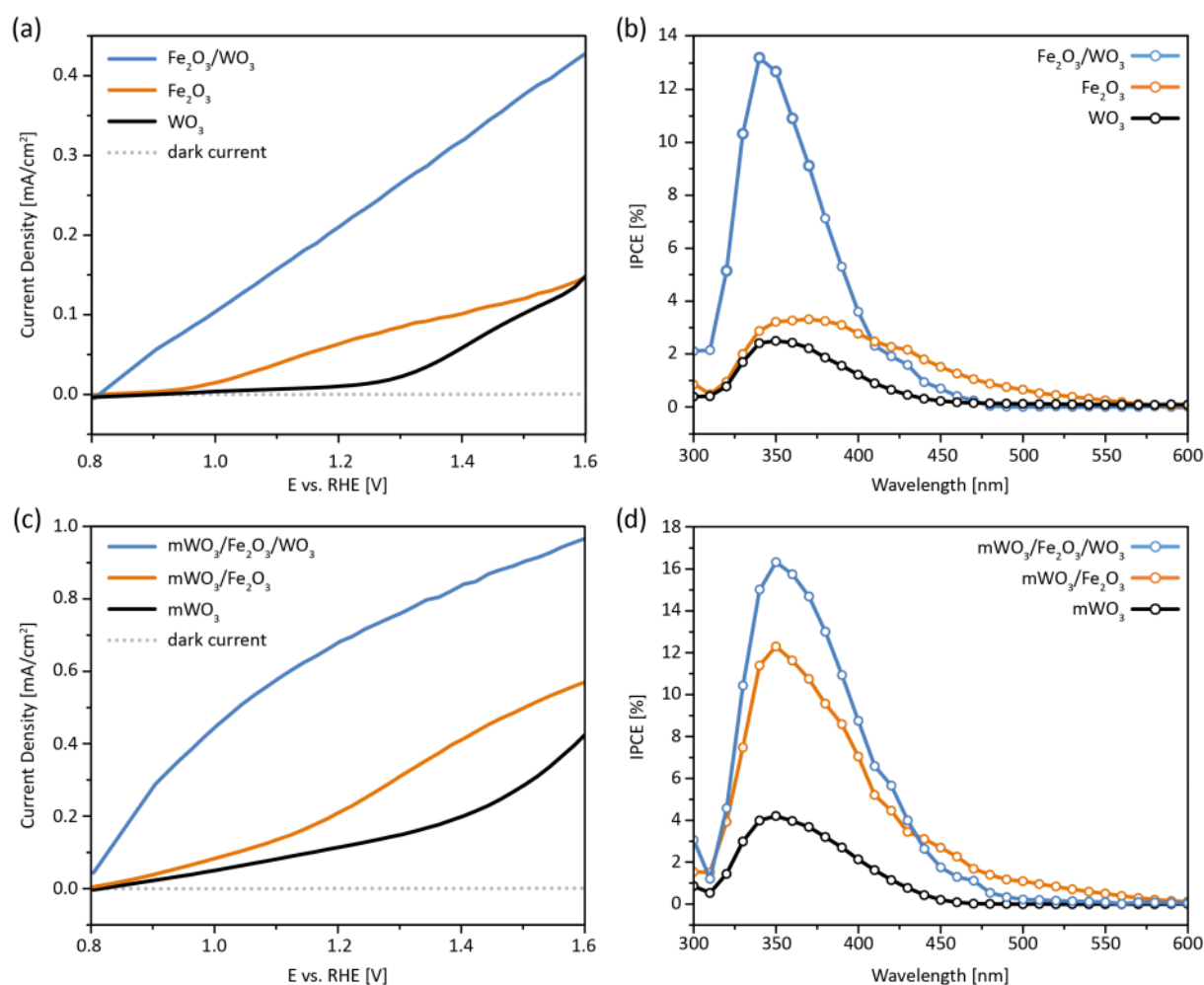


Figure 4-5: CV and IPCE measurements of flat (a and b) and macroporous layers (c and d) measured under AM 1.5 illumination.

The macroporous films show trends similar to the flat layer model systems (Figure 4-5). The performance of the macroporous WO₃ scaffolds is strongly increased compared to WO₃ flat layers. As shown by UV/Vis measurements, the deposition of Fe₂O₃ leads to increased light absorption in the visible range and a shift of the IPCE curve, increasing the current density up to 0.24 mA/cm² at 1.23 V vs. RHE. A substantial increase of current density to 0.7 mA/cm² at 1.23 V vs. RHE with a maximum IPCE of 17 % at 350 nm is achieved by depositing an additional WO₃ layer. As for Fe₂O₃/WO₃, CV measurements of mWO₃/Fe₂O₃/WO₃ show a

steep current onset at 0.8 V vs. RHE. $m\text{WO}_3/\text{Fe}_2\text{O}_3$, which is also composed of both materials, does not show such a steep onset. The strong performance increase compared to flat layers could be explained by the increase in porosity and therefore surface area, or by the WO_3 scaffold acting as a current collector as described in the literature.^{16,27} We note the strong performance increase when applying WO_3 as a surface layer, compared to having it as a scaffold. Interface-related effects such as suppressed recombination due to the WO_3 surface layer could therefore play a major role. Another possible explanation is the role of WO_3 as a reflective or scattering layer, thereby increasing the light harvesting efficiency of Fe_2O_3 .

The photocurrents discussed so far were measured under AM 1.5 illumination. However, with the band structures of Fe_2O_3 and WO_3 and based on our UV/Vis measurements, different processes are expected to take place under illumination with UV and with visible light (Figure SI 4-3).¹⁵ Under UV illumination, electrons generated in Fe_2O_3 can be injected into WO_3 and holes generated in WO_3 can be injected into Fe_2O_3 (Figure 4-6a). Light of longer wavelength, however, only generates electron-hole pairs in Fe_2O_3 , of which the electrons can, according to the band diagram, be injected into WO_3 (Figure SI 4-3). To gain further insights into the behavior of the dual absorber system, photocurrent transients were measured under chopped illumination with UV (365 nm) and blue (455 nm) light. Due to increased light absorption by both Fe_2O_3 and WO_3 in the UV, steady-state photocurrents acquired under UV illumination are consistently higher than those measured with blue light (Figure 4-6b). WO_3 is a highly efficient photocatalyst, leading to higher photocurrents than Fe_2O_3 under UV illumination.¹³ Blue light, however, is not absorbed by WO_3 (Figure 4-4) and higher photocurrents are reached with Fe_2O_3 .

4 Dual Absorber WO₃/Fe₂O₃ Host-Guest Architectures for Improved Charge Generation and Transfer in Photoelectrochemical Water Splitting

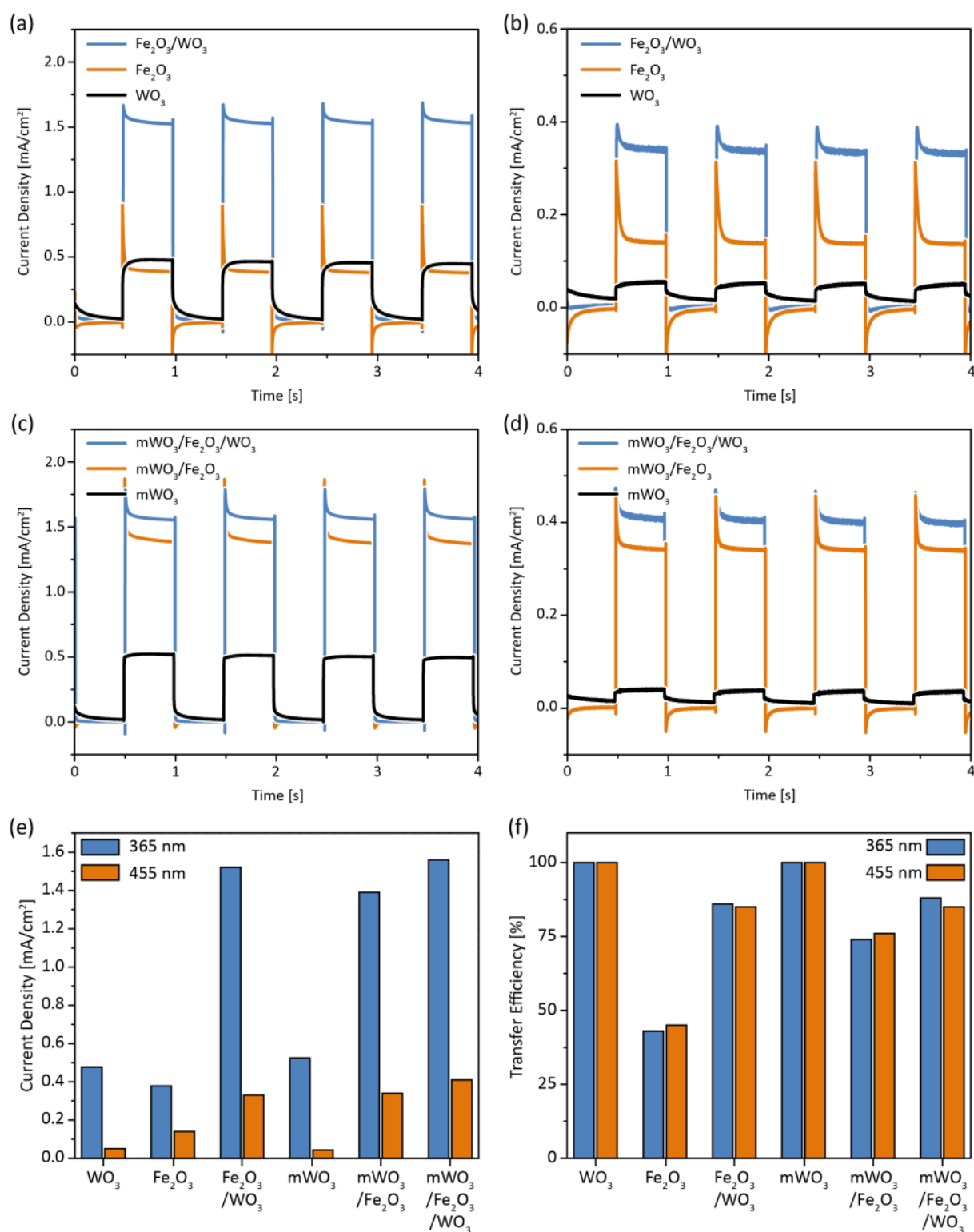


Figure 4-6: Photocurrent transients of flat layers under (a) UV (365 nm) and (b) blue (455 nm) illumination at an applied potential of 1.23 V vs. RHE. Photocurrent transients of the macroporous layers under 365 nm and 455 nm illumination are shown in (c) and (d),

respectively. e) Steady-state photocurrent densities under illumination with 365 nm and 455 nm light at a potential of 1.23 V vs. RHE f) Transfer efficiencies under illumination with 365 nm and 455 nm light extracted from photocurrent transients measured at 1.23 V ca. RHE.

Photocurrent transients reflect all processes influencing charge transfer and transport in the electrode (Figure 4-6).^{26, 34} Upon illumination, movement of photo-generated holes to the surface leads to a charging or displacement current. If holes accumulate, either due to slow surface kinetics or due to slow electron transport to the back contact, they recombine with electrons, and the initial photocurrent decays to a lower steady-state photocurrent. For Fe₂O₃, this leads to a characteristic “spike and overshoot” photocurrent, whereas fast surface kinetics and good electron conductivity of pure WO₃ lead to a rectangular transient form suggestive of complete charge carrier extraction.³⁴ By depositing Fe₂O₃ on a WO₃ scaffold, the difference between initial and steady-state photocurrent decreases compared to Fe₂O₃ and deposition of an additional WO₃ layer further brings the shape of the photocurrent transient even closer to a rectangle. As is to be expected from the fast surface kinetics and good charge transport properties the material is known for, both WO₃ and mWO₃ have transfer efficiencies of 100 %.¹³ In comparison, pure Sn-doped Fe₂O₃ has a transfer efficiency of 41 %, confirming previous work by Dunn *et al.*²⁶ The transfer efficiency can be improved to 75 % by depositing the Sn-doped Fe₂O₃ layer onto a WO₃ scaffold. In line with the discussion in the literature, the WO₃ scaffold could act as a charge collector and thereby increase the electron diffusion length.^{16, 27} In comparison, surface treatment by the deposition of an additional WO₃ layer has a greater effect on the transfer efficiency than the introduction of a WO₃ scaffold, and increases the transfer efficiency to 85 and 88 % for flat Fe₂O₃/WO₃ and macroporous mWO₃/Fe₂O₃/WO₃, respectively. The improved performance could stem from an enhanced

rate of Faradaic reactions on the interface due to the surface treatment with WO₃. However, additional studies are needed to elucidate the mechanism behind this effect.

For both illumination energies, photocurrent densities reached by the dual absorbers, regardless of whether WO₃ was applied as a surface layer or as a scaffold, are very similar. This is in contrast to measurements under the full AM 1.5 solar spectrum, where a much larger difference in photocurrent densities was observed for the different morphologies. This could potentially be explained by the complex interplay of several factors, such as faster surface kinetics, improved current collection and enhanced light absorption, in which WO₃ influences Fe₂O₃. However, future studies will be necessary to fully understand this effect.

4.3 Conclusion

To analyze the effects of WO₃ on Fe₂O₃ in photoelectrochemical water splitting, dual absorbers were prepared with WO₃ as a scaffold and/or as a surface layer. Both approaches significantly increased the performance, validating both the host-guest approach and the surface layer concept. By combining them, current densities of 0.7 mA/cm² at 1.23 V vs. RHE under AM 1.5 illumination with an IPCE of 17 % at 350 nm were reached. The performance increases were investigated by CV, IPCE, photocurrent transient and UV-Vis measurements, and we could identify several beneficial effects responsible for improved charge carrier generation and transport. Importantly, WO₃ strongly reflects visible light, which is then absorbed by Fe₂O₃, resulting in higher photocurrents. The dual absorber therefore exhibits significantly increased light absorption. Compared to Fe₂O₃, a cathodic shift of the onset potential from 1.0 to 0.8 V and an increase in transfer efficiencies, reaching up to 88 %, were measured. We conclude that the investigated device architecture is a promising approach for

4. Experimental

the design of Fe₂O₃/WO₃ dual absorber photoanodes by combining different beneficial effects to generate substantially improved devices.

4.4 Experimental

Synthesis and Deposition of Polymethylmethacrylate (PMMA) Spheres

Polymethylmethacrylate (PMMA) spheres were synthesized according to a well-established procedure.^{27, 35-36} In brief, sodium dodecylsulfate (5 mg, 0.02 mmol) was added to deoxygenated water (98 ml) under nitrogen purging at 40 °C. Further, methylmethacrylate (MMA) (35.6 g, 0.35 mol) was added to the solution that was subsequently heated to 70 °C for 1 hour under reflux and vigorous stirring. Potassium peroxydisulfate (56 mg, 0.2 mmol) was dissolved in water (2 mL) and added as a polymerization initiator. The polymerization reaction was stopped after 45 min by cooling the suspension to room temperature under continuous stirring. The resulting 300 nm PMMA spheres were washed twice with water by centrifugation (19,000 rpm, 20 min) and dispersed in water.

PMMA spheres were deposited on fluorine-doped tin oxide (FTO) substrates (TEC 15 Glass, Dyesol) by placing the substrates vertically in an aqueous PMMA solution. The solution along with the substrates was placed in an 80 °C oven until the water had evaporated, resulting in opaline PMMA films on FTO.

Preparation of WO₃ Films

The precursor solution for WO₃ was prepared by adding 0.8 g of (NH₄)₆H₂W₁₂O₄₀ · xH₂O to 3 mL of deionized water (Millipore Q). To create flat layers, this solution was dip-coated onto the FTO substrate under ambient conditions at a rate of 38 mm/min. The samples were

subsequently calcined at 500 °C with a ramp of 3 °C/min and a dwell time of 5 h. By applying the same procedure to PMMA or hematite films, macroporous inverse opal scaffolds and overlayers, respectively, could be prepared.

Synthesis and Deposition of Tin-Doped Hematite

A procedure developed by Dunn *et al.*²⁶ was applied for the synthesis of tin-doped hematite. 0.25 g Pluronic® P123 were dissolved in 10 mL *tert*-butanol under vigorous stirring. 0.1106 g (0.3 mmol) Sn(CH₃COO)₄ were added to the solution and stirred for 5 h. Next, Fe(NO₃)₃ · 9 H₂O (0.505 g, 1.25 mmol) was added at room temperature and sonicated for 15 min. 2.5 mL water were then added and the solution was left to stir for 17 h under ambient conditions. Prior to spin coating, the resulting suspension was filtered through a filter with a pore diameter of 200 nm. The electrodes were prepared by depositing the filtered solution (100 μL) onto FTO or the macroporous scaffold, respectively, by spin coating at 1000 rpm for 30 s. The films were then calcined at 600 °C with a ramp of 3 °C/min and a dwell time of 30 min.

4.5 Supporting Information

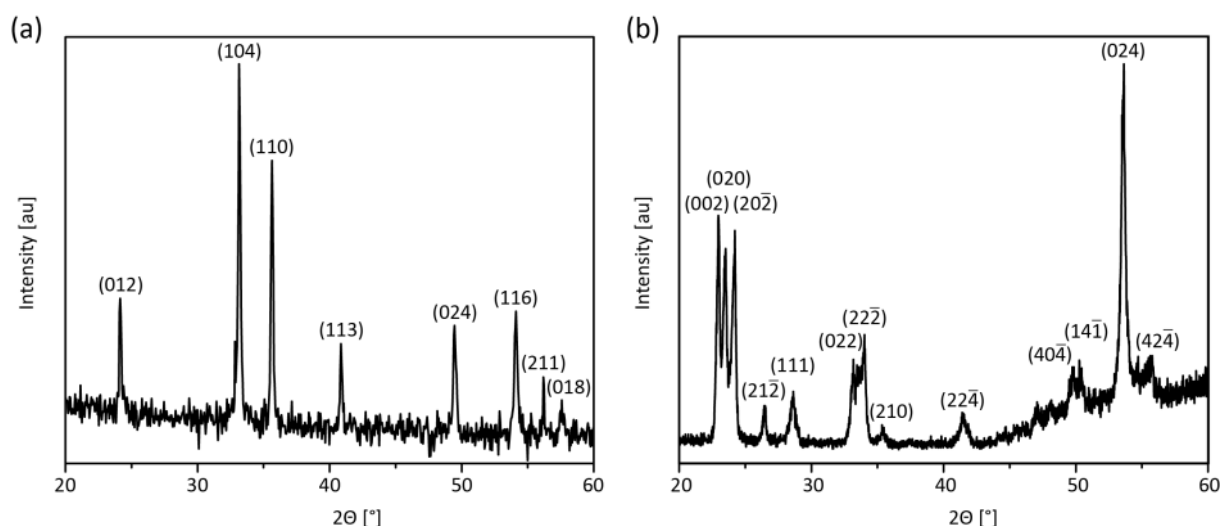


Figure S 4-1: X-ray diffractograms of a) Fe_2O_3 and b) WO_3 . The reflections were assigned using references 34 and 35 of the main text.

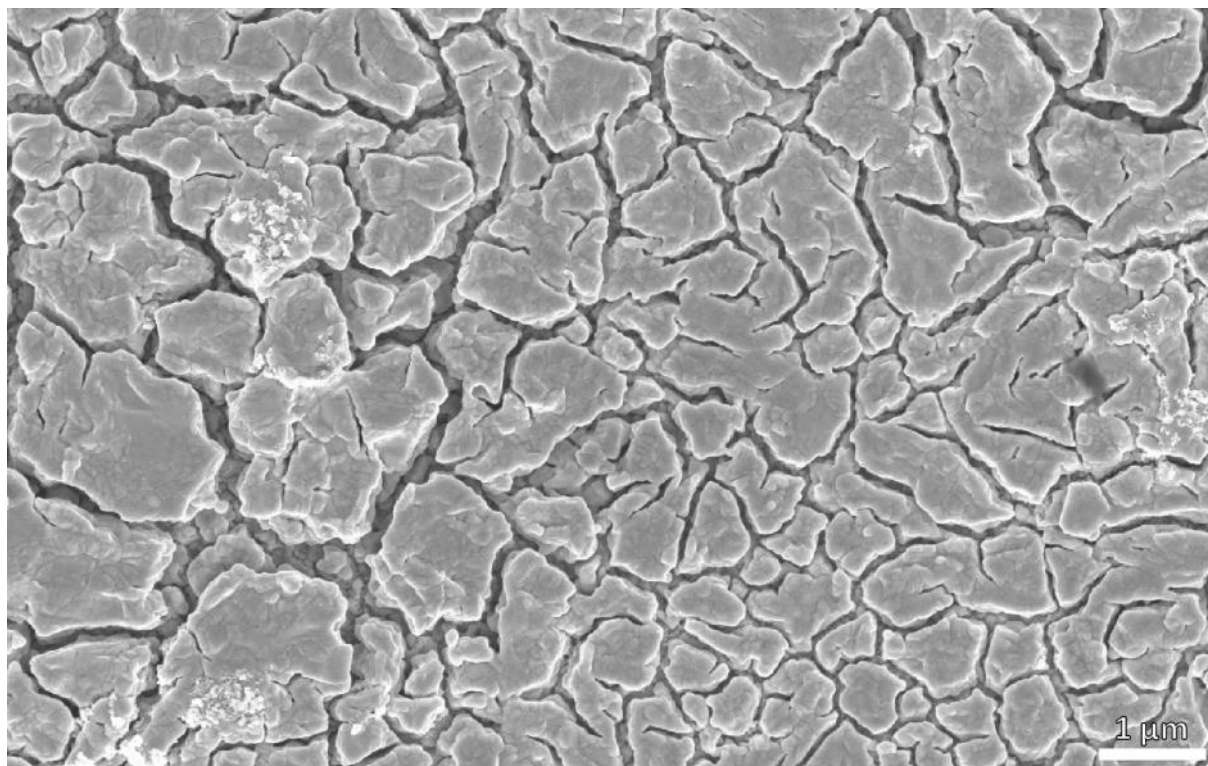


Figure S 4-2: Top-view image of a WO_3 layer, showing the differently sized platelets.

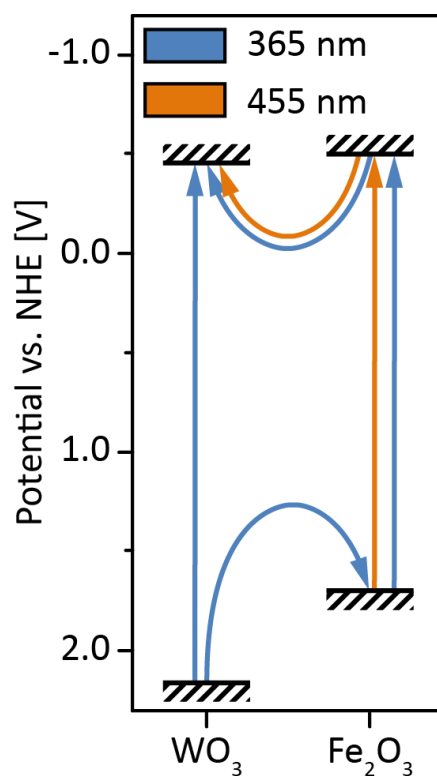


Figure S 4-3: a) Simplified band structure of WO₃ and Fe₂O₃ showing the processes taking place under UV (365 nm) and under blue (455 nm) light according to reference 15 of the main text.

4.6 References

1. Fujishima, A.; Honda, K., Electrochemical Photolysis of Water at a Semiconductor Electrode. *Nature* **1972**, *238* (5358), 37-38.
2. Gratzel, M., Photoelectrochemical cells. *Nature* **2001**, *414* (6861), 338-344.
3. Hisatomi, T.; Kubota, J.; Domen, K., Recent advances in semiconductors for photocatalytic and photoelectrochemical water splitting. *Chemical Society Reviews* **2014**, *43* (22), 7520-7535.
4. Li, Z.; Luo, W.; Zhang, M.; Feng, J.; Zou, Z., Photoelectrochemical cells for solar hydrogen production: current state of promising photoelectrodes, methods to improve their properties, and outlook. *Energy & Environmental Science* **2013**, *6* (2), 347-370.
5. Kronawitter, C. X.; Vayssieres, L.; Shen, S.; Guo, L.; Wheeler, D. A.; Zhang, J. Z.; Antoun, B. R.; Mao, S. S., A perspective on solar-driven water splitting with all-oxide hetero-nanostructures. *Energy & Environmental Science* **2011**, *4* (10), 3889-3899.
6. Wang, J.; Han, Y.; Feng, M.; Chen, J.; Li, X.; Zhang, S., Preparation and photoelectrochemical characterization of WO₃/TiO₂ nanotube array electrode. *Journal of Materials Science* **2011**, *46* (2), 416-421.
7. Su, J.; Guo, L.; Bao, N.; Grimes, C. A., Nanostructured WO₃/BiVO₄ heterojunction films for efficient photoelectrochemical water splitting. *Nano letters* **2011**, *11* (5), 1928-1933.
8. Luan, P.; Xie, M.; Liu, D.; Fu, X.; Jing, L., Effective charge separation in the rutile TiO₂ nanorod-coupled α -Fe₂O₃ with exceptionally high visible activities. *Scientific reports* **2014**, *4*.
9. Sivula, K.; Le Formal, F.; Grätzel, M., Solar Water Splitting: Progress Using Hematite (α -Fe₂O₃) Photoelectrodes. *ChemSusChem* **2011**, *4* (4), 432-449.
10. Hodes, G.; Cahen, D.; Manassen, J., Tungsten trioxide as a photoanode for a photoelectrochemical cell (PEC). *Nature* **1976**, *260* (5549), 312-313.
11. Liu, X.; Wang, F.; Wang, Q., Nanostructure-based WO₃ photoanodes for photoelectrochemical water splitting. *Physical Chemistry Chemical Physics* **2012**, *14* (22), 7894-7911.
12. Granqvist, C. G., Electrochromic tungsten oxide films: review of progress 1993–1998. *Solar Energy Materials and Solar Cells* **2000**, *60* (3), 201-262.

13. Santato, C.; Ulmann, M.; Augustynski, J., Photoelectrochemical properties of nanostructured tungsten trioxide films. *The Journal of Physical Chemistry B* **2001**, *105* (5), 936-940.
14. Murphy, A.; Barnes, P.; Randeniya, L.; Plumb, I.; Grey, I.; Horne, M.; Glasscock, J., Efficiency of solar water splitting using semiconductor electrodes. *International journal of hydrogen energy* **2006**, *31* (14), 1999-2017.
15. van de Krol, R.; Liang, Y.; Schoonman, J., Solar hydrogen production with nanostructured metal oxides. *Journal of Materials Chemistry* **2008**, *18* (20), 2311-2320.
16. Sivula, K.; Formal, F. L.; Grätzel, M., WO₃-Fe₂O₃ photoanodes for water splitting: A host scaffold, guest absorber approach. *Chemistry of Materials* **2009**, *21* (13), 2862-2867.
17. Kishi, T.; Aritsuka, M., Photo-anodic behaviour of α -ferric oxide film electrodes coated with various metal oxides. *Surface and Coatings Technology* **1988**, *34* (3), 345-353.
18. Osterloh, F. E., Inorganic nanostructures for photoelectrochemical and photocatalytic water splitting. *Chemical Society Reviews* **2013**, *42* (6), 2294-2320.
19. Zhang, P.; Gao, L.; Song, X.; Sun, J., Micro-and Nanostructures of Photoelectrodes for Solar-Driven Water Splitting. *Advanced Materials* **2015**, *27* (3), 562-568.
20. Luo, W.; Yu, T.; Wang, Y.; Li, Z.; Ye, J.; Zou, Z., Enhanced photocurrent-voltage characteristics of WO₃/Fe₂O₃ nano-electrodes. *Journal of Physics D: Applied Physics* **2007**, *40* (4), 1091.
21. Memar, A.; Daud, W. R. W.; Hosseini, S.; Eftekhari, E.; Minggu, L. J., Study on photocurrent of bilayers photoanodes using different combination of WO₃ and Fe₂O₃. *Solar Energy* **2010**, *84* (8), 1538-1544.
22. Hosseini, S.; Eftekhari, E.; Soltani, S. M.; Memar, A.; Babadi, F. E.; Jamnani, B. D.; Ismail, M. H. S.; Minggu, L. J., Effect of intermediate layer in photocurrent improvement of three-layer photoanodes using WO₃ and Fe₂O₃. *Journal of Environmental Chemical Engineering* **2013**, *1* (4), 1309-1314.
23. Hosseini, S.; Eftekhari, E.; Soltani, S. M.; Babadi, F. E.; Minggu, L. J.; Ismail, M. H. S., Synthesis, characterization and performance evaluation of three-layered photoanodes by introducing a blend of WO₃ and Fe₂O₃ for dye degradation. *Applied Surface Science* **2014**, *289*, 53-61.
24. Mao, A.; Kim, J. K.; Shin, K.; Wang, D. H.; Yoo, P. J.; Han, G. Y.; Park, J. H., Hematite modified tungsten trioxide nanoparticle photoanode for solar water oxidation. *Journal of Power Sources* **2012**, *210*, 32-37.

25. Jin, T.; Diao, P.; Wu, Q.; Xu, D.; Hu, D.; Xie, Y.; Zhang, M., WO₃ nanoneedles/ α -Fe₂O₃/cobalt phosphate composite photoanode for efficient photoelectrochemical water splitting. *Applied Catalysis B: Environmental* **2014**, *148*, 304-310.
26. Dunn, H. K.; Feckl, J. M.; Muller, A.; Fattakhova-Rohlfing, D.; Morehead, S. G.; Roos, J.; Peter, L. M.; Scheu, C.; Bein, T., Tin doping speeds up hole transfer during light-driven water oxidation at hematite photoanodes. *Physical Chemistry Chemical Physics* **2014**, *16* (44), 24610-24620.
27. Kondofersky, I.; Dunn, H.; Müller, A.; Mandlmeier, B.; Feckl, J. M.; Fattakhova-Rohlfing, D.; Scheu, C.; Peter, L. M.; Bein, T., Electron collection in host-guest nanostructured hematite photoanodes for water splitting: the influence of scaffold doping density. *ACS Applied Materials & Interfaces* **2015**.
28. Riha, S. C.; DeVries Vermeer, M. J.; Pellin, M. J.; Hupp, J. T.; Martinson, A. B. F., Hematite-based Photo-oxidation of Water Using Transparent Distributed Current Collectors. *ACS Applied Materials & Interfaces* **2013**, *5* (2), 360-367.
29. Sun, Y.; Chemelewski, W. D.; Berglund, S. P.; Li, C.; He, H.; Shi, G.; Mullins, C. B., Antimony-Doped Tin Oxide Nanorods as a Transparent Conducting Electrode for Enhancing Photoelectrochemical Oxidation of Water by Hematite. *ACS Applied Materials & Interfaces* **2014**.
30. Wang, L.; Palacios-Adrós, A.; Kirchgeorg, R.; Tighineanu, A.; Schmuki, P., Enhanced Photoelectrochemical Water Splitting Efficiency of a Hematite–Ordered Sb:SnO₂ Host–Guest System. *ChemSusChem* **2014**, n/a-n/a.
31. Qiu, Y.; Leung, S.-F.; Zhang, Q.; Hua, B.; Lin, Q.; Wei, Z.; Tsui, K.-H.; Zhang, Y.; Yang, S.; Fan, Z., Efficient Photoelectrochemical Water Splitting with Ultrathin films of Hematite on Three-Dimensional Nanophotonic Structures. *Nano Letters* **2014**, *14* (4), 2123-2129.
32. Maslen, E.; Streltsov, V.; Streltsova, N.; Ishizawa, N., Synchrotron X-ray study of the electron density in α -Fe₂O₃. *Acta Crystallographica Section B: Structural Science* **1994**, *50* (4), 435-441.
33. Tanisaki, S., Crystal structure of monoclinic tungsten trioxide at room temperature. *Journal of the Physical Society of Japan* **1960**, *15* (4), 573-581.
34. Peter, L. M.; Wijayantha, K. U.; Tahir, A. A., Kinetics of light-driven oxygen evolution at α -Fe₂O₃ electrodes. *Faraday discussions* **2012**, *155*, 309-322.

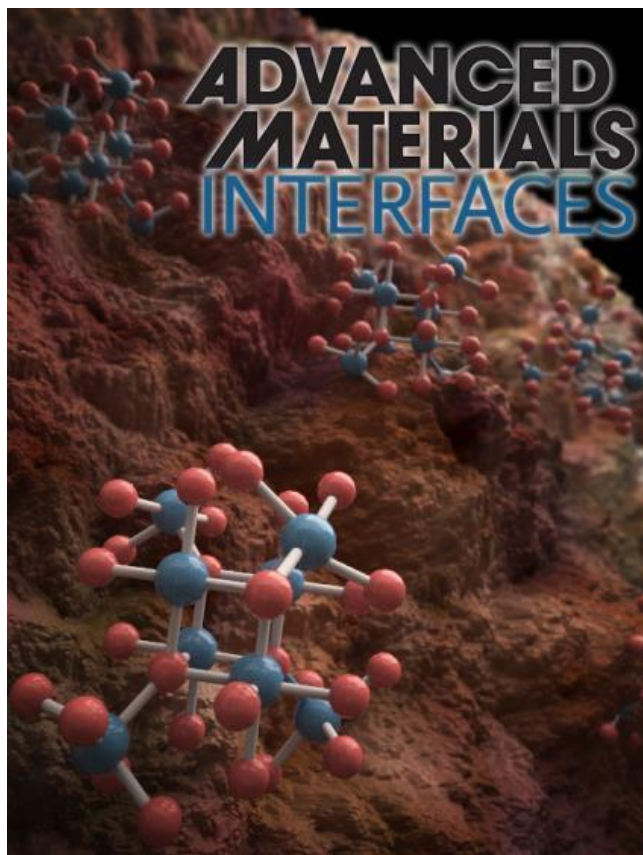
35. Mandlmeier, B.; Minar, N.; Feckl, J. M.; Fattakhova-Rohlfing, D.; Bein, T., Tuning the crystallinity parameters in macroporous titania films. *Journal of Materials Chemistry A* **2013**.
36. Liu, Y.; Peters, K.; Mandlmeier, B.; Müller, A.; Fominykh, K.; Rathousky, J.; Scheu, C.; Fattakhova-Rohlfing, D., Macroporous indium tin oxide electrode layers as conducting substrates for immobilization of bulky electroactive guests. *Electrochimica Acta* **2014**, *140*, 108-115.

5 Ultrasmall Co_3O_4 nanocrystals strongly enhance solar water splitting on mesoporous hematite

This chapter is based on the following publication:

Johann M. Feckl, Halina K. Dunn, Peter M. Zehetmaier, Alexander Müller, Stephanie R. Pendlebury, Patrick Zeller, Ksenia Fominykh, Irina Kondofersky, Markus Döblinger, James R. Durrant, Christina Scheu, Laurence Peter, Dina Fattakhova-Rohlfing and Thomas Bein, *Adv. Mater. Interf.* **2015**, 2, 1500358.

The joint project is a collaboration of different groups involving synthesis of Co_3O_4 nanoparticles (J. M. Feckl and P. M. Zehetmaier), their electrochemical characterization (K. Fominykh), photoelectrochemical and transition absorption spectroscopy characterization (H. K. Dunn, S. R. Pendlebury, I. Kondofersky and J. R. Durrant), XPS (P. Zeller) and TEM analysis (A. Müller, M. Döblinger and C. Scheu). The following experiments were performed by I. Kondofersky: synthesis of mesoporous tin-doped hematite electrodes and deposition of Co_3O_4 nanocrystals, photoelectrochemical characterization of their water oxidation performance and oxygen evolution experiments.



Abstract

We report the synthesis of crystalline, non-agglomerated and perfectly dispersible Co₃O₄ nanoparticles with an average size of 3–7 nm using a solvothermal reaction in *tert*-butanol. The very small size and high dispersibility of the Co₃O₄ nanoparticles allow for their homogeneous deposition on mesoporous hematite layers serving as the photoactive absorber in the light-driven water splitting reaction. This surface treatment leads to a striking photocurrent increase. While the enhancement of hematite photoanode performance by cobalt oxides is known, the preformation and subsequent application of well-defined cobalt oxide nanoparticles is novel and allows for the treatment of arbitrarily complex hematite morphologies. Photoelectrochemical and transient absorption spectroscopy studies show that this enhanced performance is due to the suppression of surface electron/hole recombination on time scales of milliseconds to seconds.

5.1 Introduction

The spinel Co_3O_4 is interesting for applications such as gas sensing,¹ electrochemical lithium ion storage,²⁻⁴ and as catalyst for lithium air batteries,⁵ for the combustion of CH_4 ,⁶ for the oxidation of CO ,⁷ for the oxygen reduction reaction in fuel cells⁸ or for electrochemical water oxidation.⁹ Co_3O_4 has the highest turnover frequency for dark electrochemical water oxidation among the various cobalt oxides, and the catalytic activity is enhanced with decreasing crystallite size.⁹ Interest in Co_3O_4 for photoelectrochemical water splitting was sparked by the work of Kanan and Nocera,¹⁰ and several other groups demonstrated the high efficiency of various cobalt compounds¹¹⁻¹⁷ including Co_3O_4 ¹⁸⁻²⁰ as oxygen evolving catalysts. The effect is pronounced in combination with hematite photoanodes. Hematite offers several features attractive for solar water splitting,²¹⁻²⁴ but also suffers from serious limitations including the sluggish kinetics of the oxygen evolution reaction²⁵⁻²⁷ and the high rate of electron-hole recombination at the surface.^{17, 28-30} The photoelectrochemical water splitting efficiency of hematite photoanodes was found to improve significantly upon surface treatment with different cobalt compounds.^{11-14, 16-17, 31} The role of these surface treatments is not yet fully understood,³¹ although some of them were found to suppress surface recombination but not to catalyze the hole transfer.^{11, 16, 32} The reported synthetic methods rely either on electrochemical deposition,¹¹⁻¹⁴ *in-situ* growth^{16, 20, 33} or atomic layer deposition.^{17, 31} However, the former methods are sensitive to the growth conditions or surface properties of the photoabsorber material and not always applicable to complex electrode geometries, while the latter is not easily and economically scalable.¹¹⁻¹⁴ Consequently, the development of a facile procedure for the low-temperature deposition of Co_3O_4 with well-defined properties on any type of photoabsorber substrate, independent of surface properties or morphology, is very desirable. Dispersible nanoparticles are particularly interesting for this purpose, as their deposition from solution can easily be controlled.

Compared to an *in-situ* growth process, the formation of nanocrystals in a separate process allows for a much better control of properties such as size, shape and chemical composition. Although several Co₃O₄ morphologies such as nanotubes,^{4, 34} needles,³ rods,⁸ hollow spheres,⁶ nanoboxes³⁵ and nanoparticles^{9, 33, 36-39} are synthetically available, it appears that none of these have so far been applied to photoabsorbers for water splitting. Here we report the solvothermal synthesis of dispersible, non-agglomerated and crystalline Co₃O₄ nanoparticles with sizes in the range of 3 to 7 nm. The nanoparticles can be dispersed in ethanol and homogeneously distributed on the surface of mesoporous hematite photoanodes by a simple drop-casting process. This treatment leads to a more than fivefold increase in photocurrent under AM 1.5 illumination compared to the untreated hematite electrodes. The performance enhancement is more pronounced for thicker films, suggesting that the reason for the increased photocurrents is enhanced electron collection in the mesoporous nanoparticle-containing hematite electrodes rather than acceleration of hole transfer at the hematite/solution interface. Efficient extraction of photogenerated electrons from a mesoporous photoanode requires retardation of their recombination with the photogenerated holes (and with intermediates in the water oxidation reaction), resulting in significantly more long-lived surface-accumulated holes, which are required for water oxidation on hematite. This observation was supported by transient absorption spectroscopy (TAS), which showed an increased lifetime of long-lived (ms-s time scale) photogenerated holes at or near the hematite surface.

5.2 Results and Discussion

For the synthesis of dispersible crystalline Co₃O₄ nanoparticles we developed a solvothermal procedure in *tert*-butanol. This solvent has already been shown to be suitable for the

preparation of dispersible, crystalline and ultrasmall metal-oxide nanoparticles such as different titania compounds, NiO and tin oxide.⁴⁰⁻⁴⁵ For the preparation of Co_3O_4 nanoparticles, $\text{Co}(\text{OAc})_2$ was dispersed in a solution of Pluronic P123 in *tert*-butanol. After the addition of concentrated nitric acid to the reaction solution, the mixture was autoclaved at 120 °C for 17 h. Only a combination of $\text{Co}(\text{OAc})_2$, nitric acid and Pluronic P123 led to the formation of small non-agglomerated particles. The use of $\text{Co}(\text{NO}_3)_2$ as an alternative precursor causes the fast growth of larger nanocrystals whose size cannot be decreased by changing reaction conditions or by adding stabilizing ligands. On the other hand, using $\text{Co}(\text{OAc})_2$ as a precursor leads to the formation of mostly amorphous material. We believe that the combination of $\text{Co}(\text{OAc})_2$ with nitric acid leads to the *in-situ* formation of reactive $\text{Co}(\text{NO}_3)_2$ that can form Co_3O_4 . It seems reasonable to assume that the particles are capped by acetate ligands, limiting the particle growth. The presence of Pluronic P123 additionally stabilizes and limits the particle growth.

After cooling to room temperature, the nanoparticles could be collected simply by centrifugation or by drying the processed solution. X-ray diffraction of the obtained solid proves the formation of about 7 nm small Co_3O_4 nanoparticles (size calculated according to the Scherrer equation from the broadening of the 311 reflection; Figure 5-1a). The high background in the XRD pattern is attributed to the fluorescence common for cobalt-containing materials when using Cu K_α radiation. Additionally, the Raman spectrum of the nanoparticles shows modes characteristic of Co_3O_4 (Figure 5-1b).⁴⁶ The solid is easily re-dispersible in ethanol by adding a drop of concentrated acetic acid. This was proven by dynamic light scattering measurements (DLS) in Figure 5-1c, which show a narrow peak at around 7 nm.

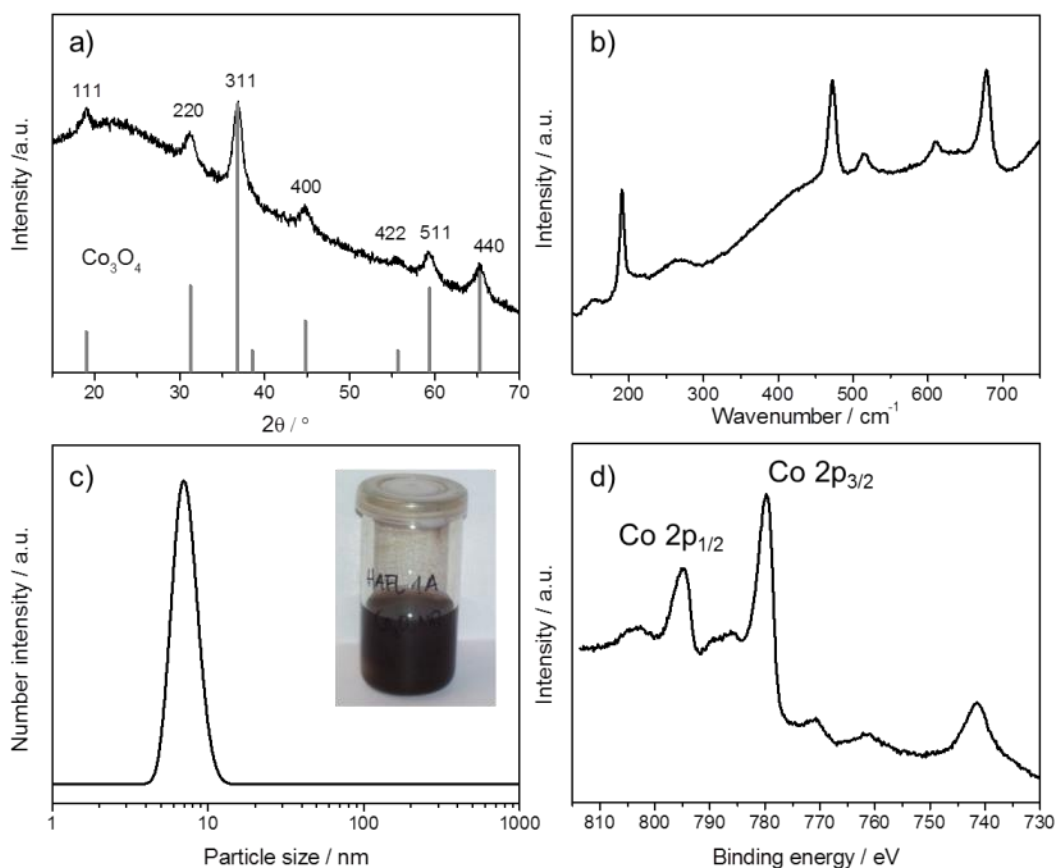


Figure 5-1: Morphology and composition of as synthesized Co₃O₄ nanoparticles prepared via the *tert*-butanol route: a) XRD pattern of nanoparticles with the corresponding ICDD card 00-043-1003 of Co₃O₄; b) Raman spectrum of the Co₃O₄ nanoparticles. The peaks at 190.7 (F_{2g}), 472.7 (E_g), 513.1 (F_{2g}), 610.0 (F_{2g}), 678.6 (A_{1g}) cm⁻¹ correspond to the Raman modes characteristic of Co₃O₄.^[21]; c) DLS measurement of a diluted Co₃O₄ nanoparticle dispersion, the inset shows a photograph of a dispersion with a concentration of 22.8 mg Co₃O₄ nanoparticles after drying, dispersed in 4 mL ethanol; d) XPS spectrum of Co₃O₄ nanoparticles showing the Auger transitions of oxygen at 742 and 761 eV and the Co 2p signals, which are split by spin-orbit coupling into Co 2p_{3/2} (779.9 eV) and 2p_{1/2} (795.0 eV).

XPS measurements were performed to determine the oxidation states of the cobalt oxide nanoparticles. Figure 5-1d shows the Auger transitions of oxygen at 742 and 761 eV and the

Co 2p signals that are split by spin-orbit coupling into Co 2p_{3/2} and 2p_{1/2}. The binding energy of the Co 2p_{3/2} peak (779.9 eV) and the absence of a satellite at about 786 eV (which would indicate CoO) identifies the samples as Co₃O₄.⁴⁷ The XPS spectra before and after electrochemical testing look very similar, suggesting no significant changes in the material during the electrochemical reactions (see Figure S 5-6 in Supporting Information).

In good agreement with the data obtained by XRD and DLS, high-resolution transmission electron microscope images (HRTEM) show monocrystalline nanoparticles with *d*-spacings typical of Co₃O₄ (Figure 5-2). The particles sized 3–7 nm are non-agglomerated and evenly distributed on the surface of the TEM grid, indicating high dispersibility in ethanol (Figure 5-2a).

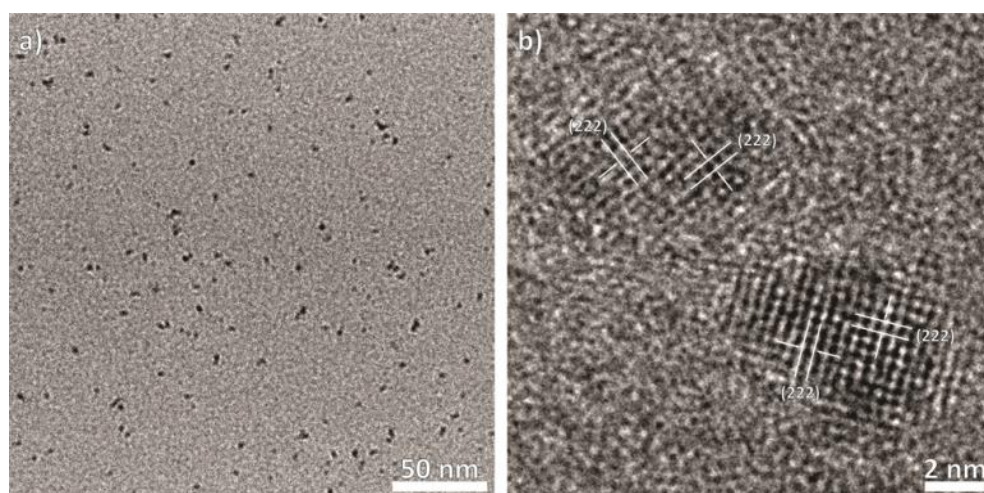


Figure 5-2: (a) TEM image of finely dispersed Co₃O₄ nanoparticles. (b) HRTEM image of two individual Co₃O₄ nanoparticles.

The ultrasmall and dispersible Co₃O₄ nanoparticles were applied as a surface treatment on mesoporous, Sn-doped hematite layers prepared by a wet chemical deposition described by Dunn *et al.*⁴⁸ The hematite electrodes prepared in this way feature a disordered mesoporous structure composed of elongated crystalline nanoparticles with an average size of around 40 x 80 nm. The thickness of the electrodes can be varied from about 50 nm to 400 nm by

repetitive coating.⁴⁸ Even though the photocurrents are lower than those of state-of-the-art hematite photoelectrodes,⁴⁹ the morphology and photocurrents of the hematite films used in this study are similar to those prepared by other solution-based synthetic routes and therefore provide an excellent model system.⁵⁰ The Co₃O₄ nanoparticles were deposited onto the mesoporous hematite electrodes by drop-casting from an ethanolic dispersion. The degree of coating of the hematite photoanodes by Co₃O₄ could easily be controlled by diluting the particle dispersions to the desired concentration. After the deposition step, the samples were heated to 180 °C. This step was necessary to provide good adhesion of the nanoparticles to the mesoporous layer. TEM analysis showed that the Co₃O₄ nanoparticles (which could be identified by lattice spacings, EDX measurements, and size) were for the most part homogeneously distributed throughout the whole volume of the mesoporous hematite layer. For a rather low nanoparticle loading depicted in Figure S 5-7 (Supporting Information), individual non-agglomerated nanoparticles are evenly distributed on the hematite crystals, which can be attributed to their excellent dispersibility.

The Co₃O₄-treated hematite films fabricated as described above were tested as photoanodes for the photoelectrochemical oxygen evolution reaction (OER). The current-voltage curves obtained under AM 1.5 illumination are displayed in Figure 5-3 for a 350 nm thick mesoporous hematite film with and without the Co₃O₄ nanoparticle surface treatment. The photocurrent of the hematite electrodes with deposited Co₃O₄ nanoparticles is significantly higher than that of the untreated hematite films. The increase in photocurrent depends on the illumination direction, a phenomenon that will be discussed later. The increase in photocurrent is accompanied by an increase in the amount of detected oxygen (see Figure S 5-8 in Supporting Information and Experimental part), indicating that the observed effect stems from the water oxidation process and not from any other reactions such as photocorrosion or the oxidation of organics. We detect a cathodic shift in the photocurrent

onset potential, although the observed effect is small compared to other reported cobalt treatments.^{29, 51} Such a shift can indicate either catalysis of charge transfer or a lowering of surface recombination; the analysis of possible effects will be given below.

When deposited directly onto FTO, the Co_3O_4 nanoparticles do not produce any photocurrent, indicating that the observed improvements originate from the synergy between the hematite and the nanoparticles (see Figure S 5-9 in the Supporting Information). We note that the Co_3O_4 nanoparticles lower the onset potential of water oxidation in the dark, acting as catalysts for electrochemical water oxidation. To quantify the dark electrocatalytic activity, we prepared thin films by depositing particle dispersions on the Au electrodes of piezoelectric quartz crystal microbalance chips (QCM). Using Au/QCM crystals as substrates allows for an accurate determination of the mass loading,⁵² which enables a direct calculation of turnover frequencies (TOF) from voltammetric data (Figure S 5-10 in Supporting Information). The TOF values can either be calculated based on the mass loading of Co_3O_4 assuming that all Co atoms are catalytically active (TOF_{min}) or by using the BET surface area based on the assumption that the catalytically active sites are located only on the surface of the electrode (TOF_{max}). We applied both methods to compute the TOF values for our Co_3O_4 nanoparticles. For example the TOF_{min} values at the overpotentials of $\eta = 300$ mV and $\eta = 400$ mV are 0.003 s^{-1} , and 0.01 s^{-1} , respectively. The TOF_{max} at the same overpotentials were calculated as 0.021 s^{-1} and 0.63 s^{-1} , which is an order of magnitude higher than the corresponding TOF_{min} . The obtained results indicate that Co_3O_4 nanoparticles act as a reasonably good dark catalyst for the OER, although the TOF values do not surpass those of other cobalt oxide structures reported in the literature.^{18, 53-56} It should be also noted that good dark catalysts do not necessarily act as catalysts when deposited on photoelectrodes.^{55, 57} The explanation for this possibly lies in the different mechanisms of the light and dark OER, as the former involves minority carriers, whereas the latter involves majority carriers.

To elucidate how the Co₃O₄ nanoparticles improve the performance of hematite photoanodes, we compared their effect on the photocurrent for substrate (SI) and electrolyte side (EI) illumination. A scheme illustrating the various pathways of photogenerated charges in a mesoporous electrode is shown in Figure 5-3a. In porous hematite layers made up of particles of the same size, photogenerated holes (red arrows in Figure 5-3a) travel the same short distance to reach the oxide/solution interface, independent of the illumination direction. Photogenerated electrons, in contrast, must travel through the porous layer to the FTO substrate, and for strongly absorbed light (i.e. at wavelengths where the penetration depth of the light is much less than the film thickness), the average distance travelled therefore depends on the illumination direction. Under EI illumination, electron-hole pairs are generated far away from the substrate and electrons have a long collection pathway through the thickness of the film (blue arrow in Figure 5-3a). This leaves them vulnerable to recombination with surface species, such as trapped holes (this loss pathway is depicted by blue striped arrows). Under SI illumination, we expect more efficient electron collection, since the charges are generated very close to the FTO substrate. The comparison of the photocurrent under EI and SI illumination thus gives insight into electron/hole recombination in porous electrodes;^{49, 58} the description of this method for AM1.5 illumination will be published separately.

For the untreated hematite electrode, the photocurrent measured when illuminating by an AM 1.5 solar simulator through the electrolyte (EI) is approximately a quarter of that obtained when illuminating through the substrate (SI) (Figure 5-3b, c). According to the arguments outlined above, this indicates that a considerable portion of photogenerated electrons is not collected when generated far from the collecting FTO substrate. However, when applying Co₃O₄ nanoparticles to 100 – 400 nm thick mesoporous hematite layers, the photocurrent when illuminating through the substrate (SI) strongly increases by factor of 1.6 compared to

the untreated hematite electrode, reaching 0.64 mA cm^{-2} at 1.23 V vs. RHE for the 350 nm thick electrode (Figure 5-3b, d). Much higher increases of up to a factor of nearly five are observed for electrolyte illumination (EI) (Figure 5-3c, e). Given that the losses to recombination under EI are expected to scale with the film thickness, one can expect a more dramatic effect of the Co_3O_4 nanoparticles on thicker films. Figure 5-3 illustrates the photocurrent at 1.23 V vs. RHE of films of varying thickness under SI (Figure 5-3d) and EI illumination (Figure 5-3e), with and without the Co_3O_4 nanoparticle treatment. Due to electron/hole recombination losses, the deviation between EI and SI increases as a function of thickness. However, the effect is reduced for Co_3O_4 -treated photoanodes, indicating a significant reduction of this loss pathway.

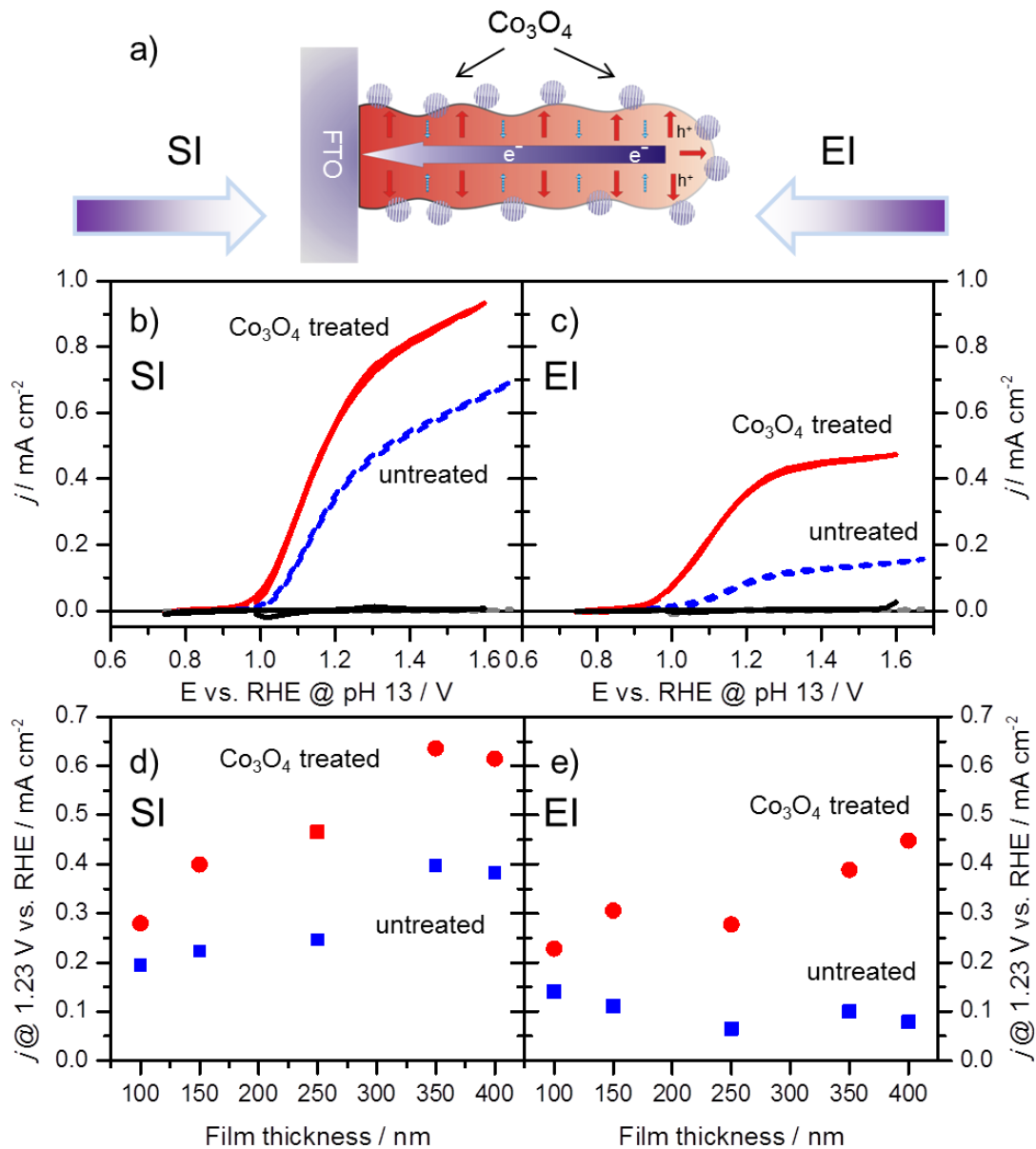


Figure 5-3: (a) Simplified illustration of the processes taking place in a porous hematite electrode during illumination. Red arrows indicate diffusion of the photogenerated holes to the hematite surface, the blue arrow indicates diffusion of photogenerated electrons to the substrate (current collector), and blue striped arrows represent their recombination with positive species, such as holes. Illumination direction is indicated as SI (substrate illumination) and EI (electrolyte illumination). (b, c) Current density – voltage curves for 350 nm nanostructured hematite films with (full red lines) and without (dashed blue lines) Co₃O₄

nanoparticle treatment under simulated AM 1.5 illumination through the substrate (b, SI) and the electrolyte (c, EI). Dark j - V curves are also shown for the Co_3O_4 treated film (full black line) and untreated film (dashed grey line). (d, e) Photocurrent at 1.23 V vs. RHE of films of varying thicknesses with (red circles) and without the Co_3O_4 treatment (blue squares), when illumination is provided through the substrate (SI, d) and electrolyte (EI, e).

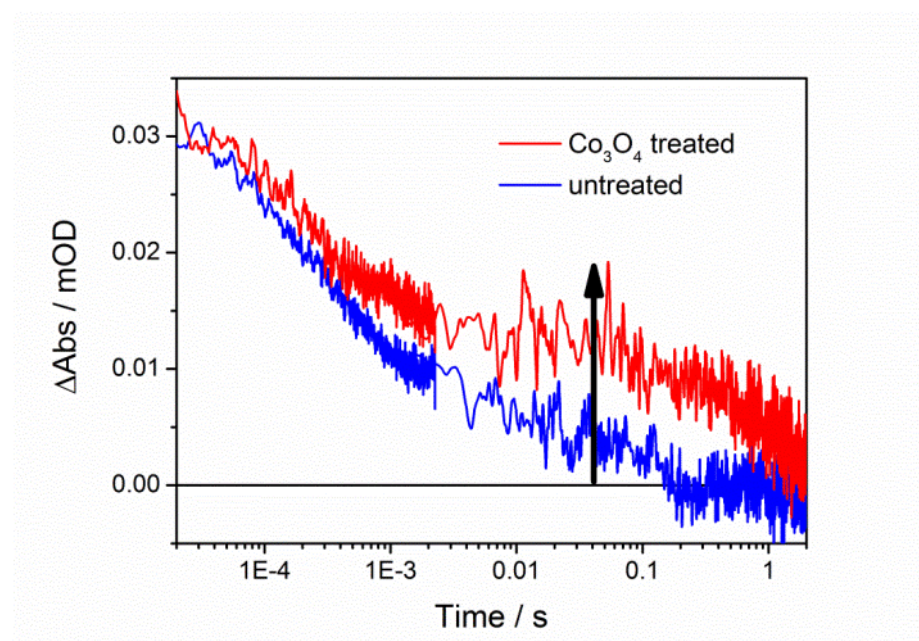


Figure 5-4: Photogenerated hole dynamics in untreated (blue) and Co_3O_4 treated (red) thin (50 nm) hematite photoanodes at open circuit in 1 M NaOH, excited at 455 nm and probed at 650 nm. The arrow indicates the increase in lifetime of photogenerated holes after treatment with Co_3O_4 nanoparticles.

The transient absorption dynamics of photogenerated holes at or near the hematite surface (probed at 650 nm, in accordance with previous studies²⁷) in untreated and Co_3O_4 -treated hematite at open circuit are shown in Figure 5-4 (the same data shown on a linear time axis is presented in Figure S 5-12 in the Supporting Information). It is apparent that the Co_3O_4

treatment significantly increases the lifetime of the photogenerated hole signal on millisecond to second times scales. These results are consistent with the effect of other Co-based treatments (such as Co-Pi and cobalt nitrate) on the lifetime of surface-accumulated holes in hematite as studied by transient absorption spectroscopy and intensity modulated photocurrent spectroscopy.^{11, 32} The increase in lifetime of photogenerated holes (of ~500 ms) on these long time scales indicates that electron-hole recombination at the semiconductor surface has been retarded by the Co₃O₄ treatment.³⁰ These results are consistent with the photocurrent increase by Co₃O₄ treatment. Interestingly, treatment with cobalt nitrate, which has been reported to increase photocurrents of different hematite photoelectrodes^{29, 38} by retarding recombination,³² had little influence on the performance (see Figure S 5-11 in Supporting Information).

The observed improvement in photocurrent depends on the mass loading of the Co₃O₄ nanoparticles in the mesoporous hematite electrodes, as shown in Figure 5-5. The best performance is observed for samples with a low loading of Co₃O₄ nanoparticles. TEM investigation of the best performing samples demonstrates that the porous hematite layers contain homogeneously distributed non-agglomerated Co₃O₄ nanoparticles, with only a few Co₃O₄ nanoparticles observed on the hematite crystals (Figure 5-4a and Figure S 5-7). In contrast, hematite photoanodes treated with concentrated nanoparticle dispersions show suppressed photocurrents compared to the non-treated photoanodes. Examination of such samples by TEM reveals a dense coverage with Co₃O₄ nanoparticles, leaving very little exposed Fe₂O₃. We tentatively attribute the suppressed photocurrent in such densely decorated hematite film to the reduced exposed surface area and an increased parasitic light absorption by the black Co₃O₄.⁵⁴

The obtained results demonstrate that the post-synthetic Co₃O₄ nanoparticle treatment significantly improves the electron collection in mesoporous hematite photoanodes.

5. Conclusion

Photoelectrochemical and transient absorption spectroscopy studies suggest that this enhanced performance is due to the suppression of surface electron/hole recombination and not due to the catalysis of charge transfer. The way by which the Co_3O_4 nanoparticles retard electron-hole recombination at the semiconductor surface is however not fully understood, so that additional studies are needed to elucidate the mechanism of this effect.

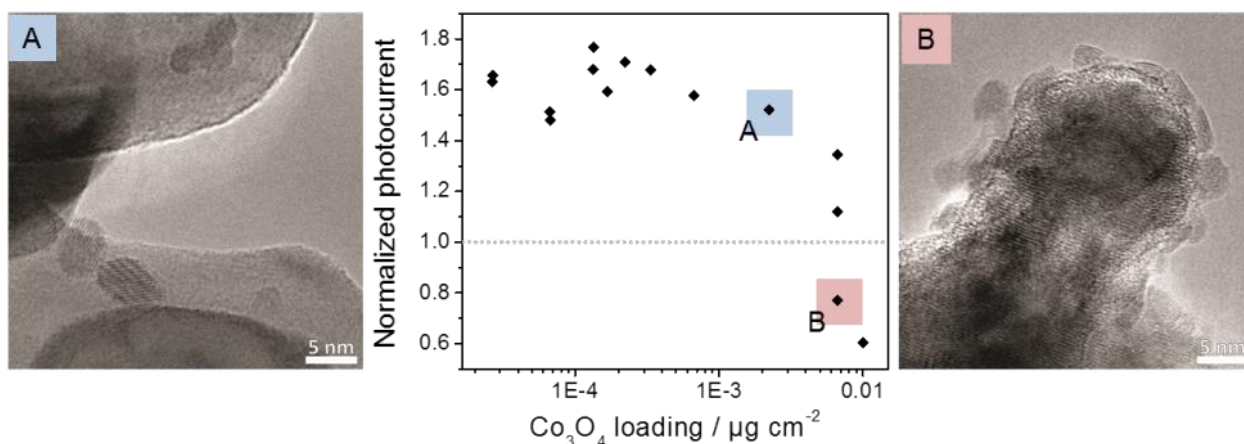


Figure 5-5: Normalized photocurrent at 1.164 V vs. RHE (pH 13) under 455 nm illumination with ca. $10^{17} \text{ cm}^{-2} \text{ s}^{-1}$ intensity, of Co_3O_4 -treated 150 nm Sn-doped hematite films as a function of Co_3O_4 nanoparticle loading on the active area of the electrodes. The normalized current is displayed as a ratio of photocurrent of Co_3O_4 nanoparticle-treated electrodes to that of an untreated electrode of the same thickness. On the left and right side the corresponding TEM images are shown to illustrate the different surface coverage.

5.3 Conclusion

Ultrasmall Co_3O_4 nanoparticles were synthesized via a newly developed *tert*-butanol solvothermal synthesis protocol. The high dispersibility and very small size of these particles were proven by XRD, DLS and TEM measurements and allow for the efficient distribution of these monocrystalline nanoparticles on mesoporous hematite films by a drop-casting process.

This treatment leads to striking improvements in photoelectrochemical water oxidation rates, increasing the obtained photocurrent by a factor of nearly five. The improvement is attributed to a significant reduction in electron/hole recombination processes on millisecond to second time scales at the surface of the mesoporous network, and strongly depends on the degree of surface coverage by the Co₃O₄ nanoparticles. This demonstrates the importance of a homogeneous distribution of the applied nanoparticles on the highly porous host materials, which can easily be achieved with the stable colloidal dispersions presented in this study.

5.4 Experimental

Co₃O₄ nanoparticle synthesis: Co₃O₄ nanoparticles were synthesized in *tert*-butanol. All chemicals were purchased from Sigma-Aldrich and used as received. *tert*-Butanol was dried over a 4 Å molecular sieve at 28 °C and filtered prior to use (Sartorius minisart cellulose acetate membrane, 220 nm). In a typical reaction 50 mg (0.2 mmol) of Co(OAc)₂ tetrahydrate was dispersed in a solution of 58 mg Pluronic P123 in 14 mL *tert*-butanol and treated for 45 min in an ultrasonic bath at room temperature. To accelerate the synthesis, 48 mg of concentrated nitric acid was added to the reaction solution. The reaction mixture was transferred into a Teflon lined steel autoclave (20 mL volume) and kept at 120 °C for 17 h. The nanoparticles can be collected by simply drying the processed solution or by centrifugation. The content of Co₃O₄ of the resulting centrifuged solid after drying at 180 °C (equivalent to the heat treatment after the deposition of the nanoparticles on the nanostructured hematite electrodes) was determined to be 70 wt% by thermogravimetric analysis. The pellet was treated with one drop of concentrated acetic acid (35 mg acetic acid per 22.8 mg solid) and then redispersed in ethanol (1 mL ethanol for 1 mg solid). This

5. Experimental

dispersion was filtered with a 220 nm syringe filter and the concentration of Co_3O_4 nanoparticles in the resulting dispersion was determined by inductively coupled plasma atomic emission spectroscopy (ICP-AES) to be 0.667 mg mL^{-1} , which agrees well with the inorganic amount of 70 wt% determined by TGA. This dispersion was then diluted with ethanol (1:50) for DLS measurements, the preparation of TEM samples and the photoelectrochemical water splitting experiments.

Photoelectrode preparation: Sn-doped hematite electrodes were prepared according to a procedure described in detail elsewhere,⁴⁸ resulting in mesoporous films of about 50 nm thickness after calcination at 600 °C. Thicker films were obtained by repeating the complete procedure. SEM cross-section images of these films are shown in Figure S 5-13 in Supporting Information.

A Co_3O_4 nanoparticle surface treatment was applied to the Sn-containing mesoporous hematite thin films by drop casting. After depositing 10 μL of the Co_3O_4 nanoparticle dispersion in ethanol as described above onto a projected electrode area of 2.25 cm^2 , the films were heated to 180 °C for 30 min. This step was necessary to provide a good adhesion of the nanoparticles to the mesoporous layer. All data reported herein are representative of several samples of each type (hematite film thickness and nanoparticle loading).

The dissolved O_2 was determined with a HANNA dissolved oxygen bench meter (HI 2400 DO Meter) using the same setup described above. The electrolyte solution was purged with N_2 before each measurement until the dissolved oxygen in solution reached 0 ppm. During electrochemical measurements N_2 was purged above the solution. The films were illuminated through the electrolyte (EI) side using a blue diode (455 nm at $10^{17} \text{ s}^{-1} \text{ cm}^{-2}$).

Current–voltage (I–V) curves were obtained by scanning from negative to positive potentials in the dark or under illumination at a 20 mV/s sweep rate. Further chronoamperometric

measurements were carried out at 1.56 V vs. RHE over 10 minutes while determining the concentration change of dissolved oxygen over time.

Transient Absorption Spectroscopy (TAS): The dynamics of photogenerated holes in untreated and Co₃O₄-treated hematite photoanodes were measured using microsecond to second timescale transient absorption spectroscopy (TAS). Band-gap excitation of hematite was achieved using a 455 nm pulsed laser (0.35 Hz, 210 $\mu\text{J cm}^{-2}$ /pulse, <20 ns pulse width), generated from the third harmonic (355 nm) of a Nd:YAG laser (Quantel Ultra, Lambda Photometrics) via an optical paramagnetic oscillator (Opolette, Opotek Inc.). This “pump” pulse was transmitted to the sample by a liquid light guide. A 100 W tungsten lamp (IL 1, Bantam) equipped with a monochromator (OBB-2001, Photon Technology International) was employed as the probe beam; holes in hematite were probed at 650 nm, in accordance with previous studies.²⁷ The sample was illuminated from the EI side (electrolyte-electrode). The transmitted probe light was filtered by several long-pass filters and a band-pass filter in order to remove scattered light from the laser before being focused on a silicon photodiode detector (S3751, Hamamatsu). Microsecond-millisecond timescale data were amplified and filtered (Costronics) and collected by an oscilloscope (TDS 2012c, Tektronics); millisecond-second timescale data were collected with a DAQ card (NI USB-6211, National Instruments). All data were acquired using home-built Labview software. Each trace shown is the average of 300 – 500 individual measurements. Signals due to laser scatter were subtracted from μs -ms timescale data.

5.5 Supporting Information

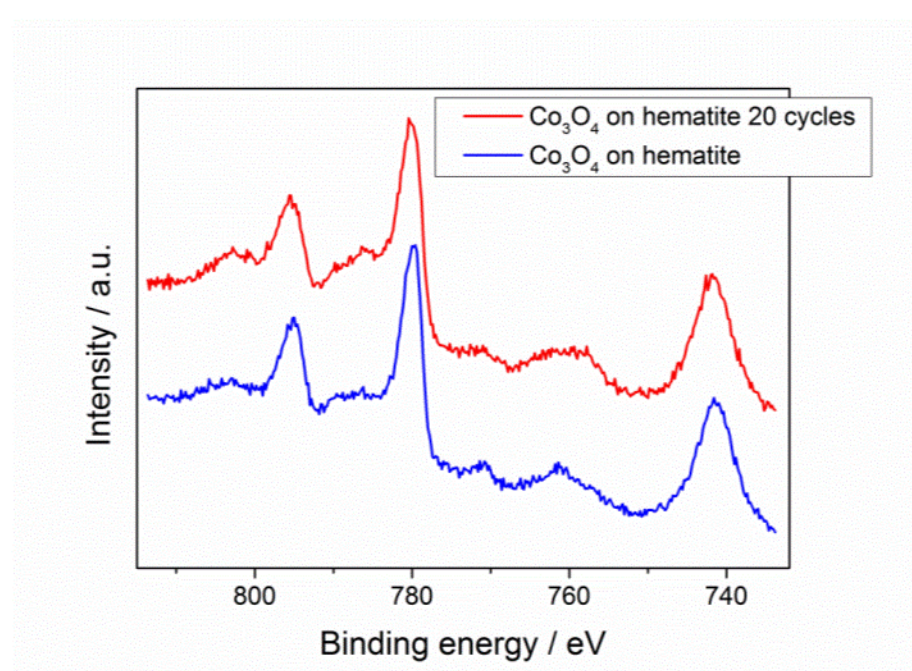


Figure S 5-6: XPS spectra of cobalt oxide nanoparticles deposited on top of Sn-doped hematite electrodes before and after 20 cyclic voltammetry scans under 455 nm illumination, incident photon flux $10^{17} \text{ cm}^{-2} \text{ s}^{-1}$. The XPS spectra exhibit the Auger transitions of oxygen at 742 and 761 eV and the Co 2p signals that are split by spin-orbit coupling into Co 2p_{3/2} (779.9 eV) and 2p_{1/2} (795.0 eV).

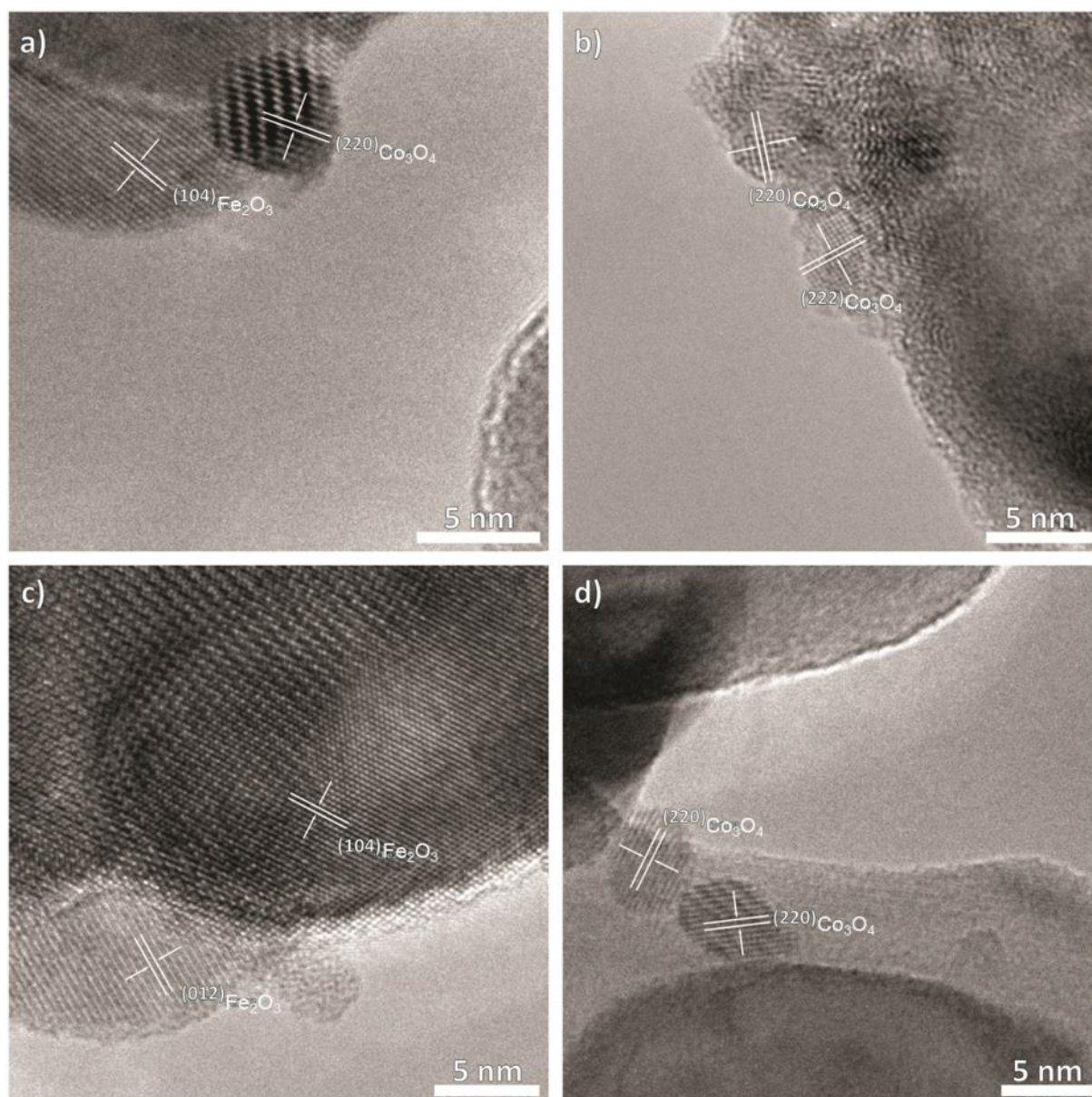


Figure S 5-7: HR-TEM images of the cobalt oxide nanoparticle-treated mesoporous hematite layers removed from the substrate. Rare occurrences of agglomerates (c) that could be observed in addition to individual nanoparticles (b) are most likely a result of nanoparticles being caught in pores during the drop-casting process.

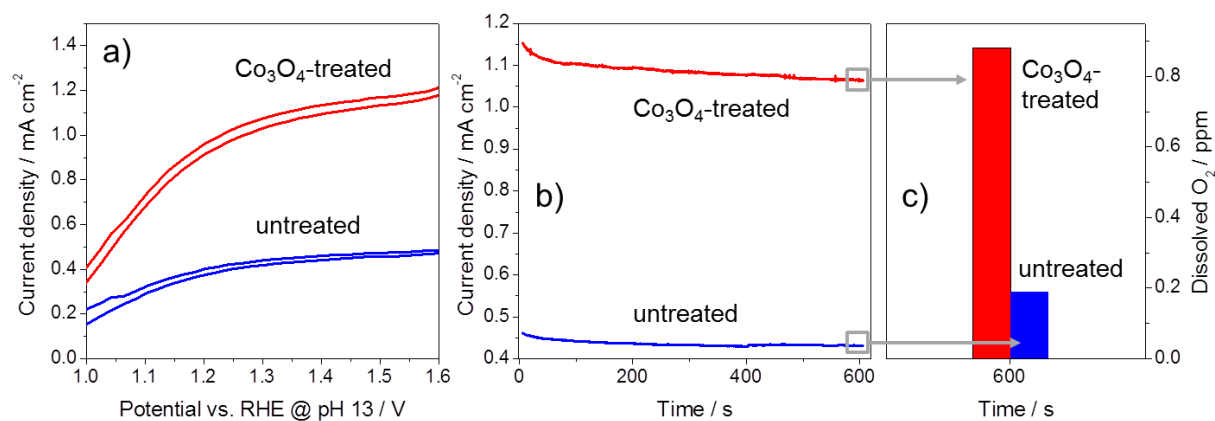


Figure S 5-8: (a) Cyclic voltammetry curves of tin-doped hematite films on FTO with (red line) and without (blue line) Co₃O₄ treatment. (b) Potentiostatic measurements on untreated (blue) and Co₃O₄-treated (red) tin-doped hematite samples at 1.56 V vs. RHE over 10 minutes. (c) Amount of dissolved oxygen in electrolyte after 10 minute measurement at 1.56 V vs. RHE and under illumination (455 nm LED, with ca. 10^{17} cm⁻² s⁻¹ intensity).

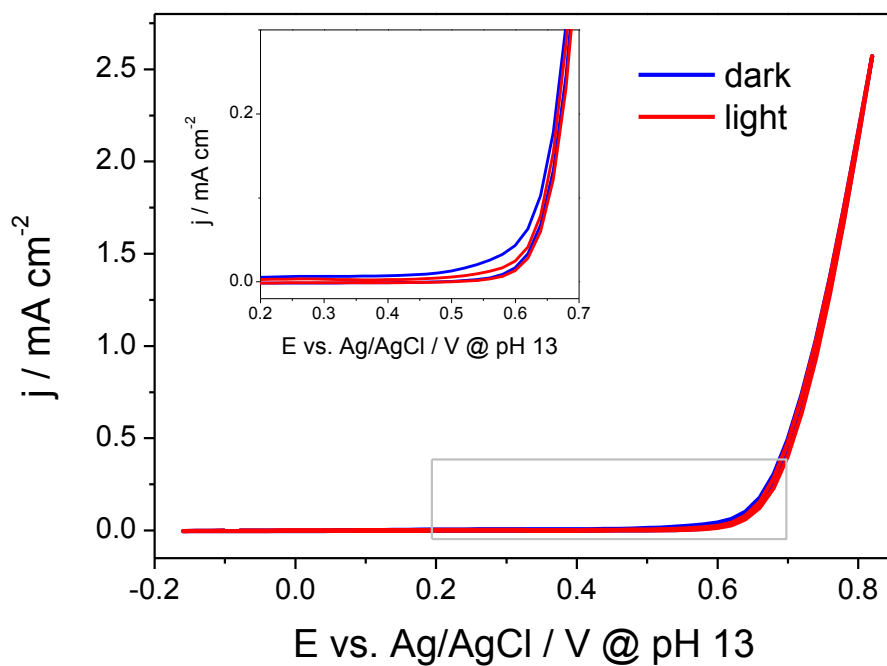


Figure S 5-9: Cyclic voltammograms of a Co₃O₄ treated (red) FTO electrode in the dark (blue) and under illumination (455 nm LED, with ca. 10^{17} cm⁻² s⁻¹ intensity) (red). An inset shows a zoomed area marked in grey.

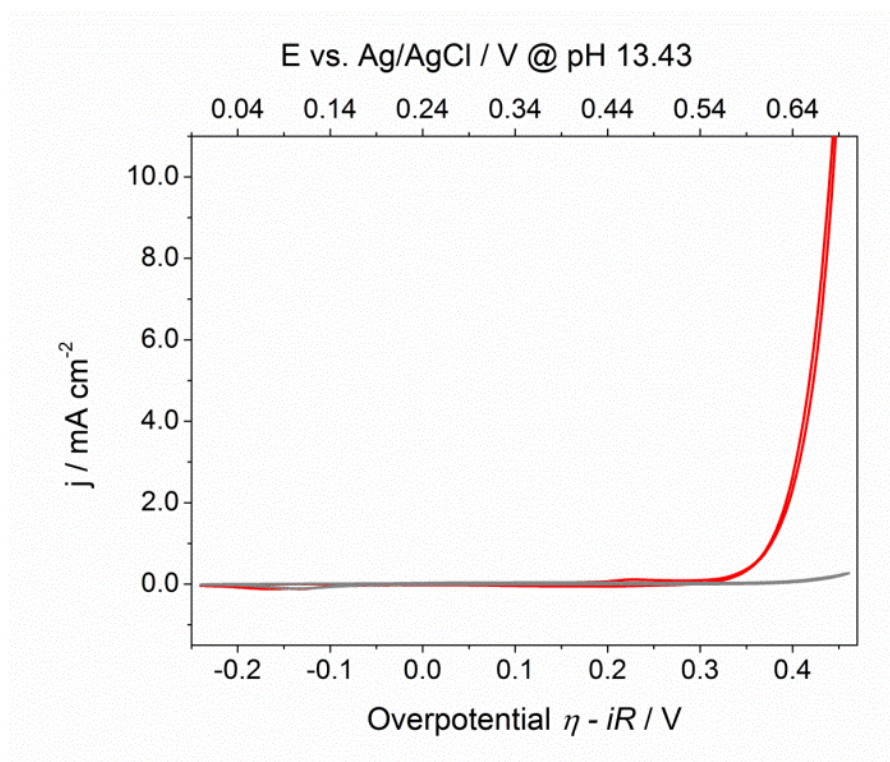


Figure S 5-10: Dark CV curves of a Co₃O₄ electrode prepared on a Au/QCM crystal (red line) and a bare Au/QCM crystal (grey line). The electrodes were cycled vs. Ag/AgCl in 0.5 M KOH with the scan rate of 20 mV s⁻¹. The reduction peak at the potential of ca. 0.1 V vs. Ag/AgCl corresponds to the Au electrode and is visible in both CV curves.

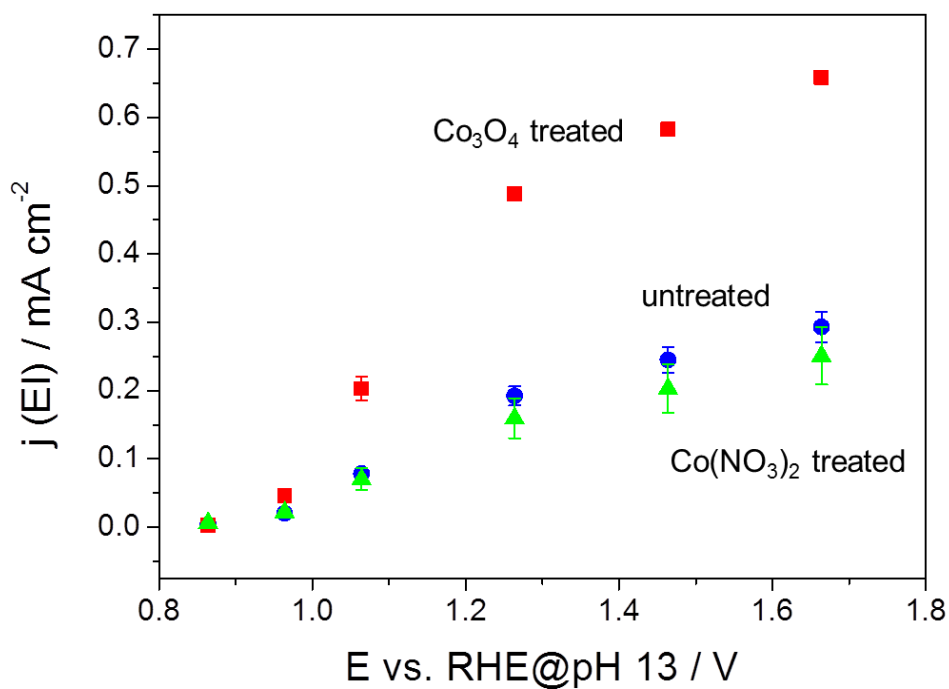


Figure S 5-11: Steady state photocurrent under 455 nm illumination with about $10^{17} \text{ cm}^{-2} \text{ s}^{-1}$ intensity from the electrolyte side of 150 nm Sn-doped hematite films (blue), as well as identical films treated with Co₃O₄ (red) and Co(NO₃)₂ (green).

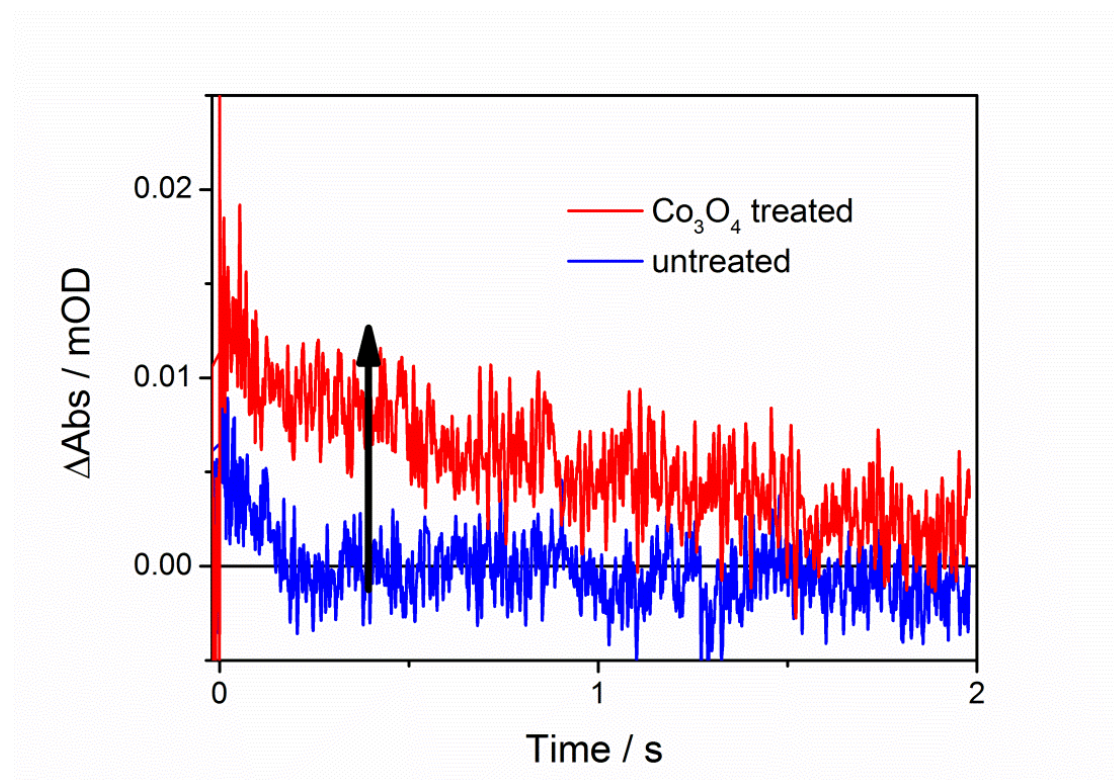


Figure S 5-12: Dynamics of surface-accumulated photogenerated holes in untreated (blue) and Co₃O₄ treated (red) thin (50 nm) hematite photoanodes at open circuit in 1 M NaOH, excited at 455 nm and probed at 650 nm, shown on a linear time-axis. The arrow indicates the increase in lifetime of photogenerated holes after treatment with Co₃O₄.

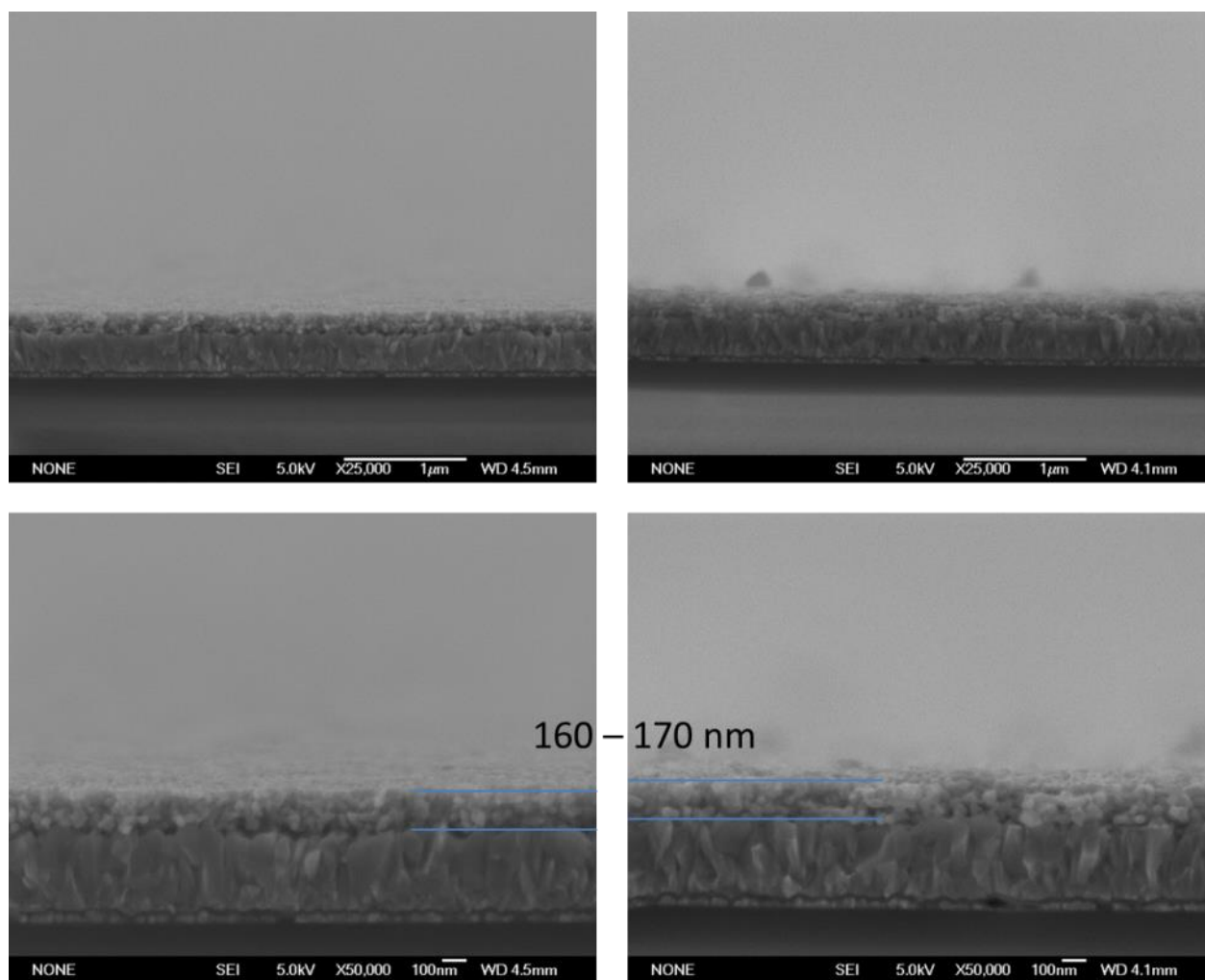


Figure S 5-13: SEM cross-section images of Sn-doped hematite films on FTO. The top row shows overview images indicating the homogeneous coverage of the film throughout a large area of the substrate. The bottom row shows higher magnification images in which the film thickness of both samples was determined to be about 160 – 170 nm.

5.6 References

1. Su, D.; Liu, H.; Ahn, H.; Wang, G., Synthesis of Highly Ordered Mesoporous Co₃O₄ for Gas Sensing. *Journal of nanoscience and nanotechnology* **2013**, *13* (5), 3354-3359.
2. Liu, D.; Wang, X.; Wang, X.; Tian, W.; Bando, Y.; Golberg, D., Co₃O₄ nanocages with highly exposed {110} facets for high-performance lithium storage. *Scientific reports* **2013**, *3*.
3. Lou, X. W.; Deng, D.; Lee, J. Y.; Feng, J.; Archer, L. A., Self-supported formation of needlelike Co₃O₄ nanotubes and their application as lithium-ion battery electrodes. *ADVANCED MATERIALS-DEERFIELD BEACH THEN WEINHEIM-* **2008**, *20* (2), 258.
4. Du, N.; Zhang, H.; Chen, B.; Wu, J.; Ma, X.; Liu, Z.; Zhang, Y.; Yang, D.; Huang, X.; Tu, J., Porous Co₃O₄ Nanotubes Derived From Co₄ (CO)₁₂ Clusters on Carbon Nanotube Templates: A Highly Efficient Material For Li-Battery Applications. *Advanced Materials* **2007**, *19* (24), 4505-4509.
5. Sun, C.; Li, F.; Ma, C.; Wang, Y.; Ren, Y.; Yang, W.; Ma, Z.; Li, J.; Chen, Y.; Kim, Y., Graphene-Co₃O₄ nanocomposite as an efficient bifunctional catalyst for lithium-air batteries. *Journal of Materials Chemistry A* **2014**, *2* (20), 7188-7196.
6. Wang, C.-A.; Li, S.; An, L., Hierarchically porous Co₃O₄ hollow spheres with tunable pore structure and enhanced catalytic activity. *Chemical Communications* **2013**, *49* (67), 7427-7429.
7. Xie, X.; Li, Y.; Liu, Z.-Q.; Haruta, M.; Shen, W., Low-temperature oxidation of CO catalysed by Co₃O₄ nanorods. *Nature* **2009**, *458* (7239), 746-749.
8. Xu, J.; Gao, P.; Zhao, T., Non-precious Co₃O₄ nano-rod electrocatalyst for oxygen reduction reaction in anion-exchange membrane fuel cells. *Energy & Environmental Science* **2012**, *5* (1), 5333-5339.
9. Chou, N. H.; Ross, P. N.; Bell, A. T.; Tilley, T. D., Comparison of Cobalt-based Nanoparticles as Electrocatalysts for Water Oxidation. *ChemSusChem* **2011**, *4* (11), 1566-1569.
10. Kanan, M. W.; Nocera, D. G., In situ formation of an oxygen-evolving catalyst in neutral water containing phosphate and Co²⁺. *Science (New York, N.Y.)* **2008**, *321* (5892), 1072-1075.
11. Barroso, M.; Mesa, C. A.; Pendlebury, S. R.; Cowan, A. J.; Hisatomi, T.; Sivula, K.; Grätzel, M.; Klug, D. R.; Durrant, J. R., Dynamics of photogenerated holes in surface

modified α -Fe₂O₃ photoanodes for solar water splitting. *Proceedings of the National Academy of Sciences* **2012**, *109* (39), 15640-15645.

12. Klahr, B.; Gimenez, S.; Fabregat-Santiago, F.; Bisquert, J.; Hamann, T. W., Photoelectrochemical and impedance spectroscopic investigation of water oxidation with “Co–Pi”-coated hematite electrodes. *Journal of the American Chemical Society* **2012**, *134* (40), 16693-16700.

13. Zhong, D. K.; Gamelin, D. R., Photoelectrochemical water oxidation by cobalt catalyst (“Co– Pi”)/ α -Fe₂O₃ composite photoanodes: Oxygen evolution and resolution of a kinetic bottleneck. *Journal of the American Chemical Society* **2010**, *132* (12), 4202-4207.

14. Zhong, D. K.; Sun, J.; Inumaru, H.; Gamelin, D. R., Solar water oxidation by composite catalyst/ α -Fe₂O₃ photoanodes. *Journal of the American Chemical Society* **2009**, *131* (17), 6086-6087.

15. Artero, V.; Chavarot-Kerlidou, M.; Fontecave, M., Splitting water with cobalt. *Angewandte Chemie International Edition* **2011**, *50* (32), 7238-7266.

16. Cummings, C. Y.; Marken, F.; Peter, L. M.; Tahir, A. A.; Wijayantha, K. G. U., Kinetics and mechanism of light-driven oxygen evolution at thin film [small α]-Fe₂O₃ electrodes. *Chemical Communications* **2012**, *48* (14), 2027-2029.

17. Riha, S. C.; Klahr, B. M.; Tyo, E. C.; Seifert, S. n.; Vajda, S.; Pellin, M. J.; Hamann, T. W.; Martinson, A. B., Atomic layer deposition of a submonolayer catalyst for the enhanced photoelectrochemical performance of water oxidation with hematite. *ACS nano* **2013**, *7* (3), 2396-2405.

18. Blakemore, J. D.; Gray, H. B.; Winkler, J. R.; Müller, A. M., Co₃O₄ nanoparticle water-oxidation catalysts made by pulsed-laser ablation in liquids. *ACS Catalysis* **2013**, *3* (11), 2497-2500.

19. Jiao, F.; Frei, H., Nanostructured Cobalt Oxide Clusters in Mesoporous Silica as Efficient Oxygen-Evolving Catalysts. *Angewandte Chemie International Edition* **2009**, *48* (10), 1841-1844.

20. Xi, L.; Tran, P. D.; Chiam, S. Y.; Bassi, P. S.; Mak, W. F.; Mulmudi, H. K.; Batabyal, S. K.; Barber, J.; Loo, J. S. C.; Wong, L. H., Co₃O₄-decorated hematite nanorods as an effective photoanode for solar water oxidation. *The Journal of Physical Chemistry C* **2012**, *116* (26), 13884-13889.

21. Hamann, T. W., Splitting water with rust: hematite photoelectrochemistry. *Dalton Transactions* **2012**, *41* (26), 7830-7834.

22. Lin, Y.; Yuan, G.; Sheehan, S.; Zhou, S.; Wang, D., Hematite-based solar water splitting: challenges and opportunities. *Energy & Environmental Science* **2011**, *4* (12), 4862-4869.
23. Sivula, K.; Le Formal, F.; Grätzel, M., Solar Water Splitting: Progress Using Hematite (α -Fe₂O₃) Photoelectrodes. *ChemSusChem* **2011**, *4* (4), 432-449.
24. Katz, M. J.; Riha, S. C.; Jeong, N. C.; Martinson, A. B.; Farha, O. K.; Hupp, J. T., Toward solar fuels: Water splitting with sunlight and “rust”? *Coordination Chemistry Reviews* **2012**, *256* (21), 2521-2529.
25. Bolton, J. R.; Strickler, S. J.; Connolly, J. S., Limiting and realizable efficiencies of solar photolysis of water. *Nature* **1985**, *316* (6028), 495-500.
26. Brillet, J.; Yum, J.-H.; Cornuz, M.; Hisatomi, T.; Solarska, R.; Augustynski, J.; Graetzel, M.; Sivula, K., Highly efficient water splitting by a dual-absorber tandem cell. *Nat. Photonics* **2012**, *6* (12), 824-828.
27. Pendlebury, S. R.; Cowan, A. J.; Barroso, M.; Sivula, K.; Ye, J.; Grätzel, M.; Klug, D. R.; Tang, J.; Durrant, J. R., Correlating long-lived photogenerated hole populations with photocurrent densities in hematite water oxidation photoanodes. *Energy & Environmental Science* **2012**, *5* (4), 6304-6312.
28. Cesar, I.; Kay, A.; Gonzalez Martinez, J. A.; Grätzel, M., Translucent thin film Fe₂O₃ photoanodes for efficient water splitting by sunlight: nanostructure-directing effect of Si-doping. *Journal of the American Chemical Society* **2006**, *128* (14), 4582-4583.
29. Kay, A.; Cesar, I.; Grätzel, M., New benchmark for water photooxidation by nanostructured α -Fe₂O₃ films. *Journal of the American Chemical Society* **2006**, *128* (49), 15714-15721.
30. Le Formal, F.; Pendlebury, S. R.; Cornuz, M.; Tilley, S. D.; Grätzel, M.; Durrant, J. R., Back electron-hole recombination in hematite photoanodes for water splitting. *Journal of the American Chemical Society* **2014**, *136* (6), 2564-2574.
31. Gamelin, D. R., Water splitting: Catalyst or spectator? *Nature chemistry* **2012**, *4* (12), 965-967.
32. Peter, L. M.; Wijayantha, K. U.; Tahir, A. A., Kinetics of light-driven oxygen evolution at α -Fe₂O₃ electrodes. *Faraday discussions* **2012**, *155*, 309-322.
33. Liang, Y.; Li, Y.; Wang, H.; Zhou, J.; Wang, J.; Regier, T.; Dai, H., Co₃O₄ nanocrystals on graphene as a synergistic catalyst for oxygen reduction reaction. *Nature materials* **2011**, *10* (10), 780-786.

34. Zhuo, L.; Ge, J.; Cao, L.; Tang, B., Solvothermal synthesis of CoO, Co₃O₄, Ni (OH)₂ and Mg (OH)₂ nanotubes. *Crystal Growth and Design* **2008**, *9* (1), 1-6.
35. He, T.; Chen, D.; Jiao, X.; Wang, Y., Co₃O₄ Nanoboxes: Surfactant-Templated Fabrication and Microstructure Characterization. *Advanced Materials* **2006**, *18* (8), 1078-1082.
36. Staniuk, M.; Hirsch, O.; Kränzlin, N.; Böhlen, R.; van Beek, W.; Abdala, P. M.; Koziej, D., Puzzling Mechanism behind a Simple Synthesis of Cobalt and Cobalt Oxide Nanoparticles: In Situ Synchrotron X-ray Absorption and Diffraction Studies. *Chemistry of Materials* **2014**, *26* (6), 2086-2094.
37. Farhadi, S.; Safabakhsh, J.; Zaringhadam, P., Synthesis, characterization, and investigation of optical and magnetic properties of cobalt oxide (Co₃O₄) nanoparticles. *Journal of Nanostructure in Chemistry* **2013**, *3* (1), 1-9.
38. **!!! INVALID CITATION !!!**
39. Shi, N.; Cheng, W.; Zhou, H.; Fan, T.; Niederberger, M., Facile synthesis of monodisperse Co₃O₄ quantum dots with efficient oxygen evolution activity. *Chemical Communications* **2015**, *51* (7), 1338-1340.
40. Feckl, J. M.; Fominykh, K.; Döblinger, M.; Fattakhova-Rohlfing, D.; Bein, T., Nanoscale porous framework of lithium titanate for ultrafast lithium insertion. *Angewandte Chemie International Edition* **2012**, *51* (30), 7459-7463.
41. Fominykh, K.; Feckl, J. M.; Sicklinger, J.; Döblinger, M.; Böcklein, S.; Ziegler, J.; Peter, L.; Rathousky, J.; Scheidt, E. W.; Bein, T., Ultrasmall Dispersible Crystalline Nickel Oxide Nanoparticles as High-Performance Catalysts for Electrochemical Water Splitting. *Advanced Functional Materials* **2014**, *24* (21), 3123-3129.
42. Szeifert, J. M.; Feckl, J. M.; Fattakhova-Rohlfing, D.; Liu, Y.; Kalousek, V.; Rathousky, J.; Bein, T., Ultrasmall titania nanocrystals and their direct assembly into mesoporous structures showing fast lithium insertion. *Journal of the American Chemical Society* **2010**, *132* (36), 12605-12611.
43. Liu, Y.; Szeifert, J. M.; Feckl, J. M.; Mandlmeier, B.; Rathousky, J.; Hayden, O.; Fattakhova-Rohlfing, D.; Bein, T., Niobium-doped titania nanoparticles: Synthesis and assembly into mesoporous films and electrical conductivity. *ACS nano* **2010**, *4* (9), 5373-5381.

44. Fominykh, K.; Chernev, P.; Zaharieva, I.; Sicklinger, J.; Stefanic, G.; Döblinger, M.; Müller, A.; Pokharel, A.; Böcklein, S.; Scheu, C., Iron-Doped Nickel Oxide Nanocrystals as Highly Efficient Electrocatalysts for Alkaline Water Splitting. *ACS nano* **2015**.
45. Peters, K.; Zeller, P.; Stefanic, G.; Skoromets, V.; Němec, H.; Kužel, P.; Fattakhova-Rohlfing, D., Water-dispersible small monodisperse electrically conducting antimony doped tin oxide nanoparticles. *Chemistry of Materials* **2015**, *27* (3), 1090-1099.
46. Hadjiev, V.; Iliev, M.; Vergilov, I., The Raman spectra of Co₃O₄. *Journal of Physics C: Solid State Physics* **1988**, *21* (7), L199.
47. Biesinger, M. C.; Payne, B. P.; Grosvenor, A. P.; Lau, L. W.; Gerson, A. R.; Smart, R. S. C., Resolving surface chemical states in XPS analysis of first row transition metals, oxides and hydroxides: Cr, Mn, Fe, Co and Ni. *Applied Surface Science* **2011**, *257* (7), 2717-2730.
48. Dunn, H. K.; Feckl, J. M.; Muller, A.; Fattakhova-Rohlfing, D.; Morehead, S. G.; Roos, J.; Peter, L. M.; Scheu, C.; Bein, T., Tin doping speeds up hole transfer during light-driven water oxidation at hematite photoanodes. *Physical Chemistry Chemical Physics* **2014**, *16* (44), 24610-24620.
49. Cesar, I.; Sivula, K.; Kay, A.; Zboril, R.; Grätzel, M., Influence of Feature Size, Film Thickness, and Silicon Doping on the Performance of Nanostructured Hematite Photoanodes for Solar Water Splitting. *The Journal of Physical Chemistry C* **2008**, *113* (2), 772-782.
50. Sivula, K.; Zboril, R.; Le Formal, F.; Robert, R.; Weidenkaff, A.; Tucek, J.; Frydrych, J.; Grätzel, M., Photoelectrochemical Water Splitting with Mesoporous Hematite Prepared by a Solution-Based Colloidal Approach. *J. Am. Chem. Soc.* **2010**, *132* (21), 7436-7444.
51. McDonald, K. J.; Choi, K.-S., Synthesis and photoelectrochemical properties of Fe₂O₃/ZnFe₂O₄ composite photoanodes for use in solar water oxidation. *Chemistry of Materials* **2011**, *23* (21), 4863-4869.
52. Sauerbrey, G., Use of quartz vibration for weighing thin films on a microbalance. *J. Physik* **1959**, *155*, 206-212.
53. Esswein, A. J.; McMurdo, M. J.; Ross, P. N.; Bell, A. T.; Tilley, T. D., Size-dependent activity of Co₃O₄ nanoparticle anodes for alkaline water electrolysis. *The Journal of Physical Chemistry C* **2009**, *113* (33), 15068-15072.
54. Trotochaud, L.; Ranney, J. K.; Williams, K. N.; Boettcher, S. W., Solution-cast metal oxide thin film electrocatalysts for oxygen evolution. *Journal of the American Chemical Society* **2012**, *134* (41), 17253-17261.

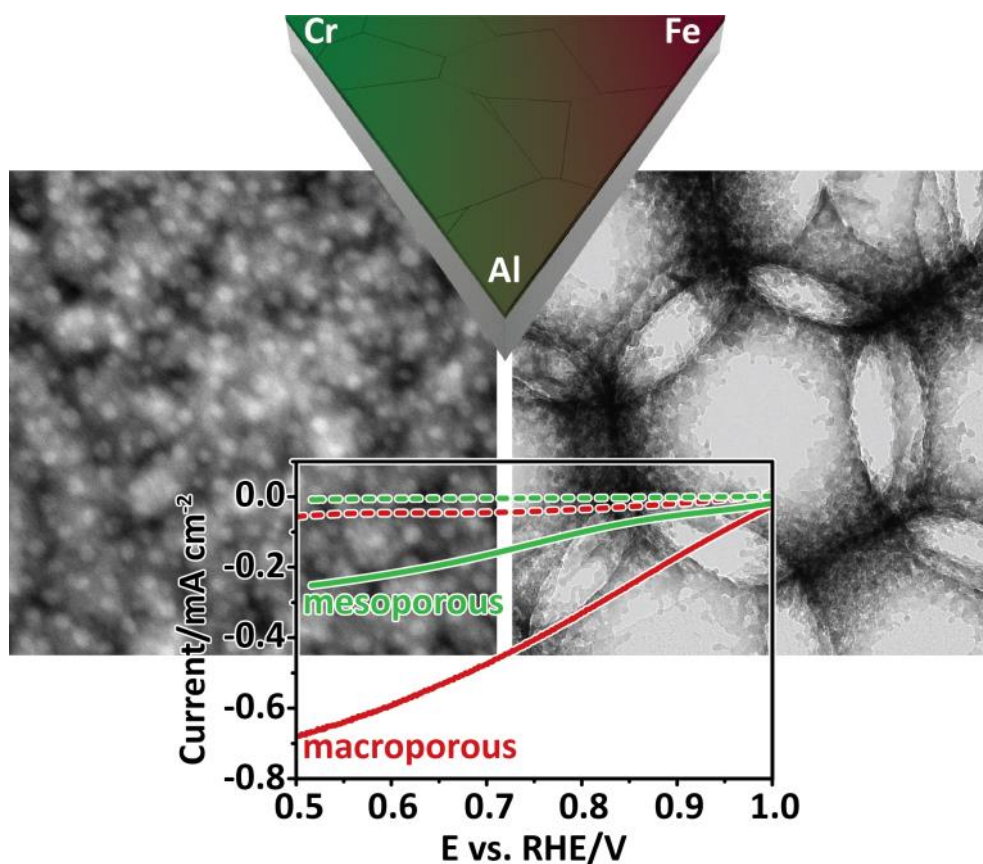
55. Lin, F.; Boettcher, S. W., Adaptive semiconductor/electrocatalyst junctions in water-splitting photoanodes. *nature materials* **2014**, *13* (1), 81-86.
56. Mills, T. J.; Lin, F.; Boettcher, S. W., Theory and simulations of electrocatalyst-coated semiconductor electrodes for solar water splitting. *Physical review letters* **2014**, *112* (14), 148304.
57. Yang, X.; Du, C.; Liu, R.; Xie, J.; Wang, D., Balancing photovoltage generation and charge-transfer enhancement for catalyst-decorated photoelectrochemical water splitting: A case study of the hematite/MnO_x combination. *Journal of Catalysis* **2013**, *304*, 86-91.
58. Sodergren, S.; Hagfeldt, A.; Olsson, J.; Lindquist, S. E., Theoretical models for the action spectrum and the current-voltage characteristics of microporous semiconductor films in photoelectrochemical cells. *J. Phys. Chem.* **1994**, *98*, 5552 - 5555.

6 Nanostructured ternary FeCrAl oxide photocathodes for water photoelectrolysis

This chapter is based on the following publication:

Ilina Kondofersky*, Alexander Müller*, Halina K. Dunn, Alesja Ivanova, Goran Štefanić, Martin Ehrensperger, Christina Scheu, Bruce A. Parkinson, Dina Fattakhova-Rohlfing and Thomas Bein, *J. Am. Chem. Soc.*, **2016**, 138(6), 1860-1867.

*These authors contributed equally.



Abstract

A sol-gel method for the synthesis of semiconducting FeCrAl oxide photocathodes for solar-driven hydrogen production was developed and applied for the production of meso- and macroporous layers with the overall stoichiometry $\text{Fe}_{0.84}\text{Cr}_{1.0}\text{Al}_{0.16}\text{O}_3$. Using transmission

electron microscopy and energy-dispersive X-ray spectroscopy, phase separation into Fe- and Cr-rich phases was observed for both morphologies. Compared to prior work and to the mesoporous layer, the macroporous FeCrAl oxide photocathode had a significantly enhanced photoelectrolysis performance, even at a very early onset potential of 1.1 V vs. RHE. By optimizing the macroporous electrodes, the device reached current densities of up to 0.68 mA cm^{-2} at 0.5 V vs. RHE under AM 1.5 with an incident photon to current efficiency (IPCE) of 28 % at 400 nm without the use of catalysts. Based on transient measurements, this performance increase could be attributed to improved collection efficiency. At a potential of 0.75 V vs. RHE, an electron transfer efficiency of 48.5 % was determined.

6.1 Introduction

Solar energy is becoming increasingly important as an abundant and renewable energy source and the photoelectrolysis of water using illuminated semiconductor electrodes is considered an important technology for the generation of hydrogen in a sustainable and efficient way.¹ The most critical issue for the development of photoelectrolysis cells is the development of suitable photoabsorber materials that combine stability and efficient solar light harvesting with fast kinetics of the interfacial water splitting reactions.² To date, numerous material systems have been investigated. Among those more intensively studied as photoanode materials are BiVO_4 ³, $\alpha\text{-Fe}_2\text{O}_3$ ⁴, WO_3 ⁵ and TiO_2 ⁶ and, as photocathode materials, p-Si⁷, Cu_2O ⁸ or CuFeO_2 ⁹. However, in spite of significant efforts, the progress towards efficient solar water splitting systems has been slow. The efficiency of all known photoabsorbers is limited by factors such as poor light harvesting, losses caused by inefficient electron-hole pair separation, bulk and interfacial recombination or high overpotentials for the overall water splitting reaction and instability of the photoelectrodes. Consequently, discovering and optimizing novel photoabsorber materials is important for the development of competitive

photoelectrochemical cells. This is a very demanding task due to the practically unlimited number of potential material classes and elemental combinations. An extremely powerful approach is offered by high-throughput theoretical¹⁰⁻¹¹ and experimental¹²⁻¹⁸ screening methods. However, the identification of promising materials with specific stoichiometries is only the first step and, aided by characterization and increasing understanding of material properties, synthesis strategies have to be refined to obtain electrodes with optimized compositions and morphologies.

Recently, the Solar Hydrogen Activity research Kit (SHArK) project, a distributed science research project¹⁹ identified a p-type ternary oxide semiconductor containing the earth-abundant and inexpensive elements Fe, Cr and Al. Combinatorial optimization identified the highest photoelectrolysis activity for the hydrogen evolution reaction at a stoichiometry near $\text{Fe}_{0.84}\text{Cr}_{1.0}\text{Al}_{0.16}\text{O}_3$. The discovered material features a band gap of 1.8 eV. While the incident photon-to-charge-carrier efficiency (IPCE) of around $1 \times 10^{-4} \%$ at 500 nm is very low, a promising photovoltage of around 0.95 V was reached. Sliozberg *et al.*²⁰ obtained higher photocurrents of $10 \mu\text{A cm}^{-2}$ at 0.5 V vs. RHE under AM 1.5 with an IPCE of 0.3 % at 350 nm by depositing thicker films using reactive magnetron co-sputtering, demonstrating that the performance of this material can be improved by employing different fabrication routes.

Inspired by the potential of this recently discovered material, we focused on the development of large-scale photocathode morphologies based on ternary FeCrAl oxides. We report a sol-gel synthesis method that yielded mesoporous thin films with photocurrents of 0.25 mA cm^{-2} at 1.23 V vs RHE and an early photocurrent onset at 1.1 V vs. RHE. The performance can be improved further by introducing a template and synthesizing a periodic, porous inverse-opal structure. After optimization, a photocurrent of 0.68 mA cm^{-2} under AM 1.5 illumination with an IPCE of 28 % at 400 nm was reached while retaining the early onset potential. We also

describe extensive structural and electrochemical studies aimed at understanding the correlation between synthesis conditions, structure and photoelectrochemical behavior of the novel material.

6.2 Results and Discussion

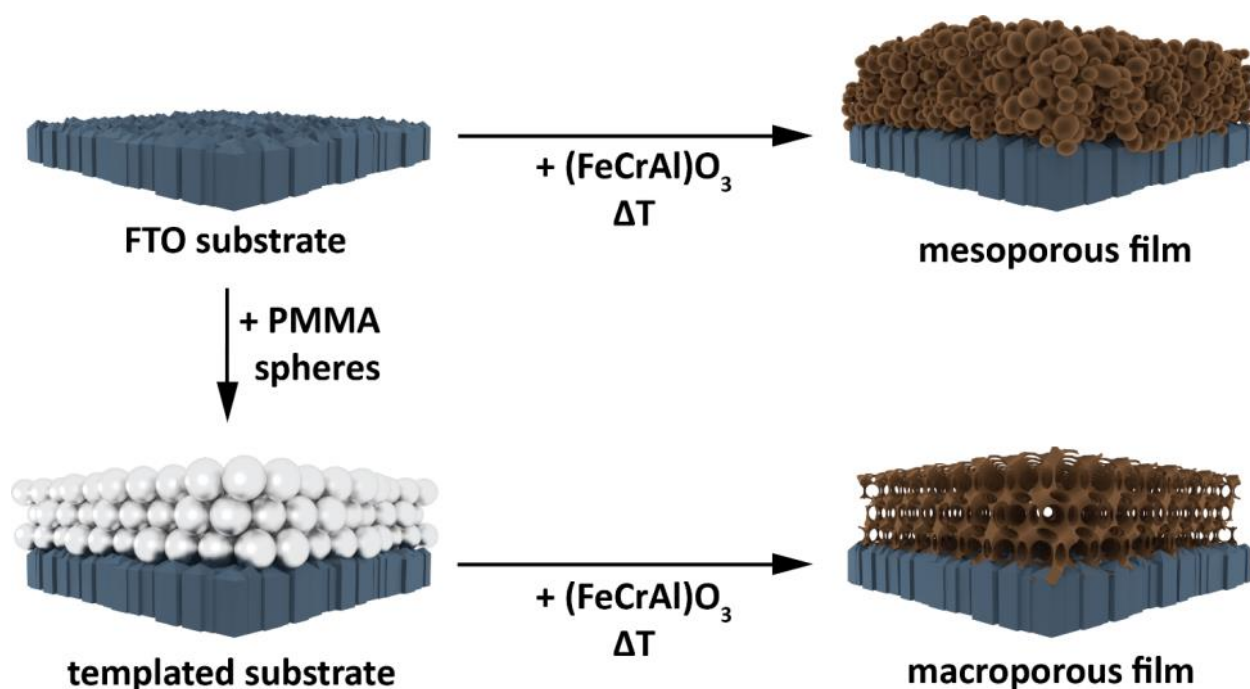


Figure 6-1: Scheme by which mesoporous and macroporous films were synthesized.

FeCrAl oxide photocathodes were synthesized via a sol-gel route (Figure 6-1). Precursor solutions were prepared by dissolving the nitrate salts of Fe^{3+} , Cr^{3+} and Al^{3+} in ethanol in a ratio of 0.43:0.5:0.08. This stoichiometry was discovered via a combinatorial optimization approach and reported to yield the highest IPCE values¹⁹. The electrodes obtained by spin-coating a freshly prepared precursor solution onto FTO and calcining in air at 525 °C are mesoporous and crack-free.

X-ray diffraction patterns of the mesoporous films can be indexed by a single phase with the corundum structure and the space group R-3c. Secondary phases with other crystal structure

6. Results and Discussion

were not found. The lattice parameters were obtained by a Le Bail²¹ refinement (Figure S 6-12) as $a = 4.9832(1) \text{ \AA}$ and $c = 13.6143(3) \text{ \AA}$. This is in excellent agreement (deviation < 1%) with the lattice parameters obtained by Rowley *et al.*¹⁹

Although XRD analysis of the powder material points to the formation of a single phase, cross section TEM analysis of the films surprisingly reveals a phase separation (Figure 6-2). The different phases found in TEM could not be resolved by XRD, indicating that both phases form in the corundum structure and have very similar lattice parameters. This was also confirmed by HRTEM and FFT measurements. Near the FTO substrate, a Cr-rich phase with an average Fe:Cr:Al ratio of $(20 \pm 4:75 \pm 5:5 \pm 1)$ at-% forms columnar grains with a size of up to 250 nm in the corundum structure. Above this region, a mesoporous network of Fe-rich nanoparticles with an average composition of Fe:Cr:Al = $(59 \pm 7:18 \pm 4:23 \pm 6)$ at-% is formed. These, also can be separated into large ellipsoid nanoparticles with a diameter of (5.6 ± 0.8) nm decorated with small spherical nanoparticles with a diameter of (1.5 ± 0.2) nm (Figure S 6-14). The chemical composition of these particles is slightly different, as the small particles are Al-enriched (Fe:Cr:Al ratio of $(71 \pm 4:9 \pm 4:21 \pm 6)$ at-%) whereas the large particles have a Fe:Cr:Al ratio of $(76 \pm 6:11 \pm 2:13 \pm 4)$ at-%).

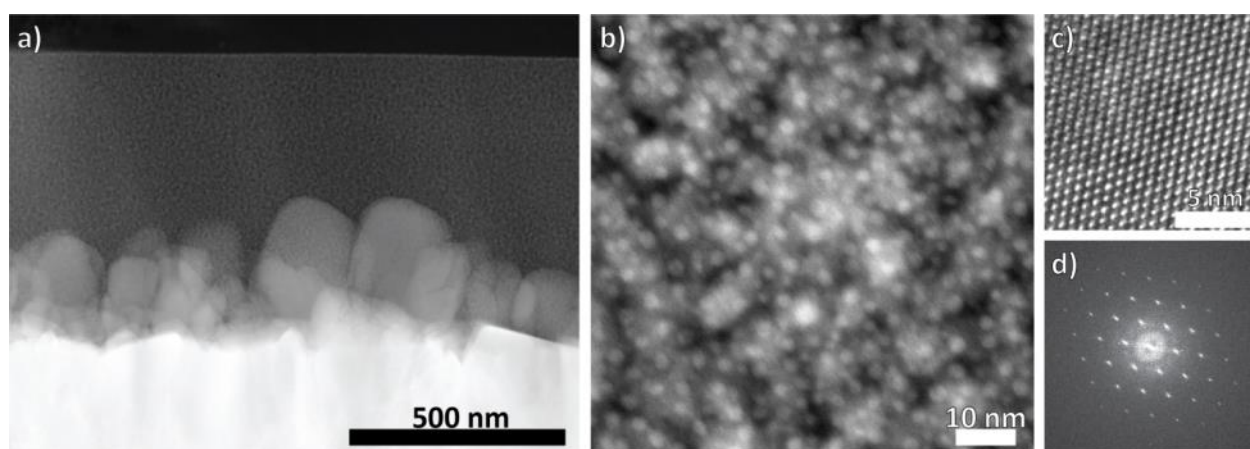


Figure 6-2: TEM images of the mesoporous FeCrAl oxide film. a) shows a cross section overview image, b) an image of the nanoparticles in the Fe-rich region. In c) and d), a HRTEM image and the corresponding FFT of the Cr-rich phase are shown. The image shows the (001) plane.

X-ray photoelectron spectroscopy was used to detect signals of iron, chromium and aluminum of the upper, Fe-rich layer of a 500 nm thick, mesoporous FeCrAl oxide film (Figure 6-3). Peak positions and shapes indicate an oxidation state of +3 for all metal ions. Assignment of the chemical species was done according to Moulder *et al.*²² Quantification yielded a Fe:Cr:Al ratio of 55:17:28, which is in good agreement with the EDX results. The valence state of Fe was estimated as +3 by comparing the energy positions of the 2p 3/2 peaks to those of the pure oxides²³ (Figure 6-3). In a similar fashion, the energy position of the Cr 2p 3/2 peak is characteristic for the oxidation state +3²³⁻²⁴. The broadening of the peak can be explained either by a shake-up peak or by trace elements of Cr in a higher oxidation state²³. As Cr⁴⁺ and Cr⁵⁺ compounds are unstable²⁵, Cr⁶⁺ would be most likely, even though the energy shift is not as big as with reference Cr⁶⁺-containing compounds. Further, no distinct Cr⁶⁺-containing compounds were found by XRD or TEM, making a shake-up peak and therefore Cr in the oxidation state +3 most likely. Despite the poor energy resolution and the small signal-to-noise ratio, the position of the Al 2p peak supports an Al³⁺-containing oxide²⁶. The valence state +3 can therefore be verified for Fe, Cr and Al in the upper region of the film.

6. Results and Discussion

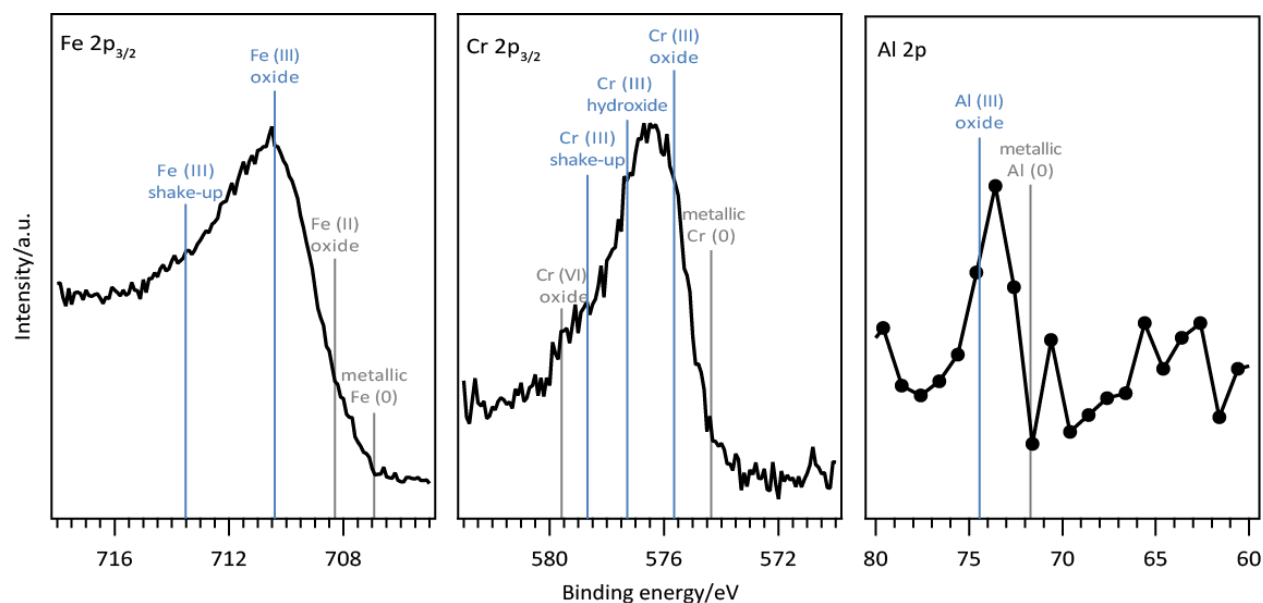


Figure 6-3: X-ray photoelectron spectra of the Fe $2p_{3/2}$, Cr $2p_{3/2}$ and Al $2p$ edges of the Fe-rich phase in the mesoporous film.

The separation into different phases, all in the corundum structure, is in contrast to previous experimental work, as Steinwehr *et al.* showed that FeCrAl oxides form solid solutions with a miscibility gap only at high Al-contents²⁷. The formation of large, compact Cr-rich nanoparticles at the FTO indicates that a heterogeneous nucleation takes place before other phases form. In accordance, the precursor $\text{Cr}(\text{NO}_3)_3 \cdot 9\text{H}_2\text{O}$ is less stable than the other two and dissociates at $100\text{ }^\circ\text{C}$ ²⁸, whereas $\text{Fe}(\text{NO}_3)_3 \cdot 9\text{H}_2\text{O}$ ²⁹ and $\text{Al}(\text{NO}_3)_3 \cdot 9\text{H}_2\text{O}$ ³⁰ are stable up to $250\text{ }^\circ\text{C}$. While these temperatures neglect the influence of the solvent, the trend should stay the same, explaining the phase separation. As an alternative, we attempted aging the precursor solution, which lead to the spontaneous formation of small nanoparticles with a homogenous elemental distribution. Experimental details, SEM (Figure S 6-10), TEM (Figure S 6-8) and elemental composition information (Table S 6-1) is provided in the supporting information.

Films synthesized by depositing these nanoparticles onto FTO, however, lead to films with very low photocurrents (Figure S 6-9).

The photoelectrochemical characteristics of mesoporous FeCrAl oxide films of different thicknesses were determined in 0.1 M perchloric acid under AM 1.5 substrate illumination. As expected, the optical absorbance increases linearly with the film thickness (Figure S 6-11). The photocurrent densities follow a similar trend, increasing linearly with the thickness up to 0.25 mA cm^{-2} under AM 1.5 (Figure 6-4a) and an IPCE of 4.9 % at 350 nm (Figure 6-4b) for a 500 nm thick film. FeCrAl oxide shows a very early onset potential of 1.1 V vs. RHE for a 100 nm thin film. A shift to more negative onset potentials is observed for samples with increasing thickness reaching values of 1.05 V vs. RHE for a 500 nm sample. Further, increasing the film thickness leads to a saturation of the photocurrent. This limiting behavior is not observed for thin films of around 40 nm, where the current density remains constant independent of the illumination direction (Figure S 6-13). The generated charge carriers can be collected equally well regardless of the sample being illuminated through the substrate or the electrolyte side since most of the light is transmitted resulting in only a small gradient of carrier concentration across the film and a short path to be collected at the electrode/electrolyte interface. Thicker films have carriers created more deeply in the structure and rely on charge carrier transport issues over long distances across the loosely connected, individual particles.

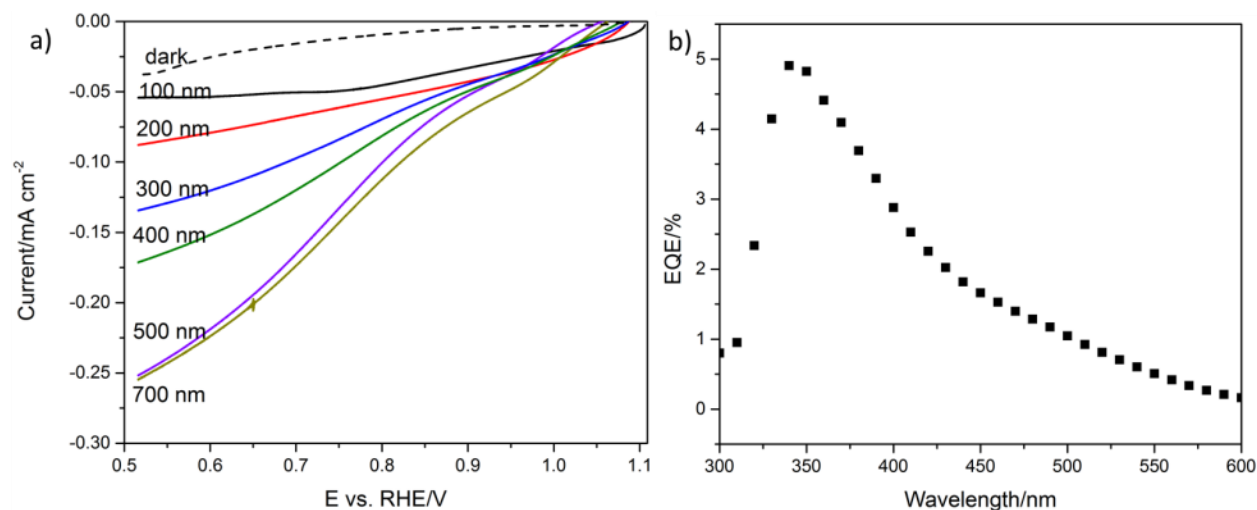


Figure 6-4: a) Linear sweep voltammograms for mesoporous FeCrAl oxide electrodes in dependence of the film thickness. The samples were illuminated through the substrate with AM 1.5. b) IPCE spectrum determined for a 500 nm thick mesoporous film on FTO. The drop in photocurrent at 350 nm is attributed to light absorption by the FTO substrate.

To enhance the performance, we optimized the electrode morphology by nanostructuring the material. Nanostructuring is a proven strategy for increasing the photogenerated carrier collection efficiency by decoupling the light absorption depth from the charge collection depth.³¹⁻³³ Periodic, macroporous morphologies are particularly attractive as they provide both a continuous scaffold for the transport of photogenerated charges to the current collector and a large surface for the heterogeneous charge transfer. Furthermore, the large pore size is beneficial for the infiltration of electrolyte throughout the whole film thickness, for the diffusion of products away from the semiconductor-electrolyte interface and for lowering the current density and thereby the overpotentials for electrode reactions. A so-called colloidal crystal templating approach was used to obtain macroporous FeCrAl oxide electrodes using periodic arrays of PMMA beads as a template.³⁴ The PMMA layers were assembled on FTO substrates, and impregnated with a freshly prepared sol-gel precursor solution via spin-

coating. Calcination leads to the crystallization of the precursors and to the combustion of the PMMA template, resulting in crystalline FeCrAl oxide films with a porous, highly periodic inverse opal structure (Figure 6-5) with the FeCrAl oxide forming a continuous semiconductor scaffold. The electrodes obtained in this way have a homogeneous thickness ranging from 1 to 6 μm , good coverage, and a good adhesion to the substrate (Figure 6-5a). The electrodes used for photoelectrochemical measurements were defined by a film thickness of approximately 3 μm , having the same light harvesting efficiency as the best performing mesoporous layers of 500 nm allowing a meaningful comparison for films with different morphologies (Figure S 6-15).

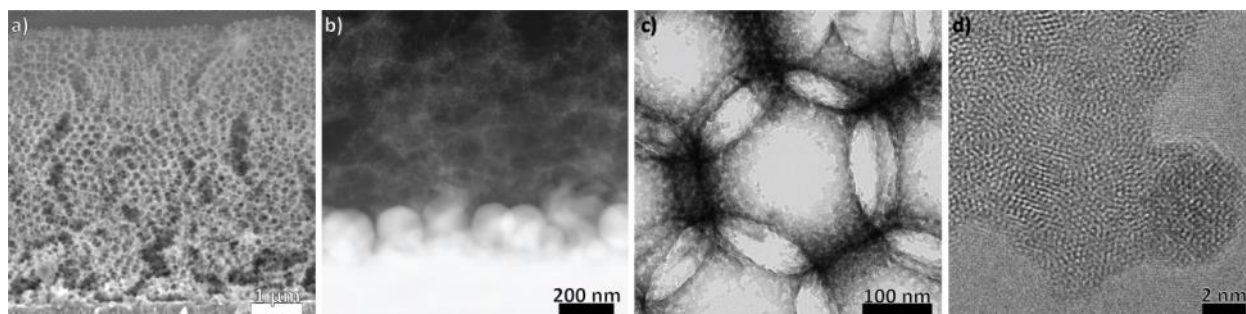


Figure 6-5: a) Cross-sectional SEM image of a macroporous film. b) Cross-sectional TEM image of a macroporous film showing the Cr-rich phase near the substrate. c) BF TEM image of a single pore. d) HRTEM image of a part of the network.

The average pore diameter of (277 ± 10) nm (Figure 6-5c) corresponds to a shrinkage by ca. 9 % during the calcination process to which we attribute the few defects shown in Figure 6-5a. Like in the mesoporous film, a phase segregation into a Cr-rich phase near the interface with an average composition of $\text{Fe:Cr:Al} = (9\pm 3:90\pm 3:1\pm 1)$ at-% and a macroporous, Fe-rich phase with an average composition of $\text{Fe:Cr:Al} = (64\pm 1:25\pm 4:11\pm 5)$ at-% is observed. The Cr-rich phase forms round nanoparticles with a diameter between 60 and 340 nm. The average composition of the Fe-rich phase was the same over the thickness of the film and no

compositional gradients through the film thickness were detected. HRTEM images show the scaffold to be polycrystalline with small grains in the order of 2 to 4 nm. This leads to improved charge transport properties compared to the nanostructured films, where the individual nanoparticles are only partly connected and charge transport is more difficult.

The photoelectrochemical performance of the macroporous FeCrAl films is shown in Figure 6-6 and reveals a dramatic photocurrent increase over the mesoporous films. Compared to a 500 nm thick, mesoporous film, the current density is increased by over 60 % reaching a value of 0.68 mA cm^{-2} at 0.5 V vs. RHE. Once again of note is the early onset potential of 1.1 V vs. RHE. The IPCE of the macroporous film is also increased significantly throughout the whole wavelength range of 300 to 600 nm, reaching a maximum of 28 % at 400 nm (Figure 6-6b).

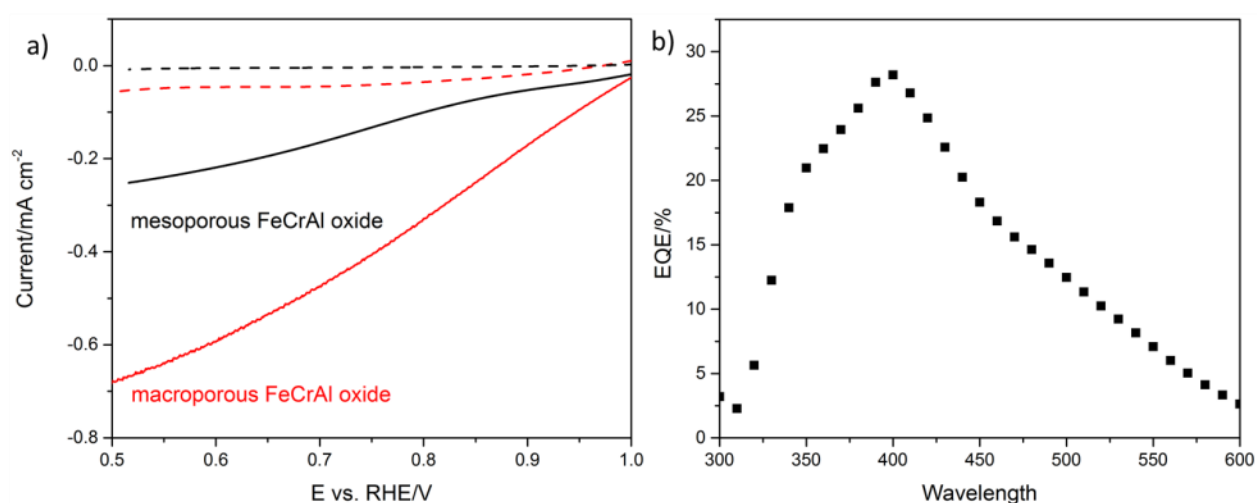


Figure 6-6: a) Linear sweep voltammograms of the macroporous FeCrAl films with AM 1.5 illumination through the substrate. Dashed curves are dark current sweeps. For comparison, the voltammogram of a 500 nm thick, mesoporous film is also shown. b) IPCE spectra determined for the same inverse opal FeCrAl film on FTO.

The IPCE maximum for macroporous films is redshifted to 400 nm, compared to the mesoporous film, which has a maximum at 350 nm. This shift is attributed to the inverse opal structure acting as a photonic crystal³⁵⁻³⁶, with transmission measurements (Figure SI 9) confirming a stop band centered at 380 nm. An additional shoulder at 350 nm is at the same position as the maximum measured for mesoporous films and can be attributed to the material itself. The drop at 350 nm is attributed to absorption of light by the FTO substrate.

The transfer efficiency of charges to the electrolyte η_{trans} can be assessed from transient current measurements. By illuminating the electrode with chopped light at different chopping frequencies and potentials, photocurrent transients can be measured. From them, the instantaneous current I_{Inst} and the steady-state current I_{ss} can be measured with the ratio of I_{Inst} and I_{ss} being a measure of the electron transfer efficiency η_{trans} .

As can be seen in Figure 6-7a, the shape of the transients is characteristic for the individual morphologies. The mesoporous sample is characterized by a spiky instantaneous current that decays to a constant steady-state current (Figure 6-7a). The transient current of the macroporous sample, on the other hand, shows an instantaneous current closer to the steady-state current, indicating a photocurrent response closer to the ideal square shape that is not limited by recombination. This observation is confirmed by determining the transfer efficiencies of both morphologies at different potentials. A 500 nm thick, mesoporous film shows a transfer efficiency of 12.5 % at 0.756 V vs. RHE. At this potential, at which the current density is 0.13 mA cm^{-2} , the transfer efficiency reaches a maximum. Under these conditions, the macroporous film has a transfer efficiency of 48.5 %, almost three times as high, indicating superior charge transport properties across the film and explaining the increased transfer efficiency in the macroporous films. The improved electron transfer efficiency has a major contribution to the increased photocurrent shown in Figure 6-6. The increased transfer efficiency indicates that recombination reactions in either the bulk and/or

on the surface are decreased. As the macroporous film has a higher surface area the surface recombination velocity should be higher and the increased transfer efficiency can be attributed to decreased bulk recombination due to the short carrier diffusion length. The short carrier diffusion length requires most photogenerated carriers to be produced in a region where there is a space charge field to separate them. In a more two dimensional geometry, with the rather low absorption coefficients especially in the red region of the spectrum, most carriers are generated in the bulk of the grains and recombine before they can diffuse to a space charge region. In the macroporous films, the carriers are very likely to be created in or near a region with a space charge field formed by the electrolyte/semiconductor interface. Therefore there is a higher probability that they will be collected as photocurrent especially in the spectral regions with low absorption coefficients.

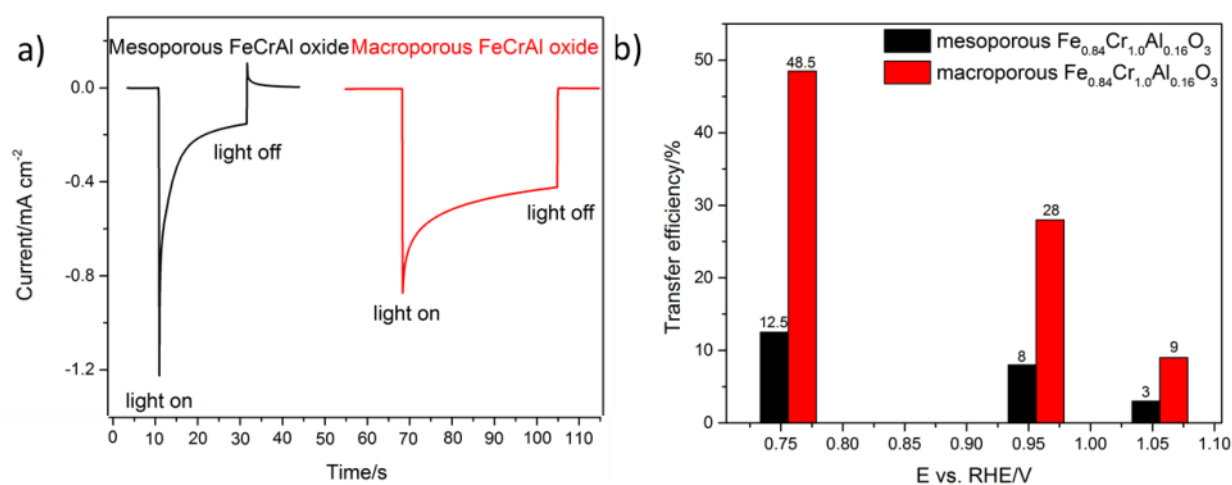


Figure 6-7: a) Photocurrent transients of a mesoporous and a macroporous FeCrAl oxide film. b) Collection efficiency η_{trans} determined for mesoporous and inverse opal macroporous FeCrAl oxide films by transient photocurrent response measurements. The samples were illuminated with a 455 nm diode through the substrate side.

The presence of metal oxide phases with different composition raises the question about the photoelectrochemical activity of each individual phase. Theoretical work by Praveen et al.³⁷ has shown that the band gap can be tuned between 2.5 and 3.1 eV by varying the Fe:Cr:Al ratio. Phase separation can therefore lead to the efficient absorption of large parts of the solar spectrum. In addition, both Cr- and Al-doping of hematite improve charge transport properties.³⁸⁻⁴⁰ Even the formation of the Cr-rich phase can enhance the properties, as Cr₂O₃ has been shown to act both as a catalyst and as an oxygen barrier, preventing the direct formation of water from hydrogen and oxygen.⁴¹⁻⁴²

Photoelectrochemical characterization of the electrodes revealed that the macroporous structure was not only beneficial for the device architecture, regarding the solid to electrolyte junction, but also proved beneficial for the charge transport across the metal oxide film. Macroporous structures show a nearly threefold increase of current density compared to the mesoporous FeCrAl oxide film, reaching values of up to 0.68 mA cm⁻² at 0.5 V vs. RHE under AM 1.5 without any additional catalysts. Compared to devices reported so far in literature, we demonstrate a 68-fold current density increase²⁰ as a result of introducing macropores. The main contribution to this electrochemical performance was achieved by the increased electron transfer efficiency to the electrolyte and therefore reduced recombination.

The macroporous FeCrAl oxide photoabsorber shows the highest currents not only for this particular system but, to our knowledge, also among the published metal oxide photocathodes. The best known example for a metal oxide photocathode, Cu₂O⁸, reaches current densities of about 0.8 mA cm⁻² at 0 V vs. RHE under uncatalyzed conditions with a photocurrent onset at 0.4 V vs. RHE. CuFeO₂⁹ on the other hand shows a current density of about 20 μA cm⁻¹ at 0 V vs. RHE in a non-oxygen saturated electrolyte with a photocurrent onset at about the same potential. In contrast, the macroporous FeCrAl oxide electrodes have a very early onset potential of 1.1 V vs RHE. At potentials at which we observe 0.68 mA cm⁻¹ (0.5 V vs. RHE)

very little photocurrent is observed for Cu_2O and CuFeO . This study therefore exemplifies the importance of finding and developing new promising metal oxides as photoelectrodes for water splitting.

6.3 Conclusion

We presented the synthesis and characterization of semiconducting FeCrAl oxide photocathodes with different porous morphologies and investigated them for solar-driven hydrogen evolution. Mesoporous FeCrAl oxide films with a photocurrent onset at 1.1 V vs. RHE were synthesized using a novel sol-gel synthesis to generate large area crack-free films that were characterized and had their thickness optimized to reach a current density of 0.25 mA cm^{-2} under AM 1.5 at 0.5 V vs. RHE with an IPCE of 4.9 %. EDX measurements performed in the TEM showed that a phase separation occurs, with a Cr oxide rich phase adjacent to the substrate and a Fe rich oxide phase on the top. Template synthesis of an inverse opal macroporous $\text{Fe}_{0.84}\text{Cr}_{1.0}\text{Al}_{0.16}\text{O}_3$ electrode drastically increased the photocurrent to 0.68 mA cm^{-2} under AM 1.5 at 0.5 V vs. RHE and an IPCE of 28 % at 400 nm without the use of hydrogen evolution catalysts. The collection of minority carriers at the semiconductor/electrolyte interface increased nearly 4 times compared to the optimized mesoporous electrode and are the highest reported so far for this novel material, showing that it is a promising candidate for photoelectrochemical water splitting. Further studies on different morphologies and architectures could additionally improve the device performance. This work shows the potential of nanostructured multinary mixed metal oxides as electrode materials for photoelectrochemical water splitting.

6.4 Experimental

Mesoporous FeCrAl oxide layers were prepared by dissolving the precursor salts $\text{Fe}(\text{NO}_3)_3 \cdot 9\text{H}_2\text{O}$, $\text{Cr}(\text{NO}_3)_3 \cdot 9\text{H}_2\text{O}$ and $\text{Al}(\text{NO}_3)_3 \cdot 9\text{H}_2\text{O}$ in ethanol, resulting in 0.5 M solutions. The precursor solutions were mixed in a ratio of 0.42 : 0.5 : 0.08, respectively, to achieve the targeted composition. This solution was spin coated (800 rpm for 30 s) onto fluorine-doped tin oxide glass, FTO (TEC 15 Glass, Dyesol), resulting in films that were calcined at 525 °C for 1.5 h (2 °C/min heat ramp).

Macroporous films were synthesized by pre-depositing polymethylmethacrylate (PMMA) spheres as a template. PMMA spheres with a diameter of 300 nm were prepared according to a procedure previously described by us⁴³⁻⁴⁴. In brief, the particles were synthesized by adding methylmethacrylate (MMA) (35.6 g, 0.35 mol) and sodium dodecylsulfate (SDS) (5 mg, 0.02 mmol) to deoxygenated water (98 mL) under nitrogen purging at 40 °C. The resulting emulsion was heated to 70 °C for 1 hour under reflux and vigorous stirring. The polymerization was initiated by adding potassium peroxydisulfate (56 mg, 0.2 mmol) dissolved in water (2 mL) and stopped after 2.5 hours by cooling the suspension to room temperature under atmospheric conditions. The resulting PMMA spheres were washed with water by centrifugation (19000 rpm, 20 min) and redispersed in water.

The FTO substrates were placed vertically in an aqueous PMMA solution (11 wt.-%) and the solution was dried over night at 70 °C. These templated films were infiltrated with the FeCrAl precursor solution via spin coating and calcined at 525 °C for 1.5 h (2 °C/min heat ramp).

6.5 Supporting Information

Alternative synthesis of FeCrAl oxide nanoparticles

6. Supporting Information

Aging of the FeCrAl oxide precursor solution by stirring under ambient conditions from 0 to 7 days leads to the spontaneous formation of nanoparticles. The resulting nanoparticles are around 1.5-2 nm in size after 3 days (Figure S 6-8a) and reach 5 nm after 7 days (Figure S 6-8b). TEM analysis revealed that the formed nanoparticles were already crystalline in solution without additional thermal treatment. Inductively coupled plasma atomic emission spectroscopy (ICP-AAS) analysis on the washed powder (Table S 6-1) revealed a composition of Fe:Cr:Al = 0.36:0.59:0.05, which is very close to the targeted composition of Fe:Cr:Al = 0.43:0.5:0.08. TEM-EDX analysis of several dozen individual nanoparticles shows a similar composition with a homogeneous distribution of the individual elements in each nanocrystal without any phase separation or surface enrichment. The spontaneous formation of a crystalline phase with the targeted composition provides important evidence that the metal oxide composition harnessed in a high-throughput experiment indeed corresponds to a new thermodynamically stable solid solution and not a mixture of individual oxides.

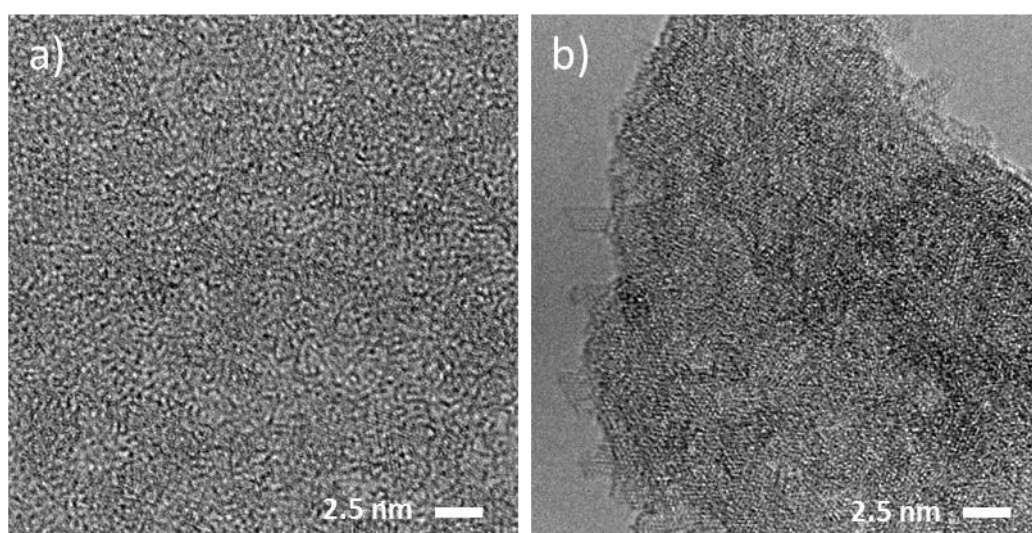


Figure S 6-8: TEM images of uncalcined FeCrAl nanoparticles formed in the precursor solution after a) 3 days and b) 7 days.

Table S 6-1: Elemental composition of FeCrAl oxide nanoparticles formed in the precursor solution. ICP-AAS and TEM-EDX analysis were performed with the particles to compare the element content.

Element	Targeted concentration	ICP-AAS (mol-%)	TEM-EDX (atomic-%)
Fe	0.84	0.72	89
Cr	1.00	1.17	99
Al	0.16	0.11	11

Although aging of the precursor solutions described above leads to a direct formation of targeted crystalline nanoparticles, the films prepared from these solutions show very low photocurrent of 1 nA cm^{-2} at 0.55 V vs. RHE (Figure S 6-9). The SEM images (Figure S 6-10) indicate that the films obtained after calcination of aged solutions deposited on FTO substrates are composed of large platelets with an average size of 400 nm and 40 nm thickness. The platelets are randomly oriented on the substrate exposing a large fraction of the FTO substrate. The poor coverage of the conducting substrate and poor electrical contact between the single platelets could account for the low electrode performance.

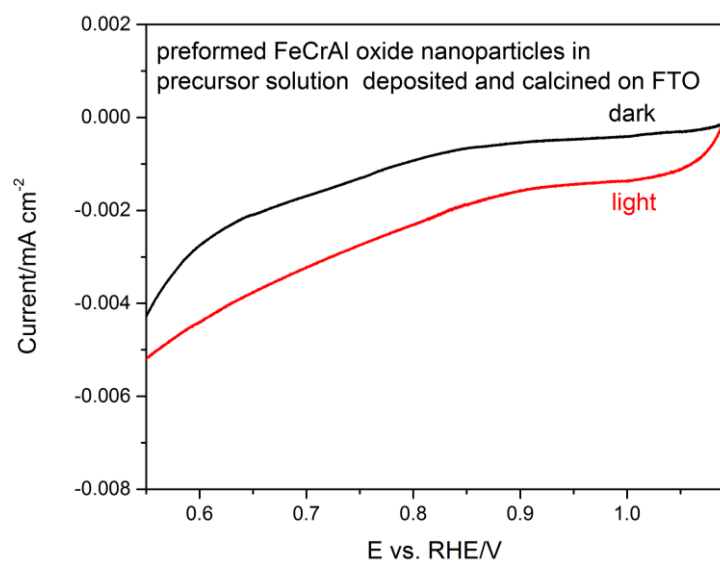


Figure S 6-9: Cyclic voltammetry curves for a calcined FeCrAl oxide film on FTO synthesized from preformed crystalline nanoparticles in the precursor solution. The photoelectrochemical measurements were performed under substrate illumination and AM 1.5 in 0.1 M perchloric acid as electrolyte.

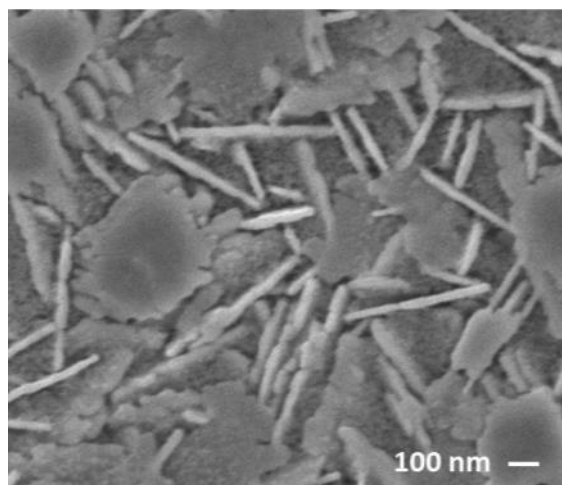


Figure S 6-10: SEM images of FeCrAl oxide films obtained from a precursor solution aged for 4 days. The precursor solution was deposited on FTO substrate via spin-coating and calcined at 525 °C.

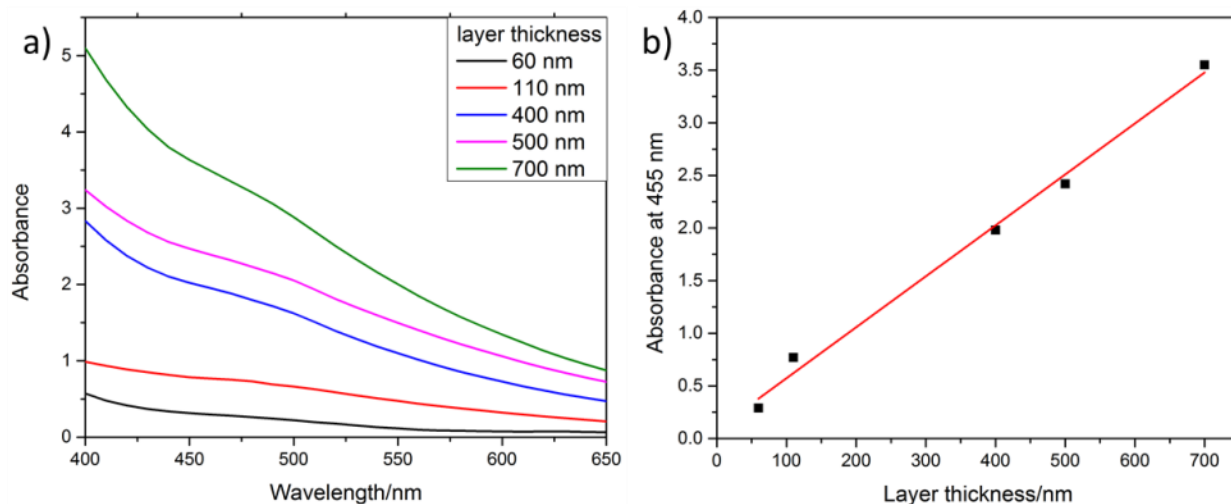


Figure S 6-11: a) Absorbance spectra of mesoporous FeCrAl oxide layers coated on FTO with increasing film thickness. b) Linear absorbance increase of FeCrAl oxide layers at 455 nm with film thickness.

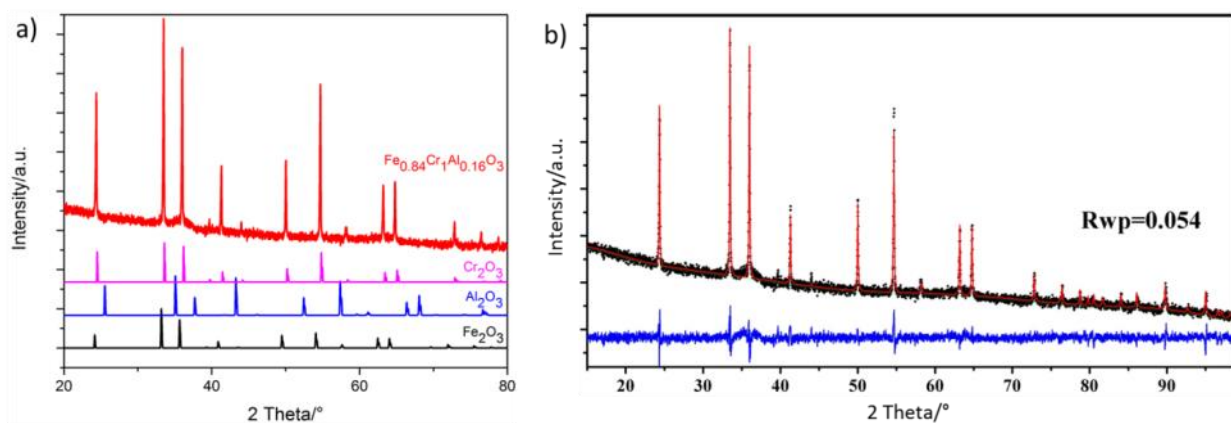


Figure S 6-12: a) Powder-XRD pattern of mesoporous FeCrAl oxide. The individual metal oxides Cr₂O₃ (ICDD card number 38-1479), Fe₂O₃ (ICDD card number 33-664) and Al₂O₃ (ICDD card number 46-1212) are shown for comparison. b) Results of the whole-powder-pattern profile refinement (Le Bail method). The observed intensity data are plotted in the upper field as ♦, the calculated pattern is shown as a red line in the same field, and the

6. Supporting Information

difference between the observed and calculated patterns is shown as a blue line in the lower field.

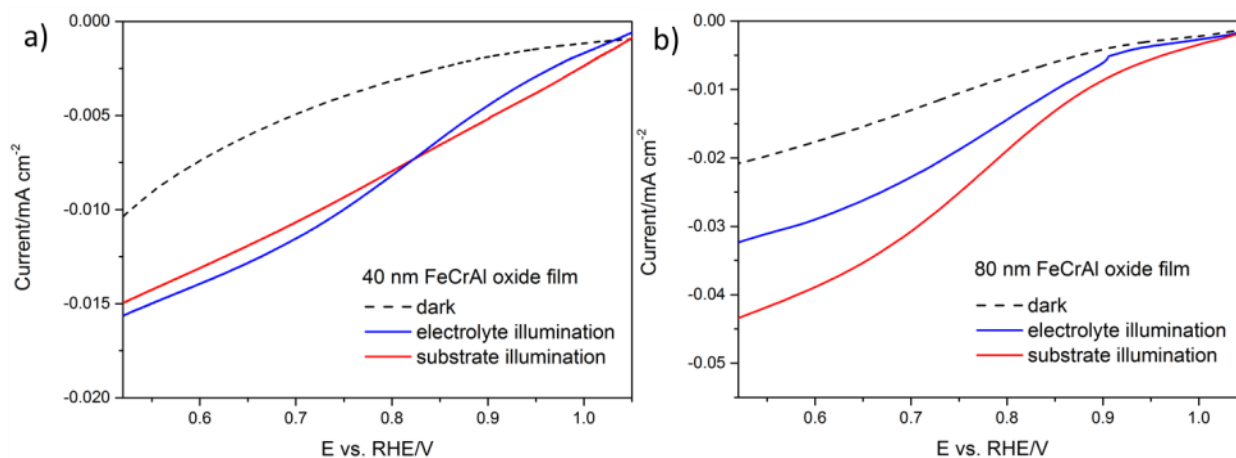


Figure S 6-13: Cyclic voltammetry curves for a) 40 nm and b) 80 nm mesoporous FeCrAl oxide films on FTO under electrolyte and substrate illumination. The photoelectrochemical measurements were performed under AM 1.5 in 0.1 M perchloric acid.

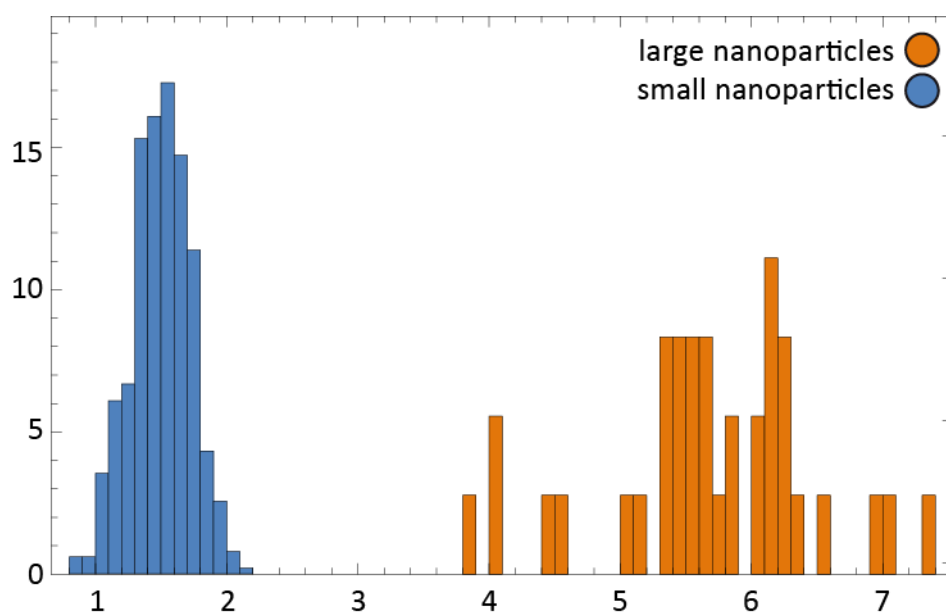


Figure S 6-14: TEM-based particle size distribution of the two different kinds of Fe-rich nanoparticles in a mesoporous FeCrAl oxide film.

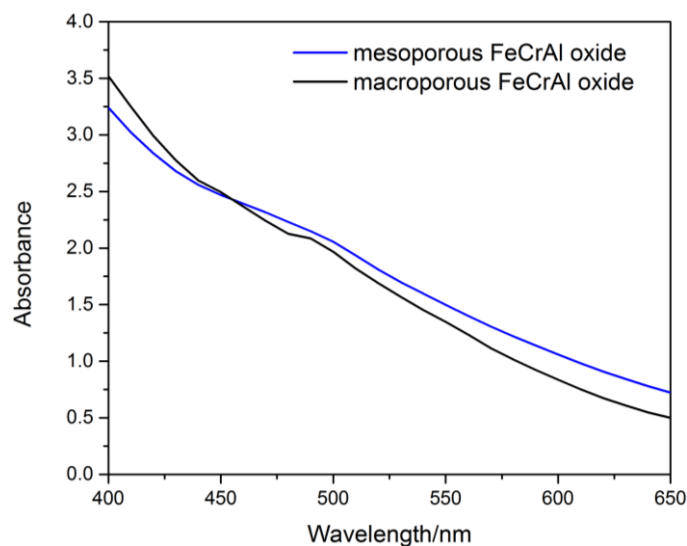


Figure S 6-15: Absorbance spectra of a 500 nm mesoporous and a 3 μm macroporous FeCrAl oxide film.

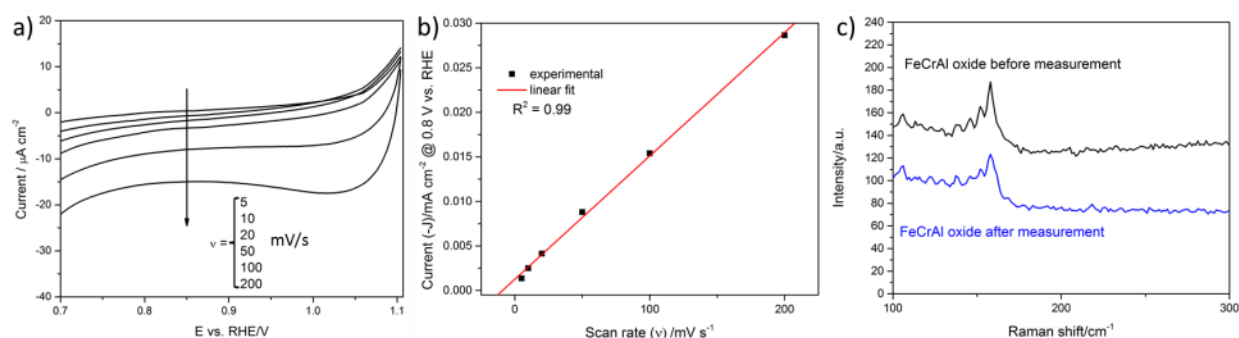


Figure S 6-16: (a) Dark current of mesoporous FeCrAl oxide electrodes in 0.1M HClO_4 at different scan rates (in mV/s). (b) Dependence of current density measured at 0.8 V vs. RHE on the scan rate showing a linear dependence of current on the scan rate characteristic for the capacitive charging of high surface area porous electrodes. (c) Raman spectra of FeCrAl oxide electrodes before and after photoelectrolysis in 0.1M HClO_4 for 60 min.

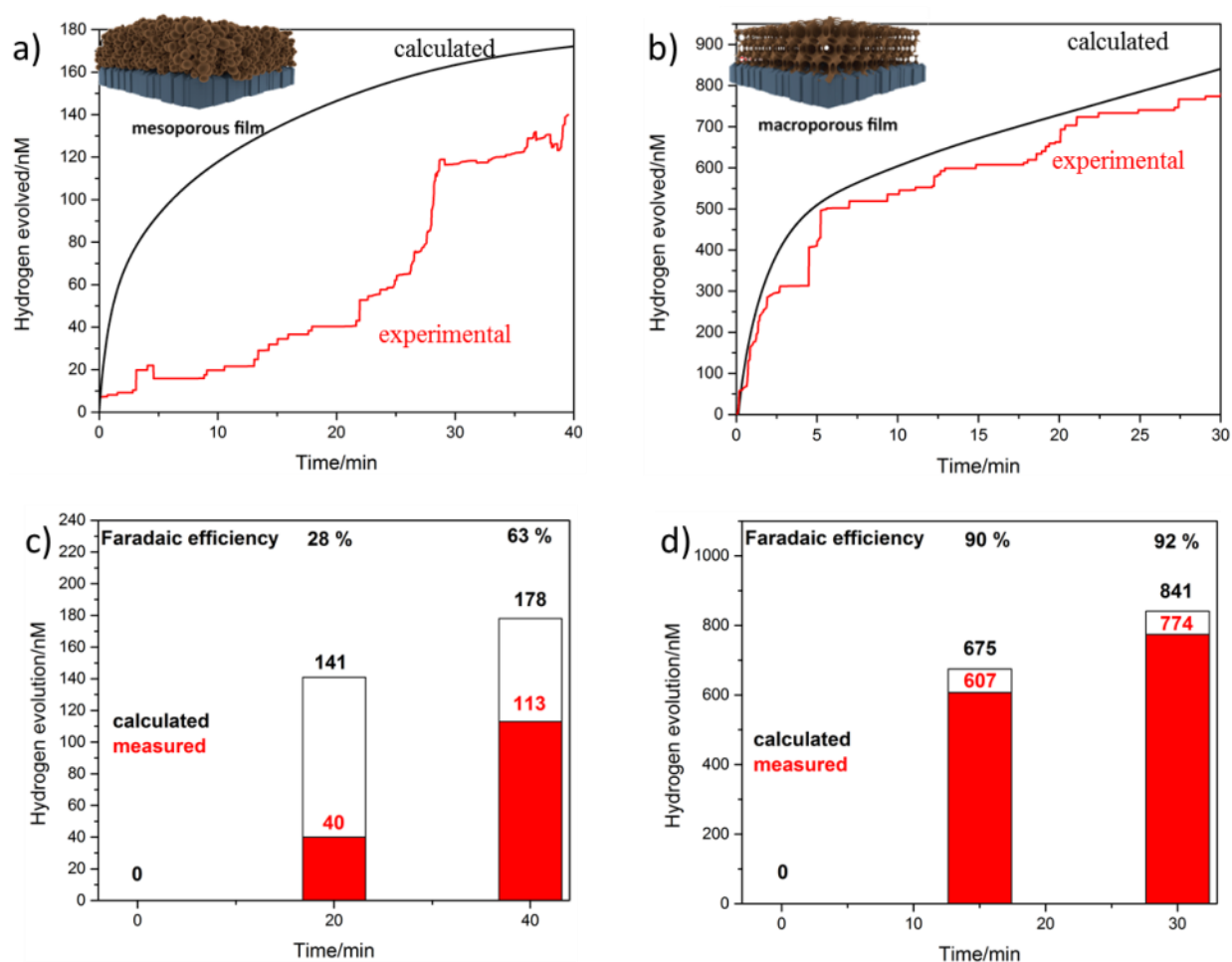


Figure S 6-17: Hydrogen evolution measurements performed on (a) mesoporous and (b) macroporous FeCrAl oxide electrodes. (c) and (d) show bar diagrams of the theoretically and experimentally determined hydrogen amounts for mesoporous and macroporous electrodes, respectively, allowing a comparison of the Faradaic efficiency.

6.6 References

1. Gratzel, M., Photoelectrochemical cells. *Nature* **2001**, *414* (6861), 338-344.
2. Walter, M. G.; Warren, E. L.; McKone, J. R.; Boettcher, S. W.; Mi, Q.; Santori, E. A.; Lewis, N. S., Solar Water Splitting Cells. *Chemical Reviews* **2010**, *110* (11), 6446-6473.
3. Abdi, F. F.; Han, L.; Smets, A. H. M.; Zeman, M.; Dam, B.; van de Krol, R., Efficient solar water splitting by enhanced charge separation in a bismuth vanadate-silicon tandem photoelectrode. *Nat Commun* **2013**, *4*.
4. Sivula, K.; Le Formal, F.; Grätzel, M., Solar Water Splitting: Progress Using Hematite (α -Fe₂O₃) Photoelectrodes. *ChemSusChem* **2011**, *4* (4), 432-449.
5. Tacca, A.; Meda, L.; Marra, G.; Savoini, A.; Caramori, S.; Cristino, V.; Bignozzi, C. A.; Pedro, V. G.; Boix, P. P.; Gimenez, S.; Bisquert, J., Photoanodes Based on Nanostructured WO₃ for Water Splitting. *ChemPhysChem* **2012**, *13* (12), 3025-3034.
6. Fujishima, A.; Honda, K., Electrochemical Photolysis of Water at a Semiconductor Electrode. *Nature* **1972**, *238* (5358), 37-38.
7. Dominey, R. N.; Lewis, N. S.; Bruce, J. A.; Bookbinder, D. C.; Wrighton, M. S., Improvement of photoelectrochemical hydrogen generation by surface modification of p-type silicon semiconductor photocathodes. *Journal of the American Chemical Society* **1982**, *104* (2), 467-482.
8. Paracchino, A.; Mathews, N.; Hisatomi, T.; Stefik, M.; Tilley, S. D.; Gratzel, M., Ultrathin films on copper(i) oxide water splitting photocathodes: a study on performance and stability. *Energy & Environmental Science* **2012**, *5* (9), 8673-8681.
9. Prevot, M. S.; Guijarro, N.; Sivula, K., Enhancing the Performance of a Robust Sol-Gel-Processed p-Type Delafossite CuFeO₂ Photocathode for Solar Water Reduction. *ChemSusChem* **2015**, *8* (8), 1359-1367.
10. Castelli, I. E.; Landis, D. D.; Thygesen, K. S.; Dahl, S.; Chorkendorff, I.; Jaramillo, T. F.; Jacobsen, K. W., New cubic perovskites for one- and two-photon water splitting using the computational materials repository. *Energy & Environmental Science* **2012**, *5* (10), 9034-9043.
11. Castelli, I. E.; Olsen, T.; Datta, S.; Landis, D. D.; Dahl, S.; Thygesen, K. S.; Jacobsen, K. W., Computational screening of perovskite metal oxides for optimal solar light capture. *Energy & Environmental Science* **2012**, *5* (2), 5814-5819.

12. Woodhouse, M.; Parkinson, B. A., Combinatorial approaches for the identification and optimization of oxide semiconductors for efficient solar photoelectrolysis. *Chemical Society Reviews* **2009**, *38* (1), 197-210.
13. Woodhouse, M.; Parkinson, B. A., Combinatorial Discovery and Optimization of a Complex Oxide with Water Photoelectrolysis Activity. *Chemistry of Materials* **2008**, *20* (7), 2495-2502.
14. Parkinson, B., Distributed research: a new paradigm for undergraduate research and global problem solving. *Energy & Environmental Science* **2010**, *3* (5), 509-511.
15. Anunson, P. N.; Winkler, G. R.; Winkler, J. R.; Parkinson, B. A.; Schuttlefield Christus, J. D., Involving Students in a Collaborative Project To Help Discover Inexpensive, Stable Materials for Solar Photoelectrolysis. *Journal of Chemical Education* **2013**, *90* (10), 1333-1340.
16. Borgmann, S.; Schuhmann, W., Robotic Systems for Combinatorial Electrochemistry. In *Combinatorial Methods for Chemical and Biological Sensors*, Potyrailo, R.; Mirsky, V., Eds. Springer New York: 2009; pp 331-370.
17. Sliozberg, K.; Schäfer, D.; Meyer, R.; Ludwig, A.; Schuhmann, W., A Combinatorial Study of Photoelectrochemical Properties of Fe-W-O Thin Films. *ChemPlusChem* **2015**, *80* (1), 136-140.
18. Schuppert, A. K.; Savan, A.; Ludwig, A.; Mayrhofer, K. J. J., Potential-resolved dissolution of Pt-Cu: A thin-film material library study. *Electrochimica Acta* **2014**, *144* (0), 332-340.
19. Rowley, J. G.; Do, T. D.; Cleary, D. A.; Parkinson, B. A., Combinatorial Discovery Through a Distributed Outreach Program: Investigation of the Photoelectrolysis Activity of p-Type Fe, Cr, Al Oxides. *ACS Applied Materials & Interfaces* **2014**, *6* (12), 9046-9052.
20. Sliozberg, K.; Stein, H. S.; Khare, C.; Parkinson, B. A.; Ludwig, A.; Schuhmann, W., Fe-Cr-Al Containing Oxide Semiconductors as Potential Solar Water-Splitting Materials. *ACS Applied Materials & Interfaces* **2015**, *7* (8), 4883-4889.
21. Le Bail, A.; Duroy, H.; Fourquet, J. L., Ab-initio structure determination of LiSbWO₆ by X-ray powder diffraction. *Materials Research Bulletin* **1988**, *23* (3), 447-452.
22. Moulder, J. F.; Chastain, J.; King, R. C., *Handbook of X-ray photoelectron spectroscopy: a reference book of standard spectra for identification and interpretation of XPS data*. Perkin-Elmer Eden Prairie, MN: 1992.

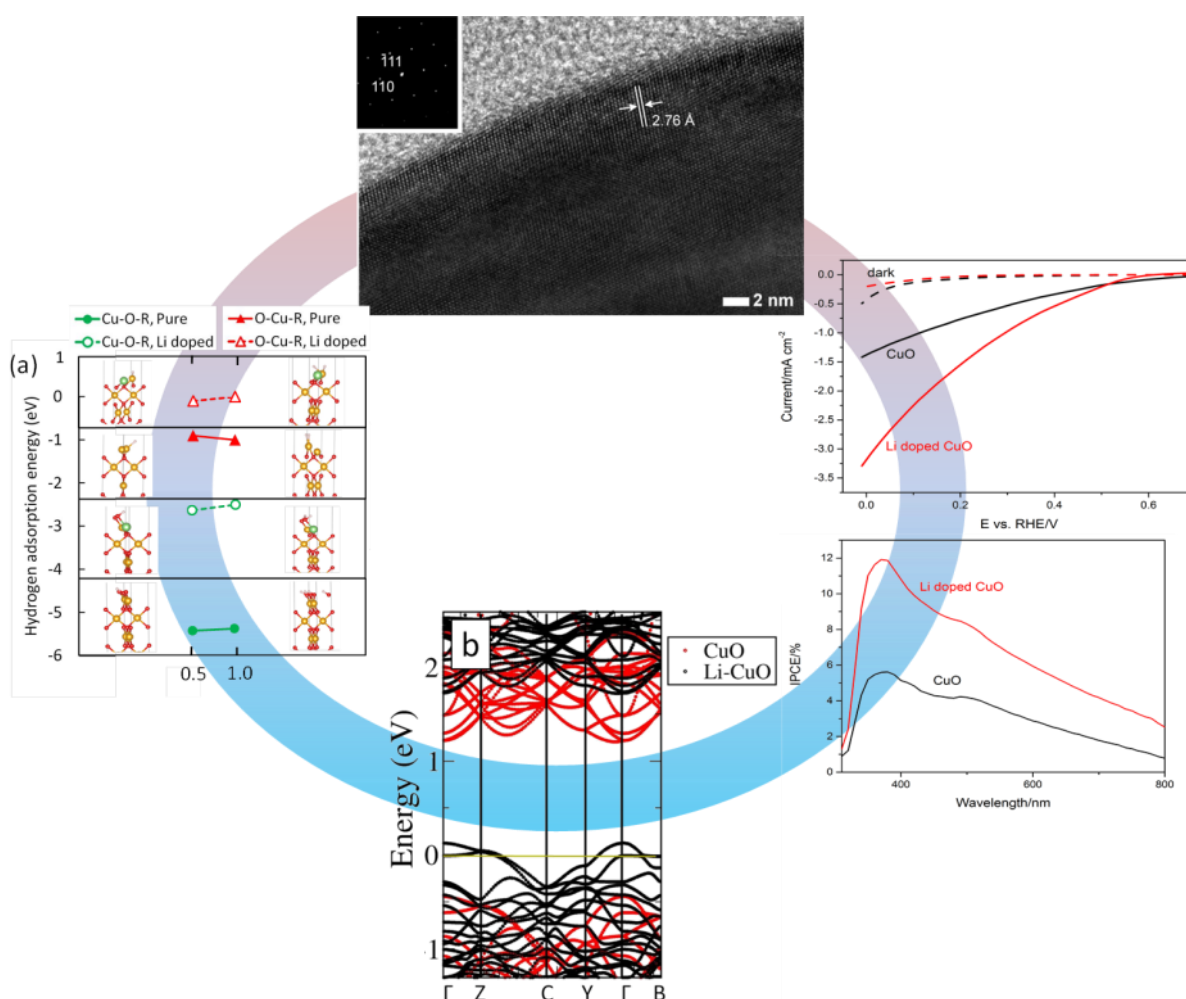
23. Biesinger, M. C.; Payne, B. P.; Grosvenor, A. P.; Lau, L. W. M.; Gerson, A. R.; Smart, R. S. C., Resolving surface chemical states in XPS analysis of first row transition metals, oxides and hydroxides: Cr, Mn, Fe, Co and Ni. *Applied Surface Science* **2011**, *257* (7), 2717-2730.
24. Galtayries, A.; Warocquier-Clérout, R.; Nagel, M. D.; Marcus, P., Fibronectin adsorption on Fe–Cr alloy studied by XPS. *Surface and Interface Analysis* **2006**, *38* (4), 186-190.
25. Wiberg, E.; Wiberg, N., *Inorganic Chemistry*. Academic Press: 2001.
26. Strohmeier, B. R., An ESCA method for determining the oxide thickness on aluminum alloys. *Surface and Interface Analysis* **1990**, *15* (1), 51-56.
27. STEINWEHR, H., Gitterkonstanten im System α -(Al, Fe, Cr) $2O_3$ und ihr Abweichen von der Vegardregel. *Zeitschrift für Kristallographie-Crystalline Materials* **1967**, *125* (1-6), 377-403.
28. Małeckı, A.; Małeckı, B.; Gajerski, R.; Łabuś, S., Thermal decomposition of chromium(III) nitrate(V) nanohydrate. *Journal of Thermal Analysis and Calorimetry* **2003**, *72* (1), 135-144.
29. Wıeczorek-Cıurowa, K.; Kozak, A. J., The Thermal Decomposition of $Fe(NO_3)_3 \cdot 9H_2O$. *Journal of Thermal Analysis and Calorimetry* **1999**, *58* (3), 647-651.
30. El-Shereafy, E.; Abousekkina, M. M.; Mashaly, A.; El-Ashry, M., Mechanism of thermal decomposition and γ -pyrolysis of aluminum nitrate nonahydrate $[Al(NO_3)_3 \cdot 9H_2O]$. *J Radioanal Nucl Chem* **1998**, *237* (1-2), 183-186.
31. Fu, Y.; Chen, J.; Zhang, H., Synthesis of Fe_2O_3 nanowires by oxidation of iron. *Chem. Phys. Lett.* **2001**, *350* (5–6), 491-494.
32. Tilley, S. D.; Cornuz, M.; Sivula, K.; Grätzel, M., Light-Induced Water Splitting with Hematite: Improved Nanostructure and Iridium Oxide Catalysis. *Angew. Chem. Int. Ed.* **2010**, *49* (36), 6405-6408.
33. Cesar, I.; Sivula, K.; Kay, A.; Zboril, R.; Grätzel, M., Influence of Feature Size, Film Thickness, and Silicon Doping on the Performance of Nanostructured Hematite Photoanodes for Solar Water Splitting. *The Journal of Physical Chemistry C* **2008**, *113* (2), 772-782.
34. Woodcock, L. V., Entropy difference between the face-centred cubic and hexagonal close-packed crystal structures. *Nature* **1997**, *385* (6612), 141-143.
35. Schroden, R. C.; Al-Daous, M.; Blanford, C. F.; Stein, A., Optical Properties of Inverse Opal Photonic Crystals. *Chemistry of Materials* **2002**, *14* (8), 3305-3315.

36. Waterhouse, G. I. N.; Waterland, M. R., Opal and inverse opal photonic crystals: Fabrication and characterization. *Polyhedron* **2007**, *26* (2), 356-368.
37. Praveen, C. S.; Timon, V.; Valant, M., Electronic band gaps of ternary corundum solid solutions from Fe₂O₃–Cr₂O₃–Al₂O₃ system for photocatalytic applications: A theoretical study. *Computational Materials Science* **2012**, *55*, 192-198.
38. Shen, S.; Jiang, J.; Guo, P.; Kronawitter, C. X.; Mao, S. S.; Guo, L., Effect of Cr doping on the photoelectrochemical performance of hematite nanorod photoanodes. *Nano Energy* **2012**, *1* (5), 732-741.
39. Kleiman-Shwarsstein, A.; Hu, Y.-S.; Forman, A. J.; Stucky, G. D.; McFarland, E. W., Electrodeposition of α -Fe₂O₃ Doped with Mo or Cr as Photoanodes for Photocatalytic Water Splitting. *The Journal of Physical Chemistry C* **2008**, *112* (40), 15900-15907.
40. Kleiman-Shwarsstein, A.; Huda, M. N.; Walsh, A.; Yan, Y.; Stucky, G. D.; Hu, Y.-S.; Al-Jassim, M. M.; McFarland, E. W., Electrodeposited Aluminum-Doped α -Fe₂O₃ Photoelectrodes: Experiment and Theory. *Chemistry of Materials* **2010**, *22* (2), 510-517.
41. Maeda, K.; Teramura, K.; Lu, D.; Saito, N.; Inoue, Y.; Domen, K., Noble-Metal/Cr₂O₃ Core/Shell Nanoparticles as a Cocatalyst for Photocatalytic Overall Water Splitting. *Angewandte Chemie International Edition* **2006**, *45* (46), 7806-7809.
42. Maeda, K.; Domen, K., Photocatalytic Water Splitting: Recent Progress and Future Challenges. *The Journal of Physical Chemistry Letters* **2010**, *1* (18), 2655-2661.
43. Mandlmeier, B.; Minar, N.; Feckl, J. M.; Fattakhova-Rohlfing, D.; Bein, T., Tuning the crystallinity parameters in macroporous titania films. *Journal of Materials Chemistry A* **2013**.
44. Kondofersky, I.; Dunn, H.; Müller, A.; Mandlmeier, B.; Feckl, J. M.; Fattakhova-Rohlfing, D.; Scheu, C.; Peter, L. M.; Bein, T., Electron collection in host-guest nanostructured hematite photoanodes for water splitting: the influence of scaffold doping density. *ACS Applied Materials & Interfaces* **2015**.

7 Li_xCuO photocathodes for improved hole collection efficiency in photoelectrochemical water splitting

This chapter is based on the following publication:

Ilina Kondofersky*, Jonathan Kampmann*, Hamid Hajiyani, Markus Döblinger, Goran Štefanić, Rossitza Pencheva, Dina Fattakhova-Rohlfing, Thomas Bein; to be submitted.



Abstract

The search for new photoactive materials has led to the emergence of novel binary, ternary as well as selectively doped metal oxides. Here, we present a direct, low temperature sol-gel synthesis approach for $\text{Li}_x\text{Cu}_{1-x}\text{O}$ photocathodes on FTO. Li-doped CuO electrodes with

increased conductivity show current density values of 3.3 mA cm⁻² at 0 V vs. RHE under AM 1.5, the highest so far reported for conventionally calcined films without the use of further catalysts. Because of the narrow band gap (1.49 eV) the Li_xCuO films show high light harvesting efficiency covering a long wavelength range reaching the IR region, as reflected in the absorption and IPCE spectra. The highest IPCE value was determined to be 12 % at 380 nm for a Li_xCu_{1-x}O film calcined at 400 °C. By determining the IPCE for electrolyte and substrate illumination a hole collection depth of 450 nm was determined, over a tenfold improvement compared to CuO. Hydrogen evolution was observed over 30 min under illumination with a 455 nm LED. To shed light on the underlying mechanisms density functional theory +*U* calculations were performed. Low concentrations of Li (3 %) indicate the formation of a *p*-type conductor where the valence band maximum is shifted to higher energies while a qualitatively different mechanism occurs at higher concentration where Cu is transformed to Cu⁺. Surface doping with Li at the (001) CuO surface causes significant structural relaxation for both Cu-O-R and O-Cu-R terminations. Increase of the HER activity is attributed to a reduction of the hydrogen adsorption energy upon doping. Both pure and doped compounds were added to a volcano plot of cathodes for direct comparison to different materials.

7.1 Introduction

Solar-driven splitting of water into hydrogen and oxygen is an attractive and an intensively explored technology for the sustainable generation of hydrogen as a carbon-free fuel¹⁻². An elegant way to implement a hydrogen generation technology based on water photoelectrolysis is to create photoactive materials which can directly reduce and oxidize water upon immersion in electrolyte. The requirements which a photoabsorber needs to meet, i.e. high

light harvesting efficiency, chemical and physical stability in the dark and under illumination, suitable band edge positions, efficient charge transport across the film and low production costs have shown to be challenging, yet not impossible. The performance of many existing photoelectrochemical systems is severely limited by numerous loss mechanisms. Therefore, the search for photoelectrode morphologies combining stability and efficient solar light harvesting with fast kinetics of the interfacial water splitting reactions is of primary importance for the development of competitive photoelectrochemical cells. This development has therefore led to the emergence of methods aiming to find novel photoactive materials applicable for photoelectrochemical water splitting, including synthesis of novel binary³ and ternary⁴ metal oxide compounds as well as well-known doped metal oxides⁵⁻⁶.

CuO is a thoroughly studied p-type semiconductor already applied in water photoelectrolysis⁷⁻⁸. In recent years it has attracted much attention as a photocathode due to its narrow band gap of 1.2-1.8 eV⁹, low toxicity and abundance making it scalable for industrial applications. One of the most important features of CuO is its chemical and photoelectrochemical stability which plays a major role in building working devices for solar-driven water splitting. Hence, it has even been used as a protective layer⁷ for Cu₂O electrodes which show good performance but undergo photocorrosion during measurement resulting in low stability^{7, 10}. Compared to Cu₂O, CuO has shown some drawbacks in regard to the photoelectrochemical performance which is often attributed to the low conductivity of the films⁵. To this date, conventionally calcined CuO photoelectrodes have reached current densities of up to 1.5 mA cm⁻²¹¹. In the aim to further improve the photoelectrochemical performance, several studies have been carried out studying the effect of doping on CuO. Introducing Li as dopant to CuO¹²⁻¹³ has shown to reduce the resistance of the film, thus increasing the conductivity¹³ and drastically decreasing the recombination of electron hole pairs in the film leading to higher current densities. By doping CuO with Li the current is drastically increased from 0.4

mA cm⁻² to values of up to 1.9 mA cm⁻² at 0.32 V vs. RHE¹³. These results prove that CuO can indeed be further enhanced by finding the right composition, morphology and synthesis parameters making it a competitive material to other top-performing metal oxide materials such as Cu₂O¹¹, Cu₃Ta₇O₁₉¹⁴ or CuFeO₂³.

Although Li doped CuO has been closely investigated, literature does not offer a thorough explanation as to what is the reason for this drastic change in photoelectrochemical behavior resulting in increased photocurrent densities. One of the main objectives of this work is to analyze the impact of Li on CuO and the thereof resulting effects by combining experimental studies with density functional theory calculations.

This work describes the development of a low temperature sol-gel synthesis method for thin film deposition of Li_xCu_{1-x}O photocathodes on FTO. The Li_xCuO electrodes were characterized with respect to their material properties by different techniques including XRD, solid state NMR, Raman, SEM and TEM. Photoelectrochemical characterization was performed by current voltammetry under AM 1.5, incident photon to current efficiency (IPCE) as well as transient measurements and stability tests. Hydrogen evolution was further determined by immersing a hydrogen sensor in the electrolyte solution during photoelectrolysis. The experimental studies are combined with state-of-the-art DFT+U calculations to achieve a detailed understanding of the experimental results. We have explored both the influence of Li-doping on the bulk electronic properties where we find a pronounced dependence on dopant concentration as well as on the hydrogen adsorption energy.

7.2 Results and Discussion

$\text{Li}_x\text{Cu}_{1-x}\text{O}$ photocathode layers were prepared by spin coating an ethanolic solution of $\text{Cu}(\text{NO}_3)_2 \cdot 3 \text{H}_2\text{O}$ and LiNO_3 onto the FTO substrate. Calcination of these coatings at 400°C resulted in homogeneous black films, whose thickness can be controllably varied from $0.7 \mu\text{m}$ to $3 \mu\text{m}$ (Figure S 7-6). Although the films can be prepared with different Li contents, we found that the best performing photocathodes are obtained when Li and Cu salts are taken in equimolar ratios. The calcined films obtained from these solutions contain large amounts of non-reacted LiNO_3 and LiCO_3 . These salts however are water soluble and can be easily removed by water, leaving the only phase similar to CuO (Figure S 7-7). The XRD analysis reveals that this phase is structurally closely related to CuO tenorite (space group: $C2/c$) but with slightly different unit cell parameters ($a = 4.6850(1) \text{ \AA}$, $b = 3.4263(1) \text{ \AA}$, $c = 5.1318(1) \text{ \AA}$ and $\beta = 99.445(1)^\circ$) as compared to pure CuO phase ($a = 4.6853(3) \text{ \AA}$; $b = 3.4257(1) \text{ \AA}$; $c = 5.1303(3) \text{ \AA}$; $\beta = 99.549(4)^\circ$). The observed difference in unit cell parameters resulting in the small increase of the unit cell volume from $81.20(1) \text{ \AA}^3$ in the pure CuO to $81.26(1) \text{ \AA}^3$ in the CuO synthesized in the presence of Li salts can result from the incorporation of a small amount of Li^+ ions with somewhat bigger ionic radius (0.76 \AA in CN = 6) compared to the ionic radius of Cu^{2+} ion (0.73 \AA in CN = 6)¹⁵ (Figure S 7-8). ICP-AAS analysis confirmed that Li ions are indeed present in this material but in low amounts reaching only 1.3 at-%.

Another evidence for the incorporation of Li in the structure is provided by solid state ^7Li -NMR, which shows a multiplet centered at 1.3 ppm in the spectrum of a carefully washed $\text{Li}_x\text{Cu}_{1-x}\text{O}$ powder (Figure S 7-9). This signal is indicative for a non-metallic single phase free of diamagnetic compound contaminations (i.e. Li_2O , LiCO_3 , LiNO_3). The observed signal splitting is caused by dipolar interactions between Li and the unpaired electrons of Cu thus confirming the formation of a single phase $\text{Li}_x\text{Cu}_{1-x}\text{O}$. The phase purity of the obtained

Li_xCu_{1-x}O is further suggested by Raman spectra, which show Raman modes typical of CuO for both undoped and Li-doped CuO. Incorporation of Li results in some difference in peak intensities, but does not lead to the appearance of some additional phases (Figure S 7-10).

The morphology of the Li-doped as well as of the undoped CuO films was investigated by scanning electron microscopy (Figure 7-1a, c). In both cases the films obtained after washing of calcined coatings are very homogeneous, covering the FTO substrate completely without cracks or delamination. Both doped and undoped films are nanostructured and composed of interconnected nanoparticles forming disordered porous layers. It can be seen that the presence of Li salts affects the morphology of the resulting films with the particles becoming bigger and more interconnected, which is confirmed also by the TEM analysis (Figure 7-1b, d). The change in morphology is reflected also in the specific surface area, which decreases from 3.0 m²/g for the undoped CuO to 1.2 m²/g for the Li_xCu_{1-x}O due to the increased crystal size of the films fabricated from Li⁺-containing solutions.

TEM images of the undoped CuO films reveal that they are composed of defect free single crystalline particles with a size of around 70-100 nm. The individual particles show little interconnectivity (Figure 7-1b). In comparison, the nanocrystals in Li_xCu_{1-x}O films are bigger (150 – 300 nm) and intergrown (Figure 7-1d). HR-TEM images (Figure 7-1f) and electron diffraction analysis of these particles (**Error! Reference source not found.**e) reveal that they are single crystalline, with pronounced Moiré patterns. The d-spacing of the monoclinic Li_xCu_{1-x}O was determined to be 2.76 Å being in good agreement with the XRD patterns.

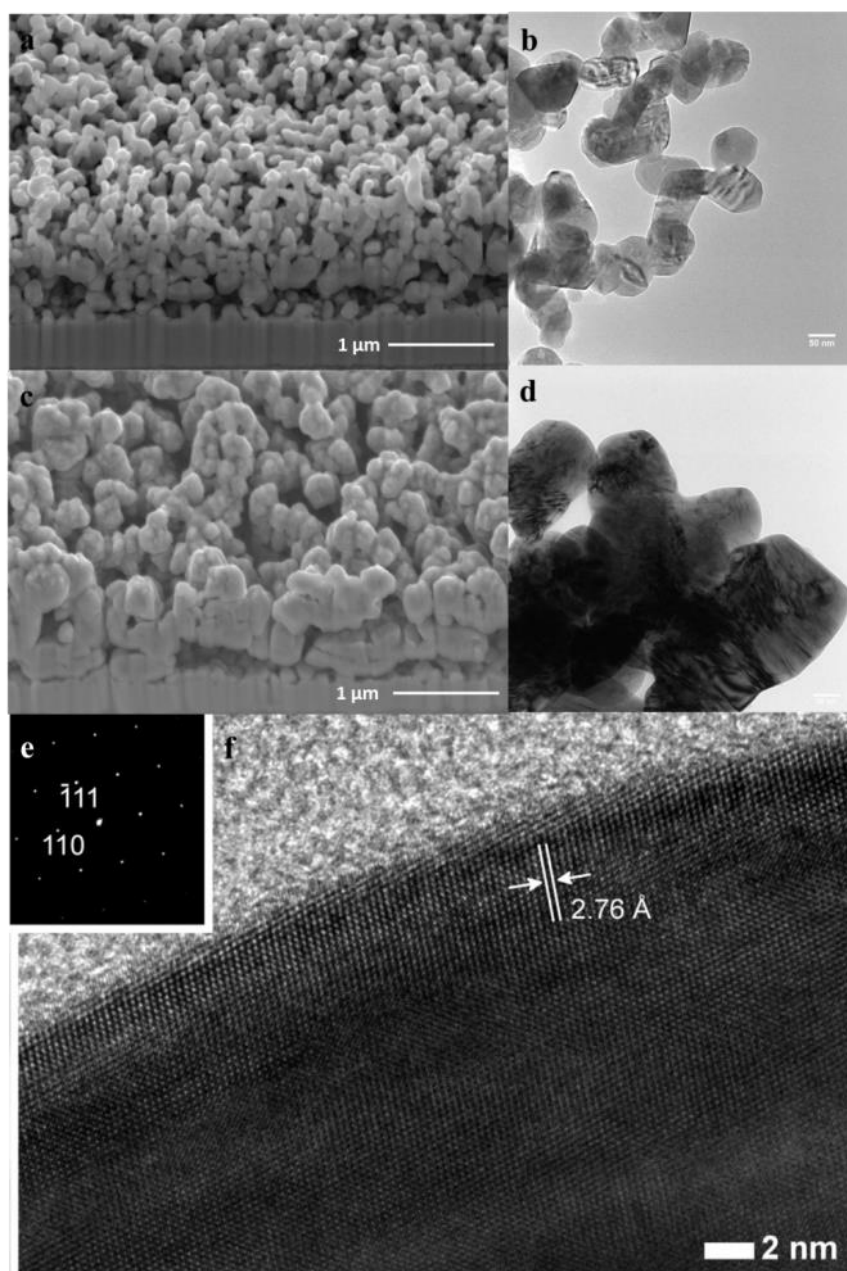


Figure 7-1: SEM cross section images of (a) CuO (c) Li_xCu_{1-x}O. TEM images of (b) CuO and (d) Li_xCu_{1-x}O particles. (f) High-resolution TEM of a highly crystalline Li_xCu_{1-x}O nanoparticle and (e) its corresponding electron diffraction pattern.

Optical properties of the photocathode layers were investigated by UV-Vis spectroscopy. Both undoped and Li-doped CuO films demonstrate good light harvesting efficiencies across a broad wavelength range between 350-900 nm covering a part of the IR range (Figure S

7-11a). As expected the absorbance scales nearly linear with film thickness. Doping with Li does not change the optical properties of the CuO layers; both films show an optical direct and indirect bandgap of 1.49 eV and 1.43 eV, respectively, obtained via Tauc plot analysis (Figure S 7-11b).

Voltammograms of undoped and Li-doped CuO photocathodes obtained under substrate AM 1.5 illumination show a photocurrent onset at 0.58 V vs. RHE (Figure S 7-6). Undoped CuO electrodes reach current densities of 1.5 mA cm⁻² at 0 V vs. RHE and an incident photon to current conversion efficiency (IPCE) of 5.5 % at 390 nm. These values compare well with the highest values reported in literature so far for the CuO photocathodes.¹⁶ Introducing Li as a dopant results in a more than twofold increase in the photocurrent density reaching 3.3 mA cm⁻² at 0 V vs. RHE (Figure 7-2a), and IPCE values of up to 12 % for 390 nm. Notably, the high IPCE values are observed for the whole investigated wavelength range including the IR region, for which a high IPCE of 2.6 % was measured at 800 nm. To ensure that the observed photocurrents are due to the water reduction but not some side processes such as reduction of the dissolved O₂ we have performed the measurements under O₂-free conditions and have observed the same photocurrents (Figure S 7-12). The Faradaic efficiency of the process determined by the measurement of evolved hydrogen (Figure S 7-13) is about 86%, so that the photocorrosion can be safely excluded as a possible reason for the photocurrent. It should be noted that the photocurrents we have obtained for the Li_xCu_{1-x}O electrodes are the highest so far reported for this system, which could be due to the optimized electrode morphology obtained by the developed fabrication procedure.

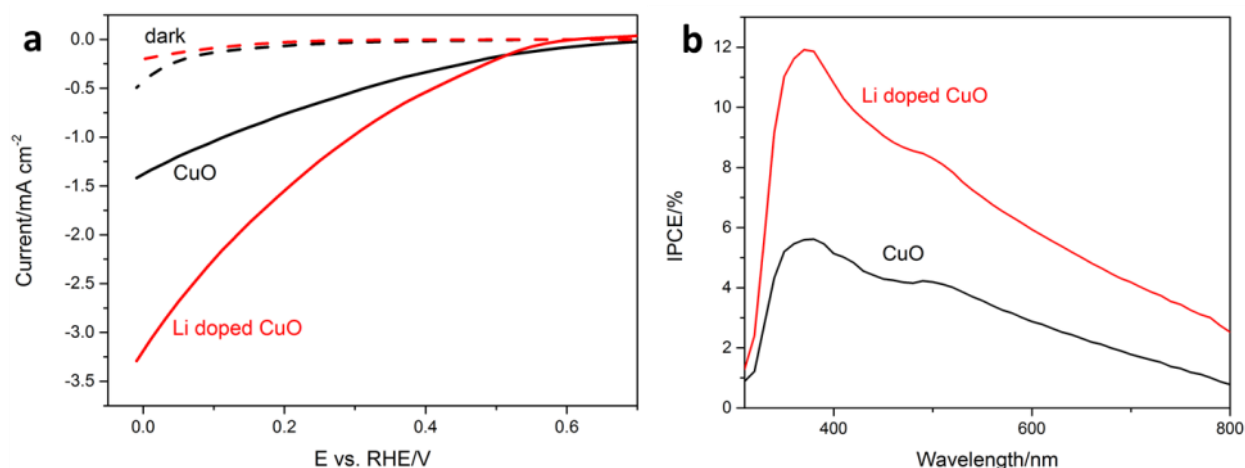


Figure 7-2: (a) Cyclic voltammetry measurements and (b) IPCE spectra of pure CuO and $\text{Li}_x\text{Cu}_{1-x}\text{O}$ films calcined at 400 °C under substrate AM 1.5 illumination. Dashed curves are dark current sweeps.

To understand the reasons for the improved performance of $\text{Li}_x\text{Cu}_{1-x}\text{O}$ photocathodes the hole collection depth in CuO and $\text{Li}_x\text{Cu}_{1-x}\text{O}$ films was determined by applying a method introduced by Södergren et al.²⁰ The proposed equation allows a calculation of the hole collection depth²¹⁻²² by comparing the IPCE under substrate and electrolyte illumination (see Experimental part for further details). According to this model, the hole diffusion length for pure CuO was determined to be 40 nm (Figure 7-3). This value is increased sufficiently upon Li insertion reaching a hole collection depth of 450 nm. Therefore, we can conclude that the improved major charge carrier collection efficiency is one of the key reasons for the improved performance of Li_xCuO .

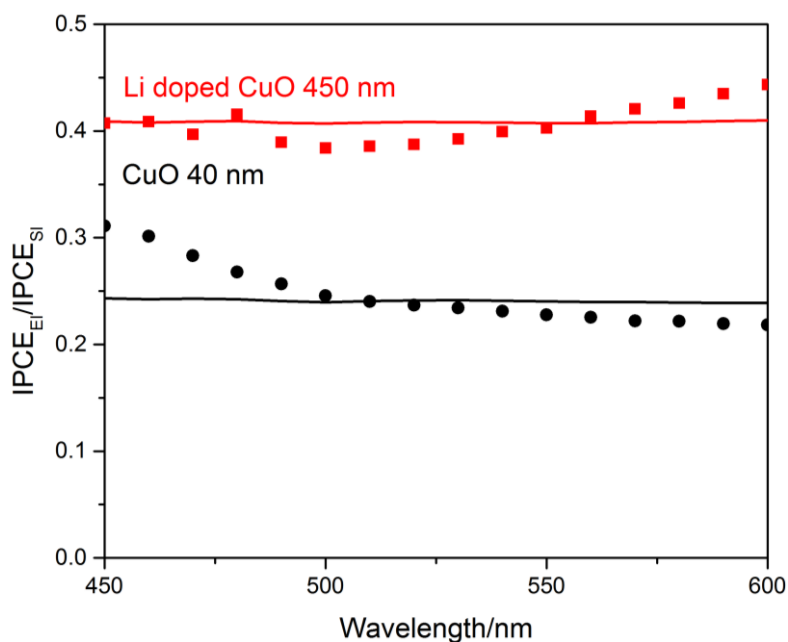


Figure 7-3: Ratio of IPCE measured from electrolyte and substrate side. Experimental data is shown for pure CuO (black dots) and Li_xCuO (red squares). The corresponding curves fitting the points are calculated using the model of Södergren et al. suggesting a hole diffusion length of 40 nm for CuO (black line) and 450 nm for Li_xCuO (red line).

Stability measurements were performed on Li_xCuO to assess the lifetime of the photocathodes. For this reason we performed the same chronoamperometry measurement as for the hydrogen evolution with and without stirring the electrolyte solution. As can be seen in Figure S 7-13b the photocurrent decreased over time for both stirring conditions stabilizing at about -0.5 mA cm^{-2} . Nevertheless, the photocurrent decay of the stirred measurement was sufficiently slower. This observation shows that the photocurrent decrease is strongly influenced by diffusion.

To understand how the introduction of Li influences the bulk and surface properties of CuO we have performed DFT calculations for Li-containing CuO by adopting the GGA+U framework. The first step of these calculations is the correct choice of Hubbard potential U

(refer to supporting information for more details). Our model predicts that the indirect band gap of CuO increases with U up to $U=8\text{ eV}$ and changes to a direct band gap of 2.1 eV for U beyond 8 eV (SI Figure 9a). The best agreement with the experimentally determined indirect band gap of 1.49 eV is achieved for $U=8\text{ eV}$; this value was used for the further calculations. The variation of lattice constants as a function of U is presented in (Figure S 7-14b). The DFT predictions are in overall agreement with experimental lattice constants (denoted by dashed lines) where a jump occurs between $U = 8\text{ eV}$ and $U = 8.5\text{ eV}$ associated with the transition from indirect to direct band gap.

To determine the preferential position of Li atoms in the CuO structure we have calculated the solution energy of Li at different lattice positions. For substitutional doping of Cu and O sites the calculated values are -4.20 and 1.04 eV , respectively, while for the interstitial doping the solution energy was determined to be -0.025 eV . Therefore, we can conclude that thermodynamically the preferred configuration corresponds to the substitutional doping of Cu sites with Li atoms.

To investigate the electronic properties, the band structure of bulk $\text{Li}_x\text{Cu}_{1-x}\text{O}$ was calculated for the high lithium content of $x_{\text{Li}}=25\text{ at\%}$ and the low content of $x_{\text{Li}}=3.5\text{ at\%}$, which is close to the experimentally determined Li level of ca. 1.3 at\% . Surprisingly, the band structure of $\text{Li}_x\text{Cu}_{1-x}\text{O}$ (Figure 7-4a and b) shows a very strong dependence of the amount of introduced Li. While for high concentration the band gap is strongly decreased to 0.64 eV , for low concentration the main effect is an upward shift of the valence band maximum that eventually crosses the Fermi level and makes the system a p -type conductor. As shown in the spin density plots in Figure 5c and d the underlying mechanisms are distinct: for $x_{\text{Li}}=25\text{ at\%}$ substitution of Li^+ leads to a change in charge state of one copper to Cu^{1+} , while for $x_{\text{Li}}=3.5\text{ at\%}$ the holes are delocalized at the oxygen sites leading to a p -type conductor. The solution

energies of $\text{Li}_{0.0312}\text{Cu}_{0.968}\text{O}$ and $\text{Li}_{0.25}\text{Cu}_{0.75}\text{O}$ are -4.2 eV and -3.1 eV respectively, indicating a reduction with increasing Li concentration due to Li-Li repulsion.

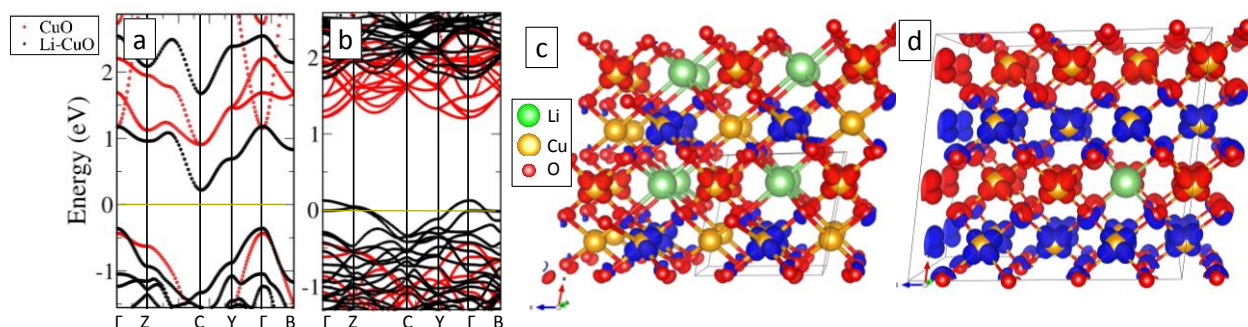
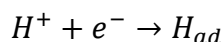


Figure 7-4: Electronic band structure of lithium doped CuO for two different Li concentrations of (a) $\text{Li}_{0.25}\text{Cu}_{0.75}\text{O}$ and (b) $\text{Li}_{0.0312}\text{Cu}_{0.968}\text{O}$. Different numbers of bands are related to different cell sizes. The yellow line marks the Fermi level. In contrast to the insulating behavior for $x_{\text{Li}}=25\%$ (note the reduced band gap w.r.t. to bulk CuO), the valence bands crossing the Fermi level for $x_{\text{Li}}=0.03\%$ indicate p-type conductivity. Spin density of lithium doped CuO in two different Li concentrations of (c) $\text{Li}_{0.25}\text{Cu}_{0.75}\text{O}$ and (d) $\text{Li}_{0.0312}\text{Cu}_{0.968}\text{O}$ (Isosurface of $0.01 \text{ e}/\text{\AA}^3$). Majority and minority densities are shown by blue and red, respectively. Note the significant contribution of oxygen for the low Li doping concentration of 3%.

In addition to the change in bulk properties, we have found that also the surface properties are strongly affected by the introduction of Li atoms. To determine the change in surface properties we have calculated the solution energy of Li atoms (SE) for the most stable (001) CuO surface for two possible terminations, Cu-O-R and O-Cu-R (Figure 7-5b) (see Experimental part for the calculation details). For both terminations, the SE of Li in the surface layers is higher than an isolated Li in bulk which is due to the large atomic radius of this atom. The SE converges to bulk value at distance of around 7\AA to the surface. The

preferable positions for Li atoms and the surface reconstruction depend on the termination. For the O-Cu-R termination, the most preferable position of Li atoms is at a Cu0 site (Li→Cu0 substitution) with the SE of -5.78 eV. The corresponding structure shows a significant oxygen reconstruction at the surface. The Li→Cu1 substitution for this termination is less beneficial, as it would lead to the lifting of Li atoms to the surface oxygen layer with a lower SE of -4.35 eV. In contrast to the O-Cu-R termination, the Cu-O-R termination features higher structural tolerance, as positioning Li atoms on both Cu0 and Cu1 sites results in equal SE of -6.3 eV. As can be seen from the side view of the relaxed structure, doping with Li leads to an inward relaxation of the surface metal layer towards the O layer. The oxidation states of surface atoms are explained in Figure S 7-16 of the supporting informations.

The hydrogen evolution reaction (HER) proceeds according to the following mechanism:



and involves the elementary steps of adsorption of hydrogen atoms to the surface (described by the Volmer equation²³) as well as desorption of H₂ from the surface. Based on the Sabatier's principle for HER the H adsorption energy should be neither too high nor too low. Hydrogen atoms should bind strong enough to cover the surface but weak enough to facilitate desorption of the H₂ product. Therefore the free energy of adsorption of hydrogen from solution should be close to zero.

To estimate the influence of Li doping on the HER, the hydrogen adsorption energy was calculated for pure and Li-doped CuO surfaces (see Experimental part for the calculation details)

For the undoped CuO, the highest hydrogen adsorption energy (HAE) was found for the Cu-O-R termination (Figure 7-5a). Doping with Li reduces the HAE for both terminations;

furthermore, the adsorption of hydrogen on the Li-doped surfaces changes the surface structure significantly. In all cases, the adsorption energy shows little dependence on H-coverage.

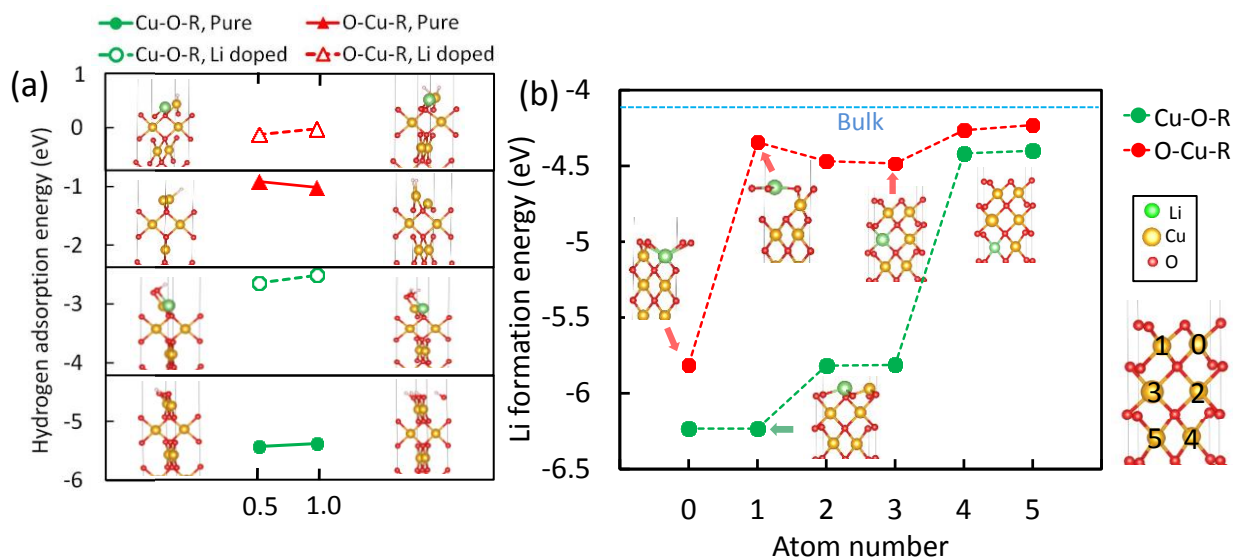


Figure 7-5: (a) Hydrogen adsorption energy of pure and Li-doped (001) CuO surfaces for Cu-O-R and O-Cu-R terminations. (b) Layer-dependent solution energy of a Li atom at the (001) CuO surface for both Cu and O terminations. Relaxed Li doped structures are shown for some points. Solution energy of an isolated Li in bulk structure is shown by a dashed line. The x axis corresponds to different Cu atoms which are marked from 0-5.

Li doping of CuO photocathodes has proven to be a very successful approach for optimizing the photoelectrochemical properties of a well-studied material. By increasing the hole diffusion length from 40 to 450 nm, the charge transport is increased resulting in reduced recombination and therefore increased charge transfer efficiency. These observations are in agreement theoretical calculations explaining the beneficial influence of Li on CuO.

7.3 Conclusion

In conclusion, we present a novel sol-gel low temperature synthesis of $\text{Li}_x\text{Cu}_{1-x}\text{O}$ photocathodes for photoelectrochemical water splitting. The films were thoroughly investigated with respect to morphology, composition and structure. Introducing low concentrations of Li to the CuO structure led to a sufficient increase of photocurrent density reaching values of 3.3 mA cm^{-2} at 0 V vs. RHE under AM 1.5. These currents are so far the highest reported for a CuO system synthesized with conventional annealing without the use of additional catalysts. IPCE measurements reveal values of 12 % at 380 nm slowly decreasing to 2.6 % for longer wavelengths of 780 nm. The hole collection depth of Li_xCuO films is increased significantly upon doping resulting in lower recombination and thus higher currents. The experimental work was supported by DFT+ U calculations which showed the beneficial influence of a low Li doping concentration on the CuO structure thus observing the formation of a p-type semiconductor. Further, Li doping lead to a significant structural relaxation for both Cu-O-R and O-Cu-R terminations. The increased photoelectrochemical activity of $\text{Li}_x\text{Cu}_{1-x}\text{O}$ was further attributed to the reduced hydrogen adsorption energy resulting from the specific doping step. This work is a representative example of how well-known materials can be further improved by finding and introducing a suitable modification such as for example doping. This work further shows the importance of collaboration between experimental and computational approaches which complement each other in the search for new promising photoabsorber and catalyst materials.

7.4 Experimental

Preparation of $\text{Li}_x\text{Cu}_{1-x}\text{O}$ films

Li_xCu_{1-x}O thin film electrodes were prepared by spin coating (1000 rpm, 30 s, 100 μL) a precursor solution containing 0.5 M Cu(NO₃)₂ · 3H₂O and 0.5 M LiNO₃ in ethanol. The films were deposited on fluorine-doped tin oxide (FTO) coated glass (TEC 15 Glass, Dyesol). The samples were subsequently calcined at different temperatures (300-600 °C) for 2 h (1.3 °C/min) in air and slowly cooled down to room temperature.

Crystallographic and Morphological Characterization

Powder X-ray diffraction (XRD) patterns were acquired on a STOE powder diffractometer (Cu-Kα1, $\lambda = 1.5406 \text{ \AA}$) equipped with a position-sensitive Mythen-1K detector in transmission geometry. Lanthanum hexaboride (NIST LaB₆ SRM 660b; space group: $Pm\bar{3}m$; $a = 4.15689(8) \text{ \AA}$) was used as an internal standard in calibration of diffraction line positions. XRD pattern of the sample and ~5% of lanthanum hexaboride were collected over a 2θ range of 10 to 81° with a step of 0.015°. Li_xCu_{1-x}O unit-cell parameters were obtained using the results from the Rietveld refinements²⁴ of a powder diffraction pattern. The observed parameters are structurally closely related to tenorite (CuO, space group: $C2/c$; $a = 4.6853(3) \text{ \AA}$; $b = 3.4257(1) \text{ \AA}$; $c = 5.1303(3) \text{ \AA}$; $\beta = 99.549(4)^\circ$; *JCPDS-ICDD PDF card No. 45-937*). A graphical representation of the final Rietveld refinement is shown in Figure SI 3. The R_{wp} index of the refined pattern was 0.041 and the R_{wp} index with subtracted background was 0.043 which indicate very good quality of least squares refinement.

Scanning electron microscopy (SEM) measurements were performed on a JEOL JSM-6500F scanning electron microscope using a 5 kV field emission gun and an Oxford energy dispersive X-ray (EDX) spectroscopy detector.

A probe-corrected *FEI Titan Themis* transmission electron microscope (TEM) with a field emission gun (X-FEG) at 300 kV was applied to determine morphology, crystallography and elemental distribution. High-resolution TEM (HRTEM) and bright field (BF) images were received with a Ceta 16M camera while scanning TEM (STEM) measurements were

7. Experimental

performed with a annular dark field (ADF) detector. The thin film material was scraped of the substrate with a razor blade and the powder was dispersed in ethanol. This liquid was deposited dropwise on a holey carbon grid to prepare the sample.

^7Li NMR

Solid-State MAS NMR: Experiments were performed at 11.74 T on a Bruker DSX 500 spectrometer equipped with a commercial 4 mm triple-resonance MAS probe at ^7Li frequencies of 194.399 MHz. All experiments were performed at room temperature.

Optical Characterization

UV-Vis spectra were obtained on a Perkin Elmer Lambda 1050 UV/Visible/NIR spectrophotometer with an integrating sphere. The absorbance of the films was calculated from both the transmittance and reflectance of the films correcting for the absorbance of the FTO substrate by applying an expression derived by Klahr *et al* to the UV-Vis data.²³

Photoelectrochemical Characterization

Current-voltage and Incident Photon to Current Efficiency (IPCE) curves were measured with a μ -Autolab III potentiostat with a FRA2 impedance analyzer. The films were masked with a Teflon-coated glass fiber adhesive tape leaving an area of 0.14 cm^2 free for illumination. The sample was placed into a quartz cell filled with an aqueous $0.1\text{ M Na}_2\text{SO}_4$ electrolyte and connected, with an Ag/AgCl reference electrode and a Pt mesh counter electrode, to the potentiostat. During the measurements the films were illuminated through the substrate side by an AM1.5 solar simulator (Solar Light Model 16S) at 100 mW cm^{-2} by scanning from positive to negative potentials in the dark or under illumination at a sweep rate of 20 mV/s .

Incident photon-to-current efficiency (IPCE) measurements were performed under monochromatic light chopped with a frequency of 1 Hz. The sample was illuminated through the substrate by a 150 W Xenon lamp equipped with a monochromator and order-sorting filters. All IPCE values were measured at a sample bias of 0.2 V vs. RHE under simulated solar irradiation. The light intensity at the electrode was measured using a certified, KG5-filtered Fraunhofer ISE silicon reference cell.

Transient current measurements were performed under substrate illumination with a 455 nm LED under 1Hz chopped light.

Hydrogen evolution measurements were performed under illumination with a 455 nm LED at a set potential of 0.2 V vs. RHE. During the chronoamperometric measurement the photocathode was immersed in an Ar purged electrolyte solution together with a calibrated hydrogen needle sensor (Unisense, H₂-NPLR) monitoring the change in hydrogen concentration over time. Stirring of the electrolyte solution was not possible due to the polarization of the H₂ microsensor.

By measuring the IPCE under substrate and electrolyte illumination and calculating the ratio of IPCE_{EI}/IPCE_{SI} the hole collection depth can be determined by fitting the experimental data using the following expression:

$$\frac{IPCE_{EI}}{IPCE_{SI}} = \frac{(1-R_{EI}) \left[(L\alpha(\lambda)+1)e^{\frac{2d}{L}} - 2L\alpha(\lambda)e^{\frac{\alpha(\lambda)d+d}{L}} + L\alpha(\lambda) - 1 \right]}{(1-R_{SI}) \left[(L\alpha(\lambda)-1)e^{\frac{\alpha(\lambda)d+2d}{L}} + (L\alpha(\lambda)+1)e^{\alpha(\lambda)d} - 2L\alpha(\lambda)e^{\frac{d}{L}} \right]}$$

R_{EI} and R_{SI} describe the reflectance measured through the electrolyte and substrate side, respectively, $\alpha(\lambda)$ is the optical absorption coefficient, d is the determined film thickness, and L_n , is the collection depth and only fitting parameter of the equation. This equation can be applied under consideration of the following assumptions: a) the electron transport in the

7. Experimental

semiconductor occurs via diffusion and b) the diffusion length of the electrons is constant throughout the film and c) recombination is assumed to be of first order²⁰.

Computational details

Density-functional theory (DFT) calculations were performed by using the VASP²⁵⁻²⁶ code with projector-augmented wave (PAW) pseudopotentials²⁷. The exchange-correlation functional was determined by applying the generalized-gradient approximation (GGA)²⁸ including an on-site the Hubbard U term. The simplified rotationally invariant approach was adopted for the GGA+ U calculations²⁹. The Hubbard- U value for Cu was taken by fitting the theoretical with the experimental band gap (1.49 eV).

To model different doping concentrations two different cell sizes with 8 and 64 atoms were adopted, corresponding to the bulk CuO and a 2x2x2 supercell, respectively.

A plane-wave cut-off of 500 eV and a Monkhorst-Pack k-point mesh of 8x8x8 and 4x4x4 were used for the small and the big cells, respectively. The (001) CuO slab was simulated by a periodic (1x1) slab model composed of seven CuO layers. We examine the (001) surface as a first step toward understanding the surface chemistry of Li doped CuO. Thereby, both Cu-O-R and O-Cu-R terminations were considered.

The Li solution energy (SE) indicates the preferred lattice positions of Li incorporation in the CuO structure and is defined as follows:

$$SE_{Li} = E_{Li_xCu_{1-x}O} - E_{CuO} - NE_{Li} + ME_{O/Cu}$$

$E_{Li_xCu_{1-x}O}$ and E_{CuO} represent the total energy of the doped and undoped structure, respectively. E_{Li} and $E_{O/Cu}$ is the elemental ground state of Lithium, Oxygen and Copper. N

is the number of lithium atoms substituted by M oxygen or copper. To calculate the solution energy a Li atom is substituted with Cu and O in the $2 \times 2 \times 2$ lattice in a fully relaxed the structure.

To find the most favorable adsorption site, the slabs were built by adding H atoms manually to the surface in different positions. The grid spacing is dense enough to sample all positions. For the first scan, two H atoms were added to both sides of slabs in 25 different initial positions. The calculations are performed with one and two hydrogen atoms on each side of the slab which corresponds to 1/2 and 1 monolayer (ML) of hydrogen. After relaxation the H atoms relaxed into different positions on the two sides of the slab with different formation energy.

A plane-wave cut-off of 500 eV and a Monkhorst-Pach k-point mesh of $8 \times 8 \times 8$ and $4 \times 4 \times 4$ were used for the big and small cells, respectively. The (001) CuO slab was simulated by the periodic (1×1) slab model composed of seven CuO layers. The (001) surface was studied as a first step toward understanding the surface chemistry of Li doped CuO. The calculations were performed for both Cu-O-R and O-Cu-R terminations.

7.5 Supporting Information

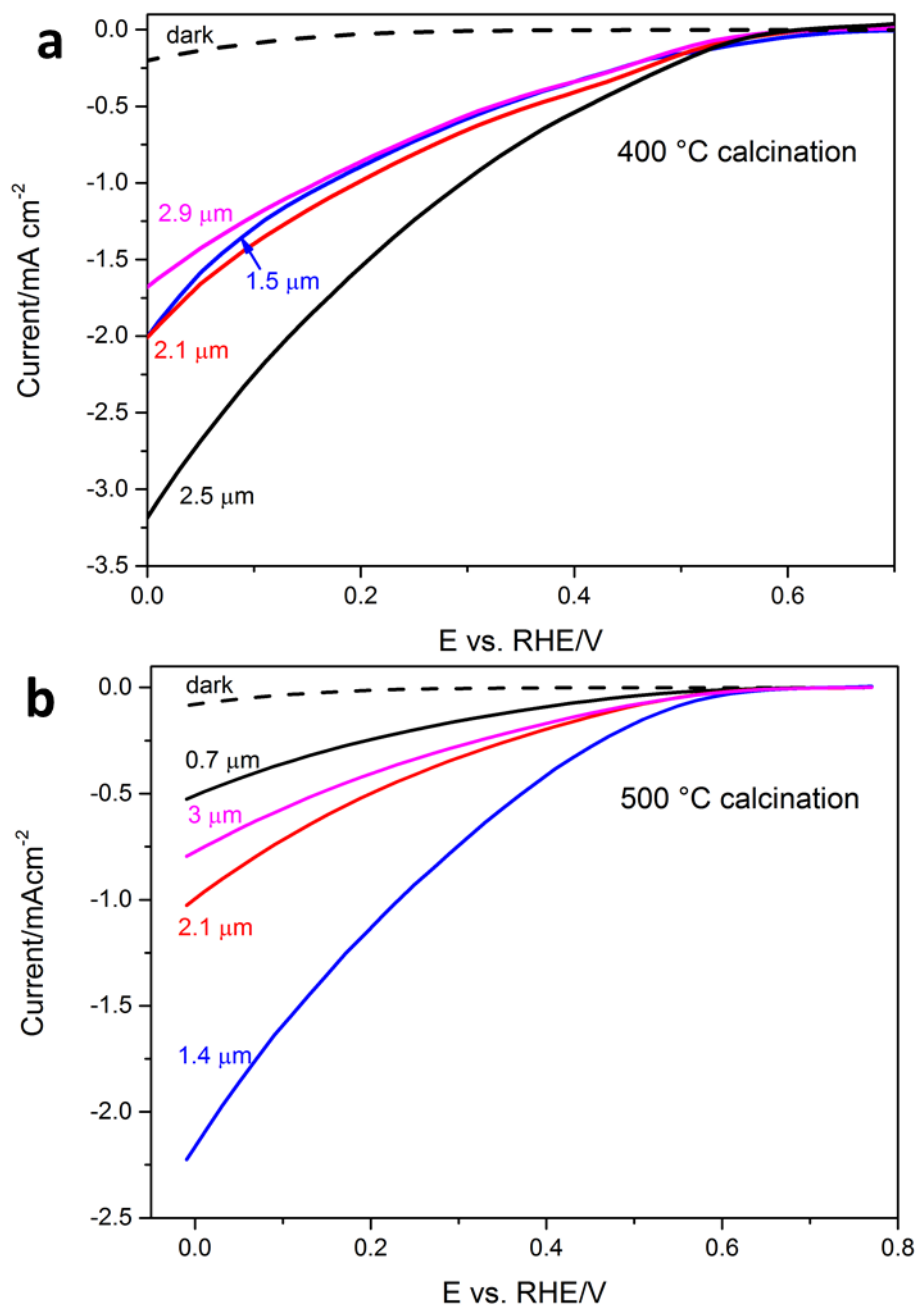


Figure S 7-6: Cyclic voltammetry measurements of Li doped CuO films calcined at 400 °C (a) and 500 °C (b) showing the influence of film thickness on the current density.

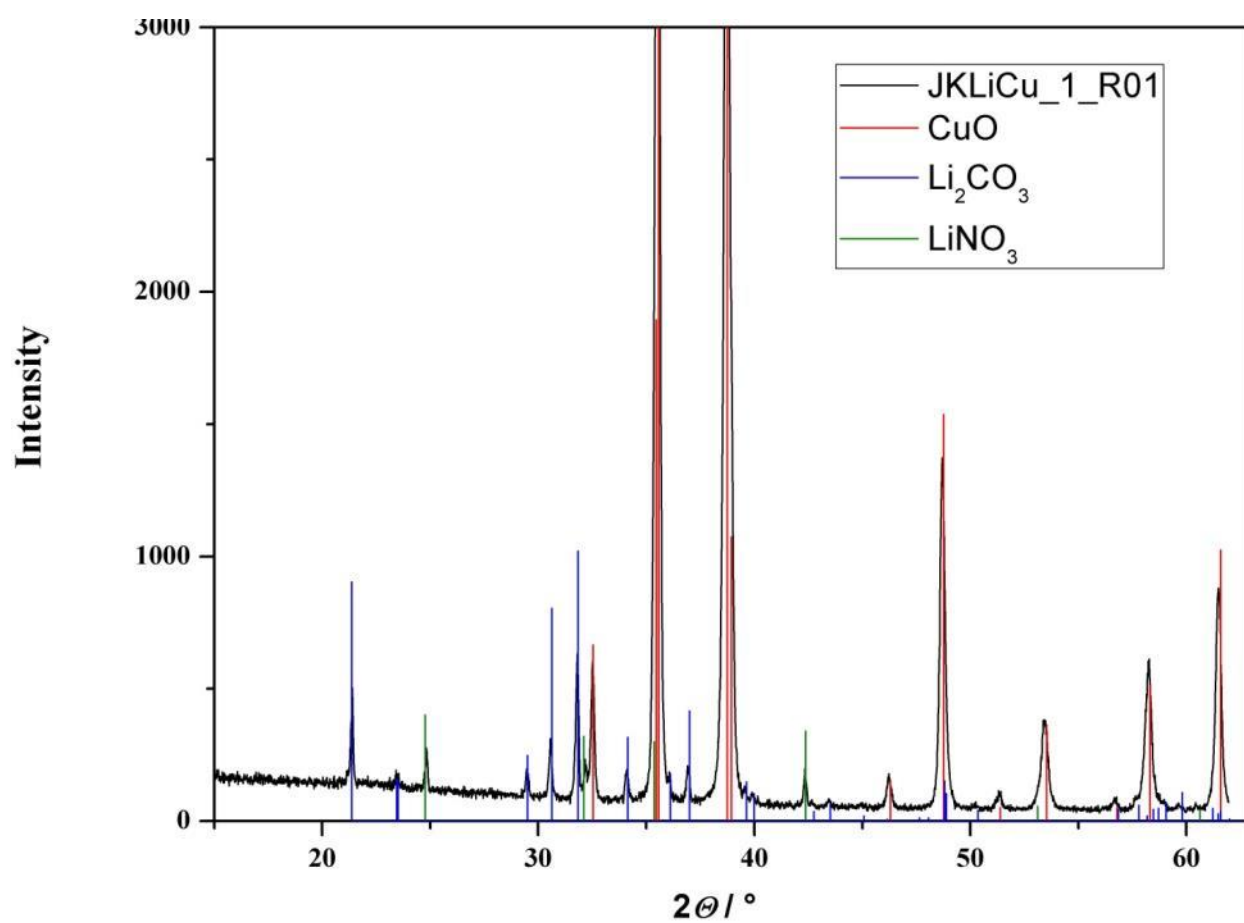


Figure S 7-7: XRD pattern of the film obtained directly after calcination. The film is a mixture of Li doped CuO, Li₂CO₃ and LiNO₃. To obtain the single Li doped CuO phase the film is immersed in water for 2 hours removing Li₂CO₃ and LiNO₃.

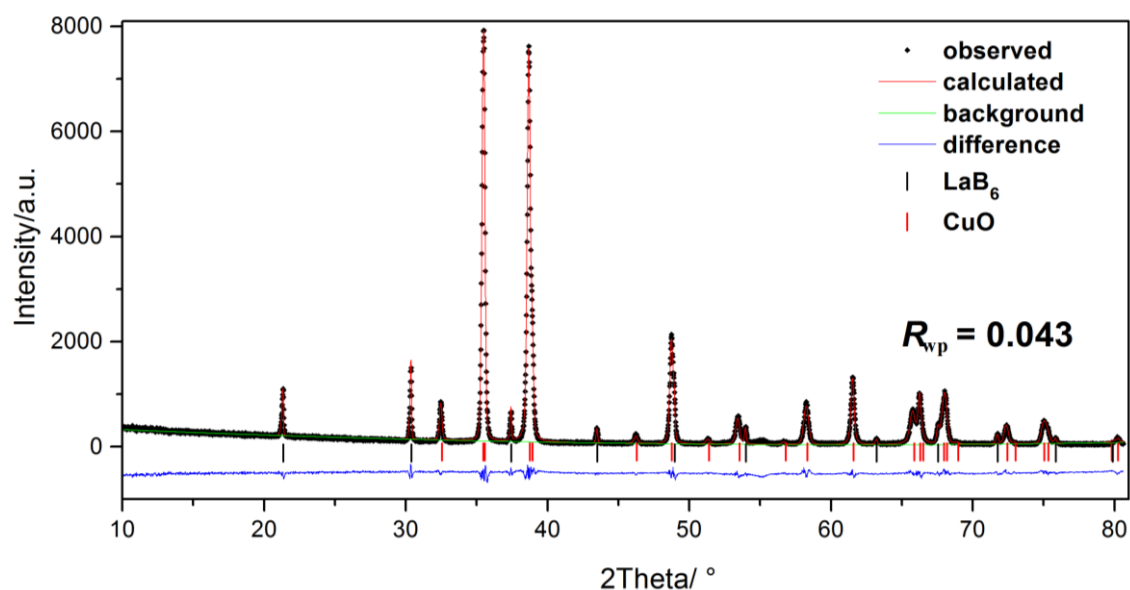


Figure S 7-8: Rietveld refinement of $\text{Li}_x\text{Cu}_{1-x}\text{O}$ with 5% LaB_6 (NIST SRM 660b) added as an internal standard. The difference between the observed data (\blacklozenge) and calculated pattern (red line) is shown as a blue line below. Black and red vertical bars mark the positions of the diffraction lines of LaB_6 and CuO (tenorite), respectively.

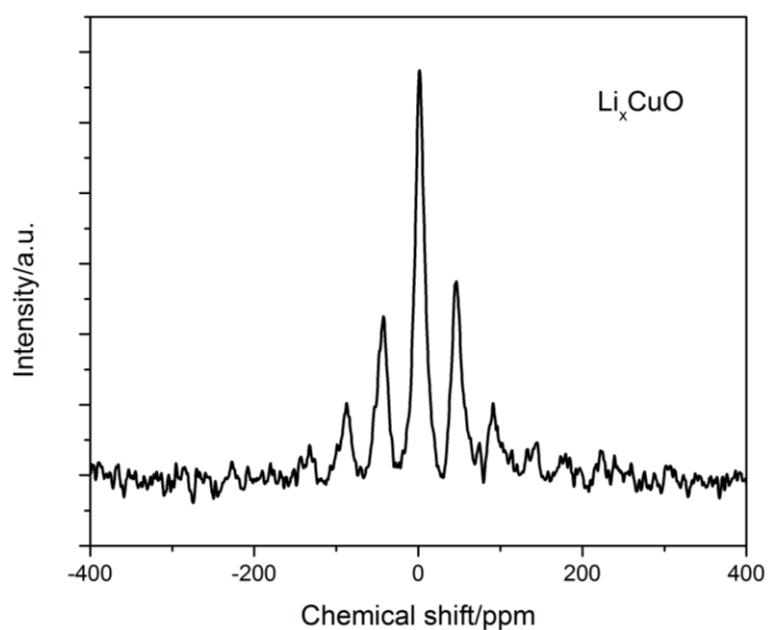


Figure S 7-9: ^7Li -NMR spectra of Li_xCuO .

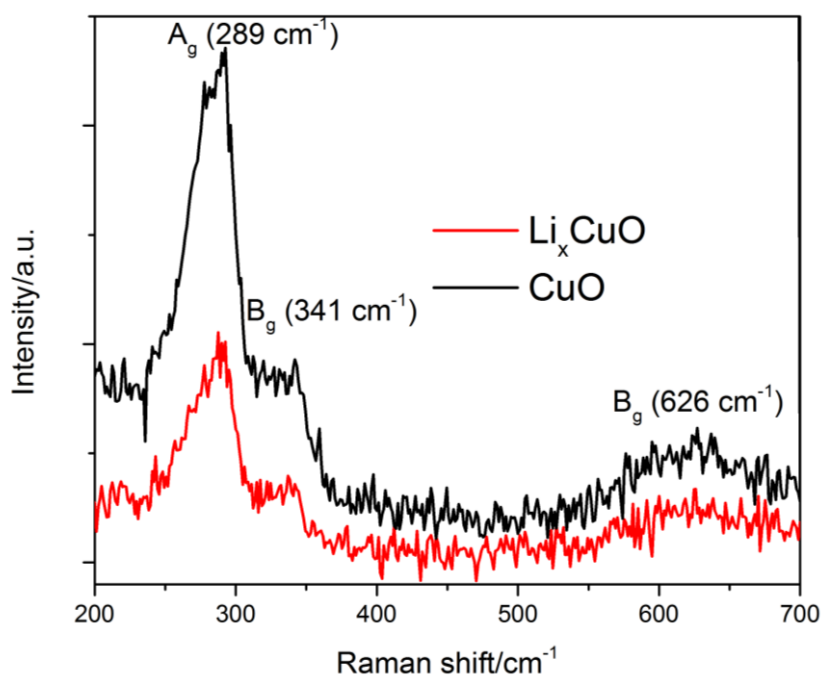


Figure S 7-10: Raman spectra of CuO and Li_xCuO.

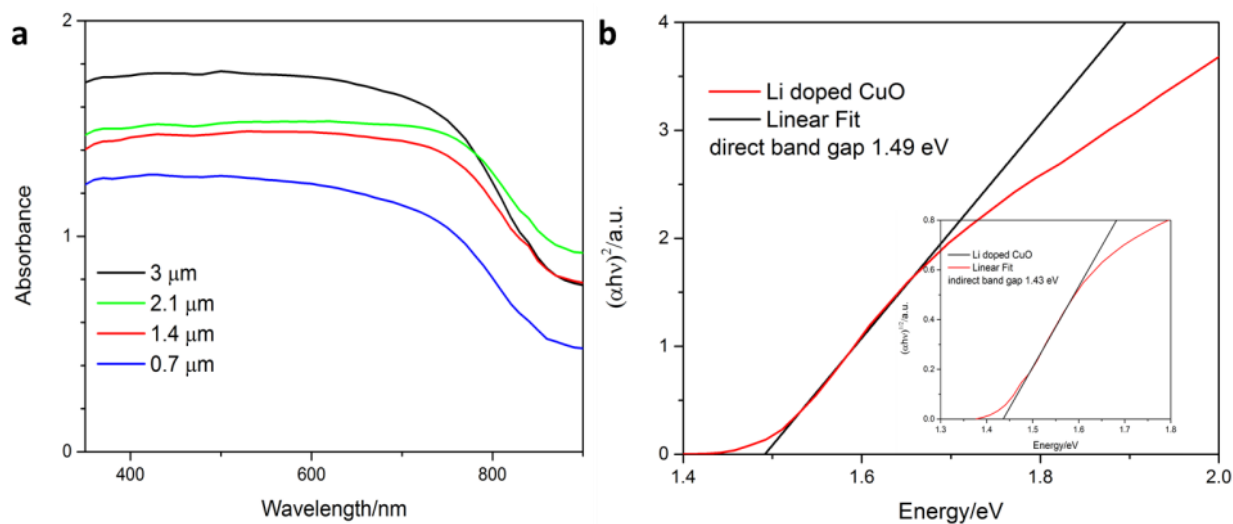


Figure S 7-11: (a) UV-Vis absorption spectra of Li_xCuO films with different thicknesses on FTO. (b) Tauc plot of Li_xCuO with a determined direct band gap of 1.49 eV.

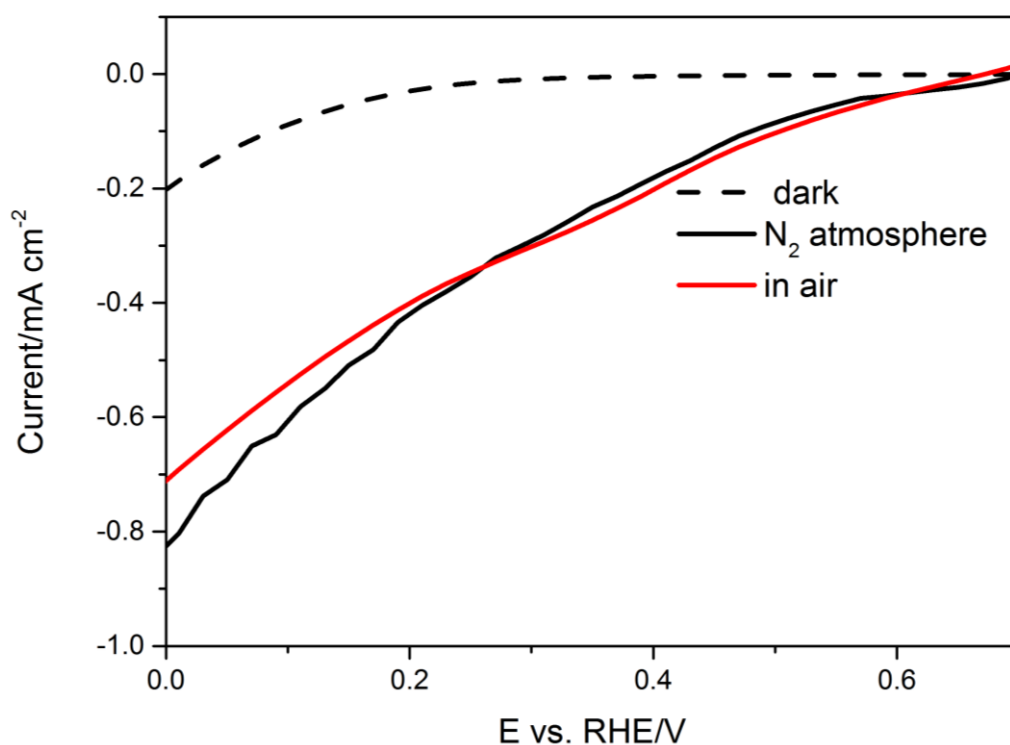


Figure S 7-12: Cyclic voltammetry measurements of Li doped CuO films N₂ atmosphere and in air. The films were illuminated with a 455 nm LED.

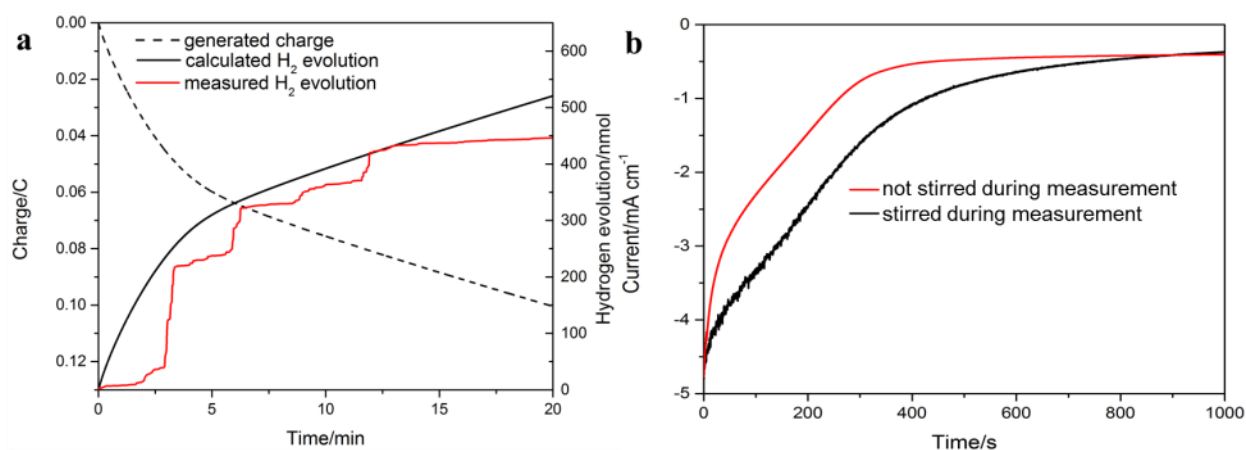


Figure S 7-13: (a) Calculated charge and hydrogen evolution as well as experimentally measured hydrogen evolution determined over 30 minutes at 0.2 V vs. RHE under 455 nm substrate illumination. (b) Stability measurements performed at 0.2 V vs. RHE under 455 nm substrate illumination show the influence of diffusion on the device performance. The current

used for calculation of generated charge and hydrogen is shown in red without stirring the electrolyte during measurement.

We have systematically explored the effect of U on the electronic properties and in particular the type and size of the gap of CuO . The results are summarized in Fig. 8a and show that the indirect band gap of CuO increases with U up to $U = 8\text{ eV}$ and switches to a direct band gap of 2.1 eV beyond 8 eV . The best compromise with respect to gap size (the experimental indirect band gap is 1.49 eV) and type can be achieved using $U = 8\text{ eV}$. The variation of lattice constants as a function of U is presented in Fig. 8b. The DFT predictions are in overall agreement with experimental lattice constants (denoted by dashed lines) where a jump occurs between $U = 8\text{ eV}$ and $U = 8.5\text{ eV}$ associated with the transition from indirect to direct band gap.

Error! Reference source not found.a shows the calculated band gap of CuO for different U values identifying a U value of 8 being in good agreement with the experimentally observed band gap of 1.49 eV . Further, the lattice constants were calculated with respect to different U values (**Error! Reference source not found.**b). The lattice constants predicted by DFT are in good agreement with the experimental values.

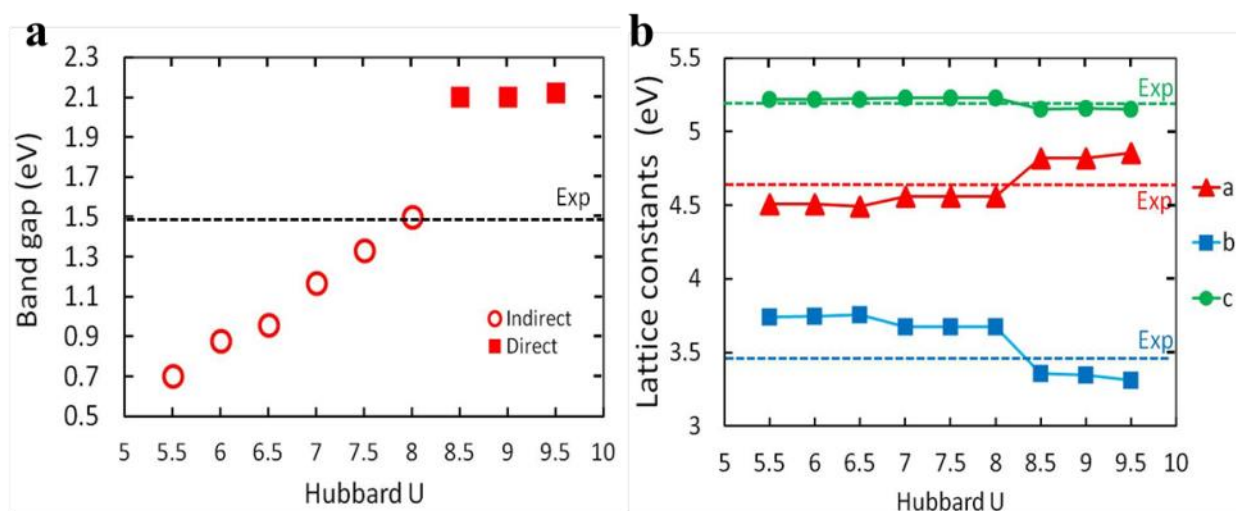


Figure S 7-14: Band gap (a) and lattice constants (b) of CuO for different U values correlated with experimental data.

The spin density of both compounds in SI **Error! Reference source not found.** In pure CuO, the magnetic moment of $0.7 \mu_B$ per Cu site implies the oxidation state of +2. For high Lithium concentrations in $\text{Li}_{0.25}\text{Cu}_{0.75}\text{O}$ the oxidation state of 1/3 of Cu atoms switches to +1 which reduces the band gap to 0.9 eV. In contrast, for low lithium concentration copper remains bulk-like (Cu^{2+}), however there is a notable delocalized contribution of oxygen to the spin density, confirming the p-type character of conductivity

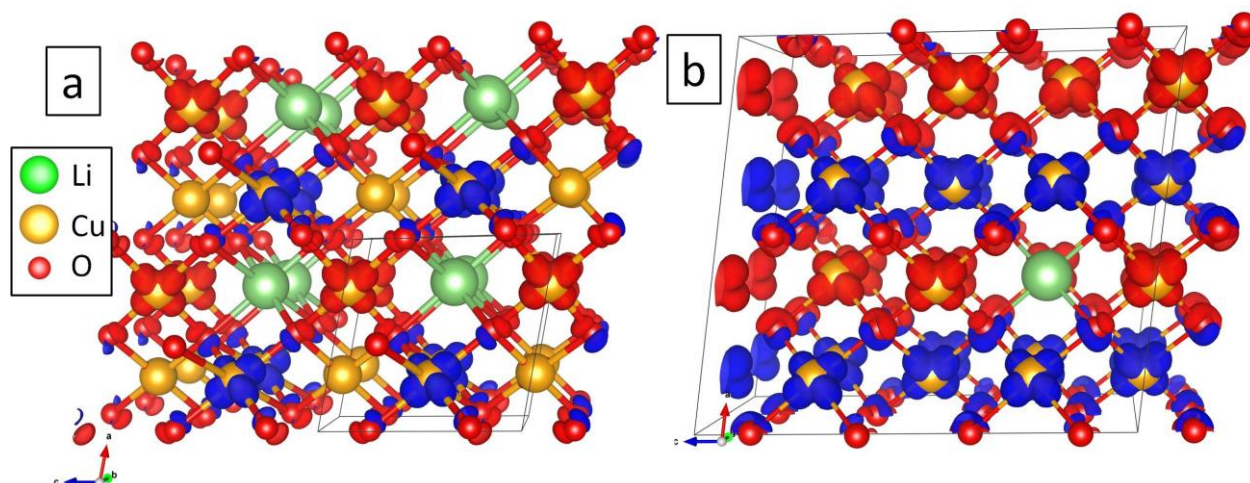


Figure S 7-15: (Color online) Spin density of lithium doped CuO in two different Li concentrations of (a) $\text{Li}_{0.25}\text{Cu}_{0.75}\text{O}$ and (b) $\text{Li}_{0.0312}\text{Cu}_{0.968}\text{O}$ (Isosurface of $0.01 \text{ e}/\text{\AA}^3$). Majority and minority densities are shown by blue and red, respectively. Note the significant contribution of oxygen for the low Li doping concentration of 3%.

In most cases of Li substitution, the copper atoms of the same layer have similar SE. The only exception is doping of Li with surface Cu atoms in O-Cu-R. To understand this behavior, we plot the charge density of pure and Li doped CuO surface in SI. In pure O-Cu-R termination (Figure xx.a and b), two types of Cu with different valence, i.e. Cu^{1+} and Cu^{2+} atoms are available which is the reason for different trends in Li doping (Fig. 11). Substitution of Cu^{+1} by Li is energetically more favorable as shown in (Fig12.c). In Cu-O-R, both surface Cu atoms have the same oxidation state of +3 and are consequently equivalent. Despite of significant surface relaxation induced by the Li doping, the oxidation state of surface Cu atoms remain unchanged.

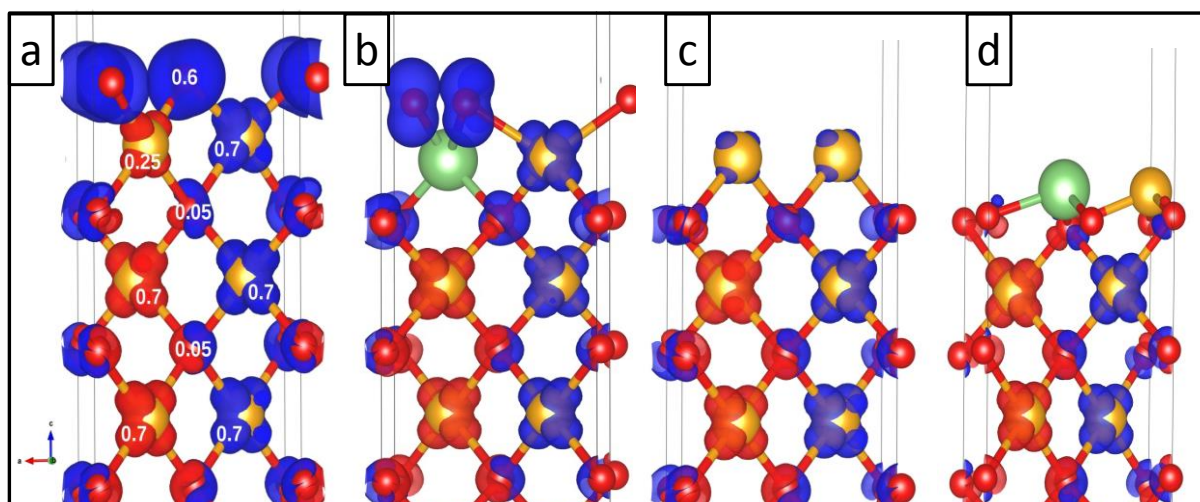


Figure S 7-16: Spin density of the pure and Li-doped CuO(001) surface for (a and b) O-Cu-R and (c and d) Cu-O-R terminations (Isosurface of $0.01 e/\text{\AA}^3$). Additionally, the magnetic moments for pure O-Cu-R are displayed in a).

To explore the electronic properties of the (001) CuO surface the surface density of states was plotted for both pure and Li doped surfaces with Cu and O terminations. The pure O-Cu-R is still a semiconductor with a small band gap of 0.2 eV. Doping with Li shifts the DOS to higher values and produces a *p* type conductor. The Cu-O-R surface is already a conductor, and the DOS shift to positive values by Li doping.

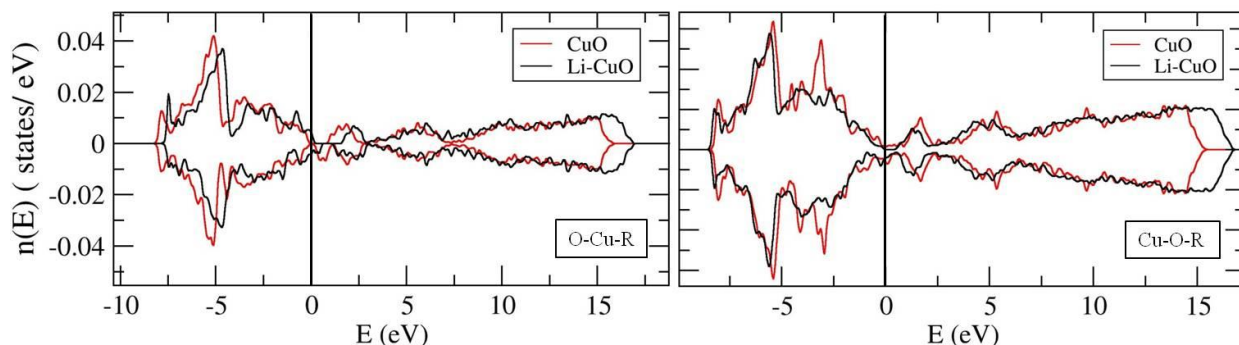


Figure S 7-17: Density of states of the pure and doped surfaces and both Cu-O-R and O-Cu-O terminations. The Fermi level is set to the zero.

7.6 References

1. Hisatomi, T.; Kubota, J.; Domen, K., Recent advances in semiconductors for photocatalytic and photoelectrochemical water splitting. *Chemical Society Reviews* **2014**, *43* (22), 7520-7535.
2. Tachibana, Y.; Vayssieres, L.; Durrant, J. R., Artificial photosynthesis for solar water-splitting. *Nat Photon* **2012**, *6* (8), 511-518.
3. Prevot, M. S.; Guijarro, N.; Sivula, K., Enhancing the Performance of a Robust Sol-Gel-Processed p-Type Delafossite CuFeO₂ Photocathode for Solar Water Reduction. *ChemSusChem* **2015**, *8* (8), 1359-1367.
4. Rowley, J. G.; Do, T. D.; Cleary, D. A.; Parkinson, B. A., Combinatorial Discovery Through a Distributed Outreach Program: Investigation of the Photoelectrolysis Activity of p-Type Fe, Cr, Al Oxides. *ACS Applied Materials & Interfaces* **2014**, *6* (12), 9046-9052.
5. Chiang, C.-Y.; Shin, Y.; Ehrman, S., Dopant Effects on Copper Oxide Photoelectrochemical Cell Water Splitting. *Energy Procedia* **2014**, *61* (0), 1799-1802.
6. Qi, X.; She, G.; Wang, M.; Mu, L.; Shi, W., Electrochemical synthesis of p-type Zn-doped [small alpha]-Fe₂O₃ nanotube arrays for photoelectrochemical water splitting. *Chemical Communications* **2013**, *49* (51), 5742-5744.

7. Zhang, Z.; Wang, P., Highly stable copper oxide composite as an effective photocathode for water splitting via a facile electrochemical synthesis strategy. *Journal of Materials Chemistry* **2012**, 22 (6), 2456-2464.
8. Guo, X.; Diao, P.; Xu, D.; Huang, S.; Yang, Y.; Jin, T.; Wu, Q.; Xiang, M.; Zhang, M., CuO/Pd composite photocathodes for photoelectrochemical hydrogen evolution reaction. *International Journal of Hydrogen Energy* **2014**, 39 (15), 7686-7696.
9. Koffyberg, F.; Benko, F., A photoelectrochemical determination of the position of the conduction and valence band edges of p-type CuO. *Journal of Applied Physics* **1982**, 53 (2), 1173-1177.
10. Chauhan, D.; Satsangi, V.; Dass, S.; Shrivastav, R., Preparation and characterization of nanostructured CuO thin films for photoelectrochemical splitting of water. *Bulletin of Materials Science* **2006**, 29 (7), 709.
11. Paracchino, A.; Laporte, V.; Sivula, K.; Grätzel, M.; Thimsen, E., Highly active oxide photocathode for photoelectrochemical water reduction. *Nat Mater* **2011**, 10 (6), 456-461.
12. Chand, P.; Gaur, A.; Kumar, A.; Kumar Gaur, U., Structural and optical study of Li doped CuO thin films on Si (100) substrate deposited by pulsed laser deposition. *Applied Surface Science* **2014**, 307 (0), 280-286.
13. Chiang, C.-Y.; Shin, Y.; Ehrman, S., Li doped CuO film electrodes for photoelectrochemical cells. *Journal of The Electrochemical Society* **2011**, 159 (2), B227-B231.
14. Fuoco, L.; Joshi, U. A.; Maggard, P. A., Preparation and Photoelectrochemical Properties of p-type Cu₅Ta₁₁O₃₀ and Cu₃Ta₇O₁₉ Semiconducting Polycrystalline Films. *The Journal of Physical Chemistry C* **2012**, 116 (19), 10490-10497.
15. Shannon, R., Revised effective ionic radii and systematic studies of interatomic distances in halides and chalcogenides. *Acta Crystallographica Section A* **1976**, 32 (5), 751-767.
16. Jang, Y. J.; Jang, J.-W.; Choi, S. H.; Kim, J. Y.; Kim, J. H.; Youn, D. H.; Kim, W. Y.; Han, S.; Sung Lee, J., Tree branch-shaped cupric oxide for highly effective photoelectrochemical water reduction. *Nanoscale* **2015**, 7 (17), 7624-7631.
17. Peter, L.; Ponomarev, E.; Fermin, D., Intensity-modulated photocurrent spectroscopy: reconciliation of phenomenological analysis with multistep electron transfer mechanisms. *Journal of Electroanalytical Chemistry* **1997**, 427 (1), 79-96.

18. Peter, L. M.; Wijayantha, K. U.; Tahir, A. A., Kinetics of light-driven oxygen evolution at α -Fe₂O₃ electrodes. *Faraday discussions* **2012**, *155*, 309-322.
19. Ponomarev, E.; Peter, L., A generalized theory of intensity modulated photocurrent spectroscopy (IMPS). *Journal of Electroanalytical Chemistry* **1995**, *396* (1), 219-226.
20. Soedergren, S.; Hagfeldt, A.; Olsson, J.; Lindquist, S.-E., Theoretical Models for the Action Spectrum and the Current-Voltage Characteristics of Microporous Semiconductor Films in Photoelectrochemical Cells. *The Journal of Physical Chemistry* **1994**, *98* (21), 5552-5556.
21. Leng, W. H.; Barnes, P. R. F.; Juozapavicius, M.; O'Regan, B. C.; Durrant, J. R., Electron Diffusion Length in Mesoporous Nanocrystalline TiO₂ Photoelectrodes during Water Oxidation. *The Journal of Physical Chemistry Letters* **2010**, *1* (6), 967-972.
22. Wang, H.; Lindgren, T.; He, J.; Hagfeldt, A.; Lindquist, S.-E., Photoelectrochemistry of Nanostructured WO₃ Thin Film Electrodes for Water Oxidation: Mechanism of Electron Transport. *The Journal of Physical Chemistry B* **2000**, *104* (24), 5686-5696.
23. Nørskov, J. K.; Bligaard, T.; Logadottir, A.; Kitchin, J.; Chen, J.; Pandelov, S.; Stimming, U., Trends in the exchange current for hydrogen evolution. *Journal of The Electrochemical Society* **2005**, *152* (3), J23-J26.
24. Rietveld, H., A profile refinement method for nuclear and magnetic structures. *Journal of Applied Crystallography* **1969**, *2* (2), 65-71.
25. Kresse, G.; Hafner, J., *Ab initio* molecular-dynamics simulation of the liquid-metal/amorphous-semiconductor transition in germanium. *Physical Review B* **1994**, *49* (20), 14251-14269.
26. Kresse, G.; Furthmüller, J., Efficiency of ab-initio total energy calculations for metals and semiconductors using a plane-wave basis set. *Computational Materials Science* **1996**, *6* (1), 15-50.
27. Blöchl, P. E., Projector augmented-wave method. *Physical Review B* **1994**, *50* (24), 17953-17979.
28. Perdew, J. P.; Burke, K.; Ernzerhof, M., Generalized Gradient Approximation Made Simple. *Physical Review Letters* **1996**, *77* (18), 3865-3868.
29. Dudarev, S. L.; Botton, G. A.; Savrasov, S. Y.; Humphreys, C. J.; Sutton, A. P., Electron-energy-loss spectra and the structural stability of nickel oxide: An LSDA+U study. *Physical Review B* **1998**, *57* (3), 1505-1509.

8 Conclusion and Outlook

Photoelectrochemical water splitting has been investigated for over 50 years to deliver a variety of photoabsorber materials, morphologies and catalysts capable of reaching high solar to hydrogen conversion efficiencies. Yet, the industrial implementation of stand-alone photoelectrochemical systems has not been accomplished. Although the concept of a direct solar water offers numerous advantages, it has not reached the required efficiencies, making research in this area challenging and exciting.

The main focus of the presented thesis was the development and improvement of photoabsorber systems for solar-driven water splitting. The first part concentrated on improving well known photoelectrode systems such as Fe_2O_3 or WO_3 . The preparation of high surface area macroporous scaffolds with a defined inverse opal structure was one of the first steps to the implementation of the host guest architectures. The preparation of highly ordered PMMA opal structures on FTO and the subsequent synthesis development of inverse opals from different metal oxides were of central importance. The successful deposition of an absorber layer on the scaffold showed that a host guest architecture can influence the electrode performance beneficially. First, the scaffold acts as a majority carrier extraction material thus reducing recombination in the photoabsorber. As a result, the deposition of a photoabsorber, in this case Fe_2O_3 , on a suitable scaffold showed to increase the majority carrier diffusion length in the electrode sufficiently. Second, the high surface area of the host offers a larger deposition platform for the photoabsorber compared to a flat layer. The increased material loading results in higher light harvesting efficiency and therefore higher currents. The material absorbance is further enhanced by the increased scattering from the macroporous host structure.

Host guest architectures were further improved by depositing an additional absorber layer as a surface treatment, as was shown in Chapter 4 for a macroporous $\text{WO}_3/\text{Fe}_2\text{O}_3/\text{WO}_3$ system. The WO_3 acts as an absorber layer in the UV range and as a reflection layer for visible light thus increasing the light harvesting efficiency of Fe_2O_3 resulting in higher photocurrents. Furthermore a shift of the onset potential by 200 mV could be observed.

As seen in literature, most of the materials investigated as photoabsorbers so far have not delivered the promised performance. A possible solution of the problem is therefore the discovery of new active material classes such as binary or ternary oxides. A combinatorial screening approach identified a new compound, a $\text{Fe}_{0.84}\text{Cr}_1\text{Al}_{0.16}\text{O}_3$, as a promising photocathode for photoelectrochemical water splitting by measuring a few microampere photoresponse upon illumination. In the project presented in Chapter 6 we have focused on the large-scale synthesis and structure optimization of this material composition to achieve the highest photocurrent and IPCE values reported so far for this system. The composition and the crystalline structure of the novel electrode morphologies was thoroughly analysed by TEM measurements revealing a phase separation of the mixed metal oxide on the nanoscale. By introducing a macroporous inverse opal structure to the FeCrAl oxide the device performance increased by over three times. This observation was further confirmed by quantitative and qualitative hydrogen evolution measurements showing the increase in evolved hydrogen gas.

The concept of finding new potential photoabsorber candidate materials was further pursued by synthesizing a Li doped CuO photocathode which outperformed other similar electrodes reported in literature as described in Chapter 7. We focus on the thorough characterization of the film in the search for an explanation as to why Li doped CuO electrodes outperform pure CuO photocathodes. Next to a strong impact on the morphology and crystallinity we found that Li insertion leads to a 10-fold increase of the hole diffusion length in the film.

Furthermore, a change in the electronic structure and particularly an upward shift of band levels due to Li dopin could be identified by DFT calculations. Computational analysis confirmed that Li doping increased the p-type behavior of the CuO electrode and decreased the hydrogen adsorption energy thus reducing the reaction overpotential according to the Sabatier principle.

In conclusion, this thesis presented different strategies to improve the process of water splitting in the hope that it will become an industrially applicable clean energy resource in the near future. Solar-driven water splitting requires thorough research on many levels from the choice of the right photoabsorber over the application of efficient catalysts to the stabilization of the device. All compoments of the water splitting device have to play in concert in order to deliver an efficient technology for sustainable energy production.

10 Publications and Presentations

10.1 Publications

1. Electron Collection in Host-Guest Nanostructured Hematite Photoanodes for Water Splitting: The Influence of Scaffold Doping Density

Kondofersky, I.; Dunn, H. K.; Mueller, A.; Mandlmeier, B.; Feckl, J. M.; Fattakhova-Rohlfing, D.; Scheu, C.; Peter, L. M.; Bein, T. *Chem. ACS Appl. Mater. & Interf.* **2015**, 7(8), 4623-4630.
2. Ultrasmall Co₃O₄ Nanocrystals Strongly Enhance Solar Water Splitting on Mesoporous Hematite

Feckl, J. M.; Dunn, H. K.; Zehetmaier, P. M.; Mueller, A.; Pendlebury, S. R.; Zeller, P.; Fominykh, K.; Kondofersky, I.; Doeblinger, M.; Durrant, J. R.; Scheu, C.; Peter, L.; Fattakhova-Rohlfing, D.; Bein, T., *Adv. Mater. Interf.*, **2015**, 2(18).
3. Nanostructured Ternary FeCrAl Oxide Photocathodes for Water Photoelectrolysis

Kondofersky, I.; Mueller, A.; Dunn, H. K.; Ivanova, A.; Stefanic, G.; Ehrensperger, M.; Scheu, C.; Parkinson, B. A.; Fattakhova-Rohlfing, D.; Bein, T. *J. Am. Chem. Soc.*, **2016**, 138(6), 1860-1867.
4. Dual Absorber WO₃/Fe₂O₃ Host-Guest Architectures for Improved Charge Generation and Transfer in Photoelectrochemical Water Splitting

Kondofersky, I.; Müller, A.; Folger, A.; Fattakhova-Rohlfing, D.; Scheu, C. and Bein, T., submitted.

5. Li_xCuO photocathodes for improved hole collection efficiency in photoelectrochemical water splitting

Kondofersky, I.; Kampmann, J.; Hajiyani, H.; Döblinger, M.; Štefanić, G.; Pencheva, R.; Fattakhova-Rohlfing, D.; Bein, T., to be submitted.

10.2 Oral presentations

1. Novel materials for photoelectrochemical water splitting: Structuring FeCrAl oxide

Irina Kondofersky, Alexander Müller, Halina Dunn, Bruce Parkinson, Dina Fattakhova-Rohlfing, Christina Scheu and Thomas Bein

SPP 1613 Solar Fuels Meeting, **2014**, Darmstadt, Germany

2. Nanostructured p-type ternary oxides for photoelectrochemical water splitting

Irina Kondofersky, Alexander Müller, Jonathan Kampmann, Bruce Parkinson, Dina Fattakhova-Rohlfing, Christina Scheu and Thomas Bein

SolTech Conference **2016**, Munich, Germany.

10.3 Poster presentations

3. Ordered macroporous tin oxide nanostructures as an anode host scaffold for water splitting applications

Irina Kondofersky, Benjamin Mandlmeier, Johann Feckl, Halina Dunn, Dina Fattakhova-Rohlfing and Thomas Bein

Center for NanoScience (CeNS) Workshop, **2012**, Venice, Italy.

4. Macroporous host-guest nanostructures as anode scaffolds for water splitting applications

Iilina Kondofersky, Halina Dunn, Alexander Müller, Christina Scheu and Thomas Bein

2nd International Congress Next Generation Solar Energy, **2012**, Erlangen, Germany.

5. Electron Collection in Host-Guest Nanostructured Hematite Photoanodes

Iilina Kondofersky, Halina Dunn, Alexander Müller, Dina Fattakhova-Rohlfing, Christina Scheu and Thomas Bein

SPP 1613 Solar Fuels Meeting, **2013**, Ellwangen, Germany.

6. Nanostructured p-type ternary oxides for photoelectrochemical water splitting

Iilina Kondofersky, Halina Dunn, Bruce Parkinson, Alexander Müller, Christina Scheu, Dina Fattakhova-Rohlfing and Thomas Bein

Annual Soltech Meeting, **2014**, Wildbad Kreuth, Germany.

7. Nanostructured p-type ternary oxides for photoelectrochemical water splitting

Iilina Kondofersky, Halina Dunn, Bruce Parkinson, Dina Fattakhova-Rohlfing and Thomas Bein

20th International Conference on Conversion and Storage of Solar Energy (IPS 20), 2014, Berlin, Germany.

8. Nanostructured FeCrAl oxide for photoelectrochemical water splitting

Iilina Kondofersky, Halina Dunn, Bruce Parkinson, Dina Fattakhova-Rohlfing and Thomas Bein

6th Conference of the Federation of the European Zeolite Association (FEZA), **2014**, Leipzig, Germany.

9. Electron collection in host-guest nanostructured hematite photoanodes for water splitting

Irina Kondofersky, Alexander Müller, Halina K. Dunn, Dina Fattakhova-Rohlfing, Christina Scheu, Laurence M. Peter, Thomas Bein

Solar Fuel Conference, **2015**, Mallorca, Spain.

10. Nanostructured FeCrAl oxide for photoelectrochemical water splitting

Irina Kondofersky, Alexander Müller, Halina Dunn, Bruce Parkinson, Christina Scheu, Dina Fattakhova-Rohlfing and Thomas Bein

SPP 1613 Solar Fuels Meeting, **2015**, Bergisch Gladbach, Germany.